UNIMORE
UNIVERSITÀ DEGLI STUDI DI
MODENA E REGGIO EMILIA

University of Modena and Reggio Emilia

Department of Physics, Informatics and Mathematics

PhD School in

Physics and Nanosciences

XXXVIII Cycle

Computational Study of Interfacial Processes in Electrochemical Devices

Advisors:
Prof. Elena Degoli

Co-advisor:
Prof. Rita Magri

Second co-advisor:
Prof. Alice Ruini

Candidate:
Dr. Mostafa Salimi

PhD School Coordinator:
Prof. Marco Affronte

Academic Year 2024–2025

Contents

Abbreviations

Abbreviation	Definition
AFC	Alkaline Fuel Cell
BASE	Beta-Alumina Solid Electrolyte
CDD	Charge Density Difference
DFT	Density Functional Theory
DFT+U	Density Functional Theory + Hubbard correction
DMFC	Direct Methanol Fuel Cell
EV	Electric Vehicle
FC	Fuel Cell
FCC	Face-Centered Cubic
FCV	Fuel Cell Vehicle
GGA	Generalized Gradient Approximation
HOMO	Highest Occupied Molecular Orbital
HOR	Hydrogen Oxidation Reaction
ICE	Internal Combustion Engine
LDA	Local-Density Approximation
LDOS	Local Density of State
LIB	Lithium-Ion Battery
LUMO	Lowest Unoccupied Molecular Orbital
MCFC	Molten Carbonate Fuel Cell
MEA	Membrane Electrode Assembly
ORR	Oxygen Reduction Reaction
PAFC	Phosphoric Acid Fuel Cell
PBA	Process Behavior Analysis
PBC	Process Behavior Chart
PEMFC	Proton Exchange Membrane Fuel Cell
PTFE	Polytetrafluoroethylene
PVDF	PolyVinylidene diFluoride
SEI	Solid-Electrolyte Interphase
SIE	Self-Interaction Error
SOFC	Solid Oxide Fuel Cell
vdW	van der Waals
XC	Exchange Correlation

List of Figures

List of Tables

List of Equations

List of Publications and Contributions

- **Salimi, M.**, Magri, R., Maji, R., & Degoli, E. (2025). First-principles modeling of PVdF on oxidized silicon surface for next-generation Li-ion anodes.
  Journal of Energy Storage, 140, 119079. https://doi.org/10.1016/j.est.2025.119079

- **Salimi, M.**, Degoli, E., & Magri, R. (2025). Aqueous Nafion–Platinum Interface for PEM Fuel Cells: An *ab initio* perspective.
  Manuscript under review. Preprint available at SSRN: 5240532.

- **Salimi, M.**, Magri, R., Maji, R., & Degoli, E. First-principles insights into PVdF binder interactions with oxidized silicon surfaces for enhanced lithium-ion battery anodes.
  Poster presentation at the **Psi-k Conference 2025**, SwissTech Convention Center, EPFL, Lausanne, Switzerland, 25–28 August 2025.

- **Salimi, M.**, Magri, R., & Degoli, E. Simulating the platinum–Nafion interface: A computational window into PEM fuel cell efficiency.
  Poster presentation at **Virtual Materials Design: AI, Simulation, and Workflows**, Karlsruhe Institute of Technology (KIT), Karlsruhe, Germany, 2–5 June 2025.

- **Salimi, M.**, Magri, R., & Degoli, E. Interface characterization of platinum–Nafion for fuel cell applications.
  Oral presentation at the **MOST–Spoke 12 Young Researchers Meeting**, University of Florence, Florence, Italy, 30–31 January 2025.

- **Salimi, M.**, Magri, R., Maji, R., & Degoli, E. Ab initio study of PVDF on oxidized silicon for advanced Li-ion anode materials.
  Poster presentation at the **22nd International Workshop on Computational Physics and Materials Science: Total Energy and Force Methods (SMR 3814)**, International Centre for Theoretical Physics (ICTP), Trieste, Italy, 11–13 January 2025.

Acknowledgments

The journey through a doctorate is never a solitary one. Behind every page of this dissertation, there is an invisible network of people who offered guidance, time, and trust. At the center of this network stand the supervisors, who not only shape the scientific direction of the work but also quietly sustain the person carrying it out. Their influence reaches far beyond publications and results; it defines how one learns to think, to question, and to persist.

I am deeply and sincerely grateful to my supervisors, **Prof. Rita Magri** and **Prof. Elena Degoli**, for their constant guidance and warm-hearted support throughout this journey. Their scientific insight has been a compass in complex problems, and their patience and encouragement have made even the most difficult stages manageable. I have learned from them not only how to do research, but also how to be rigorous without losing curiosity, and critical without losing kindness. It has been a privilege to grow as a researcher under their supervision.

My thanks also go to the University of Modena and Reggio Emilia (UNIMORE) and the National Research Council (CNR), in particular to the professors, researchers, and technical staff of the Department of Physics, Informatics and Mathematics (FIM-Modena), and the Department of Sciences and Methods for Engineering (DISMI-Reggio Emilia). Their dedication has created an environment where research is both demanding and genuinely stimulating. The support I received—from scientific discussions to practical assistance with laboratories, computational facilities, and administrative processes—has been essential for bringing this work to completion.

This dissertation has been made possible thanks to the financial support of PNRR (Piano Nazionale di Ripresa e Resilienza), Italy's National Recovery and Resilience Plan. I gratefully acknowledge this funding, which enabled the research activities underlying this thesis and reflects a broader commitment to advancing next-generation electrochemical technologies.

Finally, I would like to thank all those—inside and outside academia—who, through their presence, advice, and encouragement, helped transform these demanding years into a meaningful and memorable part of my life.

Dedication

I wish to express my deepest gratitude to my family, whose unwavering support, patience, and encouragement have accompanied me through every stage of my life. Their love has been a constant source of strength and reassurance throughout this journey.

In loving memory of my father, whose values, wisdom, and presence continue to guide and inspire me, even in his absence.

This dissertation is dedicated to my wife, ***Lida****, whose understanding, inspiration, and steadfast emotional support have been indispensable during this important chapter of my life. Her belief in me has given meaning and direction to this work.*

Introduction

Electrochemical energy-conversion and energy-storage technologies lie at the heart of the global transition toward cleaner and more sustainable power systems. Devices such as proton exchange membrane fuel cells (PEMFCs) and lithium-ion batteries (LIBs) play crucial roles in decarbonizing transportation, enabling renewable-energy integration, and powering portable electronics. Their performance, durability, and efficiency, however, are governed not only by their bulk materials but by the atomic-scale processes that occur at their internal interfaces. Charge transfer, ion transport, polymer degradation, and mechanical stability all originate from nanoscale interactions between electrodes, electrolytes, catalysts, and polymeric components. Understanding these interactions from first principles is therefore essential for the rational design of next-generation electrochemical devices.

Among the many interfaces in these systems, two are particularly critical. In PEMFCs, the boundary between Nafion ionomer and platinum catalyst determines the effectiveness of proton conduction and the stability of the catalyst layer. Conversely, in silicon-based LIB anodes, the interaction between Si surfaces and polymeric binders such as poly(vinylidene fluoride) (PVDF) controls mechanical adhesion, solid-electrolyte interphase (SEI) formation, and long-term cycling behavior. Despite their technological importance, both interfaces remain challenging to study experimentally due to their buried nature and complex chemical environment. Here, first-principles simulations based on density functional theory (DFT) offer a powerful route to uncovering the mechanisms that govern interfacial stability and charge redistribution.

The work presented in this dissertation employs DFT to investigate, at the atomistic level, how polymer orientation, hydration structure, and surface chemistry influence polymer-electrode interactions in PEMFCs and LIBs. For the fuel-cell system, three distinct configurations of Nafion monomers interacting with hydrogen-covered Pt(111) surfaces were constructed to assess how proximity and functional-group orientation affect charge transfer, hydronium formation, and structural stability. The results show that the optimized configurations depend sensitively on the initial placement of the $–SO_3H$ group relative to the Pt surface, which acts as a computational artifact guiding the relaxation toward different local minima. When the group is initially placed too close to the surface, relaxation leads to polymer degradation and significant surface distortion. By contrast, starting from a larger initial separation of 4 Å allows the system to relax into a lower-energy configuration characterized by hydronium formation without damaging either the polymer or the Pt surface.

In the battery study, the adsorption of both α- and β-phase PVDF on oxidized Si(110) surfaces was systematically analyzed, including the effects of oxygen coverage and surface –OH formation. The two phases exhibit markedly different behaviors: the non-polar α-phase interacts weakly through reversible hydrogen bonding, whereas the polar β-phase shows strong orientation-dependent adhesion governed by dipole alignment. Surface hydroxylation further amplifies these effects through modified charge transfer and interfacial polarization. Together, these results establish clear design principles for selecting or engineering binder materials capable of improving interfacial adhesion, stabilizing the SEI, and enhancing the mechanical robustness of silicon anodes.

Overall, this dissertation provides a unified atomistic framework for understanding polymer-electrode interfaces in two of the most important electrochemical devices of our time. By linking molecular-level interactions to macroscopic performance, the study delivers both fundamental insight and practical guidelines for designing more efficient, durable, and chemically resilient fuel-cell membranes and high-capacity battery anodes.

"Everything we call real,
is made of things,
that cannot be regarded as real."

— *Niels Bohr* —
Nobel Prize Laureate in Physics – 1922

1. Fundamentals of Electrochemical Energy Devices

In this chapter, we examine electrochemical energy conversion and storage devices, focusing on fuel cells (Sec. 1.1) and batteries (Sec. 1.2), which are pivotal to addressing global energy challenges. Fuel cells, with their diverse chemistries and applications, offer clean energy solutions, while lithium-ion batteries (LIBs) dominate portable and grid-scale storage due to their high efficiency and scalability. We begin with historical context and classifications, then delve into material-specific challenges, including electrocatalysts, electrolytes, and interfacial phenomena. The chapter concludes with a discussion of persistent limitations and the objectives of this work (Sec. 1.3), setting the stage for subsequent chapters.

❖ Chapter Outline

- **Fuel Cells (Sec. 1.1)**
  - Historical evolution and operational principles.
    (Sec. 1.1.1)
  - Comparative analysis of fuel cell types (AFC, PAFC, SOFC, etc.) and their electrochemistry.
    (Sec. 1.1.2.1-1.1.2.6)
  - Critical materials: Platinum-based electrocatalysts and Nafion electrolytes.
    (Sec. 1.1.3-Sec. 1.1.5)
- **Batteries (Sec. 1.2)**
  - Development and dominance of lithium-ion technology.
    (Sec. 1.2.1)
  - Component-level breakdown: Anodes, cathodes, electrolytes, and interfacial layers.
    (Sec. 1.2.2)
- **Challenges and Objectives (Sec. 1.3)**
  - Key bottlenecks in efficiency, cost, and durability
  - Research aims to overcome these barriers

1.1 Fuel Cells

Fuel cells are open thermodynamic systems that operate based on electrochemical reactions, continuously consuming reactants supplied from an external source. Unlike conventional power generation methods that rely on combustion, fuel cells generate electricity and heat directly through an electrochemical process, which can be considered the reverse of electrolysis. In essence, a fuel cell is an energy conversion device that efficiently transforms chemical energy into electrical energy through redox reactions, typically involving hydrogen and oxygen as the primary reactants [1–4].

Despite the promising efficiencies and environmental benefits offered by fuel cell technology, translating early scientific advancements into commercially viable industrial products has proven challenging [5–7]. This difficulty may be partially attributed to the insufficient development of comprehensive theoretical studies, along with the lack of advanced modeling and simulation tools for fuel cells. The main aims of this study are to address this gap, providing a deeper understanding of the underlying principles and enhancing the predictive capabilities of fuel cell systems, ultimately advancing their commercialization and practical application.

1.1.1 Historical Overview: Two Centuries of Development

The origins of fuel cells remain a topic of debate. According to the U.S. Department of Energy [8], German chemist Christian Friedrich Schönbein first observed the fuel cell phenomenon in 1838, publishing his findings in Philosophical Magazine in early 1839. However, other sources credit Sir William Grove, who that same year demonstrated a hydrogen fuel cell by immersing platinum electrodes in sulfuric acid while exposing them separately to hydrogen and oxygen, generating a continuous electric current [9]. Further advancements came in 1893 when Friedrich Wilhelm Ostwald, a pioneer of physical chemistry, established the theoretical framework for fuel cells by defining the roles of electrodes, electrolytes, and ion transport [10]. While Grove had hypothesized about the gas battery's reaction zones, Ostwald's research provided the first comprehensive explanation of the electrochemical processes of the gas battery. The transition toward practical applications began in 1896 with William W. Jacques, who developed an early fuel cell prototype. By 1900, Walther Nernst introduced zirconium-based solid electrolytes, paving the way for modern advancements in fuel cell technology [11].

In the 20th century, fuel cell technology advanced from theoretical concepts to practical applications. Early contributions came from William W. Jacques and Emil Baur, with Baur developing the first molten carbonate fuel cell in 1921 and experimenting with solid oxide electrolytes in the 1930s [12]. A major breakthrough occurred in 1933 when Thomas Francis Bacon built the first hydrogen-oxygen fuel cell capable of practical use. By 1939, he had developed a high-pressure alkaline fuel cell, which later found military applications in World War II. His research eventually led to the fuel cells used in NASA's Apollo missions. The 1950s marked another turning point with the introduction of polytetrafluoroethylene (PTFE), known as Teflon, which improved the stability and efficiency of fuel cells. Thomas Grubb and Leonard Niedrach at General Electric pioneered the proton exchange membrane fuel cell (PEMFC) by incorporating ion-exchange membranes and platinum catalysts, leading to its use in NASA's Gemini program. By the 1960s, phosphoric acid fuel cells (PAFCs) emerged, and further developments throughout the 1970s focused on improving efficiency, durability, and cost reduction [13]. In 1990, NASA's Jet Propulsion Laboratory, in collaboration with the University of Southern California, developed the first direct methanol fuel cell, marking a significant milestone in the commercialization of fuel cell technology.

The 21st century has witnessed a significant expansion of fuel cell technology, transitioning from research and development to widespread commercial applications [14]. Today, numerous

manufacturers are actively working on fuel cell systems across diverse industries, with particular emphasis on transportation, stationary power generation, and portable energy solutions.

- **Stationary Applications:** Fuel cells have become a reliable source of clean energy for critical infrastructure. Over 2,500 fuel cell systems have been deployed globally in hospitals, hotels, office buildings, schools, and elderly care centers. These systems operate either as supplementary power sources connected to the electrical grid or as independent generators in remote areas. In the telecommunications sector, where uninterrupted power supply is essential, fuel cells have demonstrated exceptional reliability, achieving an uptime of 99.999% [15–20].

- **Applications in Transportation:** The transportation industry has seen remarkable advancements in fuel cell technology, with major automotive manufacturers incorporating hydrogen fuel cells into their vehicle designs. In 2007, Honda introduced the FCX Clarity, the first mass-produced hydrogen fuel cell vehicle, marking a milestone in the commercialization of this technology. Since then, fuel cells have been integrated into various modes of transport, including buses, trains, ships, trucks, and even aircraft [21, 22].

- **Portable Power Solutions:** Fuel cells have also found applications in portable power generation, particularly in off-grid locations. In outdoor recreational settings, such as camping sites, fuel cells provide a cleaner and quieter alternative to diesel generators, reducing environmental impact while ensuring a stable power supply [23].

- **Micro Power and Consumer Electronics:** One of the most promising developments in fuel cell technology is its potential to revolutionize consumer electronics. Companies like Motorola, Toshiba, Samsung, Panasonic, and Sony have explored fuel cells as an alternative power source for mobile phones and laptops, offering significantly longer battery life and rapid recharge times. Direct methanol fuel cells (DMFCs) have emerged as a preferred choice for these applications, demonstrating twice the runtime of LIBs with a recharge time of just 10 minutes [24, 25].

As a summary, Fig. 1.1 presents a chronological overview of the key milestones and major contributions to fuel cell development from its early discoveries in the 19^{th} century to its modern advancements in the 21^{st} century. As fuel cell technology continues to evolve, ongoing advancements in efficiency, cost reduction, and infrastructure development are paving the way for a future where clean hydrogen energy plays a crucial role in global energy sustainability.

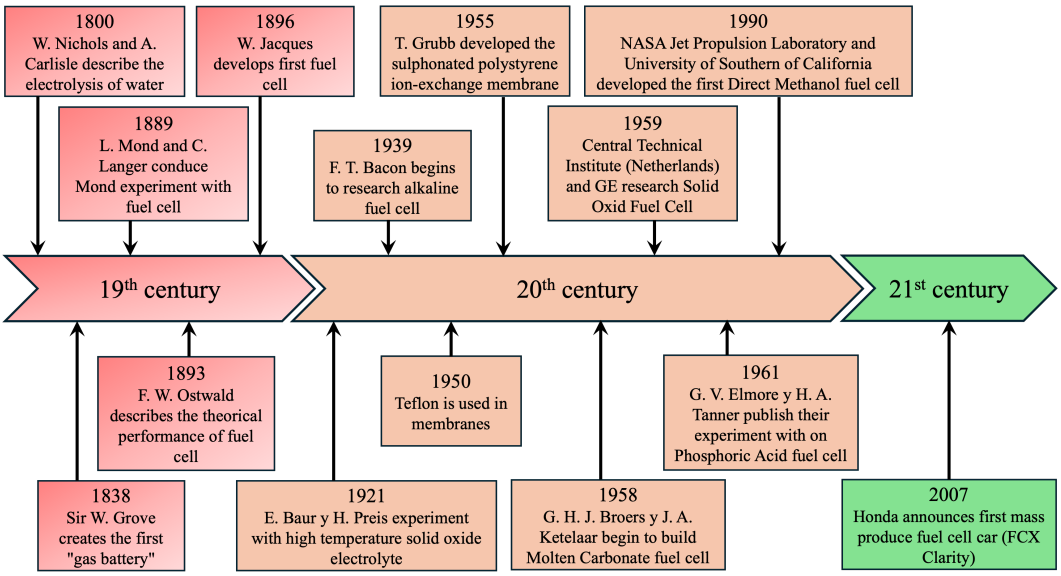

Fig. 1.1: Historical timeline of major advancements in fuel cell technology, highlighting key discoveries, innovations, and applications from the 19th century to the present.

1.1.2 Classification of Fuel Cells

A fuel cell consists of four fundamental components: the anode, cathode, electrolyte, and an external circuit. At the anode, hydrogen undergoes oxidation, producing protons and electrons. The electrons travel through the external circuit, generating electrical power, while the protons migrate through the electrolyte to the cathode. At the cathode, oxygen is reduced and combines with the protons to form water as the only byproduct.

Fuel cells vary in terms of operating temperature, efficiency, applications, and costs. They are primarily classified based on the type of fuel and electrolyte used, forming six major categories [26]. Each type differs in power output, operating temperature, electrical efficiency, and suitability for specific applications.

1.1.2.1 Alkaline Fuel Cell (AFC)

Alkaline fuel cells (AFCs) generate electrical power by utilizing an alkaline electrolyte, typically a potassium hydroxide (KOH) solution in water. The movement of hydroxyl ions (OH^-) through the electrolyte completes the circuit, allowing electrical energy to be extracted. Fig. 1.2 illustrates the structure and operation of an alkaline fuel cell. At the anode, two hydrogen gas molecules react with four hydroxyl ions (OH^-), producing four water molecules and releasing four electrons. This oxidation reaction is expressed as follows [27]:

$$2\,H_2 + 4\,OH^- \rightarrow 4H_2O + 4\,e^- \qquad \text{(Oxidation)} \qquad \text{(Eq. 1.1)}$$

The released electrons travel through the external circuit to the cathode, where they participate in a reduction reaction. At the cathode, an oxygen molecule reacts with two water molecules and absorbs four electrons to form four hydroxyl ions (OH^-), as represented by the following equation:

$$O_2 + 2\,H_2O + 4\,e^- \rightarrow 4\,OH^- \qquad \text{(Reduction)} \qquad \text{(Eq. 1.2)}$$

AFCs typically operate at temperatures between 60 °C and 90 °C, though recent advance-

ments have enabled operation at lower temperatures, ranging from 23 °C to 70 °C. They are classified as low-temperature fuel cells and benefit from cost-effective catalysts. Nickel is the most commonly used catalyst in both the anode and cathode, enhancing the electrochemical reactions in AFCs.

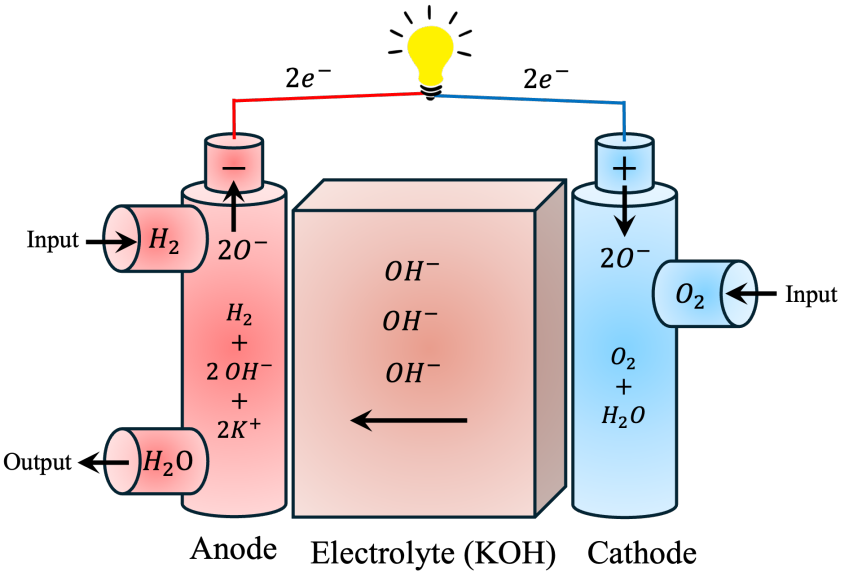

Fig. 1.2: Schematic representation of an Alkaline Fuel Cell (AFC).

1.1.2.2 Phosphoric Acid Fuel Cell (PAFC)

Phosphoric Acid Fuel Cells (PAFCs) utilize carbon paper electrodes and a liquid phosphoric acid (H_3PO_4) electrolyte. Phosphoric acid, a clear, colorless liquid composed of 3.09% hydrogen, 31.6% phosphorus, and 65.3% oxygen, is commonly used in fertilizers, detergents, food flavoring, and pharmaceuticals. Due to its low ionic conductivity at lower temperatures, PAFCs typically operate within a temperature range of 150−220 °C.

In this type of fuel cell, the charge carriers are hydrogen ions (H^+ or protons), which migrate from the anode to the cathode through the electrolyte. The expelled electrons travel through the external circuit, generating an electrical current. At the cathode, water is formed through the reaction of electrons, protons, and oxygen in the presence of a platinum catalyst, which accelerates the electrochemical process.

As illustrated in Fig. 1.3, hydrogen molecules at the anode split into four protons and four electrons. The oxidation reaction occurs at the anode (Eq. 1.3), while at the cathode, the reduction reaction (Eq. 1.4) takes place, where four protons and four electrons combine with oxygen to form water [28–30].

$$2\,H_2 \rightarrow 4H^+ + 4\,e^- \qquad \text{(Oxidation)} \tag{Eq. 1.3}$$

$$O_2 + 4\,H^+ + 4\,e^- \rightarrow 2\,H_2O \qquad \text{(Reduction)} \tag{Eq. 1.4}$$

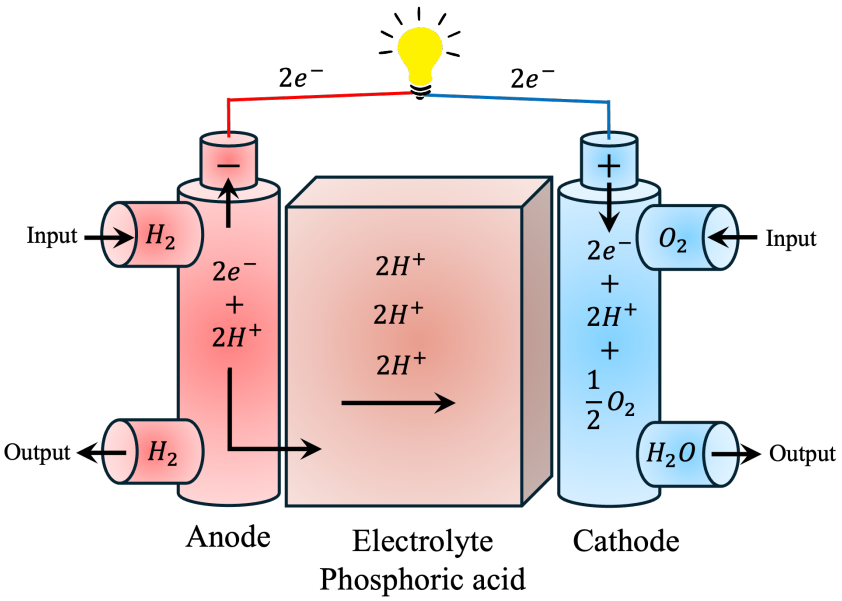

Fig. 1.3: Schematic representation of a Phosphoric acid fuel cell (PAFC).

1.1.2.3 Solid Oxide Fuel Cell (SOFC)

Solid Oxide Fuel Cells (SOFCs) are a class of high-temperature fuel cells that utilize a solid ceramic electrolyte composed of metal oxides. Fig. 1.4 illustrates the basic structure of an SOFC. These fuel cells typically operate at temperatures around 1000 °C and commonly employ a mixture of hydrogen and carbon monoxide produced through internal reforming of hydrocarbon fuels-as the fuel, while atmospheric oxygen serves as the oxidant [2]. The most widely used electrolyte in SOFCs is yttria-stabilized zirconia (YSZ), due to its excellent chemical and thermal stability, as well as its high ionic conductivity [31,32].

At the cathode (also referred to as the air electrode), oxygen undergoes a reduction reaction, forming oxide ions. These ions then migrate through the electrolyte to the anode, where they participate in the oxidation of the fuel. The anode must be porous to allow fuel to reach the reaction sites and to facilitate the removal of the byproducts of fuel oxidation from the electrode-electrolyte interface [33,34]. The oxidation of the fuel at the anode is described by Eq. 1.5, while the reduction of oxygen at the cathode is shown in Eq. 1.6.

$$O_2{}^-(s) \rightarrow (1/2)\,O^2(g) + 2\,e^- \qquad \text{(Oxidation)} \qquad \text{(Eq. 1.5)}$$

$$H_2O\,(g) + 2\,e^- \rightarrow O^{2-}(s) + H_2\,(g) \qquad \text{(Reduction)} \qquad \text{(Eq. 1.6)}$$

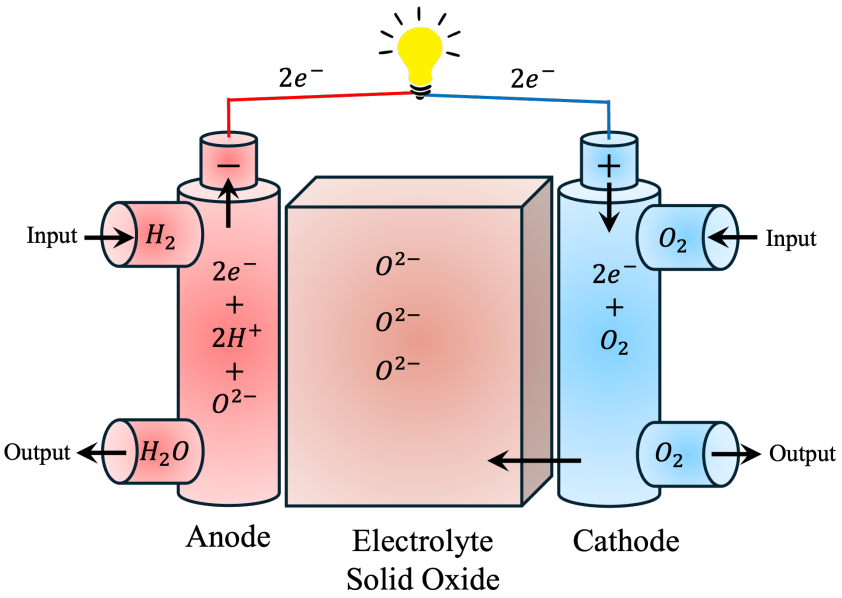

Fig. 1.4: Schematic representation of a Solid Oxide Fuel Cell (SOFC), illustrating the high-temperature electrochemical reactions occurring at the anode and cathode using a solid oxide electrolyte.

1.1.2.4 Molten Carbonate Fuel Cell (MCFC)

Molten Carbonate Fuel Cells (MCFCs) are high-temperature electrochemical devices that utilize a molten carbonate salt mixture as the electrolyte. This electrolyte is typically retained within a porous, chemically inert ceramic matrix, often composed of beta-alumina solid electrolyte (BASE) [29]. A schematic of a typical MCFC is shown in Fig. 1.5.

In an MCFC, the electrochemical reaction at the anode involves hydrogen fuel reacting with carbonate ions (CO_3^{2-}), producing carbon dioxide (CO_2), water (H_2O), and electrons. The feed gas, typically methane (CH_4) mixed with steam (H_2O), undergoes internal reforming at the anode to generate hydrogen (H_2), carbon monoxide (CO), and carbon dioxide (CO_2), which then participate in the fuel cell reactions.

$$CH_4 + H_2O \rightarrow CO + 3\,H_2 \qquad \text{(Reform 1)} \qquad \text{(Eq. 1.7)}$$

$$CO + H_2O \rightarrow CO_2 + H_2 \qquad \text{(Reform 2)} \qquad \text{(Eq. 1.8)}$$

Simultaneously, two electrochemical reactions occur at the anode, where hydrogen and carbon monoxide are consumed, and electrons are released. These reactions, represented by Eq. 1.9 and Eq. 1.10, both utilize carbonate ions (CO_3^{2-}) from the electrolyte as reactants.

$$H_2 + {CO_3}^{2-} \rightarrow CO_2 + H_2O + 2\,e^- \qquad \text{(Oxidation 1)} \qquad \text{(Eq. 1.9)}$$

$$CO + {CO_3}^{2-} \rightarrow 2CO_2 + 2\,e^- \qquad \text{(Oxidation 2)} \qquad \text{(Eq. 1.10)}$$

At the cathode (Eq. 1.11), a reduction reaction occurs in which oxygen (O_2) and carbon dioxide (CO_2) combine to form new carbonate ions (CO_3^{2-}). These generated ions migrate through the electrolyte toward the anode, where they participate in the oxidation reactions.

The flow of electrons through the external circuit between the electrodes generates an electric current and cell voltage [35].

$$(1/2)\,O_2 + CO_2 + 2\,e^- \rightarrow {CO_3}^{2-} \qquad \text{(Reduction)} \qquad \text{(Eq. 1.11)}$$

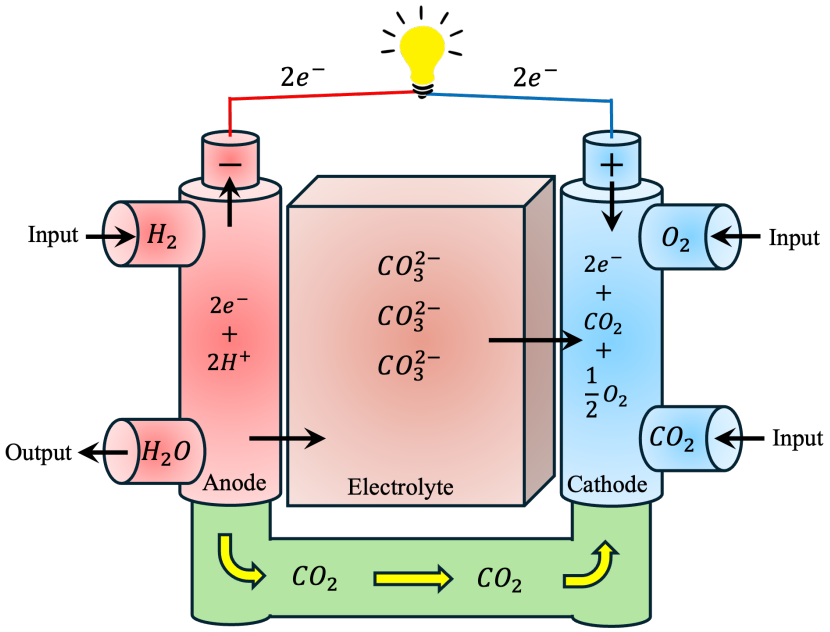

Fig. 1.5: Schematic representation of a Molten Carbonate Fuel Cell (MCFC), highlighting the electrochemical reactions at the electrodes and the transport of carbonate ions through the electrolyte.

1.1.2.5 Proton Exchange Membrane Fuel Cell (PEMFC)

In Proton Exchange Membrane Fuel Cells (PEMFCs), hydrogen molecules are dissociated at the anode by a platinum-based catalyst, producing protons (H^+) and electrons (e^-). The protons migrate through the polymer electrolyte membrane toward the cathode, while the electrons are directed through an external circuit, generating electrical power. At the cathode, the electrons recombine with protons and oxygen to produce water. The electrochemical reactions at the anode and cathode are represented in Eq. 1.12 and Eq. 1.13, respectively. A schematic diagram of a PEMFC is shown in Fig. 1.6.

$$H_2(g) \rightarrow 2H^+ + 2e^- \qquad \text{(Anode)} \qquad \text{(Eq. 1.12)}$$

$$(1/2)\,O_2(g) + 2\,H^+ + 2\,e^- \rightarrow H_2O(l) \qquad \text{(Cathode)} \qquad \text{(Eq. 1.13)}$$

$$H_2(g) + (1/2)\,O_2(g) \rightarrow H_2O(l) \qquad \text{(Overall Reaction)} \qquad \text{(Eq. 1.14)}$$

The Proton Exchange Membrane Fuel Cell (PEMFC) primarily consists of bipolar plates and a membrane electrode assembly (MEA). The MEA is composed of a proton-conducting membrane, a catalyst layer, and a gas diffusion layer, typically made of carbon cloth. The membrane selectively allows proton transport from the anode to the cathode, while preventing the passage of electrons and reactant gases. The gas diffusion layer ensures the uniform distribution of

reactants across the electrode surface. The resulting electron flow through the external circuit constitutes the usable electrical output of the cell.

PEMFCs operate at relatively low temperatures, typically between 60 °C and 100 °C. Their compact design, lightweight structure, and fast start-up capabilities make them well-suited for portable and automotive applications. Compared to other fuel cell types, PEMFCs offer easier sealing due to the solid nature of the electrolyte, extended operational lifetimes, and lower production costs [36–38].

PEMFC systems are typically employed in portable and stationary applications. Among these, transportation stands out as the most promising application due to its ability to provide a continuous electrical energy supply with high efficiency and power density. Additionally, PEMFCs require minimal maintenance since the power-generating stacks do not contain moving parts. Fuel cell vehicles (FCVs) represent the most viable application of PEMFC technology, as the observable advancements in this field can significantly enhance the public acceptance of such systems. According to a report by McNicol et al. [39], FCVs have the potential to compete effectively with conventional internal combustion engine (ICE) vehicles. However, the initial cost of FCVs remains higher than that of ICE vehicles.

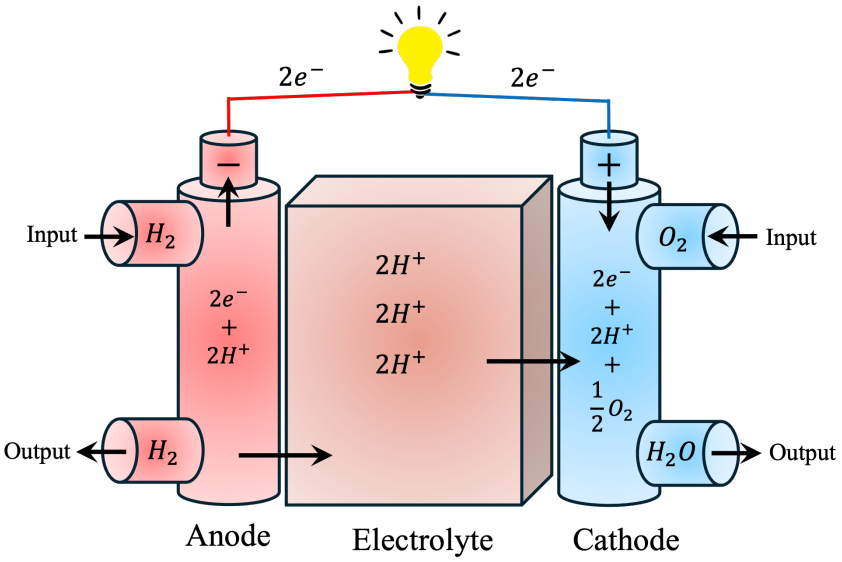

Fig. 1.6: Schematic representation of a Proton Exchange Membrane Fuel Cell (PEMFC), showing the membrane electrode assembly (MEA), bipolar plates, and the flow of protons, electrons, and reactant gases during operation.

1.1.2.6 Direct Methanol Fuel Cell (DMFC)

The Direct Methanol Fuel Cell (DMFC) is an advanced type of PEMFC, specifically designed for portable energy applications. It is considered an ideal power source due to its low-temperature operation, extended lifespan, and rapid refueling capabilities. Additionally, DMFCs do not require recharging, positioning them as a clean and renewable energy solution. Fig. 1.7 depicts a direct methanol fuel cell (DMFC).

In DMFC systems, methanol serves as the energy source. At the anode, methanol undergoes reforming to produce carbon dioxide (CO_2), while at the cathode, steam or water is generated through a reaction with the oxygen in the air. The corresponding reactions are presented in Eq. 1.15 and Eq. 1.16:

$$CH_3OH + H_2O \rightarrow CO_2 + 6\,H^+ + 6e^- \qquad \text{(Anode)} \qquad \text{(Eq. 1.15)}$$

$$(3/2)\,O_2 + 6\,e^- + 6\,H^+ \rightarrow 3H_2O \qquad \text{(Cathode)} \qquad \text{(Eq. 1.16)}$$

DMFC systems are typically categorized into active and passive types. Active DMFCs are high-efficiency, reliable systems that include components such as a methanol feed pump, CO_2 separator, fuel cell stack, methanol sensor, circulation pump, pump drivers, and controllers. In contrast, passive DMFC systems eliminate the need for methanol pumping devices and external air-blowing processes. In these systems, oxygen from ambient air diffuses into the cathode through the air-breathing feature of the cell, while methanol diffuses into the anode from an integrated feed reservoir, driven by the concentration gradient between the anode and the reservoir. Passive systems are more cost-effective, simpler in design, and capable of significantly reducing parasitic power loss and system volume.

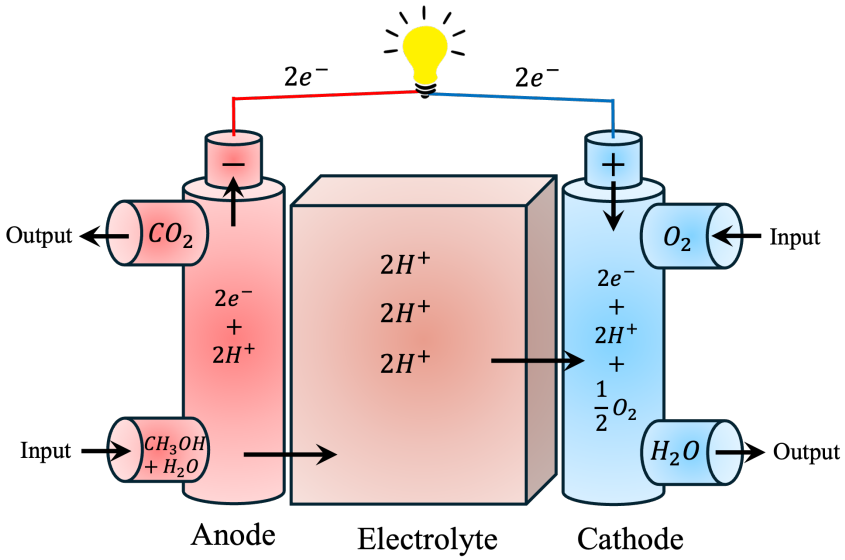

Fig. 1.7: Schematic representation of a Direct Methanol Fuel Cell (DMFC), illustrating the conversion of methanol at the anode to carbon dioxide (CO_2) and the formation of steam or water at the cathode through a reaction with oxygen from the air.

Among the various types of fuel cells, PEMFCs stand out due to their broad range of applications. They offer several advantages, including high flexibility, low operating temperatures, exceptional efficiency, minimal emissions, and quiet operation [40, 41]. These features make PEMFCs particularly well-suited for transportation applications, where they are considered the most promising option. They provide high power density, fast start-up times, and are easy to handle safely, all of which contribute to their growing potential in clean energy solutions. Despite these benefits, PEMFCs are currently hindered by high production costs, making them economically uncompetitive for widespread adoption. However, ongoing research and technological advancements hold the promise of reducing these costs, potentially unlocking their full commercial potential. To summarize the key characteristics and operating conditions of various types of fuel cells discussed, Table 1.1 provides a comparative overview, highlighting differences in fuel type, electrolyte, mobile ion, and operating temperature [42].

Table 1.1: Characteristics of different fuel cell types

Type	Fuel	Electrolyte	Mobile Ion	Temp. (°C)
AFC	H_2	Aqueous KOH	OH^-	100−250
PAFC	H_2	H_3PO_4	H^+	150−250
SOFC	CO	$(Zr,Y)O_2$	O^{2-}	700−1000
MCFC	CO	$(Na,K)_2CO_3$	CO_3^{2-}	500−700
PEMFC	H_2, CH_3OH	Nafion®	$(H_2O)_nH^+$	70−110

The key materials currently under development for PEMFC stacks include construction materials for the cell frames, electrocatalysts for the fuel and air electrodes, and ion-conducting membranes. A critical challenge lies in the electrocatalyst, particularly for operation with pure hydrogen and air, where platinum is the most effective material. To reduce costs, platinum nanoparticles supported on carbon have been developed, aiming to minimize the use of noble metals without compromising cell performance. The electrode catalysts (mostly platinum) and membranes (Nafion®) are essential components in PEMFCs, and a more detailed discussion of them will be provided in the following sections.

1.1.3 Platinum as an Electrode Material

Platinum (Pt) is widely recognized as the most efficient and active electrocatalyst for both the hydrogen oxidation reaction (HOR) at the anode and the oxygen reduction reaction (ORR) at the cathode in proton exchange membrane fuel cells (PEMFCs). Its high catalytic activity, exceptional selectivity for water formation, and remarkable electrochemical stability make it the benchmark material for fuel cell electrodes.

In the context of ORR, an ideal catalyst must selectively facilitate the four-electron reduction pathway, leading to water production while minimizing the formation of undesired intermediates such as hydrogen peroxide. Platinum-based materials excel in this regard, efficiently utilizing protons transported through the membrane to complete the reaction. Among available materials, Pt exhibits the highest intrinsic activity, combined with superior durability and chemical resilience under the acidic and oxidative conditions of PEMFC operation.

However, platinum's scarcity in the Earth's crust, coupled with its high market price (approximately $1,000 per ounce), poses significant economic limitations. In response, substantial efforts have been made over the past three decades to reduce platinum loading in fuel cell stacks, from initial values of around 4 mg.cm^2 to less than 0.1 mg.cm^2 [43]. Despite these advancements, the catalyst still accounts for roughly 41% of the total fuel cell cost, surpassing the contributions of other components such as membranes, gas diffusion layers, and bipolar plates.

The exceptional ORR activity of Pt is partly attributed to its favorable oxygen adsorption behavior. As illustrated in Fig. 1.8, three primary oxygen adsorption models on Pt surfaces have been proposed:

- **Griffiths Model** – a single-site adsorption mechanism where both oxygen atoms are coordinated to a single metal atom.
- **Pauling Model** – another single-site mechanism where only one oxygen atom binds to the metal surface; this model typically supports the two-electron reduction pathway.
- **Bridge Model** – a dual-site adsorption mechanism in which each oxygen atom binds to a separate Pt atom, associated with the preferred four-electron reduction pathway [44, 45].

To further enhance the catalytic efficiency and reduce the Pt content, platinum nanoparticles are commonly dispersed on high-surface-area carbon supports, such as Vulcan XC-72. This

configuration, known as Pt/C, increases the electrochemically active surface area, improving overall catalyst utilization. Nanostructured catalysts typically consist of Pt particles ($\sim 2-5$ nm) deposited on carbon primary particles, forming agglomerates ($100-300$ nm), which further assemble into larger aggregates ($1-3$ μm). The electrode catalyst layer is formed through the self-organization of Pt/C and ionomer during ink deposition, leading to a phase-separated structure that optimizes ion and electron transport [46, 47].

As research continues, strategies to reduce Pt usage without compromising performance remain a central focus in PEMFC development, including alloying with transition metals, using novel supports, and applying machine learning-guided design of catalyst architectures.

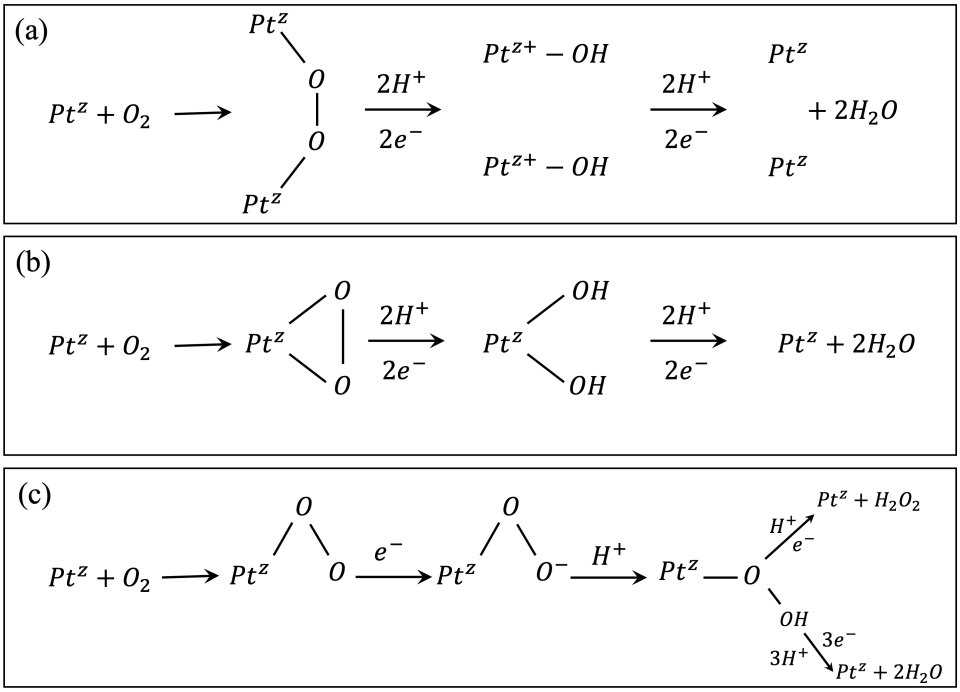

Fig. 1.8: Schematic representation of the oxygen reduction reaction (ORR) mechanisms on platinum surfaces, illustrating three adsorption models (z is the oxidation state): (a) Bridge model (each oxygen atom bonding to a different Pt atom), (b) Griffiths model (dual oxygen bonding to a single Pt atom), and (c) Pauling model (single oxygen atom bonding to Pt). These adsorption geometries influence the reaction pathway, with the bridge and Griffiths models favoring the four-electron pathway to water, while the Pauling model is associated with the two-electron pathway.

1.1.4 Platinum-Based Electrocatalysts

The development of alternative electrocatalysts with reduced platinum content has been a major research focus over the past decades, driven by the need to lower the overall cost of PEMFCs and DMFCs, making them more economically competitive with conventional energy sources. The initial motivation for exploring platinum alloys arose from PAFCs, aiming to discover electrocatalysts with higher activity than pure Pt.

In the early 1980s, Ross and Landsman systematically studied the oxygen reduction reaction (ORR) on a range of Pt-M alloys (where M is a first-row transition metal) in phosphoric acid and observed enhanced catalytic activity compared to pure platinum [48, 49]. These alloys often exhibited an ordered Pt_3M structure. Following their work, numerous researchers synthesized Pt_3M-type alloy catalysts and evaluated them in PAFC systems. Early patents de-

scribed the alloying of Pt with metals such as Ti, V, Mn, Mo, and Al, with vanadium showing particularly promising performance [49,50]. Later patents indicated that Pt-Cr and Pt-Fe alloys demonstrated superior ORR activity, even surpassing Pt-V systems [51].

Watanabe et al. further advanced the field by demonstrating that ordered Pt-Co alloys exhibit higher activity than both disordered Pt-Co and pure Pt in phosphoric acid electrolytes [51]. Additionally, ternary alloys such as Pt-Co-Cr emerged as effective and stable catalysts for ORR [52,53], showing significant improvements in catalytic performance and durability [54].

In the early 1990s, Mukerjee et al. extended these investigations to PEMFCs by evaluating a series of binary Pt-M (M = Ni, Cr, Co) alloys with an ordered Pt_3M structure [55]. Among these, Pt-Cr alloys exhibited the highest activity and good stability, maintaining performance for up to 400−1200 hours. Later, Shim et al. synthesized ternary Pt-Fe-M (M = Cr, Mn, Co, Ni, Cu) alloys and tested them in PEMFCs [56]. All tested alloys outperformed pure Pt, with Pt-Fe-Co showing the highest catalytic activity.

More recently, Pt-V alloys have gained attention. Antolini et al. reported that ordered Pt-V alloys demonstrated a significant enhancement in ORR activity in PEMFC systems [57]. Similar studies in DMFCs by Neergat et al. evaluated binary Pt-M (M = Co, Cr, Ni) and ternary Pt-Co-M (M = Cr, Ni) alloys [58]. They found that while Pt-Co and Pt-Co-M formed ordered structures, Pt-Cr and Pt-Ni remained disordered. The ordered Pt-Co alloy exhibited the best catalytic performance in DMFCs. Subsequent work by Shukla et al. confirmed that Pt-Fe alloys, especially in ordered form, showed superior ORR activity compared to pure Pt in DMFC systems [59].

Currently, platinum or platinum-transition metal alloy nanoparticles as PtCo [60] and PtRu [61], dispersed on high-surface-area carbon supports, are widely used as electrocatalysts in PEMFCs [62]. Despite significant progress using Pt-based nanostructures such as nanowires and nanotubes [63–65], challenges remain in achieving precise control over their size, morphology, and compositional uniformity, which are critical factors for optimizing catalytic activity and long-term stability [66].

1.1.5 Proton-Conducting Electrolytes

The development of electrolytes in PEMFCs dates back to the 1950s, initiated by the U.S. General Electric Company (GE). However, the long-term viability and widespread interest in PEMFCs were significantly bolstered by the introduction of Nafion, a perfluorosulfonic acid (PFSA) polymer developed by DuPont. Nafion quickly became the benchmark electrolyte material in PEMFC systems due to its unique combination of chemical stability and high proton conductivity.

Structurally, Nafion consists of a polytetrafluoroethylene (PTFE)-like perfluorinated backbone, which ensures excellent mechanical, thermal, and chemical stability. This backbone is grafted with perfluoroether side chains terminating in sulfonic acid groups (–SO_3H). These sulfonic acid end-groups are hydrophilic and tend to cluster into nano-scale domains upon hydration, forming ionic channels that facilitate efficient proton transport. The hydrated acidic regions within Nafion are primarily responsible for its high ionic conductivity, which is essential for PEMFC operation. However, this hydration-dependent conductivity restricts Nafion's performance to low operating temperatures (typically below 100 °C), beyond which dehydration leads to a dramatic drop in conductivity.

Nafion was initially developed for use in chlor-alkali cells for industrial chlorine production [67]. By the 1990s, major technical barriers in PEMFC systems had been addressed, and researchers in the United States and Japan began focusing on improving the material properties of Nafion [68]. Modifications such as incorporating shorter side chains in the copolymer structure led to enhanced ionic conductivity and improved membrane performance. Additionally,

research highlighted the importance of reducing gas permeability and enhancing resistance to small-molecule crossover, particularly relevant in DMFCs.

An ideal polymer electrolyte membrane for fuel cell applications must meet several key criteria:

- high proton conductivity, typically achieved through a sufficient degree of sulfonation and optimized membrane thickness;
- robust mechanical, thermal, and chemical stability, often requiring reinforcement or a highly stable polymer backbone;
- low gas permeability to minimize fuel crossover; and
- in the case of DMFCs, a low electro-osmotic drag coefficient to reduce methanol crossover.

Nafion meets many of these requirements, making it the most commonly implemented membrane in commercial PEMFC stacks.

Nevertheless, Nafion has notable limitations. Its relatively high cost and dependence on fluorinated compounds have driven efforts to develop alternative, cost-effective membrane materials. Many of these newer membranes are hydrocarbon-based and fluorine-free; however, they often suffer from inadequate thermal or chemical stability. To overcome this, researchers are increasingly incorporating aromatic structures into hydrocarbon backbones to enhance membrane durability under fuel cell operating conditions.

Despite extensive experimental advancements, the interaction between Nafion as the electrolyte and platinum as the electrode surface remains poorly understood. This knowledge gap is primarily due to the limited number of theoretical and simulation studies addressing the atomistic and electronic-level behavior at the Nafion/Pt interface. A deeper understanding of these interactions is essential, as they directly influence the efficiency, durability, and performance of PEM fuel cells. Therefore, further development and optimization of Nafion's properties require comprehensive theoretical and modeling approaches, an effort that constitutes the primary focus of this study.

1.2 Batteries

Batteries are electrochemical devices that convert stored chemical energy into electrical energy through redox reactions. They are composed of three essential components: a cathode (positive electrode), an anode (negative electrode), and an electrolyte that facilitates ionic transport between the two electrodes. During discharge, electrons flow from the anode to the cathode through an external circuit, while ions travel through the electrolyte to maintain charge neutrality. Depending on their chemistry, batteries can be classified as either primary (non-rechargeable) or secondary (rechargeable) systems [69]. Among the latter, lithium-ion batteries (LIBs) have become the dominant technology in portable electronics, electric vehicles, and grid storage applications due to their high energy density, light weight, and long cycle life [70–72].

Despite significant advancements, batteries still face several challenges related to energy density, safety, cost, environmental impact, and material sustainability [73,74]. Future research is increasingly focused on developing next-generation batteries, such as solid-state batteries, lithium-sulfur, and lithium-air systems, which promise higher performance and improved safety. Innovations in electrode materials, electrolyte formulations, and nanostructured architectures are crucial to overcoming current limitations. Moreover, theoretical modeling and computational simulations are playing an expanding role in understanding fundamental processes at the atomic and molecular levels, guiding the rational design of new materials. The

continued evolution of battery technology is vital for enabling a sustainable energy future, particularly in the context of renewable energy integration and electrification of transportation [75,76].

1.2.1 Historical Background

The development of modern batteries as efficient energy storage devices dates back to the pioneering work of Luigi Galvani in the 1790s, who discovered bioelectricity through his experiments with frog legs and dissimilar metals [69]. Shortly afterward, in 1800, Alessandro Volta introduced the voltaic pile, a breakthrough invention that provided a continuous current using alternating discs of dissimilar metals, typically zinc and copper, separated by electrolyte-soaked materials [77]. This invention marked the birth of electrochemical energy storage and laid the foundation for all subsequent battery technologies.

In 1802, William Cruickshank advanced Volta's concept by retaining the zinc-copper electrode pair while replacing the stacked pile with a brine-filled box configuration, yielding a more stable and scalable design [78]. This improvement made it possible to produce batteries in larger quantities, making the technology more practical for real-world applications.

The 20th century saw tremendous advancements in battery chemistry and design, especially to increase energy density and enable portability. Serious research into high-energy-density battery systems began in the 1960s, with a focus on non-aqueous primary batteries utilizing lithium as the anode material. These lithium-based systems, initially non-rechargeable, were introduced in the early 1970s, primarily for military use due to their high energy content and lightweight nature. However, widespread adoption was limited by challenges related to safety, cell architecture, and electrolyte formulation.

The pivotal moment in the development of modern rechargeable batteries came in the early 1990s when Sony successfully commercialized a practical "rocking-chair" LIB. This innovation revolutionized consumer electronics and later became the cornerstone of modern portable devices, electric vehicles, and grid-scale energy storage systems.

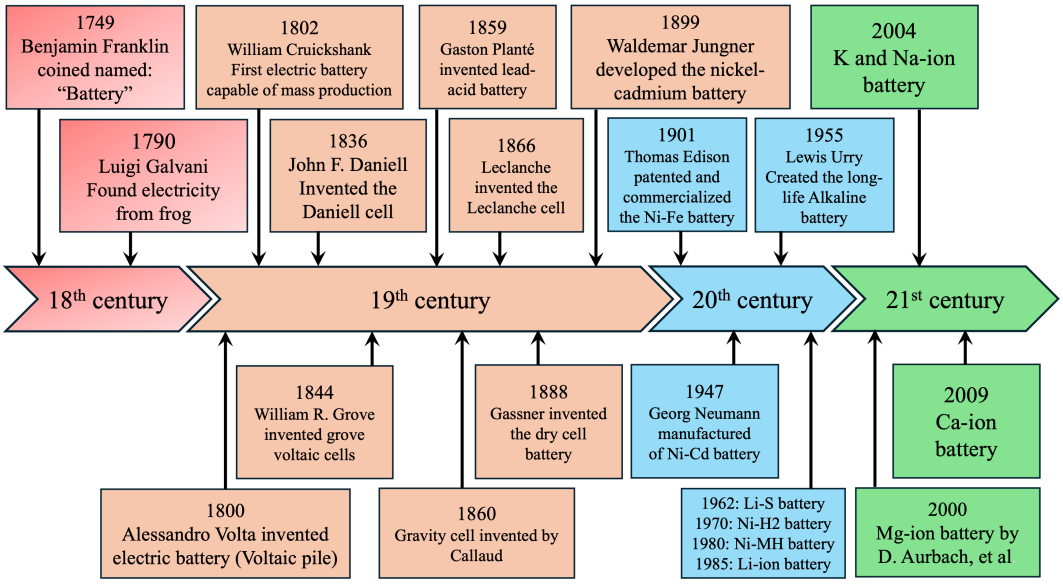

Fig. 1.9: A chronological overview of key milestones in the development of modern battery technologies, from the voltaic pile to the commercialization of LIBs.

Despite the remarkable progress, challenges such as cost, sustainability, safety, and perfor-

mance remain areas of active research. As battery technologies continue to evolve, the demand for deeper theoretical understanding and advanced materials modeling becomes increasingly important to guide future innovation. The key milestones in the history of battery development are summarized in Fig. 1.9.

This system employed lithium cobalt oxide ($LiCoO_2$) as the cathode material and refinery coke, a form of carbon, as the anode. Its key innovation was the use of a carbon-based anode capable of reversible lithium-ion intercalation, eliminating the safety concerns associated with metallic lithium. This breakthrough enabled high energy density, stable cycling, and enhanced safety qualities that quickly positioned LIBs at the forefront of portable energy storage. Over the past three decades, continuous advancements in materials, design, and manufacturing have made LIBs the dominant choice for powering consumer electronics, power tools, and increasingly, electric vehicles (EVs) and grid-scale energy storage systems. Fig. 1.10 presents a comparison of the energy densities associated with various types of rechargeable batteries. Among these systems, LIBs clearly exhibit the highest energy density, making them the most efficient choice for applications requiring lightweight and compact energy storage solutions [79].

In the next section, we will delve into the structure, working principles, and material components of LIBs, highlighting ongoing efforts in research and development aimed at optimizing their performance, safety, and sustainability.

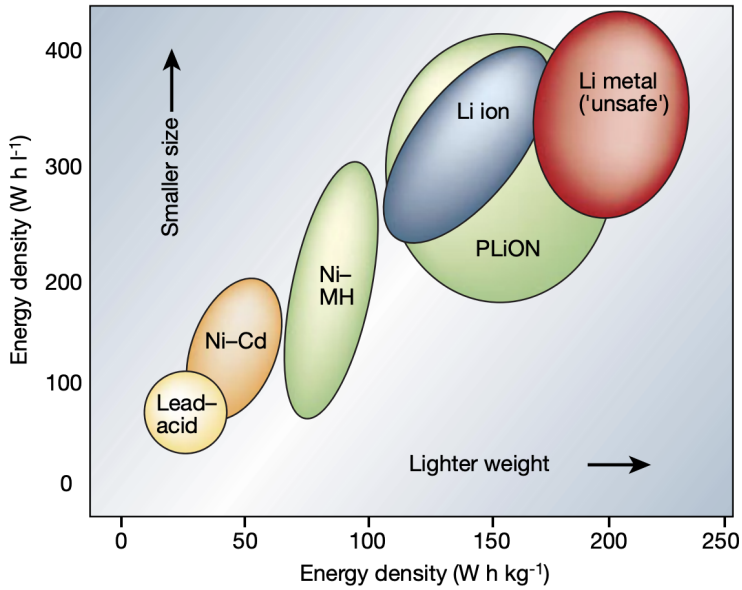

Fig. 1.10: Comparison of energy densities for different types of rechargeable batteries. LIBS exhibit the highest energy density among commercially available systems, making them ideal for portable and high-performance applications (Adapted from [79]).

1.2.2 Lithium-Ion Batteries (LIBs)

Lithium-ion batteries (LIBs) have emerged as one of the most significant energy storage technologies in modern society [80, 81]. Since their commercialization in the early 1990s, LIBs have become the dominant power source for a wide spectrum of applications, including portable electronics, EVs, and grid-scale energy storage systems [82]. Their widespread adoption is largely attributed to their high energy density, long cycle life, low self-discharge rate, and lightweight design, making them both efficient and versatile [79, 83, 84].

The increasing global demand for clean and sustainable energy solutions, driven by climate

change, fossil fuel depletion, and rapid technological advancement, further accelerated the development of LIB technologies. In particular, the electrification of transportation is a critical strategy to reduce greenhouse gas emissions, and LIBs serve as the key enabling technology for electric vehicles. As EV production scales rapidly worldwide, the need for high-performance, durable, and cost-effective LIBs becomes increasingly urgent.

A typical LIB cell is composed of four main components: a cathode, an anode, an electrolyte, and a separator. The performance characteristics of LIBs, such as energy and power density, safety, cycle life, cost, and environmental impact, are highly dependent on the selection and design of electrode materials [85]. In this regard, lithium metal is theoretically considered an ideal anode material due to its extremely high specific capacity and low electrochemical potential. However, practical challenges related to safety and stability have limited its use in commercial applications.

LIBs continue to evolve, with intensive research efforts focused on improving their performance under diverse operating conditions, such as extreme temperatures and high charge/discharge rates. Enhancing the properties of both cathode and anode materials is critical for the next generation of LIBs.

The capacity and overall performance of LIBs are governed not only by the intrinsic properties of the electrode materials but also by their interfacial interactions with binders, morphological characteristics, and cell configurations. Understanding and optimizing these factors is a key objective of this study in the context of LIB systems.

In the following sections, a more detailed analysis will be presented, focusing on the fundamental electrochemical reactions occurring at the electrodes, the materials employed for both cathodes and anodes, as well as the role and composition of the electrolyte.

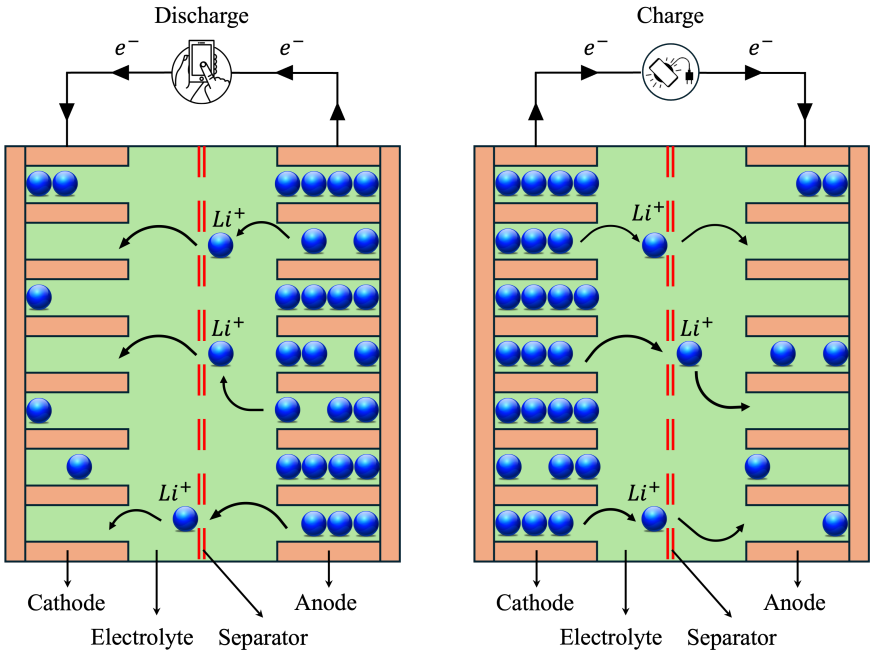

Fig. 1.11: Schematic illustration of the charge-discharge processes in a LIB. During discharge, lithium ions migrate from the anode to the cathode through the electrolyte and separator, while electrons flow through an external circuit to provide electrical energy. During charging, the process is reversed as lithium ions return to the anode. This cyclic migration enables reversible energy storage and release in LIBs, forming the basis of their operating principle.

1.2.2.1 Electrochemistry of LIBs

Lithium-ion batteries (LIBs) operate by storing energy in the form of chemical potential during charging and converting it back into electrical energy during discharge. As shown in Fig. 1.11, a typical LIB cell consists of four main components: a cathode (positive electrode), an anode (negative electrode), a lithium-ion-conducting electrolyte, and a porous separator. The anode and cathode are responsible for hosting lithium ions during charge and discharge, while the separator electrically isolates them, preventing internal short-circuits, yet allowing lithium-ion migration [86].

The electrolyte plays a crucial role in facilitating ionic transport between the electrodes while maintaining electronic insulation. To ensure electrochemical stability and prevent decomposition during operation, the electrolyte's energy levels must be carefully matched to those of the electrodes: the lowest unoccupied molecular orbital (LUMO) should be higher than the anode potential, and the highest occupied molecular orbital (HOMO) should be lower than the cathode potential, as depicted in Fig. 1.12. Otherwise, parasitic reactions could lead to irreversible capacity loss or even cell failure over extended cycling [87].

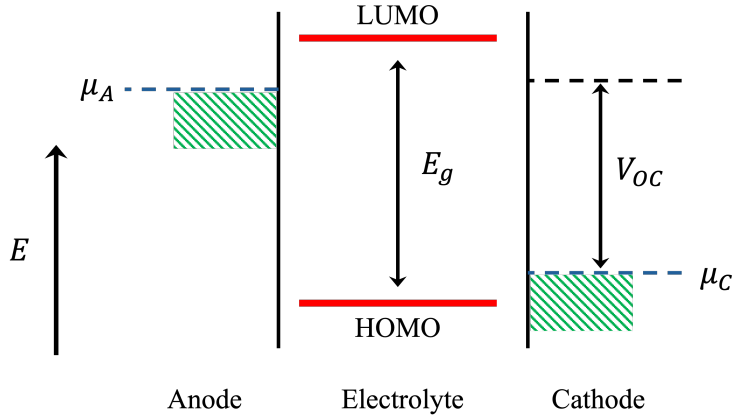

Fig. 1.12: Schematic representation of the energy level alignment in a LIB system, illustrating the importance of the electrolyte's frontier molecular orbitals. For stable electrochemical performance, the LUMO (Lowest Unoccupied Molecular Orbital) of the electrolyte must be higher in energy than the anode potential to prevent reduction, while the HOMO (Highest Occupied Molecular Orbital) should be lower than the cathode potential to avoid oxidation.

During discharge, lithium ions deintercalate from the anode material and migrate through the electrolyte and separator to the cathode, where they are re-intercalated. This ionic motion is accompanied by the flow of electrons through an external circuit, providing electrical power to connected devices. The process is reversed during charging, with lithium ions moving back to the anode.
The fundamental electrochemical reactions in a conventional LIB using graphite as the anode and lithium cobalt oxide ($LiCoO_2$) as the cathode are:

- Anode reaction:

$$Li_xC_6 \rightleftharpoons 6\,C + xLi^+ + xe^- \qquad (0<x<1) \qquad \text{(Eq. 1.17)}$$

- Cathode reaction:

$$LiCoO_2 \rightleftharpoons Li_{1-x}CoO_2 + xLi^+ + xe^- \qquad (0<x<1) \qquad \text{(Eq. 1.18)}$$

These reactions (Eq. 1.17 and Eq. 1.18) are highly reversible under ideal conditions, enabling repeated charging and discharging cycles with minimal degradation. As explained above, Fig. 1.11 schematically illustrates the working principle and internal structure of a typical LIB.

1.2.2.2 Anode Materials

Graphite is the most widely used anode material in commercial LIBs, primarily due to its structural stability and ability to reversibly intercalate lithium ions. However, it can accommodate only one lithium ion per six carbon atoms, resulting in a stoichiometry of LiC_6 and a theoretical specific capacity of 372 $mAh.g^{-1}$. The diffusion coefficient of lithium in carbon materials typically ranges from 10^{-12} to 10^{-6} cm^2s^{-1}, with graphite exhibiting values between 10^{-9} and 10^{-7} cm^2s^{-1}. This relatively slow ion transport limits the rate capability and power density of graphite-based batteries.

To overcome these limitations, the development of alternative anode materials with higher specific capacity, improved lithium-ion diffusion kinetics, and enhanced energy and power densities is essential. Among these, lithium metal offers the highest theoretical capacity ($\sim$3860 $mAh.g^{-1}$), making it an attractive candidate. However, its practical application is severely hindered by safety concerns associated with dendritic lithium growth, which can lead to internal short circuits and catastrophic cell failure.

Therefore, a key challenge in next-generation battery development lies in identifying and engineering advanced anode materials that combine high capacity, fast lithium-ion transport, long cycle life, and robust safety characteristics. This section reviews the current state-of-the-art in anode materials for LIBs, with particular emphasis on recent advances in nanostructured materials and their promising electrochemical performance. To simplify the discussion, innovative anode materials are commonly classified into three major categories according to their lithium-ion storage mechanisms and overall battery performance:

- **Intercalation/De-intercalation Materials:** These systems allow lithium ions to reversibly intercalate into the host structure with minimal structural change. Examples include carbon-based materials such as porous carbon, carbon nanotubes, graphene, as well as metal oxides like TiO_2 and $Li_4Ti_5O_{12}$.
- **Conversion-type Materials:** These materials undergo a chemical transformation during lithiation and delithiation, forming new phases. This category includes various transition metal oxides (e.g., Mn_xO_y, NiO, Fe_xO_y, CuO, Cu_2O, MoO_2), metal sulfides, phosphides, and nitrides (M_xX_y, where X = S, P, or N).
- **Alloy/De-alloy Materials:** In this group, lithium forms reversible alloys with the host elements during cycling. Typical representatives include silicon (Si), germanium (Ge), tin (Sn), aluminum (Al), bismuth (Bi), and tin oxide (SnO_2).

Table 1.2 summarizes the key characteristics of commonly studied intercalation-type anode materials used in LIBs, including their operating potentials, specific charge capacities, cycle life, safety profiles, and associated costs. These parameters are critical in determining the overall performance, efficiency, and commercial viability of LIBs.

Table 1.2: Intercalation-type negative electrode (anode).

Cathode Type	Potential (V vs. Li^+/Li)	Charge Density ($mAh.g^{-1}$)	Cycle Life [a]	Safety	Cost
Graphite	~ 0.1	~ 350	> 1000	Safe	Low
$Li_4Ti_5O_{12}$	~ 1.5	~ 160	> 5000	Safe	Medium

[a] *Cycles until capacity reaches 80% of initial capacity.*

Fig. 1.13 illustrates the redox potentials relative to Li/Li^+ alongside the corresponding specific capacities of various anode materials currently under investigation [88].

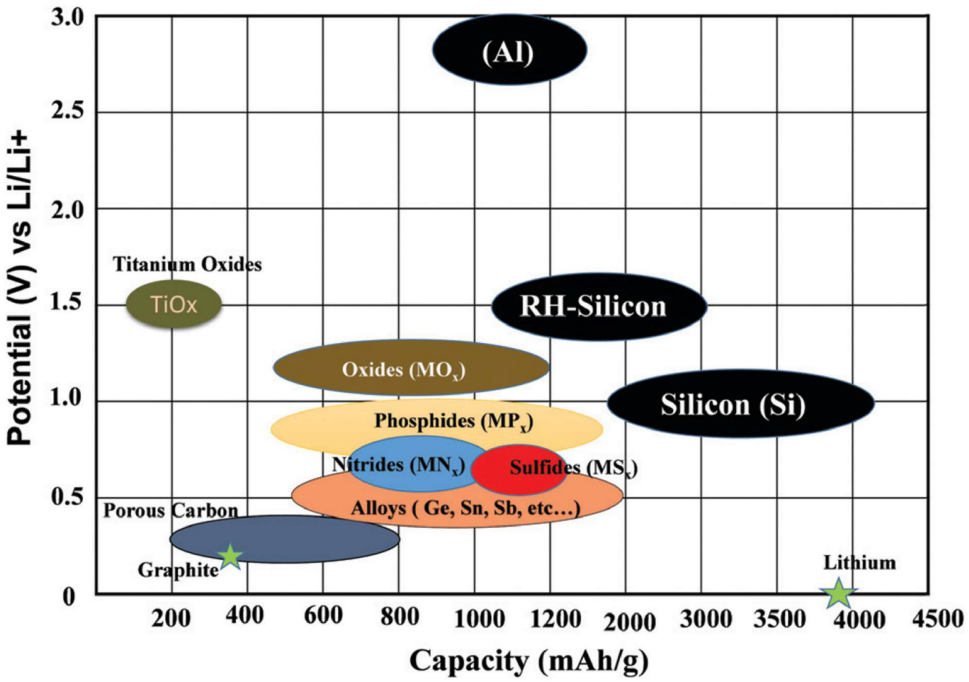

Fig. 1.13: Approximate ranges of average redox potentials (V vs. Li/Li^+) and specific capacities for commonly studied anode materials in LIBs (Adapted from [88]).

As illustrated in Fig. 1.13, among alloying-type anodes, silicon and silicon oxide–based materials are among the most extensively studied and promising candidates, exhibiting gravimetric capacities on the order of 3000–3500 $mAh.g^{-1}$ and operating at relatively low delithiation potentials of approximately 0.9–1.0 V vs. Li^+/Li [89–93]. However, despite its attractive electrochemical properties, challenges such as large volume changes during lithiation/delithiation cycles limit its practical application [94, 95]. Silicon monoxide (SiO) has emerged as a viable alternative to pure silicon. It offers a more stable cycling performance while still delivering a high theoretical capacity exceeding 1600 $mAh.g^{-1}$ [96]. The electrochemical lithiation mechanism of SiO can be described in two steps:

$$SiO + xLi \rightleftharpoons Si + Li_xO \qquad \text{(Eq. 1.19)}$$

$$xLi + Si \rightleftharpoons Li_xSi \qquad or \qquad xLi + SiO \rightleftharpoons Li_{x-y}Si_z + Li_xSiO_z \qquad \text{(Eq. 1.20)}$$

The first reaction corresponds to a conversion process, in which SiO is reduced to elemental

Si embedded in a Li_xO matrix, leading to phase segregation rather than direct alloying. Subsequent lithiation proceeds via true Li–Si alloying of the segregated Si domains, or through mixed amorphous Li–Si–O phases during cycling.

Solid silicon monoxide is thermodynamically unstable across all temperature ranges and tends to undergo a disproportionation reaction, transforming into elemental silicon and silicon dioxide upon thermal activation. Similar to pure silicon, SiO experiences substantial volume expansion and contraction during lithiation and delithiation cycles, which can lead to mechanical degradation and capacity fading. Furthermore, SiO suffers from inherently low electrical conductivity and limited lithium ion diffusion kinetics, which hinder its electrochemical performance.

To address these limitations and enhance both reversible capacity and cycling stability, various strategies have been explored. Among them, the use of advanced polymeric binders with superior electrochemical and mechanical stability has shown promise in accommodating volume changes and improving electrode integrity during cycling [97].

1.2.2.3 Cathode Materials

The evolution of LIB cathode materials has played a pivotal role in advancing rechargeable battery technology. In 1980, John B. Goodenough made a groundbreaking contribution by introducing lithium cobalt oxide ($LiCoO_2$) as a cathode material, which effectively replaced the earlier titanium disulfide (TiS_2) employed by M. Stanley Whittingham [98]. This innovation marked a crucial milestone in LIB development and laid the foundation for future commercial applications.

A decade later, in 1991, Sony Corporation successfully commercialized the first rechargeable LIB system, utilizing $LiCoO_2$ as the cathode and graphite as the anode [82]. This achievement revolutionized portable electronics and solidified LIBs as a dominant energy storage technology. The pioneering work of Whittingham, Goodenough, and Akira Yoshino, who optimized the use of polymers and carbonaceous anodes, was formally recognized with the 2019 Nobel Prize in Chemistry.

Currently, the majority of commercial LIBs employ one of the following three classes of cathode materials, each exhibiting distinct electrochemical properties and structural characteristics [99–102]:

- **Layered oxides** (e.g., $LiMO_2$, where M = Co, Ni, or Mn),
- **Spinel-type oxides** (e.g., $LiMn_2O_4$), and
- **Olivine-type phosphates** (e.g., $LiFePO_4$, commonly abbreviated as LFP).

Among these, $LiCoO_2$ remains one of the most extensively used cathode materials due to its relatively high theoretical capacity of 274 $mAh.g^{-1}$ and a stable operating voltage near 3.7 V vs. Li^+/Li. However, practical limitations have emerged in its long-term performance. Notably, when charged above 4.2 V, the crystalline lattice becomes unstable, leading to structural degradation and decreased cycle life [103, 104]. As a result, its practical specific capacity is reduced to approximately 160 $mAh.g^{-1}$. Furthermore, the high cost and limited availability of cobalt, coupled with concerns over its low thermal stability, have incentivized the search for alternative and more sustainable cathode materials.

To address these challenges, ternary layered oxides, such as $LiNi_{0.8}Co_{0.15}Al_{0.05}O_2$ (NCA) and $LiNi_xCo_yMn_zO_2$ (NMC), have been developed [105–109]. These compositions substitute part of the cobalt with nickel, manganese, or aluminum, thereby improving cycling stability, thermal properties, and reducing material costs. NMC, in particular, has gained widespread

adoption in EV batteries due to its tunable electrochemical performance and relatively balanced energy density, safety, and cost. Fig. 1.14 illustrates the lamellar (layered) crystal structure of $LiCoO_2$, highlighting the alternating layers of lithium ions and cobalt-oxygen octahedra, which enable efficient and reversible intercalation of lithium ions during battery operation [110].

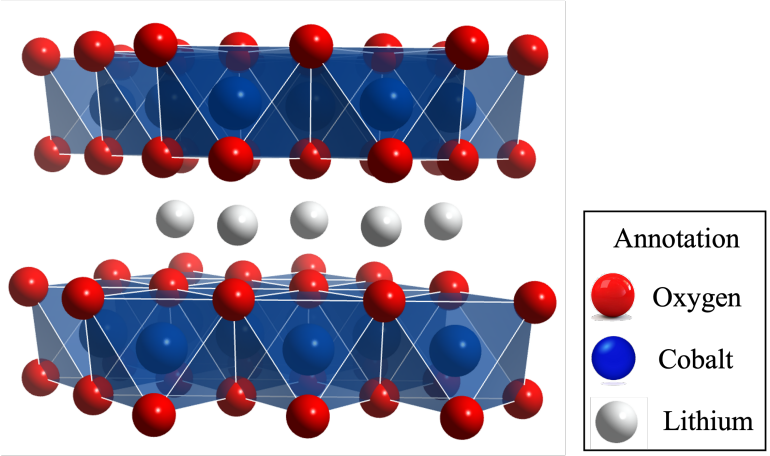

Fig. 1.14: Schematic representation of the lamellar structure of layered lithium cobalt oxide ($LiCoO_2$), where lithium ions are intercalated between alternating layers of edge-sharing CoO_6 octahedra.

An alternative class, the spinel-structured $LiMn_2O_4$ [Fig. 1.15], offers benefits such as low cost, environmental benignity, and three-dimensional lithium-ion diffusion channels, which enhance rate capability [111, 112]. However, its structural stability is compromised over extended cycles, primarily due to manganese dissolution in the electrolyte and Jahn-Teller distortion during lithium extraction.

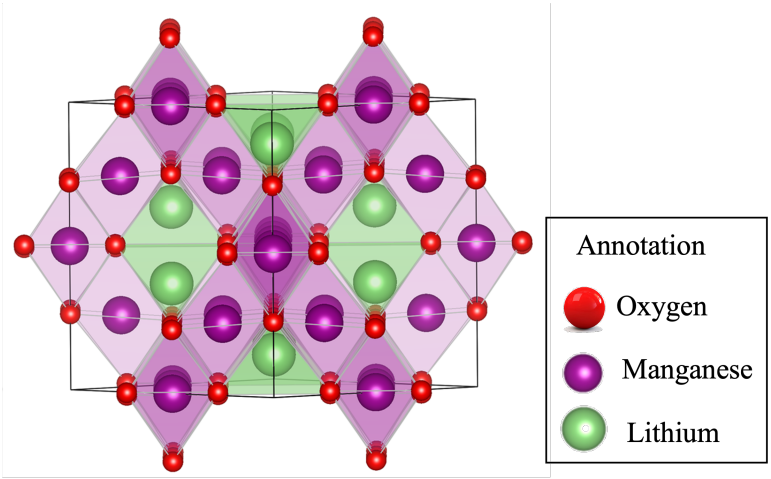

Fig. 1.15: Crystal structure of lithium manganese oxide ($LiMn_2O_4$) with a spinel framework, commonly used as a cathode material in LIBs.

The third notable candidate is $LiFePO_4$ (LFP), which crystallizes in an olivine phosphate structure. LFP is distinguished by its exceptional thermal stability, high cycle life, flat voltage profile, and low cost-attributed to the abundance of iron and phosphate precursors [113, 114].

Lithium iron phosphate ($LiFePO_4$) undergoes a reversible redox reaction, where Fe^{2+} is oxidized to Fe^{3+} during delithiation, forming $FePO_4$, and reduced back to $LiFePO_4$ upon lithiation.

As illustrated in Fig. 1.16 (b), a miscibility gap exists between these two phases. $LiFePO_4$ delivers a stable discharge voltage of approximately 3.4 V vs. Li_+/Li and a theoretical capacity of 170 $mAh.g^{-1}$-surpassing that of $LiCoO_2$ ($140-150$ $mAh.g^{-1}$)-while maintaining excellent cycling stability, primarily due to the strong covalent bonding within its phosphate framework. Although its electronic conductivity is relatively poor, this limitation has been largely mitigated through nanostructuring and carbon coating strategies.

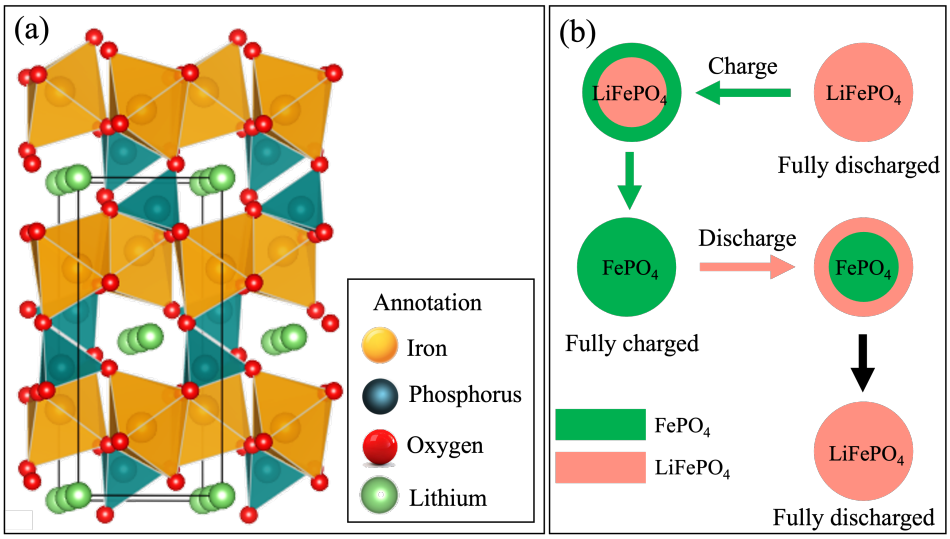

Fig. 1.16: (a) Crystal structure of $LiFePO_4$, highlighting its olivine-type framework. (b) Schematic illustration of the lithium insertion/extraction mechanism during charge and discharge cycles between $LiFePO_4$ and $FePO_4$ phases.

Table 1.3 provides a comparative overview of widely used intercalation-type cathode materials in LIBs.

Table 1.3: Intercalation-type positive electrode (cathode).

Cathode Type	**Potential (V vs. Li^+/Li)**	**Charge Density ($mAh.g^{-1}$)**	**Cycle Life**	**Safety**	**Cost**
$LiCoO_2$	~ 4.2	200	> 500	Poor	High
$LiMn_2O_4$	~ 4.2	150	> 200	Moderate	Med
$LiFePO_4$	~ 3.5	120	> 2000	Safe	Low
$LiNi_xCo_yO_2$	~ 4.2	200	> 500	Poor	High
$LiNi_yMn_xCo_zO_2$	~ 4.2	160	> 500	Poor	High

As illustrated in Fig. 1.17, electrode materials for lithium-based batteries exhibit a wide range of electrochemical potentials and specific capacities, with current and emerging cathode and anode materials strategically positioned to balance energy density, voltage, and cycling stability for both lithium-ion and lithium-metal systems.

In summary, the development and optimization of cathode materials remain central to the enhancement of LIB performance. Each of the aforementioned materials offers a trade-off between energy density, safety, stability, and economic viability, and their selection is highly dependent on the specific application requirements, ranging from portable electronics to large-scale electric mobility and grid storage.

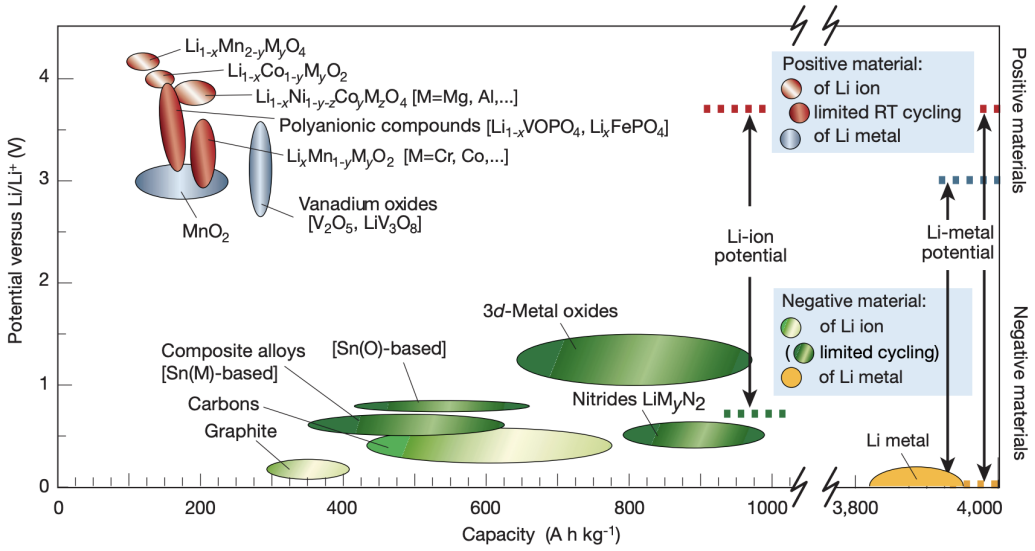

Fig. 1.17: Approximate ranges of specific capacity and average potential (versus Li/Li^+) for commonly used and actively investigated cathode and anode materials in lithium-based rechargeable batteries. The figure illustrates the voltage-capacity relationships for positive (cathode) and negative (anode) electrode materials currently in use or under serious consideration for next-generation Li-ion and Li-metal cells. Materials are classified based on their operating voltage, capacity, and compatibility with either lithium-ion or lithium-metal systems. (Adapted from [79]).

1.2.2.4 Electrolyte Materials

As shown in the Fig. 1.11, the electrolyte is a critical component of LIBs, functioning as the medium that facilitates the transport of lithium ions (Li^+) between the cathode and anode during charge and discharge cycles. While it does not participate directly in the redox reactions at the electrodes, the electrolyte plays a pivotal role in determining the overall performance, efficiency, and safety of the battery system. Its composition directly influences ion conductivity, interfacial stability, electrochemical window, and thermal behavior, all of which affect rate capabilities, cycle life, and operational safety [115].

Electrolytes in LIBs are typically classified based on their physical state (liquid or solid) and solvent nature (aqueous or non-aqueous) [116]. Among these, non-aqueous liquid electrolytes remain the most widely used in commercial LIBs due to their high ionic conductivity and compatibility with high-voltage electrode materials. An ideal liquid electrolyte should possess a high dielectric constant to enable effective ion solvation, low viscosity to facilitate rapid ion mobility, a wide electrochemical stability window, a high flash point to minimize flammability risk, and strong thermal and chemical stability across a broad range of operating conditions. Moreover, it must exhibit long-term chemical and electrochemical compatibility with both electrodes to ensure reliable performance over extended cycling.

The most common electrolyte formulations consist of lithium salts dissolved in mixtures of organic carbonate-based solvents. Widely used lithium salts include lithium hexafluorophosphate ($LiPF_6$), lithium bis (fluorosulfonyl) imide (LiFSI), lithium bis (oxalate) borate (LiBOB), and lithium tetrafluoroborate ($LiBF_4$). These salts are typically dissolved in binary or ternary blends of organic solvents such as ethylene carbonate (EC), dimethyl carbonate (DMC), ethyl methyl carbonate (EMC), and diethyl carbonate (DEC). The balance between cyclic and linear carbonates is carefully adjusted to optimize both the ionic conductivity and the stability of the

solid electrolyte interphase (SEI) layer (that will be discussed in Sec. 1.2.2.6), which is critical for the long-term performance of the battery.

In addition to the base electrolyte formulation, various functional additives are frequently introduced to enhance electrochemical performance and safety. Additives such as vinylene carbonate (VC), fluoroethylene carbonate (FEC), and lithium difluoro(oxalate)borate (LiDFOB) are known to improve the stability of the SEI layer on the anode and suppress detrimental side reactions at high voltages. These additives also help mitigate issues such as gas evolution, capacity fading, and lithium dendrite formation, especially under harsh conditions like fast charging or extreme temperatures.

Solid-state electrolytes and gel polymer electrolytes are also under intense research as next-generation alternatives, particularly for improving battery safety and enabling high energy-density designs. These solid electrolytes offer advantages such as non-flammability, wide electrochemical stability windows, and enhanced mechanical integrity. However, challenges related to low ionic conductivity and poor interfacial contact with electrodes still limit their practical application [117].

Overall, the design and engineering of electrolytes are fundamental to advancing LIB technology. Tailoring electrolyte formulations to match specific electrode materials and usage conditions-such as high-voltage cathodes, low-temperature operation, or ultra-fast charging-remains an active area of research. As demands for higher energy density and improved safety continue to rise, electrolyte development will play an increasingly central role in the evolution of LIB systems.

1.2.2.5 Separator Materials

The separator is a critical yet electrochemically inactive component of a LIB, positioned between the anode and cathode to physically prevent their direct contact and thereby avoid internal short circuits [Fig. 1.11]. While it does not participate in the electrochemical reactions, the separator plays a key role in enabling ionic conduction by acting as a permeable barrier saturated with electrolyte. Its porous structure allows for the free transport of lithium ions during charge and discharge cycles, while simultaneously ensuring electronic insulation between the electrodes.

An effective separator must exhibit a combination of essential properties, including high porosity for ion transport, excellent mechanical strength to withstand internal stresses during cycling, and robust thermal stability to prevent shrinkage or failure under elevated temperatures. These characteristics are crucial for maintaining cell integrity and ensuring long-term operational safety. Additionally, the wettability and electrolyte retention capabilities of the separator significantly influence the ionic conductivity and the overall performance of the cell.

Commercially, separators are commonly fabricated from polyolefin materials, particularly blends of polyethylene (PE) and polypropylene (PP), due to their favorable mechanical and chemical properties. In some applications, glass fiber membranes are also employed, especially in high-temperature or specialized battery designs. Advanced separators may include multi-layer structures or surface coatings to further enhance thermal shutdown behavior, electrolyte affinity, and compatibility with high-voltage systems [118].

The continuous advancement in LIB technology is driving innovation across all components, including separators. Research efforts are increasingly focused on developing next-generation separators with enhanced functionality as ceramic coatings, flame-retardant properties, or integration with solid-state electrolytes meet the demands of high-energy, fast-charging, and ultra-safe battery systems.

As the pursuit of higher energy densities, extended cycle life, and improved safety intensifies, a comprehensive understanding of the interactions between the separator, electrolyte, and

electrode materials remains critical. The optimization of separator design is thus an essential aspect of the overall strategy to improve the performance, durability, and safety of LIB across a wide range of applications.

1.2.2.6 Solid Electrolyte Interphase (SEI)

The performance, efficiency, and longevity of LIBs are critically influenced by interfacial processes, particularly at the electrode-electrolyte interface. One of the most essential and complex interfacial features in LIBs is the solid electrolyte interphase (SEI)-a passivation layer that forms spontaneously on the surface of the anode (as shown in Fig. 1.18) as a result of electrolyte decomposition during the first few charge/discharge cycles [119–124].

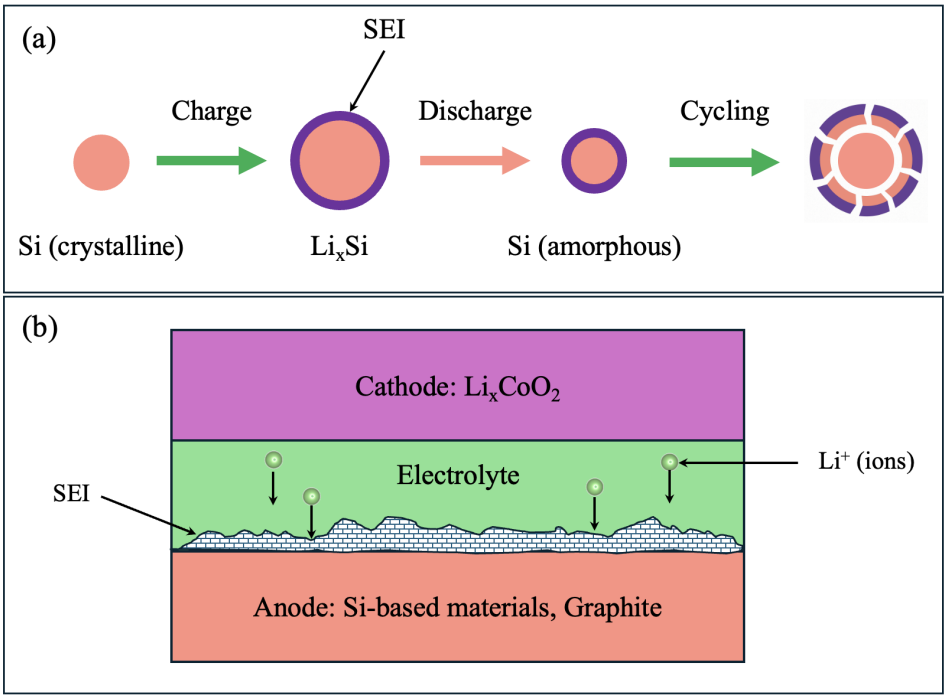

Fig. 1.18: Schematic illustration of the lithiation and delithiation processes in silicon anodes. (a) During initial lithiation, a solid electrolyte interphase (SEI) layer spontaneously forms on the silicon surface due to electrolyte decomposition. (b) Subsequent charge/discharge cycles induce significant volume expansion and contraction in the silicon, leading to mechanical stress, SEI rupture, and the formation of a thick, unstable SEI layer. These processes result in silicon pulverization and loss of electrical contact, ultimately impeding further lithium insertion and reducing the battery's cycling stability and capacity retention.

The SEI was first proposed by Peled and is recognized as a crucial component that enables the long-term stability of lithium-based batteries. It functions as a solid ionic conductor and electronic insulator, thereby preventing further reduction of the electrolyte while allowing lithium-ion transport across the interface. This dual nature is essential: while it inhibits ongoing electrolyte breakdown (thus stabilizing the interface), it must also maintain low resistance to lithium-ion diffusion to avoid performance degradation [122].

The SEI is not a uniform layer; rather, it is structurally and chemically heterogeneous, typically consisting of organic, inorganic, and polymeric species formed from the reduction products of electrolyte solvents and salts. Its composition includes compounds such as lithium

carbonate (Li_2CO_3), lithium fluoride (LiF), lithium alkoxides, and polycarbonates. This heterogeneity introduces complexity into ion transport pathways and can give rise to electron leakage and parasitic reactions that affect battery efficiency [125].

Several key characteristics define a functional SEI:

- **Optimal thickness:** It must be thick enough to block electron tunneling and suppress further electrolyte decomposition, yet thin enough to minimize lithium-ion transport resistance.
- **High lithium-ion conductivity:** Essential to maintain power performance and reduce polarization during cycling.
- **Mechanical robustness:** It must withstand the repeated volumetric changes of the electrode during lithiation/delithiation to avoid cracking or delamination.
- **Thermal and chemical stability:** To endure high-voltage operation and extended cycling without degradation.
- **Electrochemical stability:** Especially under high voltage and fast-charging conditions to ensure prolonged battery life.

During the formation of the initial SEI [Fig. 1.18], a significant portion-up to 10%-of the battery's capacity can be lost due to the irreversible consumption of lithium ions and electrolyte components. To minimize this loss, reducing the surface area of the anode is one strategy, which enhances energy density but may compromise power density due to reduced solid-state diffusion [119]. While the SEI stabilizes after initial formation, it is not entirely static. Mechanical stresses induced by repeated volume changes can lead to SEI cracking, thereby exposing fresh electrode surfaces. This triggers further electrolyte reduction and new SEI formation, continually consuming active lithium and electrolyte, and contributing to capacity fade over time. Additionally, the continual thickening of the SEI increases internal resistance, impairs lithium-ion transport, and ultimately reduces power output.

Modern battery research emphasizes the engineering and stabilization of the SEI to enhance battery performance. Strategies include:

- Designing tailored electrolyte formulations with SEI-forming additives (e.g., fluoroethylene carbonate, vinylene carbonate).
- Artificial SEI layers pre-applied to anodes to reduce initial capacity loss.
- High-concentration electrolytes and solid-state electrolytes that form more stable SEI structures.

Table 1.4 presents key electrochemical properties of selected alloying-type anode materials under investigation for LIBs, including their lithium storage capacity, operating potential, and associated volume expansion during lithiation [126].

Table 1.4: Alloying-type anode electrode and related volume expansion.

Anode Type	Potential (V vs. Li^+/Li)	Charge Density ($mAh.g^{-1}$)	Li-ion per atom	Volume expansion (%)
Li_xSi	~ 0.40	$3500-4200$	3.75	> 280
Li_xSn	~ 0.50	993	4.40	~ 240
Li_xSb	~ 0.90	660	3.00	~ 147
a-Li_xC	$\sim 0-3$	1115	$0-0.50$	~ 30

As illustrated in Fig. 1.13, silicon has attracted significant attention as a potential alternative to graphite for anode materials, owing to its remarkably high theoretical specific capacity (~ 4200 $mAh.g^{-1}$) and favorable lithiation potential [127, 128]. Despite these advantages, the practical application of silicon-based anodes in rechargeable LIBs remains limited. Table 1.4 highlights some critical challenges impeding their widespread use, including inherently low electrical conductivity, substantial volume expansion exceeding 280% during lithiation, and the formation of an unstable SEI during cycling, which results in continuous capacity fading and reduced cycle life [129–132]. To address these challenges, various surface modification strategies have been investigated. Among them, binders have emerged as a promising approach to enhance capacity retention, alleviate volume expansion, and promote the formation of a more stable SEI layer [133–136].

Indeed, numerous studies have demonstrated that the choice of binder plays a pivotal role in optimizing the performance of LIBs electrodes. Binders not only provide mechanical integrity by holding active materials and conductive additives together, but they also influence the electrode's electrochemical stability, adhesion to the current collector, and resistance to volume changes during cycling. Furthermore, an effective binder must ensure good ionic conductivity, chemical compatibility with electrolytes, and long-term structural stability to minimize capacity fading and enhance cycle life [137–141]. The most commonly used and effective binders in LIBs will be discussed in detail in the following section.

1.2.2.7 Polymer Binders for LIBs

Binders, although often comprising a relatively small fraction of the electrode composition, play a pivotal role in ensuring the mechanical and electrochemical stability of LIBs [142]. Their primary function is to maintain the structural integrity of the electrode by physically holding together the active materials and conductive agents, thereby forming a cohesive electrode film on the current collector. This cohesion is essential for maintaining consistent electronic and ionic pathways throughout charge and discharge cycles.

Despite their electrochemical inactivity, binders significantly influence the overall performance, durability, and safety of LIBs. They help accommodate mechanical stresses arising from volume changes during lithiation and delithiation processes, particularly in high-capacity materials like silicon, which undergo substantial volume expansion (Table 1.4). In such systems, inappropriate binder selection can lead to delamination, loss of electrical contact, and premature capacity fade [143].

To achieve stable and prolonged cycling, it is necessary to tailor the binder formulation and integrate it with suitable additives. An ideal binder should exhibit strong adhesion to both the active material and the current collector, good elasticity to buffer mechanical strains, chemical and electrochemical stability under cell operating conditions, and compatibility with the electrolyte system. Additionally, it should provide sufficient ionic permeability to facilitate lithium-ion transport through the electrode.

Traditionally, polyvinylidene fluoride (PVDF) dissolved in N-methyl-2-pyrrolidone (NMP) has been widely used as a binder in commercial LIBs due to its chemical stability and excellent adhesion. However, environmental and safety concerns related to NMP, along with limitations in accommodating large volume changes in advanced electrode materials, have prompted research into alternative water-soluble binders such as sodium carboxymethyl cellulose (CMC), styrene-butadiene rubber (SBR), alginate, and polyacrylic acid (PAA) [144].

Recent advancements also focus on functional binders that can participate in forming a stable SEI, enhance ionic conductivity, or chemically interact with electrode surfaces to further improve performance and cycle life. As battery technologies advance toward higher energy densities and longer lifespans, the role of binders becomes increasingly critical, not merely as passive structural supports, but as active components in engineering durable and efficient electrode architectures.

❖ Conventional Binders for LIB Anodes

In LIB research, particularly for next-generation anode materials, significant efforts have been dedicated to developing advanced binders that can overcome the limitations of conventional systems. Traditional binders often fail to accommodate the severe mechanical stress and interfacial instability associated with high-capacity anode materials, such as silicon. To address these challenges, researchers have proposed innovative binder systems, including gradient hydrogen-bonding binders and self-healing polymers such as poly(ether-thiourea) (SHPET). These advanced binders are designed to enhance the mechanical resilience, accommodate volume changes, and stabilize the SEI on silicon-based anodes, thereby improving long-term cycling performance and battery reliability [145, 146].

In the case of anodes, PVDF remains the most commonly used binder, particularly in commercial lithium-ion cells. PVDF is widely employed in both graphite anodes and $Li_{1.05}Ni_{0.33}Mn_{0.33}Co_{0.33}O_2$ (NCM)-based cathodes due to its excellent electrochemical stability, high adhesion strength, and mechanical flexibility. These properties allow PVDF to support the electrode structure during the repetitive expansion and contraction that occurs throughout charge and discharge cycles [147]. However, despite its widespread use, PVDF also presents notable drawbacks. One major concern is its potential reactivity with lithiated graphite and metallic lithium, particularly under abusive conditions such as over-discharge, low-temperature charging, or thermal shock. These reactions can be highly exothermic, significantly increasing the risk of thermal runaway and compromising battery safety. Consequently, the search for alternative binder systems that can mitigate these safety risks while maintaining or improving electrochemical performance has become increasingly important.

From a chemical standpoint, PVDF with structural formula 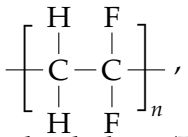 , with the repeating unit $(CH_2 = CF_2)_n$, occupies a structural position between polyethylene (PE: $(CH_2 = CH_2)_n$) and polytetrafluoroethylene (PTFE: $(CF_2 = CF_2)_n$). This intermediate configuration confers a unique balance of properties: the presence of hydrogen atoms contributes flexibility similar to PE, while the fluorine atoms introduce stereochemical rigidity and chemical resistance akin to PTFE. This dual nature enables PVDF to perform well in standard LIB environments. Nevertheless, its limitations-especially in high-energy and high-safety-demand applications-have motivated the development of next-generation binder systems with enhanced functionality, mechanical adaptability, and chemical inertness [148, 149].

Zhang et al. [150] conducted differential scanning calorimetry (DSC) on charged anodes and observed an exothermic reaction beginning around 230 °C and peaking near 300 °C, attributed

to the interaction between PVDF binder and metallic lithium. In the 1980s, polytetrafluoroethylene (PTFE) resin was extensively used as a binder in LIB anodes due to its excellent thermal and chemical stability, along with strong adhesion properties. PTFE's aqueous dispersion exhibited fibrillation, enhancing its binding capability; however, excessive fibrillation hindered uniform dispersion and reduced contact with electrode materials [151].

Polyacrylonitrile (PAN) has also been explored as a binder, mainly because of its high polarity and electrochemical stability, and is commonly used in gel polymer electrolytes (GPEs). Nevertheless, due to its high crystallinity, PAN alone lacks the mechanical properties needed for electrode adhesion, leading to fragile films that poorly attach to current collectors. To address this, Zhang and Jow proposed a copolymer, poly(acrylonitrile-methyl methacrylate) (AMMA), composed of 94% acrylonitrile (AN) and 6% methyl methacrylate (MMA). Their findings showed that AMMA is effective for both graphite anodes and lithium transition metal oxide cathodes. Compared to PVDF, AMMA promotes a more stable SEI formation on graphite and reduces self-delithiation, thereby improving calendar life [152].

In another study, Kuwabata et al. examined poly(3-n-hexylthiophene) (PHT) as a conductive binder for graphite anodes. The graphite/PHT composite demonstrated a charge capacity of 43.5 mAh.g^{-1} and coulombic efficiency of 94.6% (2.0−0 V), with a reversible capacity of 312 mAh.g^{-1} and graphite utilization of 0.92 - comparable to PVDF-based electrodes. Additionally, the conductive nature of n-doped PHT reduced irreversible capacity loss in the first cycle and enabled binding without mechanical pressing [153].

To address the significant volume expansion in silicon-based anodes, various binder strategies have been explored. The conventional binder, such as PVDF, forms weak van der Waals interactions with Si particles, which are insufficient to accommodate the large volumetric fluctuations during lithiation and delithiation. As a result, PVDF often fails to maintain adequate particle cohesion and electrical conductivity, both critical for stable battery operation. Therefore, the development of more effective binders is essential for realizing high-capacity, long-life Si anodes [152].

There remains a need to design binder matrices capable of tolerating Si volume changes while also being commercially viable. In Si electrodes, binders play a key role by forming soft matrices that offer mechanical flexibility, electrochemical stability, and enhanced electronic conductivity [154]. Shen et al. introduced an in situ thermally cross-linked PAN binder for Si anodes, showing that the modified electrode retained a reversible capacity of $\sim$ 1450 mAh.g^{-1} after 100 cycles. The improved performance was attributed to the formation of cross-linked networks and conjugated PAN structures upon heat treatment, suggesting potential for wider application across both anodes and cathodes [155].

Traditionally, Si anodes have relied on PVDF or carboxymethyl cellulose (CMC) binders. However, a pivotal study by Magasinski et al. demonstrated that poly(acrylic acid) (PAA)-which shares mechanical characteristics with CMC but contains more carboxylic groups-can surpass conventional binders in enhancing Si anode performance [156].

Table 1.5: Polymer density, silicon content (%), specific capacity at the 100th cycle (mAh.g^{-1}), and capacity retention (%) for selected high-performance binders used in silicon-based anodes of LIBs.

Binders	**PVDF**	**PAA**	**CMC**	**Ref.**
Density (g.cm^{-3})	1.8480 $\pm$ 0.0036	1.5121 $\pm$ 0.0276	1.6511 $\pm$ 0.0148	[157]
Si Content (%)	80	80	33.3	[158–160]
Specific Capacity	118.3	1155.7	1125.5	[157]
Capacity Retention	8.04	45.17	52.07	[157]

Table 1.5 summarizes the key performance metrics of some of the most effective binders used in silicon-based anodes, including polymer density, silicon content, specific capacity after 100 cycles, and corresponding capacity retention. This comparative overview highlights the critical influence of binder selection on the long-term electrochemical performance and mechanical stability of Si anodes in LIBs.

❖ Conventional Binders for LIB Cathodes

The binder in cathode fabrication plays a vital role in maintaining electrode integrity by firmly adhering to the active material and conductive additives and to the current collector [161]. Among the various binders studied, polyvinylidene fluoride (PVDF) remains the most widely adopted in the LIB industry due to its chemical stability and compatibility with cathode materials [162,163]. As illustrated in Fig. 1.19, the cathode structure requires the binder to ensure a uniform distribution of active materials and conductive agents across the electrode surface. Table 1.6 summarizes the electrochemical performance of several cathodes employing PVDF as a binder. For example, a cathode composed of 80% $Li(Li_{0.17}Ni_{0.25}Mn_{0.58})O_2$, 10% acetylene black (AB), and PVDF binder demonstrated a high discharge capacity of 238 $mAh.g^{-1}$ after 100 cycles, and 186 $mAh.g^{-1}$ at a 6C rate after 50 cycles [164].

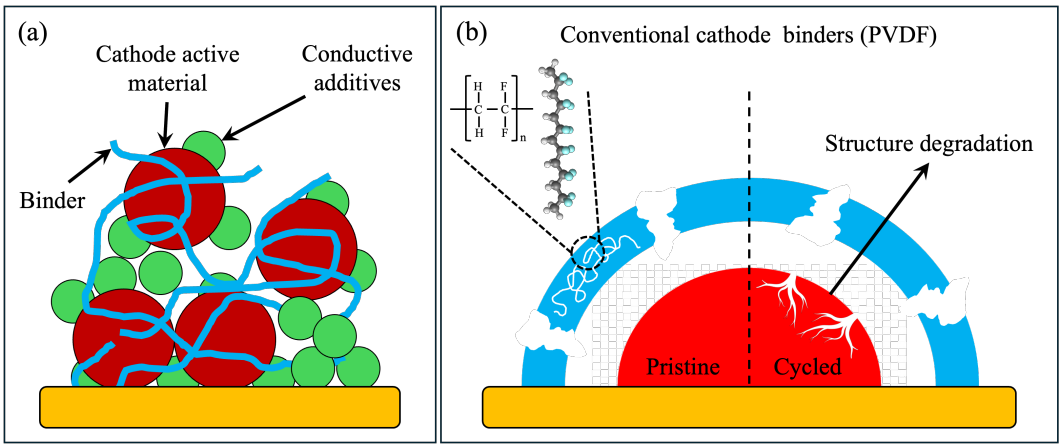

Fig. 1.19: (a) Schematic illustration of the cathode and binder structure in LIBs. (b) Structural degradation and limitations associated with conventional PVDF binders after cycling.

In a separate study, Spreafico et al. developed a novel water-based, NMP-free process for cathode preparation using PVDF binder. By coating $LiCoO_2$ cathode materials with a uniform layer of copper through an electroless deposition process, the researchers achieved comparable performance to conventional PVDF binders processed in NMP. This approach not only eliminates the need for toxic solvents but also shows potential for scale-up using semi-industrial plating techniques [165].

Furthermore, Zheng et al. investigated the effect of varying PVDF and AB ratios on cathode performance. Their results indicate that a PVDF/AB weight ratio of 5:4 provides the highest cell performance. However, increasing the ratio to 5:5 led to a decline in conductivity, attributed to insufficient particle connectivity caused by binder deficiency. These findings emphasize the importance of optimizing the binder-to-conductive additive ratio to balance mechanical cohesion and electrical conductivity [166]. Table 1.6 presents a comparative summary of the electrochemical performances (at the 100^{th} cycle) of various cathode materials employing PVDF as the binder, highlighting differences in capacity, cycle number, and retention efficiency across different material compositions and mixing ratios

Table 1.6: Electrochemical performance comparison of various cathodes fabricated using PVDF binder.

Active Materials	**Mixing Ratio**	**Electrochemical Performance (mAh.g^{-1})**	**Capacity Retention (%)**	**Ref.**
Cu-LCO	54:3:10.4	$\sim$ 100.9	97	[165]
$Ni_{0.8}Co_{0.15}Al_{0.05}$	89.4:8:4.8	$\sim$ 173	90	[166]
$Li_{0.17}Ni_{0.25}Mn_{0.58}$	8:1:1	$\sim$ 238	80	[164]

1.3 Challenges and Project Objectives

Table 1.7 summarizes the essential similarities and differences between fuel cells (FCs) and lithium-ion batteries (LIBs), emphasizing their shared reliance on interfacial electrochemistry. As discussed in Secs. 1.1 and 1.2, both systems have benefited from major technological advances, with extensive contributions from experimental studies, multiscale modeling, and high-performance simulations. Nevertheless, despite decades of progress, many of the mechanisms governing device performance and degradation remain insufficiently understood at the atomic scale.

In fuel cells, a central unresolved challenge lies in disentangling proton and electron transport at the catalyst–membrane interface. The local environment at the Pt/Nafion boundary hydration level, polymer orientation, and the formation or loss of functional groups strongly affect charge-transfer pathways and catalyst durability. Yet most existing studies rely on continuum-scale or phenomenological descriptions, leaving an important knowledge gap regarding the atomistic mechanisms that trigger structural deformation, chemical degradation, and performance loss. Ab-initio investigations of hydrated platinum surfaces interacting with Nafion fragments remain scarce, and even fewer studies examine how changes in surface hydration or sulfonic group proximity alter charge distributions and proton conduction.

A similar gap exists in lithium-ion batteries. Silicon is a promising next-generation anode, but its performance is limited by volume expansion, surface reactivity, and unstable solid-electrolyte interphase (SEI) formation. Although the behavior of crystalline and amorphous silicon has been widely simulated, the role of polymer binders, particularly poly(vinylidene fluoride) (PVDF), at oxidized Si surfaces has received far less attention. In real electrodes, silicon develops native oxides and hydroxyl groups, which strongly influence adhesion, charge transfer, and mechanical stability. However, prior computational studies typically examine PVDF in vacuum or idealized environments, overlooking oxidized and hydrated surfaces where actual battery degradation begins. Understanding how α- and β-PVDF phases interact with oxygen-rich surfaces is therefore crucial for designing electrodes that remain intact during cycling.

Table 1.7: Comparative summary of the key similarities and differences between fuel cells and batteries.

Comparison	**Fuel Cell**	**Battery**
Function	Energy conversion	Energy storage & conversion
Technology	Electrochemical reactions	Electrochemical reactions
Typical fuel	Usually pure hydrogen (or hydrocarbons)	Stored chemicals
Useful output	DC electricity	DC electricity
Main advantages	High efficiency & Reduced harmful emissions	High efficiency & High maturity
Main disadvantages	High cost & Low durability	Low operational cycles & Low durability

These challenges share a common origin: insufficient atomic-scale knowledge of how key materials-catalysts, polymers, electrolytes-interact at their interfaces under realistic operating conditions. The degradation of both FCs and LIBs often initiates at these buried boundaries, where chemical bonding, dipole alignment, proton or ion migration, and mechanical strain converge. Bridging this gap requires high-accuracy electronic-structure modeling that can

quantitatively describe charge transfer, interfacial bonding, and the energetic stability of different molecular configurations.

The primary objective of this dissertation is to provide such atomistic insights using state-of-the-art density functional theory (DFT) computational techniques. Specifically, this work aims to:

- Elucidate the interfacial charge-transfer mechanisms governing proton conduction and polymer degradation at the hydrated Pt/Nafion interface in proton exchange membrane fuel cells;
- Determine how surface oxidation, hydroxylation, and polymer phase influence PVDF adhesion and electronic coupling on Si(110), a technologically relevant surface for lithium-ion battery anodes;
- Identify structural motifs, molecular orientations, and surface terminations that enhance interfacial stability and minimize chemically driven degradation; and
- Establish general principles that connect atomic-level behavior to macroscopic performance in next-generation electrochemical energy devices.

By integrating detailed structural optimizations with charge density difference (CDD) analysis, the Bader charge analysis, local density of states (LDOS), energy interaction, and energy stability evaluations, this dissertation presents a unified theoretical framework for understanding and optimizing the interfaces that govern fuel cell and battery operation. The insights gained here are expected to guide the rational design of improved catalyst-membrane interfaces in PEMFCs and more robust binder-anode architectures in silicon-based LIBs, contributing to the advancement of durable, high-efficiency energy technologies.

**"What we observe is not nature itself,
but nature exposed to our method of questioning."**
— Werner Heisenberg —
Nobel Prize Laureate in Physics – 1932

2. Electronic Structure Theory: Methods, Techniques, and Tools

This chapter provides a foundational overview of the theoretical and computational framework used in modern quantum chemistry and condensed matter physics. It introduces key quantum mechanical principles and methods essential for first-principles calculations of materials, leading to the implementation of Density Functional Theory (DFT) and its practical use through computational packages.

❖ Chapter Outline

- **Introduction to Quantum Chemistry:** Introduces the fundamental concepts of quantum chemistry relevant to electronic structure calculations. (Sec. 2.1)
- **Schrödinger Equation:** Describes the time-independent Schrödinger equation as the central equation of non-relativistic quantum mechanics. (Sec. 2.2)
- **Born-Oppenheimer Approximation:** Explains the separation of electronic and nuclear motions. (Sec. 2.3)
- **Hartree-Fock Approximation:** Outlines the mean-field approach to solving many-body electronic systems and the concept of exchange interactions.
(Sec. 2.4)
- **Density Functional Theory (DFT):** Introduces the DFT framework as a widely used method in electronic structure theory. (Sec. 2.5)
    - Local-Density Approximation (LDA). (Sec. 2.5.1)
    - Generalized Gradient Approximation (GGA). (Sec. 2.5.2)
    - van der Waals Correlation Functions. (Sec. 2.5.3)
    - Hubbard (U) Model (DFT+U). (Sec. 2.5.4)
- **Pseudopotentials:** Explains the use of pseudopotentials to simplify the description of core electrons, making DFT calculations more efficient. (Sec. 2.6)
- **The DFT Implementation:** Details the computational implementation of DFT and its practical realization in numerical simulations. (Sec.2.7)
    - Self-Consistent Field (SCF) Methods: Describes the iterative process for achieving self-consistency in the electron density during DFT calculations. (Sec. 2.7.1)
    - Quantum ESPRESSO (QE): Introduces the QE software suite used for plane-wave DFT simulations and its relevance to this thesis. (Sec. 2.7.2)

2.1 Introduction to Quantum Chemistry

Quantum chemistry forms the foundation of theoretical and computational chemistry by applying the principles of quantum mechanics to study the behavior of atoms and molecules. It enables the accurate prediction of molecular properties, energetics, and reactivity by solving equations that govern the motion and interaction of electrons in matter.

Computational chemistry, as a broad and interdisciplinary field, plays a vital role in modern chemical research. It facilitates the prediction and interpretation of experimental results, allowing the investigation of systems or phenomena that may be experimentally inaccessible due to limitations in resolution, stability, or scale. The field encompasses both classical and quantum mechanical methods applied across various systems-from isolated atoms and molecules to extended solids and biomolecular assemblies. While classical mechanics is suitable for describing large-scale systems such as macromolecules and protein folding [167], the description of atomic and subatomic particles-particularly electrons-requires the framework of quantum mechanics due to the discrete and probabilistic nature of quantum phenomena.

Quantum mechanical methods are essential for understanding the electronic structure of matter. These methods enable the computation of key properties such as total energies, molecular geometries, electronic distributions, ionization potentials, adsorption energies, and reaction mechanisms [168]. As such, quantum chemistry offers insights into the fundamental aspects of chemical bonding, electron transfer processes, and material behavior under various thermodynamic and chemical conditions.

At the core of quantum chemistry is the Schrödinger equation, which governs the behavior of quantum systems. For a given molecular or atomic system, the solutions of the time-independent Schrödinger equation yield a set of wavefunctions corresponding to different quantum states. From these wavefunctions, observable quantities such as energy levels, bond lengths, and orbital distributions can be derived.

However, due to the complexity of solving the Schrödinger equation exactly for systems with more than one electron, a number of approximations must be employed. These approximations, ranging from the Born-Oppenheimer approximation to mean-field methods such as Hartree-Fock theory and beyond, are necessary to render quantum mechanical models computationally feasible for real-world chemical systems. Despite these approximations, quantum chemistry remains a powerful tool for elucidating molecular and material properties with remarkable accuracy.

2.2 Schrödinger Equation

In quantum chemistry, the central objective of electronic structure theory is to solve the Schrödinger equation for a given system [169]. All computational approaches developed to investigate molecular and material systems can ultimately be viewed as strategies for approximating the solution to the molecular Schrödinger equation. This equation governs the quantum mechanical behavior of a many-electron system and provides a complete description of its electronic structure.

The time-dependent many-body Schrödinger equation, which is fundamental to this analysis, is expressed as:

$$\hat{\mathcal{H}}\psi = i\hbar\frac{\partial\psi}{\partial t} \qquad \text{(Eq. 2.1)}$$

In Eq. 2.1, ψ denotes the molecular wavefunction-a mathematical expression that encapsulates the complete quantum state of the system, $\hat{\mathcal{H}}$ is the Hamiltonian operator, which includes the kinetic and potential energy terms of all particles within the system, i is the imaginary unit, defined as the square root of -1, and $\hbar$ represents the reduced Planck constant, equal to Planck's constant divided by 2π. In practical applications of the Schrödinger equation, the Hamiltonian operator is typically expressed in terms of its constituent components, which reflect the physical interactions within the system. Consequently, the explicit form of the Hamiltonian depends on the nature of the problem being addressed.

In quantum chemistry, the most commonly employed form is the non-relativistic molecular Hamiltonian within the framework of the time-independent Schrödinger equation. For a molecular system comprising N nuclei, with atomic numbers Z_i and masses M_i ($i = 1, ..., N$), and n electrons, the Hamiltonian is given by the following expression:

$$\begin{aligned}\hat{\mathcal{H}} = &- \underbrace{\sum_{\alpha=1}^{N} \frac{\hbar^2}{2M_\alpha} \nabla_\alpha^2}_{\text{nuclear kinetic energy}} - \underbrace{\sum_{i=1}^{n} \frac{\hbar^2}{2m_e} \nabla_i^2}_{\text{electron kinetic energy}} - \underbrace{\sum_{i=1}^{n} \sum_{\alpha=1}^{N} \left(\frac{e^2}{4\pi\epsilon_0} \right) \frac{Z_\alpha}{|r_i - R_\alpha|}}_{\text{electron-nuclear attraction}} \\ &+ \underbrace{\sum_{i>j}^{n} \left(\frac{e^2}{4\pi\epsilon_0} \right) \frac{1}{|r_i - r_j|}}_{\text{electron-electron repulsion}} + \underbrace{\sum_{\alpha>\beta}^{N} \left(\frac{e^2}{4\pi\epsilon_0} \right) \frac{Z_\alpha Z_\beta}{|R_\alpha - R_\beta|}}_{\text{nuclear-nuclear repulsion}}\end{aligned} \tag{Eq. 2.2}$$

In this formulation, m_e represents the electron mass, e denotes the elementary charge, and r_i corresponds to the position vector of the i^{th} electron. The coordinate of the α^{th} nucleus is given by R_α, while ϵ_0 signifies the vacuum permittivity. The Laplacian operator ∇_i^2, acting on the coordinates of the i-th particle, is defined as:

$$\nabla_i^2 = \frac{\partial^2}{\partial x_i^2} + \frac{\partial^2}{\partial y_i^2} + \frac{\partial^2}{\partial z_i^2} \tag{Eq. 2.3}$$

In quantum chemistry, it is frequently advantageous to employ atomic units rather than the conventional Système International (SI) units. This choice eliminates numerous physical constants from theoretical expressions, thereby significantly simplifying their form. Throughout this work, we consistently adopt the atomic units defined in the Table 2.1, except where explicitly noted otherwise.

Table 2.1: Fundamental atomic units used in quantum chemical calculations. All quantities are expressed in terms of the reduced Planck constant ($\hbar$), electron mass (m_e), elementary charge (e), and Coulomb's constant ($1/4\pi\epsilon_0$), yielding a simplified system where these constants become unity.

Symbol	Quantity	Atomic Units	Standard Units
e	charge	electron charge	1.6022×10^{-19} C
m_e	mass	electron mass	9.10938×10^{-31} kg
a_0	length	Bohr	5.29177×10^{-11} m
E_h	energy	Hartree	4.35974×10^{-18} J

When expressed in atomic units, the molecular Hamiltonian (Eq. 2.1) undergoes significant simplification, reducing to the following compact representation:

$$\hat{\mathcal{H}} = \underbrace{-\sum_{\alpha=1}^{N} \frac{1}{2M_\alpha}\nabla_\alpha^2}_{\hat{T}_N} \underbrace{-\sum_{i=1}^{n} \frac{1}{2}\nabla_i^2}_{\hat{T}_e} \underbrace{-\sum_{i=1}^{n}\sum_{\alpha=1}^{N} \frac{Z_\alpha}{|r_i - R_\alpha|}}_{\hat{V}_{eN}} + \underbrace{\sum_{i>j}^{n} \frac{1}{|r_i - r_j|}}_{\hat{W}_{ee}} + \underbrace{\sum_{\alpha>\beta}^{N} \frac{Z_\alpha Z_\beta}{|R_\alpha - R_\beta|}}_{\hat{V}_{NN}} \quad \text{(Eq. 2.4)}$$

Where:

- $\hat{T}_N$ is the kinetic energy operator for the nuclei.
- $\hat{T}_e$ is the kinetic energy operator for the electrons.
- $\hat{V}_{eN}$ is the potential energy operator for electron-nucleus attraction.
- $\hat{W}_{ee}$ is the potential energy operator for electron-electron repulsion.
- $\hat{V}_{NN}$ is the potential energy operator for nucleus-nucleus repulsion.

While the Schrödinger equation (Eq. 2.4) is the fundamental starting point for understanding the quantum behavior of materials, solving it exactly becomes practically impossible for systems with many electrons. This is due to the exponential complexity of the wavefunction, which exists in a $3N$-dimensional space, where N is the number of electrons.

For example, consider a unit cell of silicon, with an atomic number of 14 and 28 electrons per unit cell. The electronic wavefunction in this case depends on 84 spatial variables (3 coordinates per electron). If we attempt to compute an integral over all electronic degrees of freedom and discretize each of the 84 dimensions using just 10 points, we would need to evaluate 10^{84} values. Even with the most powerful supercomputers, capable of performing around 10^{18} operations per second, such a calculation would still take around 10^{66} seconds-which is many orders of magnitude longer than the age of the universe (approximately 10^{17} seconds).

This illustrates the inherent limitation of solving the Schrödinger equation exactly for realistic systems. As a result, approximation methods-such as the Born-Oppenheimer approximation, Hartree-Fock theory, and Density Functional Theory (DFT)-are essential tools in computational physics and quantum chemistry. These approaches, which will be discussed in the following sections, enable us to capture the essential physics of complex systems while keeping the problem computationally tractable.

2.3 Born-Oppenheimer Approximation

In the time-independent, non-relativistic molecular Schrödinger equation, the total wavefunction of a molecular system, denoted as $\Psi(\{r\}, \{\mathbf{R}\})$, depends on both the electronic coordinates (r) and the nuclear coordinates $(\mathbf{R})$. This full wavefunction describes the quantum behavior of all the constituent particles-electrons and nuclei-within the system.

However, accounting for the dynamics of both electrons and nuclei simultaneously presents a significant computational challenge in electronic structure calculations. To reduce this complexity, the Born-Oppenheimer (BO) approximation is introduced [170]. This approximation is founded on the physical insight that atomic nuclei are much heavier than electrons, typically by a factor of about 1,800 or more. Due to this large mass difference, nuclei move much more slowly compared to the rapidly adjusting electrons.

The key idea of the Born-Oppenheimer approximation is that electrons can adapt instantaneously to the positions of the much slower-moving nuclei. That is, the electronic structure adjusts adiabatically as the nuclei move. This allows us to assume that, at any given instant, the electrons are in a stationary state corresponding to fixed nuclear positions.

Mathematically, the total molecular wavefunction can then be approximated as a product of two separate components:

$$\Psi(\{r\},\{\mathbf{R}\}) \approx \Xi(\{\mathbf{R}\})\Phi(r;\{\mathbf{R}\}) \tag{Eq. 2.5}$$

where:

- $\Xi(\{\mathbf{R}\})$ is the nuclear wavefunction, treated as being independent of the electronic coordinates.
- $\Phi(r;\{\mathbf{R}\})$ is the electronic wavefunction that depends parametrically on the nuclear coordinates.

It is important to note that this approximation breaks down in systems where electronic and nuclear motions are strongly coupled, such as in cases involving non-adiabatic transitions, conical intersections, or very light nuclei (e.g., hydrogen atoms in proton transfer processes). This approach can be justified by analyzing the individual terms of the Hamiltonian, each of which depends explicitly on either the electronic or nuclear coordinates:

$$\hat{\mathcal{H}}(r,\mathbf{R}) = \underbrace{\hat{T}_N(\mathbf{R}) + \hat{V}_{NN}(\mathbf{R})}_{\hat{\mathcal{H}}_N(\mathbf{R})} + \underbrace{\hat{T}_e(r) + \hat{V}(r,\mathbf{R}) + \hat{W}(r)}_{\hat{\mathcal{H}}_e(r,\mathbf{R})} \tag{Eq. 2.6}$$

The total Hamiltonian can be expressed as the sum of an electronic Hamiltonian $\hat{\mathcal{H}}_e(r,\mathbf{R})$ and a nuclear Hamiltonian $\hat{\mathcal{H}}_N(\mathbf{R})$, where includes only those terms from Eq. 2.6 that act on the nuclear coordinates. However, this does not result in a complete separation of electronic and nuclear components, since the electron-nuclear Coulomb interaction inherently depends on both sets of coordinates. Nevertheless, by assuming a fixed nuclear geometry, the nuclear positions can be treated as parameters, and the electron-nuclear interaction term simplifies to an effective one-electron operator. This operator represents the electrostatic potential experienced by the electrons due to a static distribution of point-like nuclear charges. Consequently, an electronic Schrödinger equation can be formulated using the electronic Hamiltonian, evaluated at a fixed nuclear geometry, as follows:

$$\hat{\mathcal{H}}_e(r;\mathbf{R})\Phi_i(\{r;\mathbf{R}\}) = \left[\hat{T}_e(r) + \hat{V}(r;\mathbf{R}) + \hat{W}(r)\right]\Phi_i(\{r;\mathbf{R}\}) = \mathcal{E}_i(\mathbf{R})\Phi_i(\{r;\mathbf{R}\}) \tag{Eq. 2.7}$$

The electronic wavefunction $\Phi_i(\{r;\mathbf{R}\}$ is an eigenfunction of the electronic Hamiltonian, and the associated eigenvalue $\mathcal{E}_i(\mathbf{R})$ represents the electronic energy at a fixed nuclear geometry $(\mathbf{R})$. The set of eigenfunctions Φ_i forms a complete orthonormal basis, representing the discrete electronic energy levels of the system for a given configuration of the nuclei. Among these, Φ_0 denotes the ground-state electronic wavefunction, with its corresponding energy $\mathcal{E}_0$. The full Schrödinger equation for the molecular system at a fixed nuclear geometry can be similarly derived by extending Eq. 2.7 to incorporate the nuclear Hamiltonian $\hat{\mathcal{H}}_N$, the nuclear

wavefunction, and applying the product rule of differentiation to the total wavefunction expressed as a product of electronic and nuclear components:

$$\begin{aligned}\hat{\mathcal{H}}(r,\mathbf{R})\,\Psi_{ij}(\{r\},\{\mathbf{R}\}) &\approx \left[\hat{\mathcal{H}}_N(\mathbf{R})+\mathcal{E}_j(\mathbf{R})\right]\Xi_i(\{\mathbf{R}\})\,\Phi_j(r;\mathbf{R}\}) \\ &= E_{ij}\,\Xi_i(\{\mathbf{R}\})\,\Phi_j(\{r;\mathbf{R}\})\end{aligned} \qquad \text{(Eq. 2.8)}$$

Here, E_{ij} denotes the total energy of the molecular system when it is in the i^{th} nuclear and j^{th} electronic eigenstate. Within the framework of the Born-Oppenheimer approximation, it is assumed that the energy separation between different electronic states $\mathcal{E}_i$ is sufficiently large to prevent any significant coupling between the electronic and nuclear wavefunctions. In other words, as the nuclear positions evolve, the system remains confined to a single electronic state. Consequently, the electrostatic potential acting on the nuclei, arising from the surrounding electron cloud, is described by a potential energy surface $\mathcal{E}_i(\mathbf{R})$, corresponding to that specific electronic state.
Once a set of solutions to Eq. 2.7 has been obtained, defining the potential energy surface $\mathcal{E}_i(\mathbf{R})$, the corresponding nuclear Schrödinger equation can be expressed as:

$$\left[\hat{\mathcal{H}}_N(\mathbf{R})+\mathcal{E}_i(\mathbf{R})\right]\Xi_j(\{\mathbf{R}\}) = \left[\hat{T}_N(\mathbf{R})+\mathcal{U}_i(\mathbf{R})\right]\Xi_j(\{\mathbf{R}\}) = \mathcal{E}_j^N\,\Xi_j(\{\mathbf{R}\}) \qquad \text{(Eq. 2.9)}$$

where $\mathcal{E}_j^N$ denotes the j^{th} nuclear energy eigenvalue, and $\mathcal{U}_i(\mathbf{R})$ represents the Born-Oppenheimer potential energy surface corresponding to the i^{th} electronic state,

$$\mathcal{U}_i(\mathbf{R}) = \hat{V}_{NN}(\mathbf{R}) + \mathcal{E}_i(\mathbf{R}) \qquad \text{(Eq. 2.10)}$$

The nuclei can be treated as interacting classically rather than quantum mechanically in this context. Although this approach introduces a certain degree of approximation, the Born-Oppenheimer approximation can be effectively applied to most quantum chemical problems, thereby significantly facilitating the process of obtaining accurate and practical solutions to the electronic Schrödinger equation.

2.4 Hartree-Fock Approximation

Various methods have been developed to solve the time-independent form of the Schrödinger equation for electrons. Among the *ab initio* approaches, many begin with the Hartree-Fock approximation as a foundational framework. This method provides a mean-field description of the electronic structure, serving as a starting point for more accurate post-Hartree-Fock techniques [171].

We begin by formulating the expression for the time-independent, non-relativistic Hamiltonian $\hat{\mathcal{H}}_0$ for a system consisting of N electrons, located at positions r_i, and N_0 nuclei, located at positions $\mathbf{R}_a$.

$$\hat{\mathcal{H}}_0(\vec{r}_1,\ldots,\vec{r}_N) = \underbrace{-\frac{1}{2}\sum_{i=1}^{N}\Delta_{\vec{r}_i}}_{\hat{T}_e} \underbrace{-\sum_{i=1}^{N}\sum_{a=1}^{N_0}\frac{Z_a}{\mathbf{R}_a-\vec{r}_i|}}_{\hat{V}_{Ne}} \underbrace{+\sum_{i=1}^{N}\sum_{j=1}^{i-1}\frac{1}{|\vec{r}_i-\vec{r}_j|}}_{\hat{V}_{ee}} \underbrace{+\sum_{a=1}^{N_0}\sum_{b=1}^{a-1}\frac{Z_aZ_b}{|\mathbf{R}_a-\mathbf{R}_b|}}_{\hat{V}_{NN}} \quad \text{(Eq. 2.11)}$$

In the Eq. 2.11, the electronic kinetic energy ($\hat{T}_e$) and the nucleus-electron attraction term ($\hat{V}_{Ne}$) are represented as sums of one-electron operators, with each term depending solely on the position of a single electron. The nucleus-nucleus repulsion term ($\hat{V}_{NN}$), which is independent of the electronic coordinates, acts as a constant operator for the system. In contrast, the electron-electron repulsion operator ($\hat{V}_{ee}$) depends on the simultaneous positions of pairs of electrons. This many-body interaction introduces significant complexity, rendering the equation analytically unsolvable for systems containing more than one electron.

The Hartree-Fock (HF) approximation addresses this challenge by assuming that each electron experiences an average or mean-field potential generated by all other electrons. This approach effectively transforms the electron-electron repulsion term into a one-electron operator, thereby reducing the full many-body Hamiltonian into a sum of single-electron Hamiltonians ($\hat{\mathcal{H}}_0 \rightarrow \hat{\tilde{\mathcal{H}}}_0$):

$$\hat{\tilde{\mathcal{H}}}_0(\boldsymbol{r}_1,\ldots,\boldsymbol{r}_N) = \sum_{i=1}^{N}\hat{F}(\boldsymbol{r}_i) + \sum_{a=1}^{N_0}\sum_{b=1}^{a-1}\frac{Z_aZ_b}{|\boldsymbol{R}_a-\boldsymbol{R}_b|} \quad \text{(Eq. 2.12)}$$

The term $\hat{F}(\boldsymbol{r}_i)$ in Eq. 2.12 is referred to as the Fock operator. It is inherently dependent on its own solution, as it includes contributions from the mean-field generated by the electron density obtained through the solution of the equation itself.

❖ Fock Operator

Assuming the exact solutions are known, we can define the corresponding eigenfunctions $\chi_i(\mathbf{r})$ and their associated eigenvalues ϵ_i by the following eigenvalue equation:

$$\hat{F}(\mathbf{r}),\chi_i(\mathbf{r}) = \epsilon_i,\chi_i(\mathbf{r}), \qquad i = 1,\ldots,N \quad \text{(Eq. 2.13)}$$

where $\chi_i(\mathbf{r})$ and ϵ_i are the eigenfunctions and corresponding eigenvalues of the operator $\hat{F}$.

To incorporate the spin of the electron, the one-electron functions χ_i, referred to as orbitals, are combined with the spin function $\zeta_s(\sigma)$. This coupling results in the formation of spin-orbital functions $\phi_{i,s}$:

$$\phi_{i,s}(\mathbf{r},\sigma) = \phi_{i,s}(\mathbf{x}) = \chi_i(\mathbf{r})\zeta_s(\sigma) \quad \text{(Eq. 2.14)}$$

The eigenvectors of $\hat{\tilde{\mathcal{H}}}_0$ are represented by Slater determinants, which are antisymmetrized products of the spin-orbital functions $\phi_{i,s}$. These determinants ensure compliance with the Pauli exclusion principle and the antisymmetry requirement of fermionic wavefunctions. The general form is expressed as $|\psi_I\rangle = \left|\left[\prod_{i,s}\phi_{i,s}\right]\right\rangle$. The Fock operator can be decomposed into

three distinct components:

$$\hat{F} = \hat{h} + \sum_{k} \left(\hat{J}_k - \hat{K}_k \right) \tag{Eq. 2.15}$$

The operator $\hat{h}$ includes both the kinetic energy of the electron and the electron-nucleus attraction, and the summation index k runs over the N occupied spin-orbitals. The term $\hat{J}_k$ represents the Coulomb operator, which accounts for the electrostatic repulsion between a given electron and the average charge distribution of the others. The term $\hat{K}_k$ is the exchange operator, which arises due to the antisymmetry of the wavefunction and has no classical counterpart. The exchange operator $\hat{K}_k$ reflects a purely quantum mechanical effect with no classical analog, arising from the wave-like nature and indistinguishability of electrons. The energy associated with a single orbital within the Fock operator framework can then be expressed as:

$$\epsilon_i = h_{ii} + \sum_{k=1}^{N} \left(J_{ik} - K_{ik} \right), \qquad h_{ii} = \langle \phi_i | \hat{h} | \phi_i \rangle \tag{Eq. 2.16}$$

with

$$\begin{cases} J_{ik} \equiv \langle \phi_i | \hat{J}_k | \phi_i \rangle, \\ \langle \phi_i | \hat{J}_k | \phi_j \rangle = \delta_{s_i s_j} \iint \dfrac{\chi_i^*(\boldsymbol{r})\, \chi_j(\boldsymbol{r})\, \chi_k^*(\boldsymbol{r}')\, \chi_k(\boldsymbol{r}')}{|\boldsymbol{r} - \boldsymbol{r}'|}\, d\boldsymbol{r}\, d\boldsymbol{r}' \end{cases} \tag{Eq. 2.17}$$

and

$$\begin{cases} K_{ik} \equiv \langle \phi_i | \hat{K}_k | \phi_i \rangle, \\ \langle \phi_i | \hat{K}_k | \phi_j \rangle = \delta_{s_i s_k}\, \delta_{s_j s_k} \iint \dfrac{\chi_i^*(\boldsymbol{r})\, \chi_k(\boldsymbol{r})\, \chi_k^*(\boldsymbol{r}')\, \chi_j(\boldsymbol{r}')}{|\boldsymbol{r} - \boldsymbol{r}'|}\, d\boldsymbol{r}\, d\boldsymbol{r}' \end{cases} \tag{Eq. 2.18}$$

The ground-state (GS) wavefunction $|\psi_0\rangle$ of the mean-field Hamiltonian is obtained by occupying the spin-orbitals in order of increasing energy, with each spatial orbital accommodating two electrons of opposite spin. The total ground-state energy consists of the nucleus-nucleus repulsion energy and the sum of the eigenvalues ϵ_i of all occupied orbitals, corrected by subtracting the electron-electron interaction energy to avoid double counting. According to the variational principle, the self-consistent solution corresponds to the lowest possible energy, ensuring that the obtained wavefunction approximates the true ground state.

❖ **Variational Principle**

The variational principle states that for any trial N-electron wavefunction $|\psi\rangle$ that satisfies the normalization condition, the expectation value E of the Hamiltonian evaluated with this wavefunction will always be greater than or equal to the true ground-state energy E_0. Mathematically, this is expressed as:

$$E = \langle \psi | \bar{H} | \psi \rangle \geq \langle \psi_0 | \bar{H} | \psi_0 \rangle = E_0 \qquad \text{(Eq. 2.19)}$$

This principle forms the foundation of many approximate methods in quantum chemistry, as it ensures that the best approximation to the ground-state wavefunction is the one that minimizes the total energy [172].

2.5 Density Functional Theory (DFT)

Historically, before the 20$^{\text{th}}$ century, the concept of *first principles* appeared in philosophy, mathematics, and theoretical physics, referring to fundamental assumptions or truths that are self-evident and cannot be derived from other propositions. In philosophy, the notion traces back to ancient Greece, particularly within Aristotelian thought. In mathematics, first principles are known as axioms or postulates-statements accepted without proof. In the natural sciences, including physics, first principles approaches are those built directly upon fundamental scientific laws, without relying on empirical models or fitting parameters.

Following the development of the Schrödinger equation (Sec. 2.2) in the early 20$^{\text{th}}$ century, quantum mechanics came to be regarded as the foundational first-principles theory in physics. Today, first-principles or *ab initio* methods refer specifically to quantum mechanical approaches widely used in condensed matter physics, chemistry, and materials science.

Nonetheless, an exact solution of the Schrödinger equation for many-electron systems remains practically impossible due to the enormous computational demands associated with many-body problems. To overcome these limitations, density functional theory (DFT) has emerged as a powerful and practical alternative. Based on the foundational work of Hohenberg and Kohn (1964) [173] and the subsequent Kohn-Sham formalism (1965) [174], DFT has become a cornerstone technique in the theoretical investigation of materials, offering an efficient framework for studying complex electronic systems [175].

An important alternative to the Hartree-Fock method (Sec. 2.4) is DFT, where the electron density becomes the fundamental quantity for determining a system's properties. DFT achieves significantly lower computational cost than Hartree–Fock calculations while also recovering a portion of the electron correlation energy, which Hartree-Fock neglects.

❖ Hohenberg-Kohn (H.K.) Theorems

The concept of electron density as a central variable was first introduced in 1927 by Thomas and Fermi [176]. They proposed using a mono-electronic function, the electron density, to describe the ground-state properties of a many-electron system, which is a significantly simpler quantity than the many-body wavefunction. In quantum mechanics, the square modulus of a normalized wavefunction, $|\psi(\boldsymbol{x_1}, \boldsymbol{x_2}, \ldots, \boldsymbol{x_N})|^2 \, d\boldsymbol{x_1} \, d\boldsymbol{x_2} \ldots d\boldsymbol{x_N}$, represents the probability of simultaneously finding electron 1 within an infinitesimal volume $d\boldsymbol{x_1}$ around $\boldsymbol{x_1}$, electron 2 within $d\boldsymbol{x_2}$ around $\boldsymbol{x_2}$, and so on. The electron density is obtained by integrating the probability distribution over all electron coordinates except one, reflecting the indistinguishability of electrons:

$$n(\boldsymbol{r}) = N \int |\psi(\boldsymbol{x_1}, \boldsymbol{x_2}, \ldots, \boldsymbol{x_N})|^2 \, d\boldsymbol{x_1} \, d\boldsymbol{x_2} \ldots d\boldsymbol{x_N} \qquad \text{(Eq. 2.20)}$$

From this definition, it follows that $n(\boldsymbol{r})d\boldsymbol{r}$ represents the average number of electrons within the infinitesimal volume $d\boldsymbol{r}$ surrounding the position $\boldsymbol{r}$, and that the integral of $n(\boldsymbol{r})$ over all space yields the total number of electrons N. The electron density $n(\boldsymbol{r})$ is a measurable physical quantity and is associated with the density operator $\hat{n}$.

DFT draws heavily from the foundational ideas introduced by the Thomas-Fermi model regarding the electronic structure of materials. A major advancement came in 1965, when Hohenberg and Kohn established a rigorous formal framework for DFT through two fundamental theorems [177]. In their first theorem, they demonstrated that for any system of interacting electrons, the external potential and consequently the total energy are a unique functional of the electron density. This implies that the electron density uniquely determines the external potential acting on the electrons, and therefore all ground-state properties of the system. As a result, any ground-state property of the system, including the ground-state energy itself, can be expressed as a functional of the electron density.

- **H.K. 1st Theorem:** Each N-electron density corresponds to the ground-state density of at most one Hamiltonian $\hat{H}[v_{\text{ext}}, N]$, where the external potential v_{ext} is uniquely determined, up to an additive constant c:

$$n(\boldsymbol{r}) = n'(\boldsymbol{r}) \rightarrow v_{ext}(\boldsymbol{r}) = v'_{ext}(\boldsymbol{r}) + c \qquad \text{(Eq. 2.21)}$$

Thus, there exists a unique functional, $F_{\text{HK}}[n]$, of the electron density that enables the determination of ground-state properties.

$$\begin{aligned} \hat{H}_0^{\text{elec}}[n] &= \hat{T}_{\text{e}} + \hat{V}_{\text{ee}} + \hat{V}_{\text{Ne}} \\ &= F_{\text{HK}}[n] + \int v_{\text{Ne}}(\boldsymbol{r}) n(\boldsymbol{r}) d\boldsymbol{r} \end{aligned} \qquad \text{(Eq. 2.22)}$$

The second Hohenberg-Kohn theorem establishes that the variational principle applies to this universal functional. Although the existence and uniqueness of $F_{\text{HK}}[n]$ are guaranteed, its explicit mathematical form remains unknown.

- **H.K. 2nd Theorem:** For any positive integer N and external potential $v(\boldsymbol{r})$, there exists a density functional $F_{\text{HK}}[n]$ such that the functional $F_{\text{HK}}[n] + \int v(\boldsymbol{r}) n(\boldsymbol{r})\, d\boldsymbol{r}$ attains its minimum at the ground-state electron density corresponding to a system of N electrons in the potential $v(\boldsymbol{r})$. This minimum value corresponds to the ground-state energy $E[v]$ of the system.

Subsequent to their original formulation, the theorems were expanded and adapted, leading to the formalism that is now standard in the field [178].

❖ Kohn-Sham Method

As previously discussed, the challenge in solving the Schrödinger equation (Sec. 2.2) arises from the complexities introduced by electron-electron interactions. Building upon the second Hohenberg-Kohn theorem, which asserts that the ground-state energy of a system is the global minimum of a functional of the electronic density, Kohn and Sham proposed a method to address the many-body problem. Their approach involves substituting the interacting system

with a fictitious system of non-interacting particles, represented by a set of orthonormal orbitals α_i, allowing for the exact calculation of the non-interacting kinetic functional $T_S[n]$:

$$T_S[n] = -\frac{1}{2}\sum_i \langle \alpha_i | \, \Delta \, | \alpha_i \rangle \tag{Eq. 2.23}$$

In the Kohn-Sham framework, the fictitious electrons are subjected to a modified potential that ensures the same ground-state electron density as the real interacting system. The total energy functional is constructed by incorporating the Hartree energy functional ($E_H[n]$), which represents the classical Coulomb interaction, and the exchange-correlation energy functional ($E_{XC}[n]$), whose exact form remains unknown, into the Kohn-Sham functional. Consequently, the total energy functional $F[n]$ is expressed as:

$$F[n] = T_S[n] + E_{\mathrm{H}}[n] + E_{\mathrm{xc}}[n] \tag{Eq. 2.24}$$

And the Kohn-Sham potential related to Eq. 2.24 is:

$$v_{\mathrm{KS}}(\boldsymbol{r}) = v_{\mathrm{Ne}}(\boldsymbol{r}) + v_{\mathrm{H}}(\boldsymbol{r}) + v_{\mathrm{xc}}(\boldsymbol{r}) \tag{Eq. 2.25}$$

The electron density $n(\boldsymbol{r})$ is obtained from the Kohn-Sham orbitals α_i as:

$$n(\boldsymbol{r}) = \sum_{i=1}^{N} |\alpha_i(\boldsymbol{r})|^2 \tag{Eq. 2.26}$$

where $\alpha_i(\boldsymbol{r})$ are the Kohn-Sham orbitals. The total ground-state energy of the system corresponds to the sum of the eigenvalues of these orbitals, adjusted by the Hartree and exchange-correlation energies, as given by:

$$\begin{aligned} E_0 &= \min_{\{a_i\}} \left\{ F[n] + \int n(\boldsymbol{r}) v_{Ne}(\boldsymbol{r}) \, d\boldsymbol{r} \right\} \\ &= \min_{\{a_i\}} \left\{ T_S[n] + E_H[n] + E_{xc}[n] + \int n(\boldsymbol{r}) v_{Ne}(\boldsymbol{r}) \, d\boldsymbol{r} \right\} \end{aligned} \tag{Eq. 2.27}$$

Finally, the one-electron Kohn-Sham equations are solved self-consistently by iteratively adjusting the total energy functional concerning the orbitals, ensuring convergence to the ground-state electron density:

$$\left[-\frac{1}{2}\Delta + v_{\mathrm{KS}}(\boldsymbol{r}) \right] \alpha_i(\boldsymbol{r}) = \epsilon_i^{\alpha} \alpha_i(\boldsymbol{r}) \tag{Eq. 2.28}$$

The energies ϵ_i^{α} correspond to the eigenvalues associated with the Kohn-Sham orbitals. The primary challenge of the method lies in accurately determining the exchange-correlation (E_{xc})

functional.

The current challenge lies in identifying an exchange-correlation functional that most accurately approximates the true exchange-correlation potential. DFT is a rigorous formalism in which the electronic density is represented within an independent particle model, described by a single determinant. While this approach greatly simplifies calculations, it introduces significant complexity within the exchange-correlation term. To improve the description of interactions, numerous approximations to the exchange-correlation energy, treated as a functional of spin density, have been developed and tested. Modern functionals include the local density approximation (LDA), the generalized gradient approximation (GGA), and other components or parameters designed to enhance the accuracy of the overall functional. The ideal universal functional should provide an accurate description of any system under study, whether a molecule, a solid, or any other system. However, this exact functional remains unknown, and thus, we rely on approximations derived either from physical construction (*ab initio*) or experimental fitting. These approximations are classified according to Jacob's ladder (see Fig. 2.1) and will be discussed in the following sections.

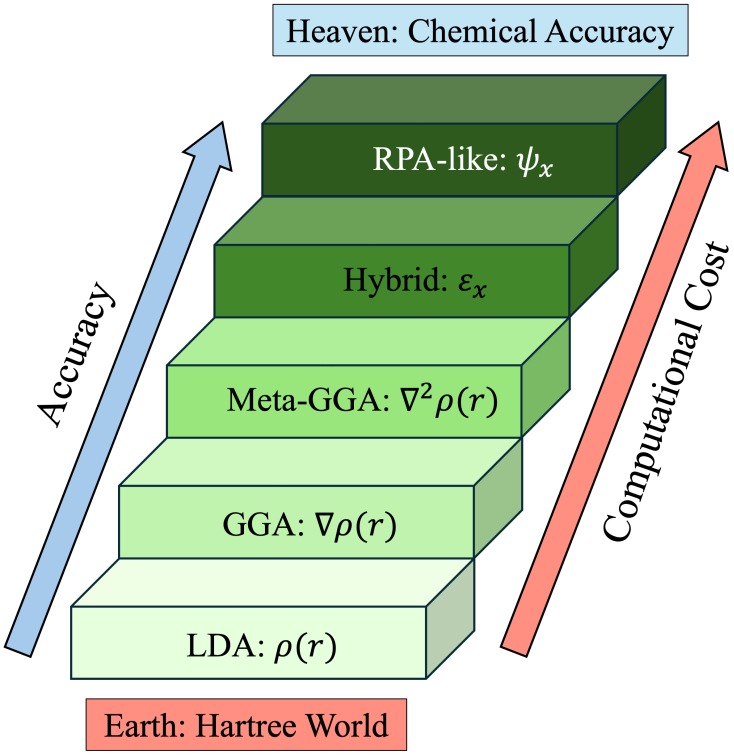

Fig. 2.1: Jacob's ladder, showing the first five rungs leading towards the theoretical universal functional.

2.5.1 Local-Density Approximation (LDA)

The first rung of Jacob's ladder is represented by the local density approximation (LDA) or local spin density approximation (LSDA), in which the exchange-correlation functional is dependent only on the electronic density [174]:

$$E_{\mathrm{xc}}^{\mathrm{LDA}}[n(\boldsymbol{r})] = \int n(\boldsymbol{r})\varepsilon_{\mathrm{xc}}(n(\mathbf{r}))\, d\boldsymbol{r} \qquad \text{(Eq. 2.29)}$$

In Eq. 2.29, ε_{xc} represents the exchange-correlation energy per unit volume of the uniform electron gas. In the LDA, the exchange component of the energy functional closely resembles Slater's description, with the primary difference being the pre-factor. The correlation component of the functional was derived analytically using quantum Monte Carlo simulations of the uniform electron gas [179]. While LDA serves as a reasonable starting approximation and yields accurate results for delocalized electronic charge systems, it performs best for systems with slowly varying electron densities. Although the energy at each point is not explicitly influenced by its surrounding environment, this approach still produces reasonably accurate results in many practical applications. Despite its many successes, LDA has notable limitations, such as a tendency for strong over-binding. Consequently, it has found broader application in solid-state physics, where electron delocalization is more pronounced, rather than in computational chemistry. Overall, LDA falls short in providing an accurate description of real chemical systems, prompting the development of extensions to improve its accuracy.

2.5.2 Generalized Gradient Approximation (GGA)

The next step in the development of more accurate exchange-correlation functionals involves incorporating the gradient of the electron density. The Generalized Gradient Approximation (GGA) extends LDA by assuming that the exchange-correlation energy depends not only on the local electron density, $n(\boldsymbol{r})$, but also on its gradient, $\nabla n(\boldsymbol{r})$. In other words, GGA represents a significant advancement over LDA by incorporating approximate non-local effects. In GGA, the exchange-correlation energy is determined by the local electron density and also by its gradient, enabling the functional to capture variations in the density more effectively. Although GGA remains a semi-local approximation, the inclusion of the density gradient allows each point in space to reflect some information about its immediate surroundings. As a result, GGA generally provides improved accuracy over LDA in a wide range of systems, while maintaining a relatively low computational cost. For this reason, GGA functionals are often referred to as semi-local functionals.

GGA functionals generally provide a significant improvement over LDA, particularly in describing systems with density inhomogeneities. They offer better accuracy for total energies, atomization energies, molecular geometries, and reaction barriers. Mathematically, GGA functionals are typically expressed as:

$$E_{xc}^{GGA}[n(\boldsymbol{r})] = \int n(\boldsymbol{r})\, \varepsilon_{xc}\big(n(\boldsymbol{r}), \nabla n(\boldsymbol{r})\big)\, d\boldsymbol{r} \qquad \text{(Eq. 2.30)}$$

GGA functionals typically offer better predictions of binding energies, equilibrium geometries, and reaction barriers compared to LDA. They have been widely adopted in both condensed matter physics and quantum chemistry. Several formulations have been developed to describe the exchange-correlation energy density (ε_{xc}) within the GGA framework, including PW91 [180], PBE [181], and BLYP [182], among others. Among these, the widely used Perdew-Burke-Ernzerhof (PBE) functional has been adopted in the present study [181,183]. These functionals are favored due to their balance between accuracy and computational efficiency. Despite these improvements, GGA still has limitations, particularly in describing Van der Waals (dispersion) interactions and strongly correlated systems, motivating the development of even more sophisticated approximations.

2.5.3 van der Waals Functionals

van der Waals (vdW) interactions were first identified by Johannes Diderik van der Waals in 1873, an achievement that ultimately earned him the Nobel Prize in Physics in 1910 [184]. These interactions refer to weak attractive or repulsive forces between atoms, molecules, or molecular groups that do not arise from covalent or ionic bonding. Instead, they originate from quantum mechanical fluctuations and electrostatic interactions between charge distributions. vdW forces can be categorized into three primary components [185]:

- **Keesom interactions:** arising from electrostatic attractions between permanent dipoles;
- **Debye interactions:** due to the interaction between a permanent dipole and an induced dipole;
- **London dispersion forces:** resulting from instantaneous dipole-induced dipole interactions, present even in non-polar systems.

While these forces are relatively weak compared to covalent or ionic bonds, they play a crucial role in a variety of physical, chemical, and biological processes, particularly in soft matter and molecular assemblies. In traditional 3D bulk crystals, where strong chemical bonding dominates, van der Waals interactions are often negligible. However, their significance becomes pronounced in low-dimensional systems, such as two-dimensional (2D) materials, where interlayer bonding is weak or absent. In such cases, van der Waals forces govern interlayer cohesion and strongly influence structural, mechanical, and electronic properties.

From the perspective of DFT, conventional approximations such as LDA and GGA do not adequately describe dispersion forces, as these methods rely on local or semi-local information about the electron density and neglect long-range electron correlation effects. To address this limitation, van der Waals correlation functionals have been developed. These include empirical corrections (e.g., DFT-D methods), non-local correlation functionals (e.g., vdW-DF family), and hybrid approaches that aim to accurately capture dispersion interactions while maintaining computational efficiency. The inclusion of van der Waals interactions is essential for the realistic modeling of layered materials, molecular crystals, surface adsorption, and other systems where weak interactions play a defining role.

❖ Empirical Dispersion Corrections (DFT-D)

One widely used approach is the empirical dispersion correction method, commonly referred to as DFT-D. This method adds an additional pairwise interaction term to the conventional DFT energy [186, 187]:

$$E_{\text{DFT-D}} = E_{\text{DFT}} + E_{\text{Disp}} \tag{Eq. 2.31}$$

where E_{Disp} is a dispersion energy term typically expressed as a sum over atom pairs:

$$E_{\text{Disp}} = -\frac{1}{2}\sum_{i,j} C_{6ij}\left[\sum_{\vec{\mathbf{R}}} |\vec{r}_{ij} + \vec{\mathbf{R}}|^{-6} f_{\text{damp}}\left(|\vec{r}_{ij} + \vec{\mathbf{R}}|\right)\right] \tag{Eq. 2.32}$$

In Eq. 2.32, f_{damp} is a damping function that ensures the correction vanishes at short range to

avoid double-counting:

$$f_{\text{damp}}\left(|\vec{r}_{ij}+\vec{\mathbf{R}}|\right)=s_6\cdot\left\{1+\exp\left[-d\cdot\left(\frac{|\vec{r}_{ij}+\vec{\mathbf{R}}|}{r_0}-1\right)\right]\right\}^{-1} \quad \text{(Eq. 2.33)}$$

Where, $\vec{r}_{ij}=(\vec{r}_j-\vec{r}_i)$ is atom-atom distance vector, $\vec{\mathbf{R}}(=l\vec{a}+m\vec{b}+n\vec{c})$ is a lattice vector, s_6 is functional-dependent scaling parameter, d is a parameter that tunes the steepness of the damping function ($d=20$, $s_6=0.75$ in PBE), r_0 is computed by the simple sum of vdW radii of the atom pairs ($r_0=r_{0i}+r_{0j}$), and C_{6ij} is a coefficient computed for each atom pair by the geometric mean of atomic terms ($C_{6ij}=\sqrt{C_{6i}.C_{6j}}$). These methods are simple, computationally efficient, and widely supported in modern DFT codes.

In our calculations, van der Waals interactions were accounted for using the DFT-D method, which provides an accurate correction to the total energy while maintaining compatibility with standard GGA functionals.

❖ Non-local van der Waals Functionals (vdW-DF)

An alternative and more physically motivated approach involves the use of non-local correlation functionals, such as those implemented in the van der Waals density functional (vdW-DF) method. Unlike DFT-D, vdW-DF introduces a non-local correlation term directly into the exchange-correlation functional:

$$E_{\text{xc}}[n]=E_x^{\text{GGA}}[n]+E_c^{\text{LDA}}[n]+E_c^{\text{nl}}[n]. \quad \text{(Eq. 2.34)}$$

where $E_c^{\text{nl}}[n]$ is the non-local correlation energy that explicitly accounts for long-range vdW interactions. Variants of this approach include vdW-DF1, vdW-DF2, optB88-vdW, and others, each differing in their exchange functional and parameterization. This method avoids empirical fitting and is particularly suitable for systems where dispersion interactions are critical, such as layered materials, molecular crystals, and physisorbed surfaces. However, it is generally more computationally demanding than DFT-D.

In cases where higher accuracy is required, especially for weakly bonded systems, the vdW-DFT framework was employed using the DFT-D functional to ensure a more rigorous treatment of dispersion interactions. The DFT-D approach provides a computationally efficient correction to standard DFT functionals, improving the description of non-covalent and van der Waals interactions at interfaces. This treatment captures long-range dispersion forces essential for accurately describing adsorption energies and interfacial stability, in line with previous DFT studies [186].

2.5.4 Hubbard (U) Formalism (DFT+U)

In strongly correlated systems, the motion of electrons between localized orbitals on different lattice sites is significantly hindered due to strong on-site Coulomb repulsion. As a result, electrons tend to remain localized, forming states reminiscent of a Wigner crystal. This behavior is particularly pronounced in materials with partially filled f or $d-$shells, where electron correlation effects play a dominant role in determining the material's electronic properties.

The standard DFT approach, based on semilocal functionals such as LDAs, GGAs, or meta-GGAs, typically underestimates electron correlation in such systems. These functionals often

treat electrons as delocalized, leading to an overestimation of their ability to hop between lattice sites. This limitation makes conventional exchange correlation functionals inadequate for accurately describing materials with narrow energy bands and strong electron-electron interactions [188–190].

To address this deficiency, the DFT+U approach was developed. It supplements semilocal functionals with an additional term that introduces a penalty for fractional occupations of localized orbitals. This correction term, commonly referred to as the Hubbard U term, acts to localize the electrons more appropriately, effectively enhancing the treatment of on-site Coulomb interactions [189]. DFT+U can be viewed as a pragmatic or semi-empirical extension of DFT. Rather than applying the U correction to all orbitals, it is typically restricted to selected correlated orbitals (such as $3d$ or $4f$), where conventional functionals fail. The rest of the system, especially delocalized bonding orbitals, is still described using the base semilocal functional, which remains sufficiently accurate in those regions. Thus, DFT+U serves as a computationally efficient and physically motivated compromise that improves the accuracy of DFT for systems with strong electronic correlations.

As mentioned above, LDA and GGA functionals typically underestimate the band gap of semiconductors and insulators. This limitation poses significant challenges when attempting to accurately predict intermolecular interactions, transition states, and other properties that are sensitive to the electronic structure. The source of this inaccuracy is primarily attributed to the self-interaction error (SIE) inherent in standard exchange-correlation functionals. In these functionals, an electron incorrectly interacts with itself through the Coulomb term, which is not fully canceled by the approximate exchange-correlation potential. The Coulomb repulsion term can be expressed as:

$$E_{\mathrm{H}} = \frac{1}{2} \iint \frac{n(\boldsymbol{r}) n(\boldsymbol{r}')}{|\boldsymbol{r} - \boldsymbol{r}'|} \, d\boldsymbol{r} \, d\boldsymbol{r}' \tag{Eq. 2.35}$$

This expression describes the interaction between the electron density $n(\boldsymbol{r})$ at position $\boldsymbol{r}$ and the density $n(\boldsymbol{r}')$ at position $\boldsymbol{r}'$. Notably, it includes the unphysical self-interaction of an electron with its own charge density, resulting in an artificial self-repulsion term. The exchange component of the LDA (and to a lesser extent, GGA) fails to fully cancel this self-interaction error. As a result, this leads to an over-delocalization of the electronic wavefunctions, which in turn causes a significant underestimation of the band gap in systems containing localized electrons [191]. The Hubbard model is a simplified framework that modifies the interaction between particles (either fermions or bosons) in a lattice, capturing essential aspects of strongly correlated systems. In this context, we consider the case of two electrons with opposite spins occupying the same atomic orbital. The Hubbard Hamiltonian consists of two primary components: a kinetic energy term, representing electron hopping between lattice sites, and an on-site Coulomb interaction term, which accounts for the energy cost when two electrons occupy the same site [192]. The Hamiltonian is typically expressed as:

$$H_{\mathrm{Hub}} = -t \sum_{\langle i,j \rangle, \sigma} (c^{\dagger}_{i,\sigma} c_{j,\sigma} + \mathrm{H.c.}) + U \sum_{i} n_{i,\uparrow} n_{i,\downarrow} \tag{Eq. 2.36}$$

The first term of Eq. 2.36 represents the kinetic energy, describing the hopping of electrons between neighboring lattice sites. In this term, a fermion is annihilated at site j and created at site i, and vice versa. The notation $\langle i, j \rangle$ indicates a summation over nearest-neighbor pairs. The operators $c_i^{\dagger}$ and c_i denote the creation and annihilation of an electron at site i, respectively. The

second term accounts for the on-site Coulomb interaction energy, with the interaction strength represented by the parameter U. This term describes the energy penalty when two electrons with opposite spins occupy the same lattice site. The operators $n_{i,\uparrow}$ and $n_{i,\downarrow}$ represent the spin-resolved electron number operators for spin-up and spin-down electrons at site i, respectively. The total electron density at site i is given by $n_i = n_{i,\uparrow} + n_{i,\downarrow}$. The spin index σ labels the electron spin and can take the values up or down.

The Hubbard model is based on the premise that electrons are strongly localized around atomic sites and do not move freely across the lattice. Instead, they can "hop" between neighboring atoms, with this hopping governed by the hopping integral (or transfer integral), denoted by t, which quantifies the strength of electronic coupling between adjacent sites. In contrast, the on-site Coulomb repulsion, represented by U, quantifies the energetic penalization associated with electrons occupying the same localized site.

The competition between these two parameters-hopping strength t and Coulomb repulsion U−determines the electronic character of a material. When $U \gg t$, double occupancy is energetically penalized, suppressing electron hopping and leading to a Mott insulating state. Conversely, when $t > U$, the electrons are more delocalized, and the material exhibits metallic conductivity.

Within this framework, the balance between the on-site interaction U and the hopping parameter t governs electron localization. Building on this physics, the DFT+U approach embeds a Hubbard-like correction into density functional theory to improve the description of strongly correlated systems, particularly those with partially filled d or f states.

❖ DFT+U Method

Accordingly, DFT+U augments standard DFT with a Hubbard-like on-site correction to treat localized, strongly correlated electrons. This correction specifically targets electrons in localized orbitals, such as those in d or f shells, which are inadequately treated by standard semilocal exchange-correlation functionals. The remaining, more delocalized valence electrons continue to be described using conventional DFT. The correction is characterized by two key parameters: the on-site Coulomb repulsion U and the on-site exchange interaction J. These parameters effectively mitigate the self-interaction error present in traditional DFT functionals and help to localize electrons more realistically. Although U and J can, in principle, be obtained from first-principles calculations, they are often determined semi-empirically to reproduce experimental results or benchmark calculations.

One of the major advantages of the DFT+U method is its ease of implementation, as it operates within the same formalism as conventional DFT codes. Moreover, its computational cost remains comparable to that of standard DFT, with only a marginal increase in complexity. A further benefit is its flexibility, as the method can be applied in conjunction with a variety of exchange-correlation functionals, such as LDA (LDA+U) or GGA (GGA+U). The total exchange-correlation energy within the DFT+U framework is therefore formulated as the sum of the conventional DFT exchange-correlation energy and the Hubbard correction term. However, this inclusion introduces the issue of double counting, since the electron-electron interactions in the correlated orbitals are already partially included in the original DFT functional. To address this, a double-counting correction term is subtracted from the total energy. As a result, the total energy in the LDA+U (or more generally DFT+U) framework can be expressed as:

$$E_{LDA+U} = E_{LDA}[\rho(\boldsymbol{r})] + E_{Hub}[n^{I\sigma}_{mm'}] - E_{DC}[n^{I\sigma}] \qquad \text{(Eq. 2.37)}$$

The quantity $n^{I\sigma}_{mm'}$ represents the occupation matrix elements for atomic site I with spin σ, where m and m' denote atomic orbitals sharing the same angular momentum quantum number l. The total occupation number for spin σ on site I is given by the trace of this matrix, expressed as $n^{I\sigma} = \sum_m n^{I\sigma}_{mm}$. The definition of the double-counting correction term E_{DC} varies depending on the physical nature of the system under consideration, and several formulations have been developed to address different scenarios. Among the most widely adopted approaches is the fully localized limit (FLL), proposed by Liechtenstein and Anisimov [188, 189, 193]. This scheme is particularly suitable for systems with strongly localized electrons, such as those in d or f orbitals. The corresponding potential in the LDA+U formalism derived from the FLL framework is given by:

$$E = E_{LDA} + \sum_I \left[\frac{U}{2} \sum_{\substack{m,m' \\ \sigma,\sigma'}} n^{I\sigma}_m n^{I\sigma'}_{m'} - \frac{U}{2} n^I (n^I - 1) \right] \qquad \text{(Eq. 2.38)}$$

In Eq. 2.38, $n^I = \sum_{m,\sigma} n^{I\sigma}_m$, and $n^{I\sigma}_m$ is the occupation number of particular atomic orbitals. It is evident that the Hubbard correction energy depends explicitly on the orbital occupation numbers, reflecting its association with strongly correlated electronic states. These occupation numbers are typically computed by projecting the Kohn-Sham orbitals onto a set of localized atomic-like basis functions.

$$n^{I\sigma}_{mm'} = \sum_{k,v} f_{k,v} \left\langle \psi^\sigma_{kv} \middle| \phi^I_{m'} \right\rangle \left\langle \phi^I_m \middle| \psi^\sigma_{kv} \right\rangle \qquad \text{(Eq. 2.39)}$$

Here, ϕ^I_m denotes the valence orbital with magnetic quantum number m at atomic site I, while ψ^σ_{kv} represents the valence electronic wavefunction associated with the k-point (k), band index v, and spin σ. The coefficient $f_{k,v}$ denotes the occupation weight of the state defined by kv.

Although the LDA+U formulation successfully accounts for strong correlation effects, it suffers from a lack of rotational invariance. Specifically, the method depends on the choice of the localized atomic orbital basis, making the results sensitive to unitary transformations of the orbital set. To overcome this limitation, Anisimov and collaborators introduced a rotationally invariant version of the LDA+U method [190,194], in which the correction term depends explicitly on the full set of orbital-dependent Coulomb interactions. This approach is regarded as a more complete and physically consistent formulation. However, a simplified yet effective version of the rotationally invariant LDA+U approach was later proposed by Dudarev, which has gained widespread adoption due to its computational efficiency and robust performance [195]. The additional correction to the total energy in this DFT+U formalism is given by

$$E = \frac{U_{\text{eff}}}{2} \sum_{I,\sigma} Tr \left[n^{I\sigma} (1 - n^{I\sigma}) \right] \qquad \text{(Eq. 2.40)}$$

In this simplified formulation, the effective on-site Coulomb interaction is defined as $U_{eff} = U - J$, where U represents the Coulomb repulsion and J the exchange interaction parameter. This effective parameter accounts for electron-electron interactions while implicitly incorporating the exchange effects.

Studies have shown that the optimal Hubbard U parameter for a given system can vary significantly depending on both the material and the specific physical property of interest (e.g., electronic band gap, magnetic ordering, or optical response) [196–200]. Despite the widespread use of the DFT+U approach, there is currently no universally accepted standard for determining the appropriate value of the Hubbard U parameter for a given material system. In many cases, researchers empirically adjust the U value to match experimental observations-such as reproducing the correct band gap or magnetic moment. However, this trial-and-error strategy is inherently empirical and becomes impractical or unreliable for systems lacking experimental data or involving novel materials. A more rigorous and transferable approach involves computing the Hubbard U parameter from first principles. Among these, the linear response method is widely recognized as a reliable technique [201]. This method calculates U self-consistently by perturbing the localized orbitals and measuring the change in occupation, allowing the parameter to be determined directly from the electronic structure of the system without relying on external fitting. This approach not only improves the predictive power of DFT+U but also ensures better physical consistency in strongly correlated systems.

2.6 Pseudopotentials

Plane-wave basis sets are widely used in *ab initio* calculations for periodic systems due to their systematic convergence properties and suitability for Fourier-based methods. However, a significant drawback of plane-wave expansions is the large number of basis functions required to accurately describe the electronic wavefunctions, particularly near atomic nuclei. This is especially true when compared to localized atomic-like basis sets.

The core of this issue lies in the behavior of valence electrons near the nucleus. Valence electronic wavefunctions must remain orthogonal to core states, which causes them to exhibit rapid oscillations in the core region. Resolving these oscillations with a plane-wave basis set demands a very high kinetic energy cutoff, resulting in a substantial increase in computational cost. This challenge becomes even more pronounced for heavier elements, such as lanthanides and actinides, where core states are deeper and more localized.

Nevertheless, in most materials, chemical bonding and physical properties are predominantly governed by the behavior of valence electrons. The inner-core electrons are chemically inert and do not significantly contribute to bonding. Therefore, it is computationally efficient to divide the electrons into two groups: core and valence. The effect of the core electrons, including their electrostatic and exchange-correlation interactions, can be encapsulated into a simplified potential that acts only on the valence electrons. This effective interaction is known as a pseudopotential or effective core potential (ECP).

The pseudopotential approach replaces the all-electron problem with a valence-only problem, where the atomic core is represented by a smooth, non-singular potential that avoids the need to resolve the rapid oscillations near the nucleus. As a result, the valence wavefunctions become smoother and more easily represented by a modest number of plane waves, significantly reducing the computational demand.

The concept of pseudopotentials was introduced independently in the 1930s by Hellmann [202], Fermi [203], and Gombas [204], and was further developed for many-valence electron systems by Weeks and Rice [205]. Over time, several types of pseudopotentials have been developed, including norm-conserving, ultrasoft, and projector-augmented wave (PAW) methods, each offering different trade-offs between accuracy and computational efficiency.

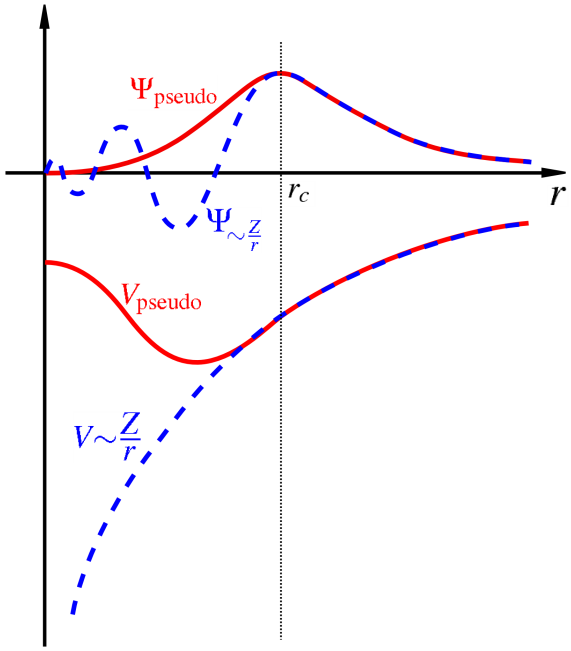

Fig. 2.2: Comparison between the all-electron wavefunction in the Coulomb potential ($\sim\frac{1}{r}$) of the nucleus (blue) and the corresponding pseudo-wavefunction (Ψ_{pseudo}) in a pseudopotential (V_{pseudo}) (red). Both the wavefunctions and potentials are constructed to match beyond a chosen cutoff radius r_c, ensuring the same scattering properties in the valence region while avoiding the need to represent the rapid oscillations near the nucleus (Adopted from [206]).

Fig. 2.2 illustrates the basic idea: the true all-electron potential is replaced by a pseudopotential that matches the scattering properties of the valence electrons outside a chosen core radius, while avoiding the need to represent the deep core behavior explicitly.

To construct a pseudopotential, let ψ_v and ψ_c denote the wavefunctions of valence and core electrons, respectively. In this framework, the valence wavefunction ψ_v is replaced by a smoother pseudo-wavefunction ψ^{sp}, while the core electrons are frozen and incorporated into an effective ionic potential acting on the valence states.

$$|\psi_v\rangle = |\psi^{\text{sp}}\rangle + \sum_c |\psi_c\rangle\, \alpha_{cv} \qquad \text{(Eq. 2.41)}$$

Here, $\alpha_{cv} = -\langle\psi_c|\psi^{\text{sp}}\rangle$, which reflects the assumption that valence and core states are orthogonal to each other. This orthogonality condition ensures that the pseudo-wavefunction ψ^{sp} remains properly decoupled from the core state ψ_c, preserving the physical accuracy of valence behavior while simplifying the computational treatment. Given that all valence states must be orthogonal to the core states, taking the inner product of Eq. 2.41 with a core state yields the following relation:

$$\langle\psi_c|\psi_v\rangle = \langle\psi_c|\psi^{\text{sp}}\rangle + \sum_d \langle\psi_d|\psi_c\rangle\, \alpha_{cv} = 0 \qquad \text{(Eq. 2.42)}$$

The second term on the right-hand side of Eq. 2.42 can be identified as the coefficient α_{dv}. Accordingly, the right-hand side of Eq. 2.42, expressed in terms of the pseudo-wavefunction ψ^{sp},

becomes:

$$|\psi_v\rangle = |\psi^{\text{sp}}\rangle - \sum_c \langle\psi_c|\psi^{\text{sp}}\rangle|\psi_c\rangle \tag{Eq. 2.43}$$

Applying the Hamiltonian operator to Equation Eq. 2.43 yields the following expression:

$$\hat{H}|\psi^{\text{sp}}\rangle + \sum_c (E_v - E_c)|\psi_c\rangle\langle\psi_c|\psi^{\text{sp}}\rangle = E_v|\psi^{\text{sp}}\rangle \tag{Eq. 2.44}$$

And finally:

$$\hat{H}^{\text{sp}}\,|\psi^{\text{sp}}\rangle = E_v\,|\psi^{\text{sp}}\rangle \tag{Eq. 2.45}$$

Eq. 2.45 is formally equivalent to the Schrödinger equation, with the following modifications or assumptions:

$$\hat{H}^{\text{sp}} = \hat{H} + \sum_c (E_v - E_c)|\psi_c\rangle\langle\psi_c| \tag{Eq. 2.46}$$

And

$$\hat{V}^{\text{sp}} = \hat{V}_{\text{eff}} + \sum_c (E_v - E_c)|\psi_c\rangle\langle\psi_c| \tag{Eq. 2.47}$$

In Eq. 2.47, the first term represents the true (all-electron) potential, while the second term accounts for the repulsive component introduced in the core region. This repulsive potential effectively cancels the strong attractive Coulomb potential near the nucleus, resulting in a smoothed, node-less pseudo-wavefunction that is computationally more tractable.

2.7 Practical Implementation of DFT

The implementation of DFT requires robust numerical methods to solve the Kohn-Sham equations iteratively, as well as software packages that efficiently handle the computational complexity of real-world systems. In this thesis, all first-principles calculations are carried out using the Quantum ESPRESSO (QE) package, a widely used open-source suite for electronic-structure calculations and materials modeling at the nanoscale. QE is based on DFT and uses plane-wave basis sets in conjunction with pseudopotentials to solve the Kohn-Sham equations efficiently [171]. Specifically, in our simulations, we employ projector-augmented wave (PAW) pseudopotentials, which offer a balanced trade-off between computational efficiency and accuracy by reconstructing the all-electron wavefunction from a pseudo-wavefunction. This framework allows us to accurately model the quantum mechanical behavior of electrons in periodic systems.

The DFT implementation in QE involves two main stages: the Self-Consistent Field (SCF) procedure and the setup of the computational framework using user-defined input files that

control parameters such as cutoff energies, k-point sampling, and convergence thresholds.

2.7.1 Self-Consistent Field (SCF) Procedure

The SCF approach lies at the heart of DFT calculations, enabling the iterative solution of the Kohn-Sham equations until convergence is achieved. In this method, an initial guess for the electron density is used to construct the Kohn-Sham Hamiltonian. The resulting wavefunctions are then computed, and a new electron density is derived. As shown in Fig. 2.3, this cycle repeats until the input and output densities differ by a negligible threshold, ensuring self-consistency. Key challenges in SCF methods include mitigating convergence issues caused by charge sloshing or poor initial guesses. To address these problems, algorithms such as the Broyden or Pulay mixing schemes are employed to stabilize the iterative process [207]. Additionally, advanced techniques like smearing of electronic occupations (e.g., Marzari-Vanderbilt cold smearing) are often incorporated to accelerate convergence in metallic systems [208]. The efficiency of SCF methods directly impacts the computational cost of DFT simulations, making their optimization critical for large-scale calculations.

2.7.2 Quantum ESPRESSO (QE)

All theoretical formulations presented above-including the total energy functional, the computation of interatomic forces and stresses, and the evaluation of the Hubbard U parameter have been implemented within the Quantum ESPRESSO (QE) distribution, specifically through the PWscf and HP packages [209–211]. QE is a widely adopted open-source software suite for performing quantum mechanical simulations of materials using DFT, plane-wave basis sets, and pseudopotential approximations. Developed by an international consortium, QE offers a robust and extensible platform for ground-state total energy calculations, structural relaxations, phonon dispersion analysis, and response function evaluations.

In this thesis, all first-principles calculations have been carried out using fully relativistic ultrasoft pseudopotentials (FR US-PPs) sourced from the PSLibrary v1.0.0 [212]. For the exchange-correlation functional, we adopted the generalized gradient approximation (GGA) in the PBEsol formulation [213], and for the EuX series (X = O, S, Se, Te), the local density approximation (LDA) parameterized by Perdew and Zunger [214] was also employed. The DFT+U calculations were performed using orthogonalized atomic orbitals, directly obtained from the pseudopotential files.

Plane-wave basis sets were used to represent the Kohn-Sham wavefunctions, as implemented in QE, owing to their efficiency and compatibility with periodic boundary conditions. Structural input parameters, such as lattice constants and atomic coordinates, were extracted from the Materials Project database [215]. The initial structures were constructed using the Avogadro molecular modeling platform [216], high-symmetry k-point paths in the Brillouin zone were determined via the SeeK-path tool [217], while analysis of structural distortions and visualization of crystal structures was performed using the VESTA software [218] and *XCrySDen* program [219].

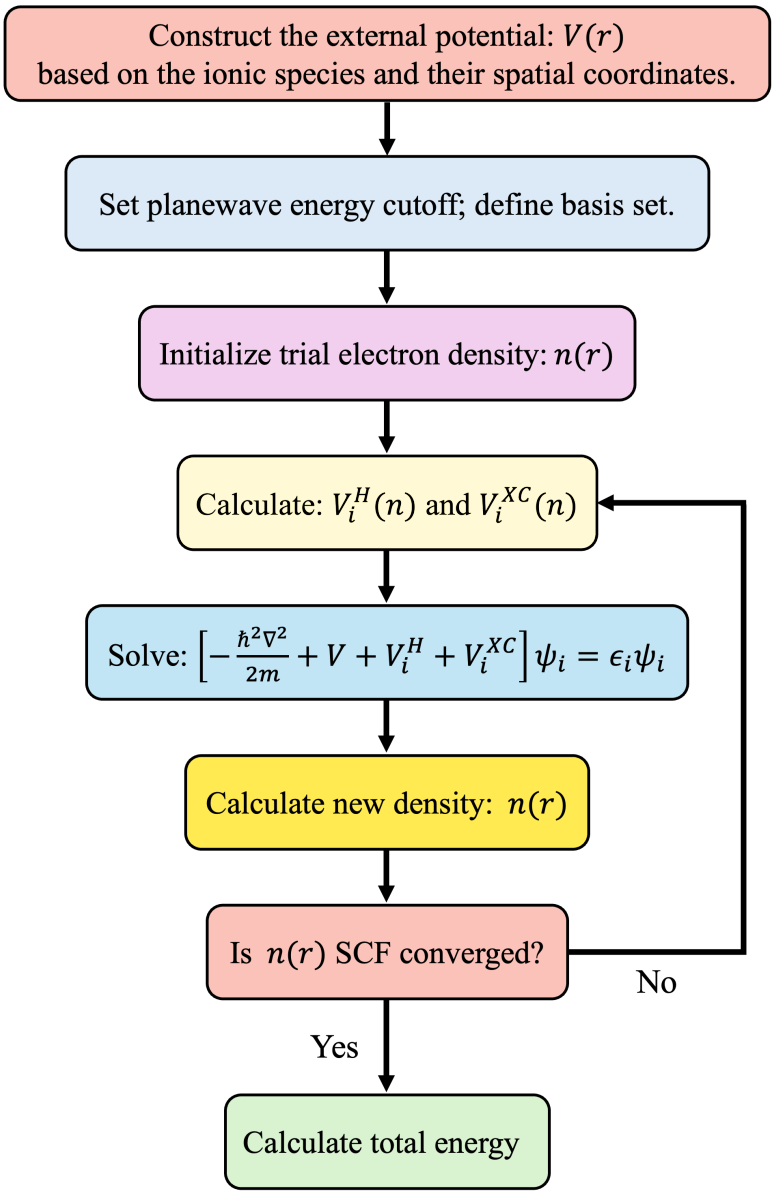

Fig. 2.3: Schematic representation of SCF procedure used in DFT calculations with plane-wave basis sets, illustrating the iterative loop for achieving convergence of the total energy and electron density.

"What I cannot create,
I do not understand."
— *Richard P. Feynman* —
Nobel Prize Laureate in Physics – 1965

3. Materials, Atomistic Modeling, and Computational Methodology

This chapter presents a detailed description of the materials, structural models, and computational approaches employed in the atomistic simulations carried out in this research. The focus is divided between two major applications: Proton Exchange Membrane Fuel Cells (PEMFCs) and Lithium-Ion Batteries (LIBs). For each system, the relevant surface models and polymeric materials are introduced, followed by a discussion of the interfacial models and simulation setup. The computational methods, including density functional theory (DFT) parameters and convergence criteria, are also discussed. This foundational chapter establishes the framework used in the subsequent analysis of interface properties and material performance.

❖ Chapter Outline

- **PEMFCs Modeling (Sec. 3.1)**
  - Pt(111) Slab: Construction and convergence of parameters; explains the selection and testing of computational parameters (e.g., energy cutoff, k-point mesh) for the Pt(111) surface to ensure reliable and accurate simulation results.
    (Sec. 3.1.1)
  - Nafion Structure: describes the chemical and structural features and their significance as a proton-conducting membrane in PEMFCs, the importance of hydration level in Nafion functionality, and the role of Nafion orientation at the Pt surface.
    (Sec. 3.1.2)
  - Modeling and Simulation of the Pt-Nafion Interface: describes the construction and simulation of the Pt(111)-Nafion interface.
    (Sec. 3.1.3)
- **LIBs Modeling (Sec. 3.2)**
  - Si(110) Slab: details the preparation and convergence testing of the Si(110) surface, which is considered as the anode material in LIBs.
    (Sec. 3.2.1)
  - PVDF Phases: introduces the structural features of the PVDF (α and β-phases), polymer binder, and explains the phase's role in enhancing the mechanical and electrochemical stability of the electrode.
    (Sec. 3.2.2)
  - Modeling and Simulation of the Si-PVDF Interface: describes the methodology used to model and analyze the Si-PVDF interface, with emphasis on interaction mecha-

nisms, adhesion, and structural stability.
(Sec. 3.2.3)

3.1 Modeling of PEMFC Interfaces

First-principles calculations, also known as *ab initio* methods, are widely employed in physics, chemistry, and materials science to investigate the properties of materials at the atomic scale. These computational approaches are grounded in quantum mechanics and do not rely on empirical parameters. Instead, they solve the fundamental equations of quantum theory-primarily the Schrödinger equation, to obtain insights into the electronic structure, total energy, and related properties of matter. A typical workflow involves constructing an atomistic model of the system of interest, followed by simulations using DFT or related techniques to extract structural, electronic, and thermodynamic characteristics.

In this study, the primary focus is the modeling and simulation of the interface between the Pt(111) surface and Nafion, a perfluorosulfonic acid polymer widely used as a proton-exchange membrane (PEM). This interface plays a key role in the performance of proton exchange membrane fuel cells (PEMFCs), where efficient electrochemical reactions are vital for energy conversion.

As illustrated in Fig. 3.1, a typical PEMFC consists of an anode and cathode separated by an ion-conducting membrane, such as Nafion. These fuel cells operate by electrochemically converting chemical energy-typically from hydrogen-into electrical energy, with water as the only byproduct. Platinum is commonly used as the catalyst at both electrodes due to its exceptional catalytic activity and stability. Despite its high cost and scarcity, Pt remains indispensable in PEMFC technology because of its ability to facilitate both the hydrogen oxidation reaction (HOR) at the anode and the oxygen reduction reaction (ORR) at the cathode [220–223].

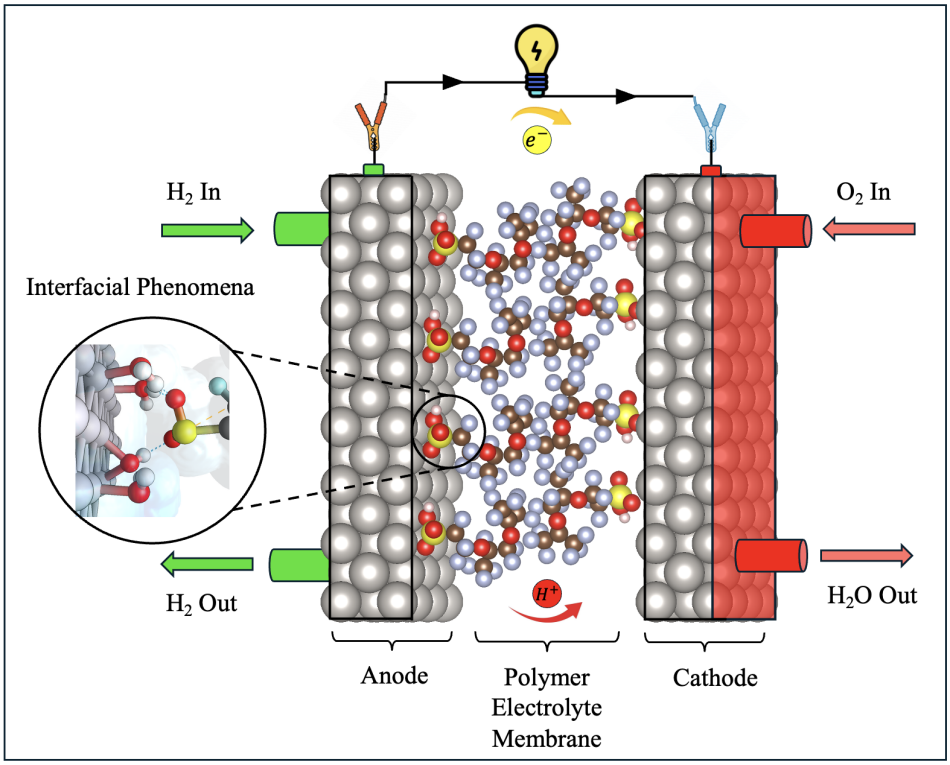

Fig. 3.1: Schematic representation of the proton exchange membrane fuel cell (PEMFC) interfacial region, the focal point of this study.

The accurate modeling of the Pt(111)/Nafion interface is therefore essential for understanding interfacial charge transfer, proton transport mechanisms, and the degradation processes

that affect cell efficiency and longevity. In the following section (Sec. 3.1.1), the procedure for constructing a Pt(111) slab model to represent the anode surface is presented. This includes the definition of the unit cell and the determination of the equilibrium lattice parameter through convergence tests, ensuring structural and energetic accuracy for subsequent simulations.

3.1.1 Construction and Convergence Analysis of the Pt(111) Surface

As discussed in Sec. 1.1.3, platinum (Pt) is a widely used noble metal with applications ranging for catalytic converters and fuel cell electrodes. Platinum has the atomic number 78 and an electron configuration of [Xe] $4f^{14}5d^{9}6s^{1}$. It crystallizes in a face-centered cubic (FCC) lattice structure ($Fm\bar{3}m$ space group), with an experimentally determined lattice constant of approximately 3.94 Å [224]. This structure is also commonly referred to as cubic close-packed (CCP), with a slightly refined lattice constant of 3.9242 Å [225].

Among various low-index surface orientations of platinum, namely Pt(100), Pt(110), and Pt(111), the Pt(111) surface is most frequently reported as the thermodynamically most stable and catalytically active configuration under polymer electrolyte membrane fuel cell (PEMFC) operating conditions [226]. This is due to its lowest surface energy and highest packing density compared to other orientations.

❖ Convergence of parameters

Quantum ESPRESSO (QE) is a widely used DFT software package that employs a plane-wave basis set and pseudopotentials for electronic structure calculations. In plane-wave-based DFT codes, one of the critical convergence parameters is the kinetic energy cutoff for the plane-wave basis, which is specified by the `ecutwfc` flag in the input file. This parameter determines the maximum kinetic energy of plane waves used to expand the electronic wavefunctions, and its proper selection is essential to ensure the accuracy and reliability of the results.

To determine the optimal energy cutoff, a convergence test was performed by calculating the total energy of the system as a function of the cutoff energy. As shown in Fig. 3.2, the total energy obtained after full SCF convergence is plotted as a function of the plane-wave cutoff energy. According to the convergence criterion adopted in this study, the cutoff is considered converged when the change in the converged total energy ($|\Delta E|$) with respect to the chosen tolerance is smaller than $\propto 10^{-5}$.

From the results in Fig. 3.2, it is evident that a cutoff energy of 60 Ry ($\sim$ 800 eV) is sufficient, as the total energy shows negligible variation beyond this point. This value was therefore chosen for all subsequent calculations to balance computational cost and accuracy. To model the Pt(111) surface accurately, we begin by constructing a slab based on the optimized FCC primitive unit cell. The initial step involves determining the equilibrium lattice parameter of bulk platinum through structural relaxation and total energy minimization. For this purpose, DFT calculations were performed using a plane-wave basis set and ultrasoft pseudopotentials, as described in Sec. 2.6. Exchange-correlation interactions were treated within the framework of the Perdew-Burke-Ernzerhof (PBE) functional [227], employing the Generalized Gradient Approximation (GGA) [180].

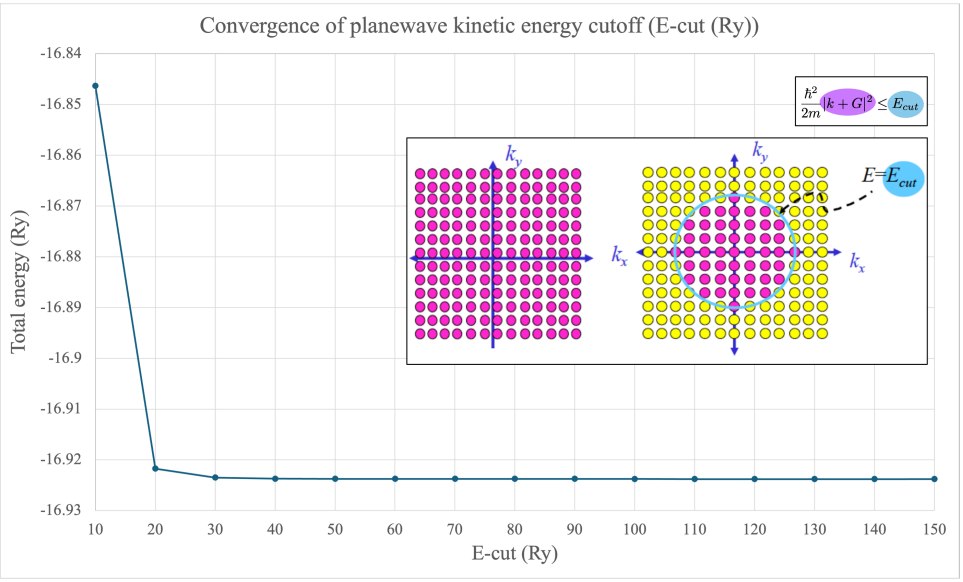

Fig. 3.2: Convergence of the total energy per atom as a function of the plane-wave kinetic energy cutoff (`ecutwfc`) for the Pt(111). The total energy stabilizes beyond 60 Ry ($\sim$ 800 eV).

The next essential step in preparing a reliable plane-wave DFT calculation is to perform a convergence test for the k-point sampling in reciprocal space. An appropriately dense k-point mesh ensures accurate integration over the Brillouin zone and reliable total energy calculations. Fig. 3.3 illustrates the variation of the total energy (in Ry) as a function of the k-point grid density. As shown, the total energy stabilizes with a k-point mesh of $7 \times 7 \times 1$, indicating that this grid is sufficient to ensure convergence for subsequent simulations.

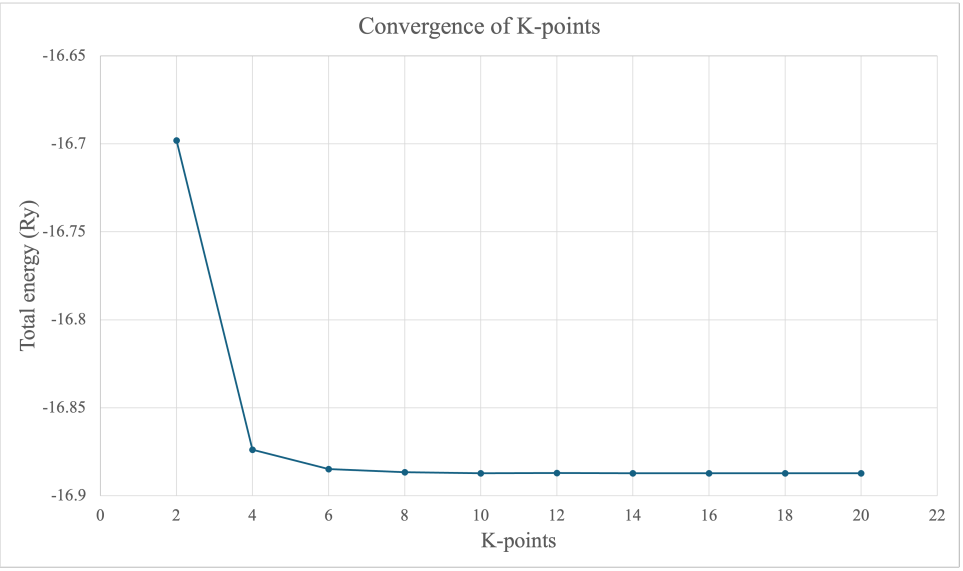

Fig. 3.3: Total energy (Ry) as a function of the in-plane k-point grid size N for an $N \times N \times 1$ Monkhorst–Pack mesh. The convergence test shows that a $7 \times 7 \times 1$ grid (49 k-points before symmetry reduction) provides sufficient accuracy, as further increases in k-point sampling result in negligible changes in total energy.

Our DFT results confirm that the FCC structure represents the most stable configuration for

bulk platinum, with a converged lattice constant of 7.251 Bohr (equivalent to 3.837 Å), as illustrated in Fig. 3.4. This optimized lattice parameter was then used to construct the Pt(111) surface slab, which serves as the starting point for simulating interfacial systems such as Pt/Nafion in PEMFCs.

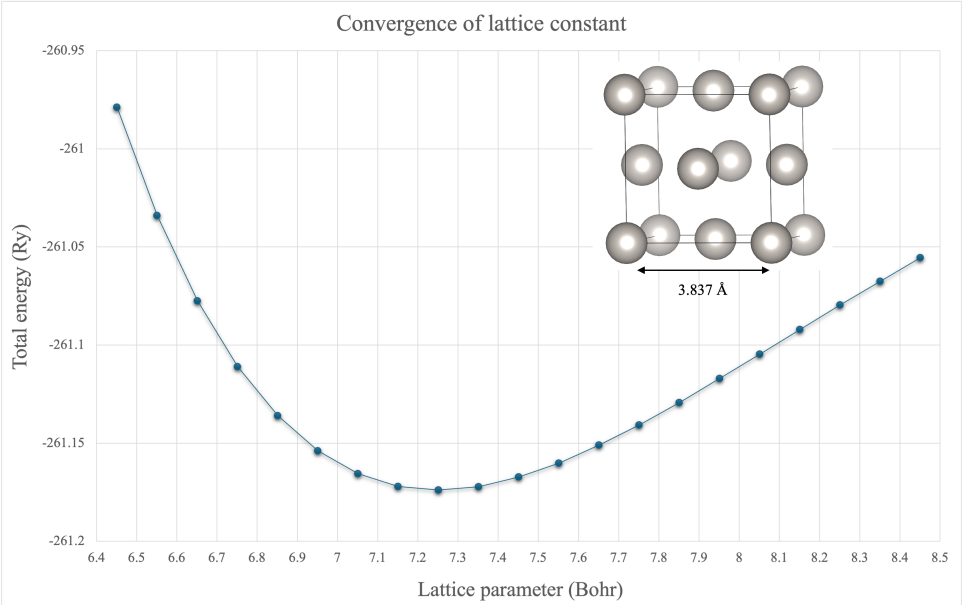

Fig. 3.4: Total energy (Ry) as a function of lattice parameter (Bohr) for the FCC structure of platinum. The minimum energy corresponds to the optimized equilibrium lattice constant.

To validate the reliability of the optimized lattice parameter and the chosen pseudopotential, we analyzed the electronic band structure together with the corresponding total density of states (DOS), verifying the consistency between band dispersions and DOS features near the Fermi level. As shown in Fig. 3.5 (a), the band structure obtained using the converged computational parameters exhibits good agreement with reference data [Fig. 3.5 (b)] reported by the Materials Project database [224]. This alignment confirms the accuracy of our structural optimization and the suitability of the selected pseudopotential for simulating the electronic properties of platinum.

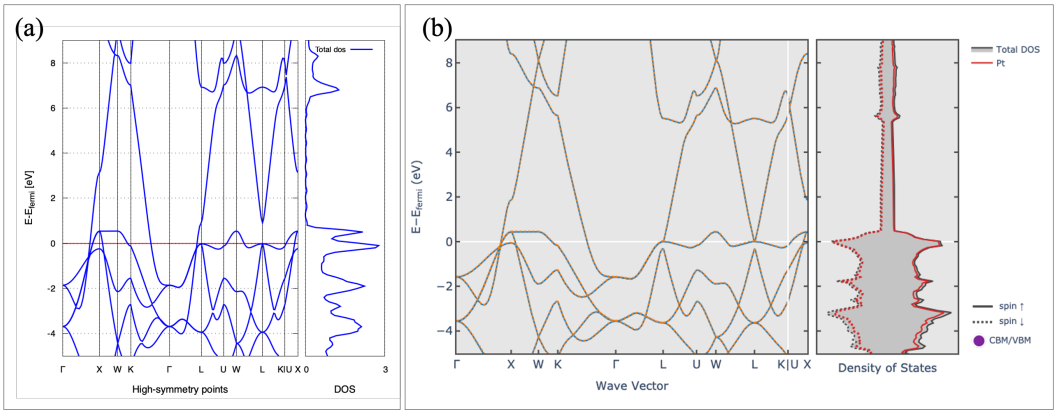

Fig. 3.5: Comparison of the calculated electronic band structure and total density of states (DOS) for Pt using the converged lattice parameter and pseudopotential. The results are validated by aligning them with reference results from Materials Project [224].

Building on this framework, first-principles methods are employed here to investigate the intrinsic properties of materials without empirical input. These computational approaches involve constructing an atomic-scale model of the material and solving the many-body electronic problem, typically within the framework of DFT, to evaluate its structural, electronic, and energetic characteristics.

In this work, a slab model of the Pt(111) surface was constructed to simulate the platinum electrode in a PEMFC. Surface simulations were performed using the supercell method, which is well-suited for modeling periodic surfaces. In this approach, the slab is considered infinite and periodic in the directions parallel to the surface and finite in the direction perpendicular to it. This setup includes a vacuum region on top of the slab to prevent artificial interactions between periodic images along the non-periodic axis.

A four-layer Pt(111) slab was generated with supercell dimensions of 14.10 Å$\times$ 10.85 Å$\times$ 26.64 Å, consisting of 96 platinum atoms. To accurately represent the semi-infinite nature of the bulk and to allow surface relaxation, the bottom two layers of the slab were kept fixed during structural optimization, while the top layers were fully relaxed. The supercell model not only allows for the investigation of surface electronic properties with accurate band dispersion but also provides a reliable framework for simulating realistic electrode surfaces in catalytic and electrochemical systems. A schematic representation of the slab and vacuum configuration is shown in Fig. 3.6, where the surface layer is highlighted in yellow.

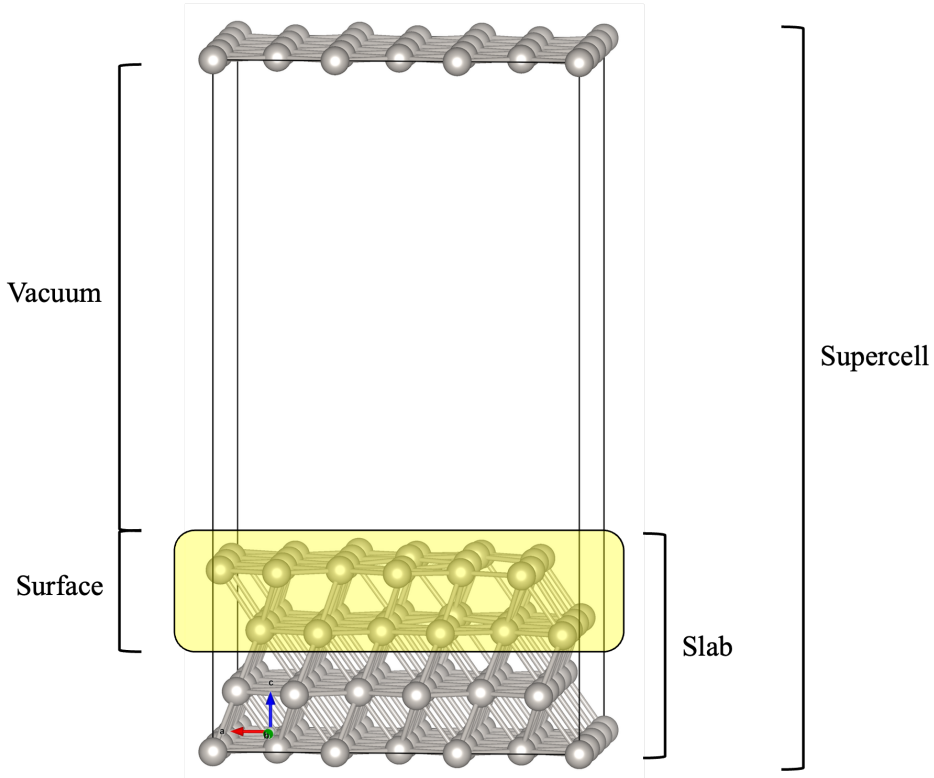

Fig. 3.6: Schematic representation of the Pt(111) supercell model used for surface simulations. The slab consists of four atomic layers of platinum, with the bottom two layers fixed to mimic bulk behavior and the top layers relaxed to capture surface effects. A vacuum region (20 Å) is added above and below the slab to eliminate spurious interactions between periodic images along the surface normal direction. The surface layer is highlighted in yellow.

The (111) surface of platinum, characterized by a hexagonal close-packed (hcp) arrange-

ment, is known to be the most stable and catalytically active surface facet under typical fuel cell operating conditions. Despite being the lowest energy termination for FCC structure, the Pt(111) surface experiences subtle atomic-level inward relaxation due to tensile stress [228], which can slightly favor the adsorption of additional species. This model provides a reliable platform for simulating surface reactions and interfacial interactions relevant to electrochemical energy conversion devices.

3.1.2 Structural and Chemical Description of Hydrated Nafion

Nafion, a perfluorosulfonic acid (PFSA) ionomer, is the most widely used proton-exchange membrane in PEMFCs due to its exceptional proton conductivity and chemical stability. Its structure consists of a hydrophobic polytetrafluoroethylene (PTFE)-like backbone with hydrophilic sulfonic acid ($-SO_3H$) side chains. When hydrated, these side chains dissociate, releasing protons (H^+) and forming interconnected hydrophilic nanochannels that facilitate proton transport. This unique microstructure enables Nafion to achieve high proton conductivity ($0.1-1$ S.cm^{-1} under fully hydrated conditions at ~ 80 °C), making it indispensable for efficient PEMFC operation [229].

In PEMFCs, Nafion serves three critical roles:
(*i*) as an electrolyte, enabling proton conduction from the anode to the cathode;
(*ii*) as a gas separator, preventing crossover of reactant gases (H_2 and O_2); and
(*iii*) as an ionomeric binder in catalyst layers, extending the three-phase boundary where electrochemical reactions occur. However, Nafion's performance is highly dependent on hydration. At low humidity or elevated temperatures (> 90 °C), its conductivity drops sharply due to membrane dehydration, limiting operational flexibility. Additionally, chemical degradation via reactive oxygen species (e.g., •OH radicals) can lead to membrane thinning and pinhole formation over time, reducing durability [230].

Despite these challenges, Nafion remains the benchmark PEM material due to its balance of conductivity and mechanical robustness. Recent research focuses on mitigating its limitations through modified PFSA membranes (e.g., 3M's Aquivion with shorter side chains), hydrocarbon-based alternatives, and composite membranes incorporating inorganic additives for enhanced water retention [231]. For high-temperature PEMFCs (> 120 °C), acid-doped polymers like polybenzimidazole (PBI) are being explored, though they face trade-offs in mechanical strength and longevity. Understanding Nafion's structure-property relationships is crucial for advancing next-generation membranes that combine high performance, durability, and cost-effectiveness for sustainable energy applications [232, 233].

❖ Nafion Structure and Its Role in PEMFCs

As shown in Fig. 3.7, Nafion comprises a PTFE backbone with grafted hydrophilic side chains. These side chains terminate in sulfonic acid groups ($–SO_3H$), which are critical to Nafion's unique transport properties and chemical functionality. This amphiphilic nature-comprising both hydrophobic and hydrophilic segments-makes Nafion highly suitable for proton exchange membrane fuel cells (PEMFCs).

A defining characteristic of Nafion in PEMFC applications is its excellent proton conductivity. The sulfonic acid ($–SO_3H$) groups form hydrophilic domains that attract and retain water, generating microscopic aqueous channels within the membrane. These water-rich regions facilitate proton conduction across the membrane. Chemically, Nafion features two contrasting domains: a hydrophobic fluorocarbon matrix that provides mechanical stability and resists water uptake, and a hydrophilic network formed by the sulfonate groups, which interact strongly with water molecules. The hydrophobic PTFE backbone prevents excessive swelling and dis-

solution in humid environments, preserving the structural integrity of the membrane and the catalyst layers. Conversely, the hydrophilic sulfonate groups ensure high proton mobility by forming hydrated clusters and pathways for proton hopping. The dual character of Nafion has been the focus of extensive research since the 1970s, particularly regarding its morphological behavior under varying operating conditions [234, 235].

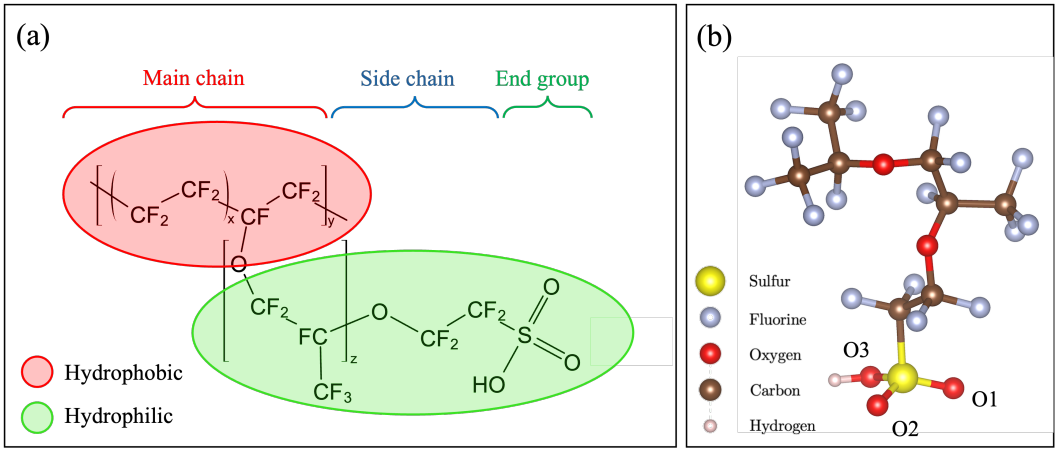

Fig. 3.7: (a) Chemical structure of Nafion showing the PTFE-like perfluorinated backbone with sulfonated side chains, and (b) Schematic representation of the physical structure of Nafion.

The sulfonic acid groups, especially those near the platinum catalyst surface, not only facilitate proton conduction but also stabilize the catalyst by attracting water and protons. This interaction reduces the risk of catalyst degradation and deactivation. As a result, the Nafion membrane plays a dual role: enabling selective proton transport while shielding the catalyst from adverse chemical conditions. Such functionality is key to achieving high durability and efficiency in PEMFCs.

❖ Degraded Nafion

In proton exchange membrane fuel cells (PEMFCs), the formation of highly reactive radical species-particularly hydrogen radicals (H•) and hydroxyl radicals (OH•), plays a crucial role in the chemical degradation of the membrane, especially Nafion. These radicals are mainly produced as a consequence of undesired side reactions occurring at both the anode and cathode sides of the membrane-electrode assembly, where the hydrogen oxidation reaction (HOR) and oxygen reduction reaction (ORR) take place. Once generated, these short-lived but extremely reactive radicals can attack the Nafion polymer, targeting specific bonds such as C–S, C–O, and C–F [236, 237]. Such radical-induced reactions lead to chain scission, side-chain detachment, and fluorine ion release, which together initiate and accelerate the overall degradation of the membrane [238–240].

Nafion's C–F bonds are particularly vulnerable to cleavage by radical species. For example, previous studies have reported degradation mechanisms in which a hydrogen radical abstracts a fluorine atom from a backbone carbon, resulting in the formation of hydrogen fluoride (HF) and a carbon-centered radical. In an alternative pathway, the attack of H_2O_2 or OH• may first oxidize a carbon atom (either in the side chain or backbone) to form a secondary alcohol. This intermediate can subsequently undergo a concerted reaction to eliminate HF and form an acyl fluoride group. In both cases, HF is released, effectively removing one fluorine atom, and a defluorinated site remains along the polymer chain [241–243]. Experimental investigations

have indeed confirmed the release of HF, providing direct evidence of fluorine loss in real Nafion-based membranes [244–246].

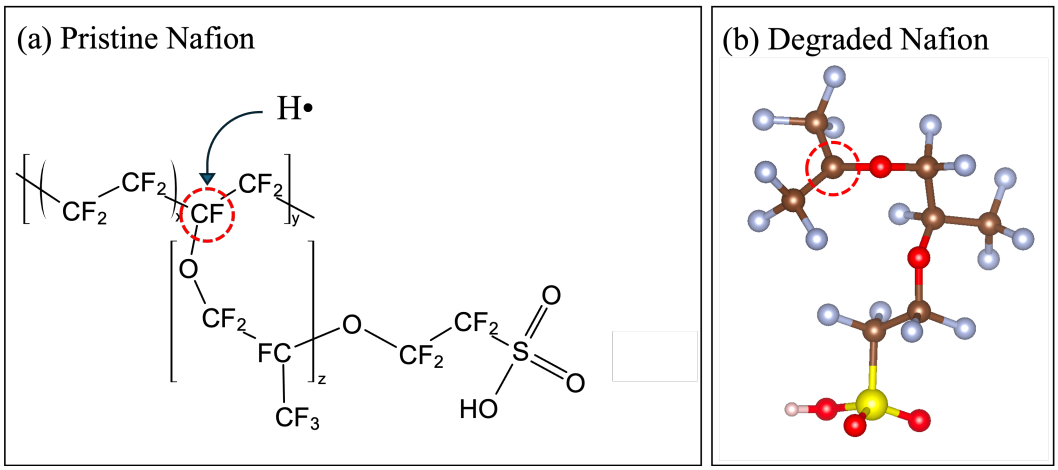

Fig. 3.8: (a) Molecular structure of pristine Nafion, composed of a perfluorinated PTFE backbone with side chains terminated by sulfonic acid groups (–SO_3H). The highlighted C–F bond indicates the most favorable site for hydrogen radical (H•) attack. (b) Structural representation of Nafion after radical-induced degradation, showing defluorination at the attack site and disruption of the polymer backbone. In section (b): Yellow: sulfur atom; Silver: fluorine atom; Red: oxygen atom; Brown: carbon atom; Light-pink: hydrogen atom.

These degradation reactions not only release HF but also alter the chemical structure and properties of Nafion. For instance, the loss of a single fluorine atom through such a mechanism reduces the fluorine count of the affected repeat unit from 17 (as in pristine Nafion, shown in Fig. 3.8 (a)) to 16 (as in degraded Nafion, shown in Fig. 3.8 (b)). Density functional theory (DFT) calculations confirm that these HF-releasing pathways are energetically favorable, and experimental observations consistently identify HF among the decomposition products of aged membranes [247, 248]. Most computational studies have traditionally employed the idealized pristine Nafion model containing 17 fluorine atoms. However, to assess the impact of chemical degradation on Nafion's properties, it is important to also consider a 16-fluorine model, representative of defluorinated structures formed through radical-induced degradation processes, as suggested in [241, 249].

❖ Importance of Hydration Level in Nafion Functionality

The proton conductivity of Nafion is highly dependent on its level of hydration. The number of water molecules available in the membrane directly affects the ability of the –SO_3H groups to transport protons [250]. The hydration level, often denoted by the parameter λ, is defined as the ratio of the number of water molecules (n_w) to the number of sulfonate groups (n_s), i.e., $\lambda = n_w/n_s$. This ratio is critical in dictating the mechanism of proton conduction within the membrane.

Depending on the hydration state, two primary mechanisms govern proton transport in Nafion. At high humidity, the Grotthuss mechanism dominates [251]. In this mode, protons are transferred via a relay-like movement along hydrogen-bonded water molecules, as shown in Fig. 3.9. This structural diffusion allows for rapid and efficient proton hopping through a dynamically rearranging hydrogen-bond network, rather than the movement of discrete hydrated ions. The process involves the continuous breaking and reformation of hydrogen bonds

between water molecules, providing an effective pathway for long-range proton conduction.

At lower humidity levels, however, the vehicular mechanism becomes predominant [252]. In this regime, protons are transported as part of hydrated complexes, such as H_3O^+, which migrate through the membrane under the influence of electrostatic interactions with the sulfonic acid groups [Fig. 3.9]. This transport is generally slower and less efficient than the Grotthuss mechanism due to the physical movement of charged species.

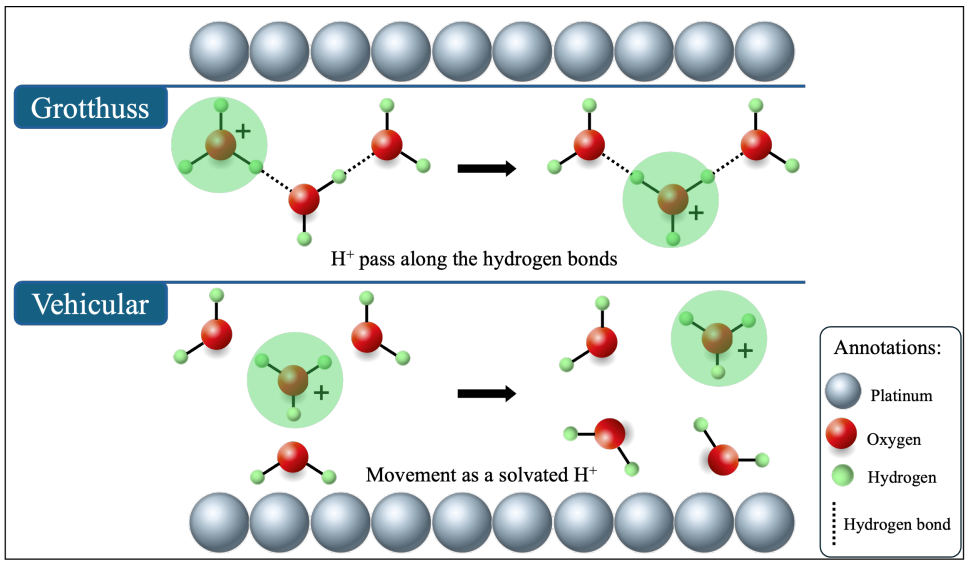

Fig. 3.9: Schematic representation of proton transport within two different mechanisms: Grotthuss mechanism, where protons are transferred through a hydrogen-bonded water network via successive bond rearrangements (proton hopping); and Vehicular mechanism, in which protons move along with water molecules.

These processes have been substantiated through both experimental and theoretical studies [253–255]. Under dry conditions, however, the lack of an extended hydrogen-bond network restricts such hopping, shifting the balance toward surface-based vehicular transport [256].

❖ Role of Nafion Orientation and Interfacial Structure

Beyond hydration, the nanoscale orientation and topological distribution of Nafion's domains within the membrane and at the electrode interfaces have a significant impact on PEMFC performance [257]. The spatial alignment of the sulfonate-rich regions toward the electrode surface is essential for efficient proton transfer. Improper orientation can impede proton accessibility and reduce electrochemical performance.

Despite extensive investigation, a full understanding of the Nafion-electrode interfacial structure remains incomplete [258–260]. This interface is where critical transport phenomena occur, such as proton delivery to the catalyst sites and water management. Due to the nanoscale dimensions and dynamic nature of this region, the interfacial structure and chemical environment are difficult to probe using conventional characterization techniques. Interfacial properties, such as domain arrangement, hydration level, and molecular orientation, collectively govern both proton transport efficiency and catalyst utilization. The interaction between Nafion's sulfonic acid groups and the Pt electrode surface plays a pivotal role in sustaining catalytic activity and minimizing degradation, thus directly impacting the fuel cell's long-term stability and power output.

3.1.3 Atomistic Modeling of the Pt(111)-Nafion Interface

To investigate the structural and functional characteristics of the catalyst-ionomer interface in PEMFCs, a series of simplified interface models was constructed. These models consist of Pt(111) surfaces representing the electrode, hydrated Nafion monomers, and explicit water molecules. The goal of this study is to elucidate how the interfacial arrangement influences proton transport and electrochemical performance.

Given the critical role of hydration in proton conductivity, different water content levels were systematically introduced to the model systems. The hydration level not only affects proton transport mechanisms but also modifies the structural orientation and interaction strength between Nafion's sulfonate groups and the platinum surface. The preferential orientation of Nafion near the Pt surface, particularly the positioning of its sulfonic acid groups ($–SO_3H$), determines the formation of water networks and the local electrostatic environment at the interface.

Furthermore, the configuration of water molecules adsorbed on Pt(111) was carefully considered. DFT studies have shown that water molecules tend to adsorb at the atop sites of the Pt surface, adopting a near-planar geometry relative to the metal plane. The optimal distance between the oxygen atoms of water and the Pt surface is approximately 2.21 Å, which promotes stable interaction without dissociation under mild conditions [261–263].

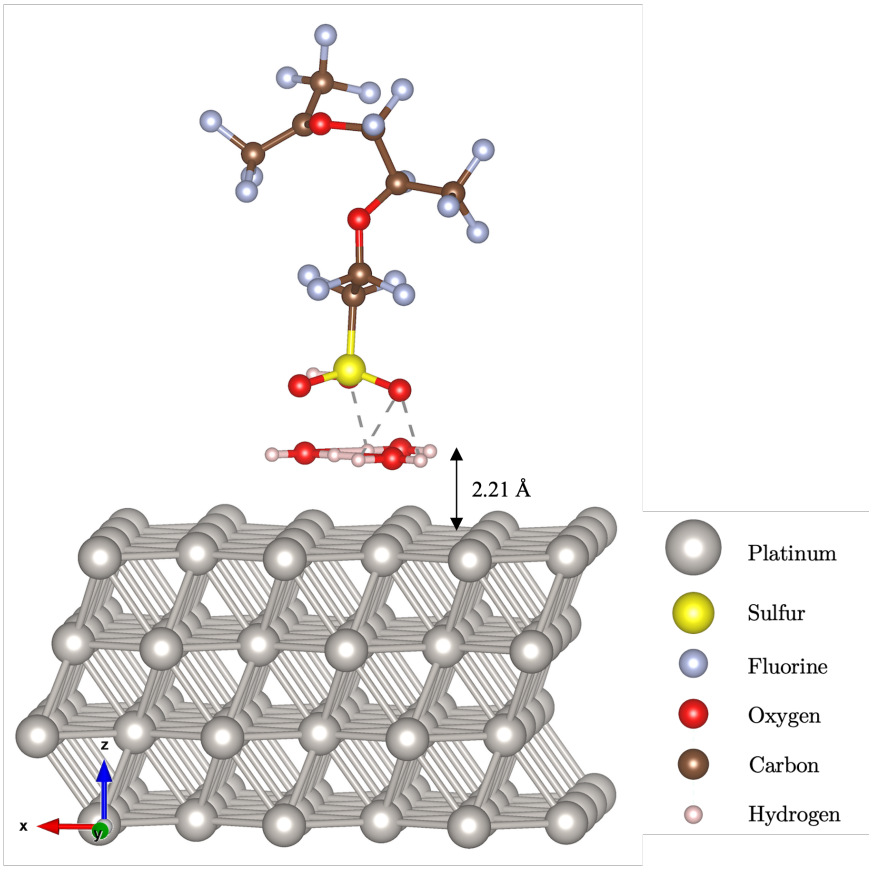

Fig. 3.10: Initial atomistic model of the Pt(111)-Nafion interface under hydrated conditions. The simulation cell includes a four-layer Pt(111) slab (bottom), hydrated Nafion monomers, and adsorbed water molecules. Water is distributed near the interface to represent different hydration levels. Nafion's sulfonic acid groups ($–SO_3H$) are oriented toward the platinum surface, allowing for interfacial interaction analysis.

Fig. 3.10 illustrates the initial configuration of the Pt(111)-Nafion interface model employed in our simulations, showcasing the interaction among Pt layers, Nafion monomers, and water molecules under controlled hydration levels. The system is designed to investigate proton behavior and interfacial structure as a function of hydration and molecular orientation. The atomic composition of the simulated Pt(111)-Nafion interface is summarized in Table 3.1.

Table 3.1: Atomic Composition of the Studied Pt(111)-Nafion Interface System (low-hydration level $\lambda = 3$).

Atom types	**Pt**	**S**	**F**	**O**	**C**	**H**	**Total**
No. of atoms	96	1	17	8	8	7	137

In this section, we presented the initial model of the Pt(111)-Nafion interface, which serves as the foundational system for investigating the interfacial interactions relevant to PEMFCs. While this section focuses on the structural setup of the simplified system, a more comprehensive investigation is carried out in the results chapter. There, we progressively build upon this initial configuration by introducing additional complexity in a stepwise manner: first analyzing the bare Pt-Nafion interface, then including adsorbed hydrogen species, and finally adding water molecules to simulate various hydration levels. This gradual approach allows us to capture the evolution of interfacial properties and proton transport mechanisms, moving from an idealized model to a more realistic representation of operating PEMFC conditions.

In addition to the pristine Nafion model, we also constructed a degraded Nafion structure based on experimentally and theoretically reported fluorine-loss mechanisms, as discussed in the previous section. This degraded model reflects the removal of a fluorine atom from the polymer chain, resulting in a modified local chemical environment at the interface. Both the pristine and degraded Nafion configurations were adsorbed on the Pt(111) surface to examine how degradation affects interfacial binding, charge distribution, and proton behavior characteristics. The results for the pristine Nafion-Pt(111) system are presented first to establish a baseline for comparison, followed by a detailed analysis of the degraded Nafion-Pt(111) structure to highlight the effects of chemical deterioration on the interfacial behavior.

3.2 Modeling of LIB Electrode-Binder Interfaces

As discussed in Sec. 1.2.2, among energy storage technologies, lithium-ion batteries (LIBs) have emerged as the dominant solution due to their superior energy density ($250-300$ Wh.kg^{-1}), long cycle life ($1000-2000$ cycles), and relatively low self-discharge rate ($< 5\%$ /month) compared to alternatives like lead-acid ($30-50$ Wh.kg^{-1}) or nickel-metal hydride (NiMH, $60-120$ Wh.kg^{-1}) batteries [72]. Their lightweight design and scalability make them indispensable for applications ranging from portable electronics to electric vehicles (EVs) and grid storage. LIBs outperform competitors in charge/discharge efficiency ($90-95\%$, versus $70-80\%$ for NiMH), enabling faster energy delivery and recovery [264]. However, challenges such as thermal instability, degradation at high voltages, volume expansion, and reliance on critical materials (e.g., cobalt) persist [265]. Computational modeling of LIBs addresses these limitations by optimizing electrode architectures, electrolyte compositions, and thermal management systems, positioning LIBs as a cornerstone for renewable energy integration and decarbonization efforts [266–268].

Building on the technological promise of LIBs, significant research has focused on simulating, modeling, and developing next-generation electrode materials to further enhance their

performance. Among these, silicon (Si) has attracted substantial attention as a potential anode material due to its exceptionally high theoretical specific capacity ($\sim$ 3579 mAh.g^{-1}), which is nearly ten times higher than that of conventional graphite anodes. However, despite this appealing capacity, the practical implementation of Si-based anodes faces critical challenges, including:
(*i*) low intrinsic electrical conductivity,
(*ii*) drastic volume expansion exceeding 300% during lithiation, and
(*iii*) the formation of an unstable solid-electrolyte interphase (SEI) during repeated cycling. These issues collectively result in rapid capacity fading and limited cycle life.

To address these obstacles, one key strategy involves precise control of interfacial surface phenomena at the anode. Surface modification techniques-particularly the use of engineered binder materials, have shown great promise in mitigating Si anode degradation. Binders play a critical role not only in maintaining the mechanical integrity of the electrode by holding active materials together but also in buffering volume changes and stabilizing the SEI layer. The choice of binder profoundly affects the electrode's mechanical resilience, electrochemical stability, and interfacial adhesion properties. Polyvinylidene fluoride (PVDF) remains the binder of choice in commercial LIBs due to its favorable chemical stability and compatibility with standard electrolytes. The selection, optimization, structural configuration, and functional properties of polymeric binders such as PVDF represent crucial aspects in the design and development of high-performance Si anodes. These binders not only determine the mechanical cohesion of the electrode but also influence key interfacial phenomena, such as lithium-ion transport, electrolyte compatibility, and the formation and stability of the SEI. Therefore, computational study, simulation, and engineering of binder materials are essential to accommodate the significant volume changes of Si during cycling, enhance electrode durability, and improve the overall electrochemical performance of LIBs.

The chemical stability and interfacial reactivity of various polymeric binders, particularly PVDF on both pristine Si and lithiated silicon (Li–Si) surfaces, have been widely investigated through experimental and theoretical approaches [268–270]. Experimental efforts have also examined the influence of silicon suboxide (SiO_x) layers and SiO_x-coated silicon anodes on lithium storage performance, along with the interactions between commercial binders and these oxidized surfaces [271–275]. However, these studies predominantly focus on macroscopic performance indicators, offering limited insight into the atomic-scale mechanisms that govern binder surface interactions and interfacial stability. Notably, despite the extensive examination of pristine and lithiated Si surfaces, theoretical studies addressing PVDF interactions with oxidized silicon interfaces remain scarce-this is a significant gap, as surface oxidation plays a critical role in dictating interfacial chemistry, especially under realistic battery operating conditions.

To address this deficiency, the present study employs DFT to deliver a detailed theoretical analysis of PVDF reactivity and binding behavior on oxidized Si surfaces. While PVDF has historically been considered suboptimal for silicon-based anodes due to poor adhesion and limited compatibility, recent findings suggest that surface engineering strategies can mitigate these drawbacks [149]. Building on this insight, our work seeks to advance the understanding of PVDF-Si interactions by exploring how variations in oxygen surface coverage, PVDF phase, and chain orientation influence interfacial energetics, charge transfer, and binding stability. By systematically examining these factors, this study uncovers how surface passivation, polarization effects, and dipole interactions govern the stability of the binder-electrode interface. These findings offer valuable guidance for the rational design of Si-based anodes with enhanced performance, contributing to the next generation of high-capacity, long-life LIBs.

Fig. 3.11 presents a schematic representation of a typical LIB, highlighting the roles of the key components. In the context of this study, the anode is composed of Si (will be discussed in Sec. 3.2.1), which is separated from the cathode-commonly a lithium metal oxide such as lithium cobalt oxide ($LiCoO_2$)-by a liquid electrolyte that also contains the polymeric binder, PVDF (Sec. 3.2.2).

This work focuses on examining the effects of oxygen content at the Si-PVDF interface, as shown in Fig. 3.11, and explores how different crystalline phases of PVDF (namely, α and β) influence the interfacial structure and binding behavior. Comparisons are made against pristine silicon surfaces to evaluate the role of surface oxidation. To elucidate the underlying interaction mechanisms, electronic structure analyses are employed to assess charge redistribution, binding energetics, and interfacial electronic properties, offering insight into the fundamental processes that govern the stability and functionality of Si-based anodes.

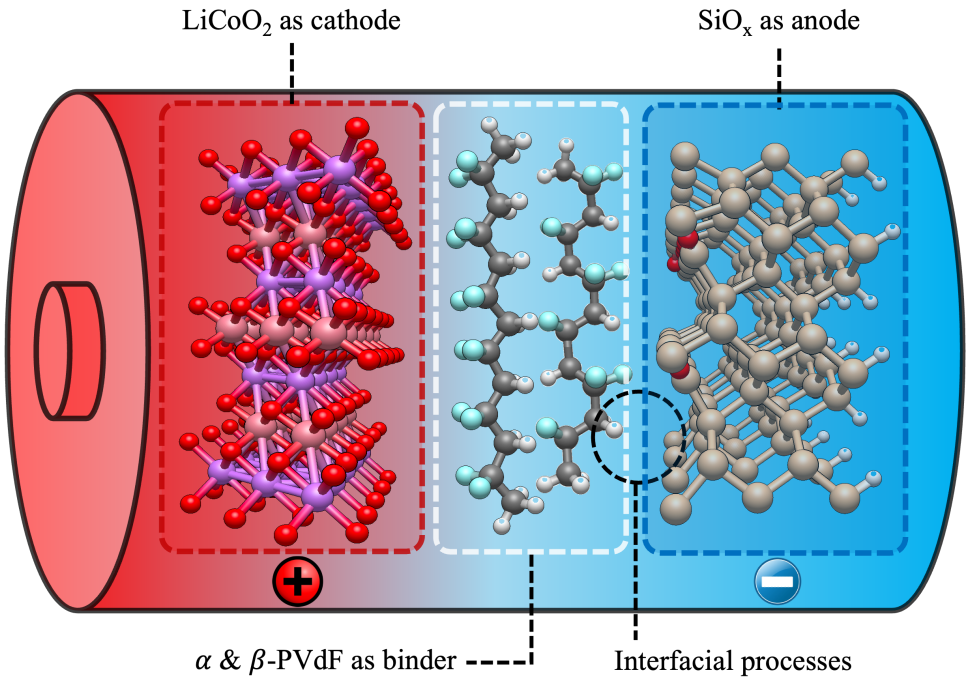

Fig. 3.11: Schematic representation of a typical LIB architecture, highlighting the anode (Si), cathode (commonly $LiCoO_2$), and the liquid electrolyte containing PVDF binder. This study focuses on the Si-PVDF interface, analyzing the effects of surface oxidation and binder phase on interfacial stability and electronic behavior.

3.2.1 Preparation and Convergence Assessment of the Si(110) Surface

Silicon (Si), with atomic number 14, and electron configuration $[\mathrm{Ne}]\,3s^2\,3p^2$, a Group IV semiconductor with a diamond cubic crystal structure (space group $Fd\bar{3}m$), exhibits a tetrahedral atomic arrangement where each Si atom forms four covalent bonds with neighboring atoms at 2.35 Å spacing. This stable lattice allows Si to theoretically accommodate lithium Li via alloying reactions (e.g., $\mathrm{Si} + x\mathrm{Li}^+ + x\mathrm{e}^- \leftrightarrow \mathrm{Li}_x\mathrm{Si}$, where $x \leq 4.4$), enabling an exceptional theoretical capacity of ~4200 mAh.g^{-1}-tenfold higher than graphite (372 mAh.g^{-1}) [276]. However, the ~300 % volume expansion during lithiation induces mechanical fracture and SEI instability, limiting cycle life [277]. In LIBs, Si anodes are often hybridized with graphene or conductive polymers, achieving practical capacities of 1500−2000 mAh.g^{-1} while improving

durability. These advancements position Si as a transformative material for next-generation high-energy-density batteries, particularly in electric vehicles and portable electronics.

In this study, we selected the Si(110) surface orientation to model the interface between silicon and polymeric binders (PVDF), including its suboxide form. This choice is motivated by several advantageous properties of the Si(110) surface compared to other orientations like Si(100) and Si(111). Firstly, the Si(110) surface exhibits a higher atomic planar density, which facilitates more robust interfacial interactions. This higher density can lead to stronger bonding with binder molecules, enhancing the stability of the interface. Secondly, the Si(110) orientation demonstrates superior mechanical properties. These characteristics are crucial for maintaining structural integrity during the charge-discharge cycles of LIBs. Additionally, the Si(110) surface has been shown to form thinner amorphous layers when interfaced with amorphous silicon, indicating a more stable and less reactive interface. This stability is beneficial for reducing unwanted side reactions that can degrade battery performance [278–282]. Considering these factors, the Si(110) orientation provides a promising platform for investigating the interfacial behavior of Si anodes with polymeric binders, aiming to enhance the performance and longevity of LIBs.

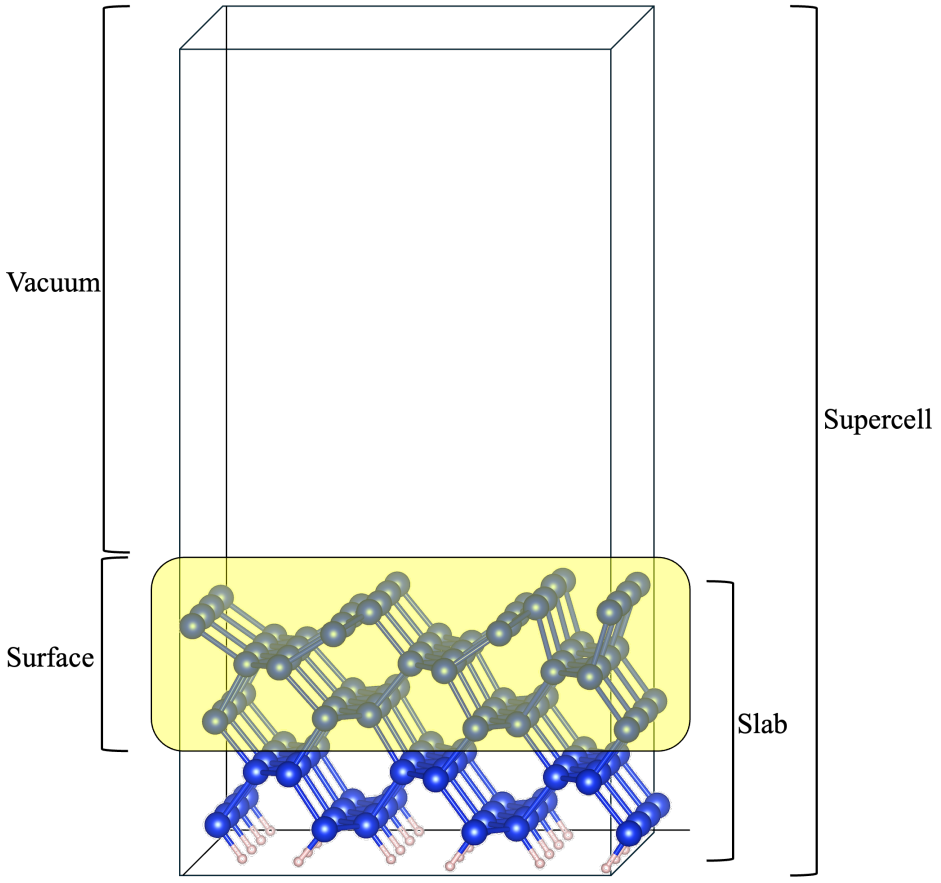

Fig. 3.12: Schematic representation of the Si(110) supercell model used for surface simulations. The slab consists of 120 silicon atoms with the bottom surface fully passivated by 24 hydrogen atoms to eliminate dangling bonds. A vacuum region (18 Å) is included to prevent interactions between periodic images. The surface layer is highlighted in yellow.

As with the Pt(111) slab, convergence tests were performed for the Si(110) surface to ensure accurate and reliable calculations. The total energy per atom was found to converge at a

plane-wave kinetic energy cutoff (`ecutwfc`) of 65 Ry (≈ 880 eV). The Brillouin zone was sampled using a Monkhorst-Pack grid of $7 \times 7 \times 1$, which was sufficient to achieve convergence of the electronic properties. A supercell approach was employed to model the surface, which enables detailed analysis of surface electronic states with accurate band dispersion and facilitates realistic simulations of electrode surfaces in catalytic and electrochemical environments. The constructed Si(110) slab consists of 120 silicon atoms; the two bottom layers of the silicon slabs are constrained during structural optimization, and the bottom layer is passivated by 24 hydrogen atoms to eliminate dangling bonds. The van der Waals (vdW) interaction was incorporated via the vdW-DFT module (`vdw_corr = 'DFT-D'`) [186]. A vacuum layer was included to avoid interactions between periodic images. As shown in Fig. 3.12, the final dimensions of the simulation cell are 15.36 Å× 16.29 Å× 28.68 Å.

3.2.2 Structural Characteristics of PVDF Phases

As previously discussed in Sec. 1.2.2.7, polyvinylidene fluoride (PVDF) is the most widely adopted binder in commercial LIBs, used in both anode and cathode formulations. Its widespread use stems from its excellent electrochemical stability, strong adhesion to active materials, and compatibility with standard electrolytes. In LIBs, PVDF functions as a cohesive matrix that binds active material particles together and anchors them to the current collector, thereby maintaining electrode integrity during repeated charge-discharge cycles and preventing huge volume expansion.

PVDF is a semi-crystalline polymer known for its multiple polymorphic phases, each characterized by distinct molecular conformations and properties. The most common phases of PVDF include the α (alpha), β (beta), γ (gamma), δ (delta), and ϵ (epsilon) phases. Among these, the α-phase is the most thermodynamically stable and typically forms under standard crystallization conditions. It adopts a "TGTG" (trans-gauche-trans-gauche) chain conformation, resulting in a non-polar crystal structure. In contrast, the β-phase, which exhibits an all-trans ("TTTT") zigzag conformation, is highly polar and demonstrates the strongest piezoelectric, ferroelectric, and pyroelectric properties, making it the most desirable phase for electrochemical and energy applications. The γ-phase features a "3GT3G" chain conformation, possessing intermediate polarity and crystallinity between α and β. Less commonly, the δ- and ϵ-phases are metastable and can be obtained through mechanical stretching, high electric fields, or copolymerization techniques. The interconversion between these phases can be induced via mechanical stretching, annealing, or electrospinning, with specific processing conditions favoring one phase over another. The structural differences among these polymorphs critically influence PVDF's dielectric, electrochemical, and mechanical properties, thereby impacting its effectiveness as a binder in LIBs, where interfacial stability and ionic conductivity are essential. Fig. 3.13 illustrates the molecular chain conformations and crystallographic structures of the major polymorphic phases of PVDF, highlighting their structural differences and relative polarity.

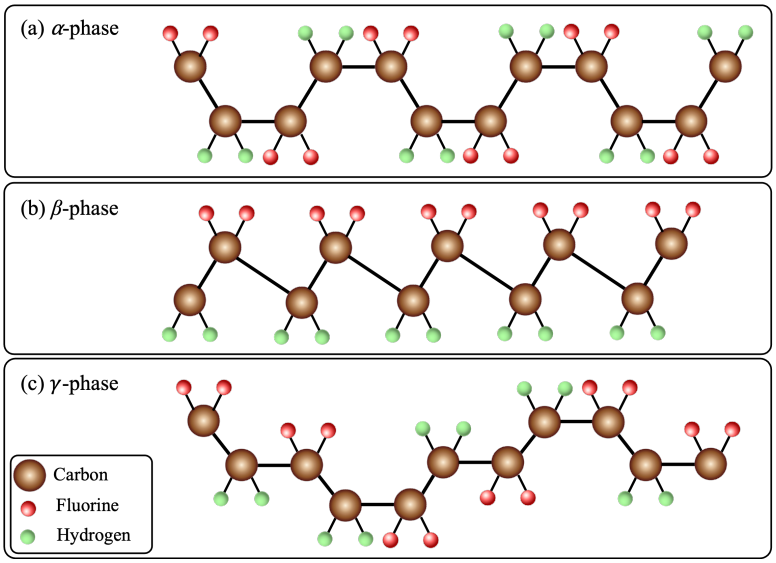

Fig. 3.13: Schematic representation of the main crystalline phases of the polyvinylidene fluoride (PVDF): α-phase, β-phase, and γ-phase. The conformational differences between these phases significantly influence PVDF's electrochemical, mechanical, and dielectric properties, which are critical in applications such as LIBs.

In this study, we focus on two representative crystalline phases of PVDF: the non-polar α-phase and the highly polar β-phase. The fully optimized atomic structures of these two phases are presented in Fig. 3.14, panels (a) and (d), respectively. Panels (b) and (e) show the corresponding side views projected onto the $z-y$ plane, which help visualize the polymer chain alignment relative to the surface. To explore the interfacial interactions with the Si(110) surface, we considered two monomer orientations for each phase: one with the hydrogen-terminated side facing the positive z-direction, and the other with the fluorine-terminated side facing the negative z-direction, as illustrated in panels (c) and (f).

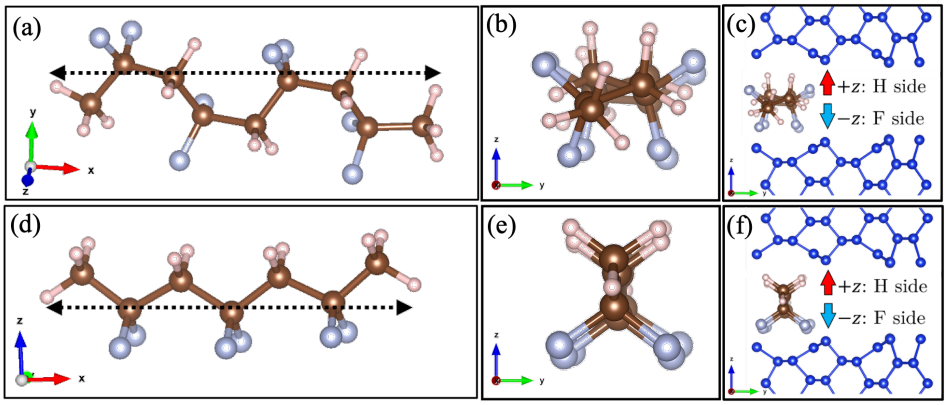

Fig. 3.14: Optimized atomic structures of the α and β phases of PVDF. Panels (a) and (d) show the front views of the α-phase and β-phase, respectively. Panels (b) and (e) display the corresponding side views projected along the $z-y$ plane. Panels (c) and (f) illustrate the monomer configurations used in this study, highlighting two orientations relative to the Si surface: one with the hydrogen-terminated side facing the positive z-direction and the other with the fluorine-terminated side facing the negative z-direction. Blue: silicon atom; Light-pink: hydrogen atom; Gray: fluorine atom; Brown: carbon atom.

Structurally, both phases share a carbon-based backbone but differ in chain conformation and molecular composition. As shown in Fig. 3.14, the α-phase consists of 9 carbon atoms per polymer chain, whereas the β-phase contains 7. These structural differences influence their dipole moments and binding characteristics, making them suitable candidates for comparative interfacial studies. The detailed atomic compositions and structural parameters for both PVDF phases are summarized in Table 3.2.

Table 3.2: Number of atoms in α and β phases of PVDF and length of each chain.

Phase	Carbon	Fluorine	Hydrogen	Total	Length (Å)
$\boldsymbol{\alpha}$	9	8	12	29	10.40
$\boldsymbol{\beta}$	7	6	10	23	9.44

3.2.3 Atomistic Modeling of the Si(110)-PVDF Interface

Extensive research on silicon-based anodes has highlighted the promising potential of silicon suboxides (SiO_x), primarily due to their substantially reduced volumetric expansion and contraction compared to pure crystalline silicon. This reduced dimensional change plays a critical role in mitigating detrimental side reactions and contributes to enhanced long-term electrochemical cycling stability of the anode materials [283–285]. Given that silicon-based electrodes are typically synthesized and processed under oxygen-rich ambient conditions [286], they are particularly prone to surface oxidation. Consequently, understanding the formation and behavior of silicon suboxides is essential for unraveling interfacial phenomena at the electrode-binder interface.

Surface oxygen content on silicon significantly influences multiple performance-related factors, including the suppression of volume-induced mechanical stress, improved adhesion and adsorption behavior of binder materials, and modulation of the system's electronic charge distribution. In particular, partially oxidized silicon nanostructures offer distinct advantages for LIB anodes. Their amorphous nature enables faster lithium diffusion, while oxygen-functional groups serve to alleviate mechanical degradation and prevent particle agglomeration. Furthermore, controlled oxygen incorporation during the deposition of silicon nanoparticles can promote the formation of lithium silicates and oxides, which are known to enhance structural robustness and improve lithium retention capabilities [287].

To optimize the performance of SiO_x-based anodes, several strategies have been proposed [288]. These include employing thin film deposition techniques to introduce controlled SiO_x surface coatings, incorporating conductive additives such as TEMPO-oxidized cellulose nanofibers, and fine-tuning synthesis parameters to modulate the oxidation degree. Through the strategic integration of these methods, substantial improvements can be realized in terms of electrochemical performance, cycling durability, and overall battery longevity [289, 290].

The stability and interfacial reactivity of various binder materials, including PVDF on pristine Si and Li-Si surfaces, have been extensively investigated through both experimental and theoretical approaches [268–270]. Experimental studies have particularly examined the role of silicon suboxide (SiO_x) layers and SiO_x-coated silicon anodes in enhancing lithium storage performance, along with the interactions between commercial binders and these modified surfaces [271–275]. However, these investigations have predominantly focused on macroscopic electrochemical outcomes, often overlooking the atomic-scale mechanisms that govern binder reactivity, adhesion, and interfacial stability.

Although considerable theoretical attention has been given to pristine and lithiated silicon

surfaces, there remains a notable lack of studies addressing PVDF interactions with oxidized silicon surfaces. This oversight is particularly significant, as surface oxidation is known to critically influence interfacial characteristics under realistic operating conditions. Understanding the binding mechanisms on oxidized surfaces is therefore essential for the rational design of high-performance silicon-based anodes.

To fill this gap, the present study offers a detailed theoretical investigation of the reactivity and binding behavior of PVDF binders on oxidized silicon surfaces, employing DFT as the primary computational framework. While PVDF has traditionally been considered incompatible with silicon-based anodes due to poor adhesion and mechanical instability, emerging research indicates that strategic surface engineering of silicon can mitigate these issues and unlock the potential of PVDF for high-performance anode applications [149].

To explore the interfacial interactions between PVDF and SiO_x surfaces, a series of atomistic models was designed in which PVDF chains were positioned atop SiO_x substrates with varying orientations and oxidation states, as illustrated in Fig. 3.14 (panels (c) and (f)). Given the inherent polarity asymmetry of PVDF-comprising a fluorine-rich side and a relatively hydrogen side-distinct interactions are anticipated depending on which face is in contact with the substrate. For both the α and β crystalline phases of PVDF, two molecular orientations were modeled: (*i*) fluorine-side facing the surface and (*ii*) hydrogen-side facing the surface. Each of these orientations was further investigated along three distinct alignments relative to the substrate: parallel to the x-axis, parallel to the y-axis, and diagonally along the $x - y$ plane. All configurations underwent full structural optimization, and those with the lowest total energy were selected as the most stable interfacial models. This systematic approach enables a comprehensive evaluation of the adsorption behavior and preferred binding orientations of PVDF on oxidized silicon.

The SiO_x surfaces used in this study were modeled in three oxidation states: (*i*) pristine (oxygen-free), (*ii*) partially oxidized (with four oxygen atoms), and (*iii*) fully oxidized (with fourteen oxygen atoms). Based on prior literature, oxygen adsorption on silicon surfaces occurs via dissociative mechanisms, leading to the displacement of surface silicon atoms and the formation of bridge-bonded Si–O–Si linkages at dimer sites [291–293]. Accordingly, oxygen atoms were adsorbed at bridge sites between neighboring surface silicon atoms to accurately represent realistic oxidation states and their influence on PVDF adhesion and interfacial stability.

Fig. 3.15 illustrates the initial configurations of (a) α-phase and (b) β-phase of PVDF, where both polymer phases are oriented with their fluorine-terminated side facing the partially oxidized silicon surface. Further structural optimizations, interfacial interactions between the binder and the substrate, and a detailed analysis of their binding mechanisms will be systematically discussed in the chapter 5.

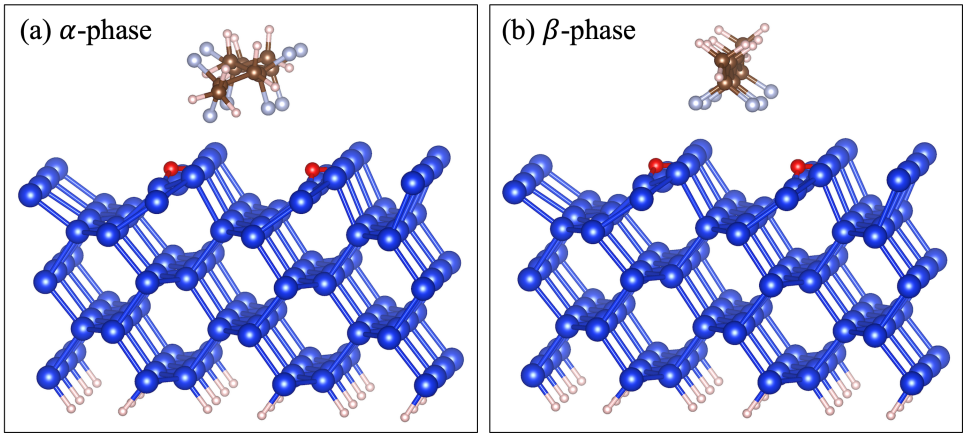

Fig. 3.15: The initially structures of (a) α and (b) β-phase of PVDF, oriented with the fluorine side toward a partially oxidized Si surface.

"There are two possible outcomes:
If the result confirms the hypothesis, then you've made a measurement,
If the result is contrary to the hypothesis, then you've made a discovery."
— Enrico Fermi —
Nobel Prize Laureate in Physics – 1938

4. Atomistic Analysis of the Pt/Nafion Interface in PEMFCs

This chapter analyzes the structural and electronic behavior of the hydrated Nafion/Pt(111) interface in PEMFCs, examining three interfacial configurations under different hydration levels to understand proton transfer, charge redistribution, polymer stability, and water-mediated interactions. The chapter concludes by comparing pristine and degraded Nafion to evaluate the impact of polymer integrity on fuel-cell performance.

❖ Chapter Outline

- **Nafion Interaction with the Pt+H Surface (Sec. 4.1)**
  - Config. 1: Nafion is positioned on the Pt+H surface with its $–SO_3H$ group.
  - Config. 2: Nafion is positioned on the Pt+H surface with its $–CF_3$ group.
  - Config. 3: Nafion is positioned on the Pt+H surface with its hydrophobic backbone.
- **Nafion Interaction with the Hydrated Pt Surface (Pt+H_2O) (Sec. 4.2)**
  - Config. 1: Nafion is positioned on the Pt+H_2O surface from its hydrophilic side at an initial distance of 2.8 Å.
  - Config. 2: Nafion is positioned on the Pt+H_2O surface with a larger initial separation to investigate how the increased distance influences its interaction with the interface.
  - Config. 3: Nafion is positioned on the Pt+H_2O surface with its $–CF_3$ group facing the interface.
- **Pristine Nafion (Sec. 4.3)**
  - The first configuration is re-examined using pristine Nafion to compare its interfacial behavior with that of the degraded Nafion.
- **Discussion (Sec. 4.4)**
  - A comparison of all configurations is presented to clarify how hydration and Nafion integrity affect interfacial stability, charge transfer, and proton-transport mechanisms.

4.1 Nafion on the Hydrogen-Covered Pt Surface (Pt+H)

The interaction between hydrogen atoms and transition-metal surfaces has been extensively studied due to its fundamental and technological importance in various fields, including hydrogen storage, fuel cell catalysis, hydrogen embrittlement of materials, and corrosion control. In particular, platinum has been the subject of numerous experimental [294–296] and theoretical [297–299] investigations, as it plays a crucial role in electrocatalytic processes such as the hydrogen evolution and oxidation reactions.

On the Pt(111) surface, the adsorption of a hydrogen atom can occur at four distinct sites, as shown in Fig. 4.1, characterized by different metal coordination environments: (a) atop site (onefold coordination), (b) bridge site (twofold coordination), (c) fcc hollow site (threefold coordination, above a third-layer Pt atom), and (d) hcp hollow site (threefold coordination, above a second-layer Pt atom). The fcc and hcp hollow sites differ only in the stacking of the underlying metal layers in the fcc lattice, yet this subtle structural variation often leads to small but measurable differences in adsorption energy and vibrational properties.

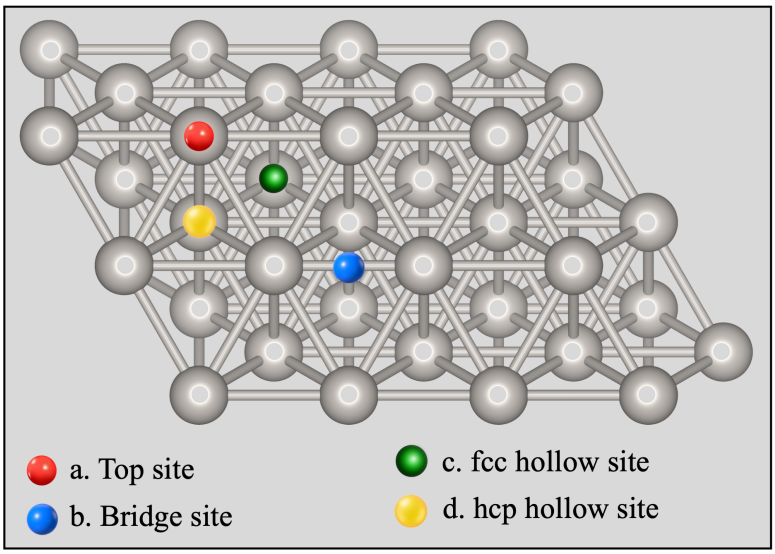

Fig. 4.1: Different adsorption sites of a hydrogen atom on the Pt(111) surface: (a) atop, (b) bridge, (c) fcc hollow, and (d) hcp hollow. The colored sphere represents the hydrogen atom, and gray spheres denote Pt atoms. In the fcc hollow site, there is no Pt atom directly beneath the adsorption site in the second layer, whereas in the hcp hollow site, a Pt atom is located directly below the adsorbed H atom.

Among these, the threefold fcc hollow site is generally recognized as the most energetically favorable position for hydrogen adsorption at low coverage, as confirmed by numerous first-principles studies. The energy differences between the fcc, hcp, and atop sites, however, are relatively small, on the order of a few tens of meV, meaning that vibrational effects, surface coverage, and temperature can slightly modify the site preference. At higher hydrogen coverage, mixed occupation of fcc and hcp sites has also been observed.

In our model, a monolayer of hydrogen atoms was placed on the fcc sites of the Pt(111) surface at the equilibrium adsorption distance (0.185 nm [300]), as illustrated in Fig. 4.2.

❖ Config. 1

In the first configuration, a Nafion monomer is positioned on the Pt surface with its sul-

fonate group oriented toward the surface. The sulfur atom is initially placed at a distance of 2.8 Å from the surface, following the setup reported in Ref. [301]. A monolayer of hydrogen atoms is adsorbed at the fcc hollow sites of the Pt surface. Fig. 4.3 illustrates the initial (a) and relaxed (b) configuration of the Nafion adsorbed on the hydrogen-covered Pt surface. After geometry optimization, the distance increases to 3.52 Å, indicating that the hydrogen-covered Pt surface exerts a repulsive interaction on the sulfonate group, pushing the Nafion monomer upward. This relaxation also leads to a slight rearrangement and disorder of the hydrogen atoms adsorbed on the Pt surface.

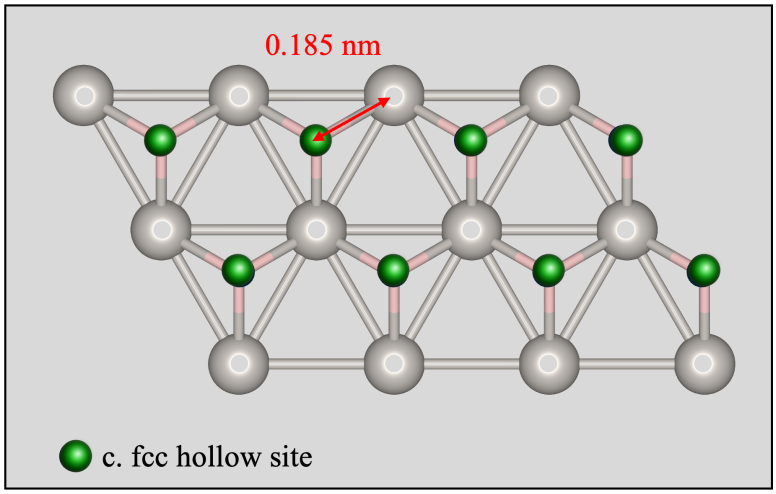

Fig. 4.2: Optimized configuration of hydrogen atoms adsorbed on the Pt(111) surface. Hydrogen atoms (green spheres) occupy the fcc hollow sites, identified as the most energetically favorable adsorption positions. The equilibrium distance between the hydrogen atoms and the platinum surface is 0.185 nm. Gray spheres represent the top-layer Pt atoms, and green spheres indicate the H atoms on fcc hollow sites.

To gain a more profound understanding of the interfacial interactions, a detailed analysis of the electronic structure at the interface is essential. In this context, we investigate the charge density difference (CDD) in three dimensions, along with the local density of states (LDOS), obtained by summing the atomic orbital projections for each atom. The CDD is a powerful and widely adopted approach for visualizing charge redistribution upon adsorption, providing insight into the nature and strength of interfacial bonding, charge transfer, and polarization effects. It reveals regions of electron accumulation and depletion, thereby clarifying how the electronic structure of each component is modified upon interaction. The charge density difference is defined as follows:

$$\Delta\rho = \rho_{(Pt+H_2O+Nafion)} - \rho_{(Pt+H)} - \rho_{(Nafion)} \qquad \text{(Eq. 4.1)}$$

In Eq. 4.1, the first term on the right-hand side represents the total charge density of the combined system, the second term corresponds to the charge density of the Pt slab with H atoms, and the last term denotes the charge density of the isolated Nafion monomer in the same configuration. This formulation allows one to isolate the net charge redistribution resulting solely from the interaction between Nafion and the hydrogenated Pt surface.

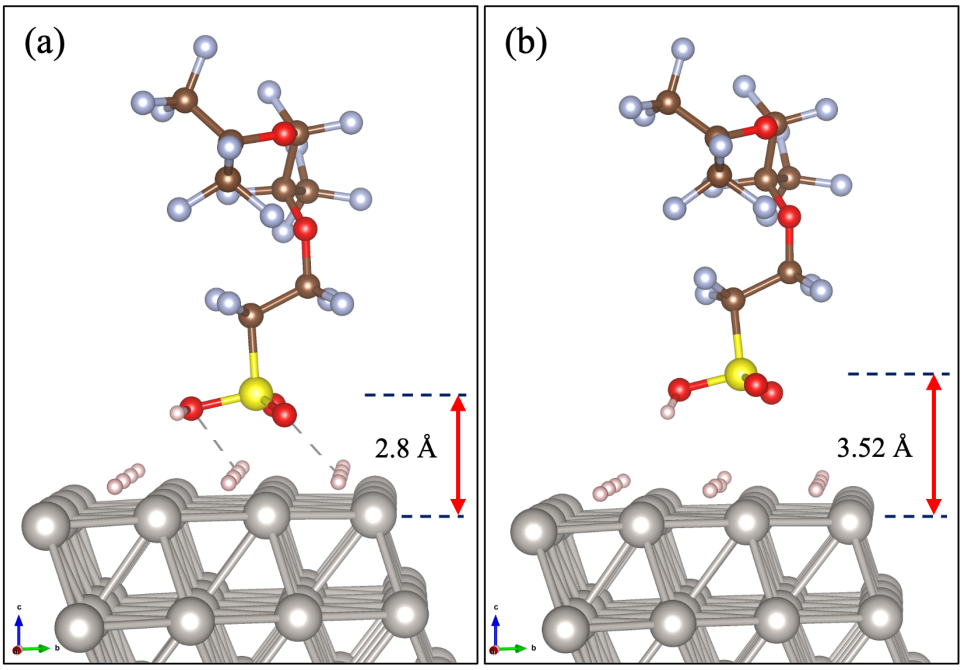

Fig. 4.3: Initial (a) and relaxed (b) structure of config. 1. The Nafion monomer is initially placed at a distance of 2.8 Å from the Pt(111) surface with hydrogen atoms occupying the fcc hollow sites. The sulfonate group of Nafion is oriented toward the surface. Gray: platinum atom; Yellow: sulfur atom; Silver: fluorine atom; Red: oxygen atom; Brown: carbon atom; Light-pink: hydrogen atom.

Fig. 4.4 shows the charge density difference (CDD) of the Nafion monomer adsorbed on the hydrogen-covered Pt surface, visualized with an isosurface level of 0.001. Green and yellow regions denote charge accumulation and depletion, respectively. Charge accumulation is observed primarily around the oxygen atoms of the sulfonate group (O-1, O-2, and O-3), indicating electron transfer from the hydrogen atoms within Nafion toward the electronegative oxygen sites. A corresponding charge depletion is visible around the hydrogen atoms of the sulfonic group and at the hydrogen-covered Pt surface, consistent with polarization effects at the interface. This redistribution leads to positively charged hydrogen species on both the surface and the polymer, giving rise to electrostatic repulsion. Nevertheless, at the equilibrium adsorption distance, this repulsive contribution is compensated by attractive interactions, such as Pt–O bonding and polarization-induced electrostatics, resulting in a stable interfacial configuration characterized by a balanced charge redistribution. The depletion regions on the oxygen atoms are oriented toward the metal surface, reflecting orbital rehybridization as the sulfonate group interacts electrostatically with the hydrogen-passivated Pt layer. The atoms labeled in this figure were specifically chosen for their significant charge redistribution (accumulation or depletion) to enable a detailed analysis of their local density of states (LDOS) in the following steps.

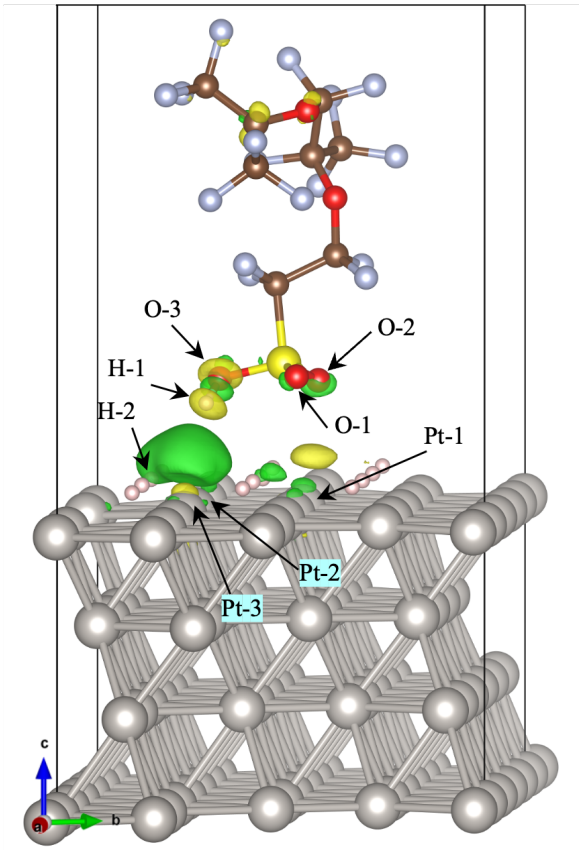

Fig. 4.4: Charge density difference (CDD) at the interface for configuration 1. Isosurfaces (isosurface level is set as 0.001 e/Å^3) depict charge redistribution, with green indicating electron accumulation and yellow indicating electron depletion. Gray: platinum atom; Yellow: sulfur atom; Silver: fluorine atom; Red: oxygen atom; Brown: carbon atom; Light-pink: hydrogen atom.

Additionally, the hydrogen atoms near the interface (H-1 and H-2) display subtle but distinct charge rearrangements, revealing a local perturbation of the H adlayer induced by Nafion adsorption. The mixed accumulation and depletion regions around these hydrogens indicate polarization within the adsorbed H network, which mediates the electrostatic coupling between Nafion and Pt. Overall, the CDD demonstrates that the interaction between Nafion and the H-covered Pt surface is primarily governed by interfacial polarization rather than complete charge transfer, with the sulfonate group acting as an electron donor and the Pt surface as a local electron acceptor. This charge redistribution is crucial for understanding the stability and electronic behavior of the interface under realistic fuel-cell operating conditions.

Fig. 4.5 presents the local density of states (LDOS) for two selected hydrogen atoms (as shown by arrows in Fig. 4.4): H-1, belonging to the sulfonic acid group of Nafion, and H-2, positioned on the Pt surface. For H-1 [Fig. 4.5 (a)], the comparison between the isolated Nafion monomer and the full interacting system (Pt+H+Nafion) reveals a notable difference near the Fermi level. The inset highlights that H-1 exhibits a small but finite LDOS contribution at $E - E_{Fermi} = 0$, only when the Nafion monomer is adsorbed on the Pt surface. In contrast, the isolated Nafion structure shows no states in this energy region, indicating that the interaction with the metal–hydrogen interface induces weak hybridization or polarization effects on the acidic hydrogen. This suggests that the electronic environment of H-1 is slightly perturbed by the proximity of the Pt-H network, even though no strong bonding interaction is formed.

For H-2 [Fig. 4.5 (b)], which represents a hydrogen atom adsorbed directly on the Pt surface, the LDOS of the isolated slab and the full system are nearly identical across the entire energy range. This confirms that the presence of Nafion does not significantly modify the electronic character of the surface hydrogen, reflecting the weak interfacial coupling between the polymer and the H-covered Pt substrate.

Overall, the LDOS analysis demonstrates that both H atoms show only very weak activity around the Fermi level, with H-1 displaying a slight induced contribution due to interfacial polarization, while H-2 remains essentially unaffected. This further supports the conclusion that the Nafion–Pt interaction is governed by weak electronic perturbations rather than strong chemical bonding.

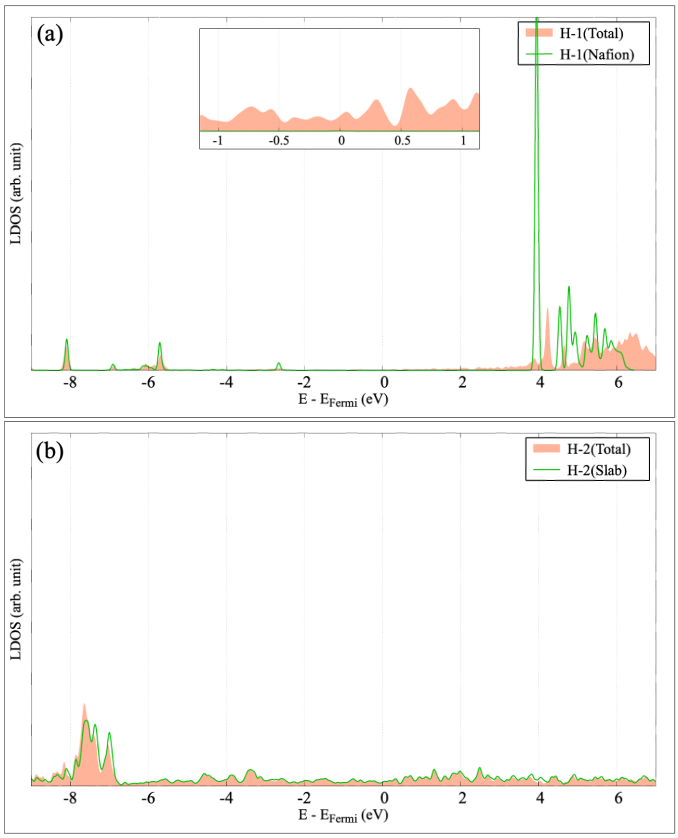

Fig. 4.5: Local density of states (LDOS) for the two selected hydrogen atoms at the Nafion-Pt interface. (a) LDOS of H-1, the hydrogen in the sulfonic acid group of Nafion, shown for the full system (Pt+H+Nafion) and for the isolated Nafion monomer. (b) LDOS of H-2, a hydrogen atom adsorbed on the Pt surface, plotted for the full system and the isolated Pt slab. In the insets, the focus is around the Fermi level ($E - E_{Fermi} = 0$).

The LDOS profiles for the three oxygen atoms of the Nafion sulfonate group (O-1, O-2, and O-3), shown in Fig. 4.6, reveal consistent electronic features across all sites. In the isolated Nafion monomer (blue curves), the oxygen states exhibit sharp, well-defined peaks, characteristic of localized molecular orbitals and the absence of strong external interactions. However, once Nafion is brought into contact with the Pt-H surface (red shaded regions), the LDOS becomes noticeably broader and more delocalized, reflecting a modification of the electronic environment induced by interfacial coupling. The zoomed insets highlight that, near the Fermi level, the isolated Nafion oxygen atoms contribute essentially no states, while the oxygen atoms in the full system display weak but non-negligible electronic states in the -1 to $+1$ eV range.

These emergent states indicate a subtle interaction between the sulfonate oxygens and the Pt-H surface, consistent with partial charge redistribution observed in the CDD analysis. Overall, the LDOS broadening and the appearance of weak states around the Fermi level signify a slight perturbation of the oxygen electronic structure due to adsorption, although the interaction remains relatively moderate, in line with the non-bonding character expected for this interface.

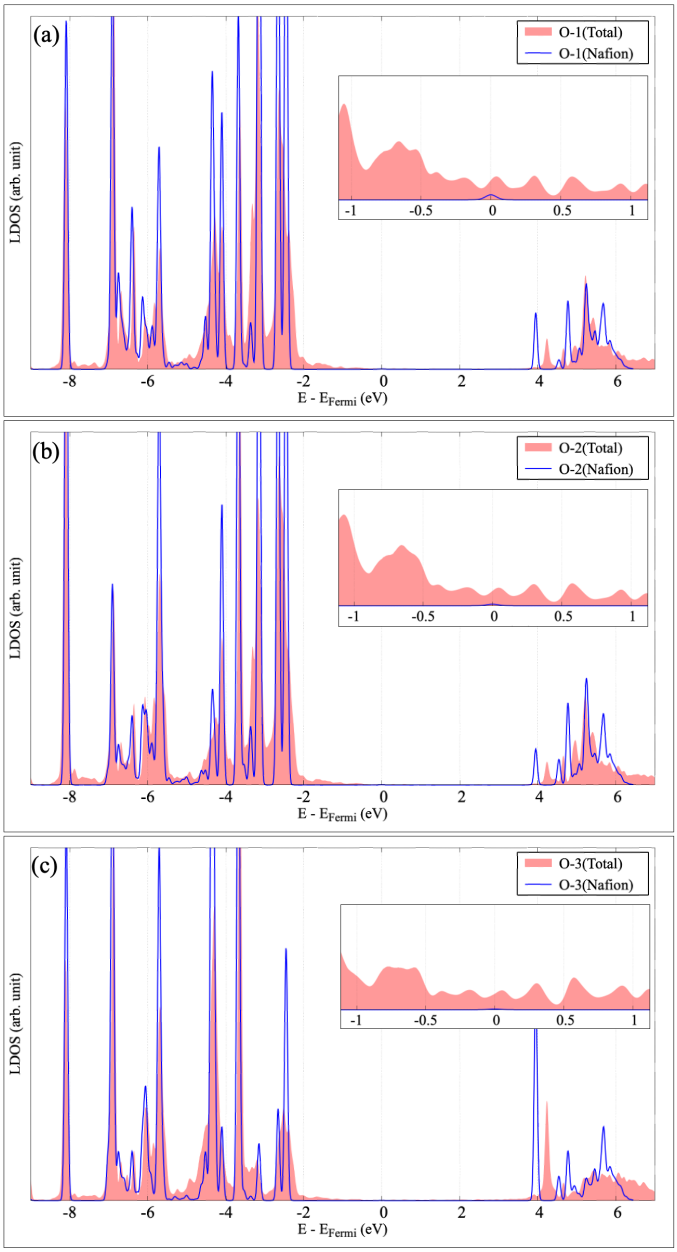

Fig. 4.6: Local density of states (LDOS) for the three selected oxygen atoms (O-1, O-2, and O-3) of the Nafion sulfonate group. Each panel compares the LDOS of the oxygen atom in the total system (Pt+H+Nafion) with that of the isolated Nafion monomer. Insets provide a magnified view of the energy region around the Fermi level ($E - E_{Fermi} = 0$).

The LDOS profiles of the three selected surface Pt atoms in Fig. 4.7 (Pt-1, Pt-2, and Pt-3) show a very similar overall electronic structure across all panels. For each atom, the LDOS of the Pt+H slab alone (red line) closely overlaps with the LDOS of the corresponding atom in

the full Pt+H+Nafion system (green filled area). The main features, such as the occupied states between approximately -8 eV and -2 eV, the broad metallic character approaching the Fermi level, and the small unoccupied contributions above 4 eV, remain essentially unchanged upon adsorption of the Nafion monomer and hydrogen species.

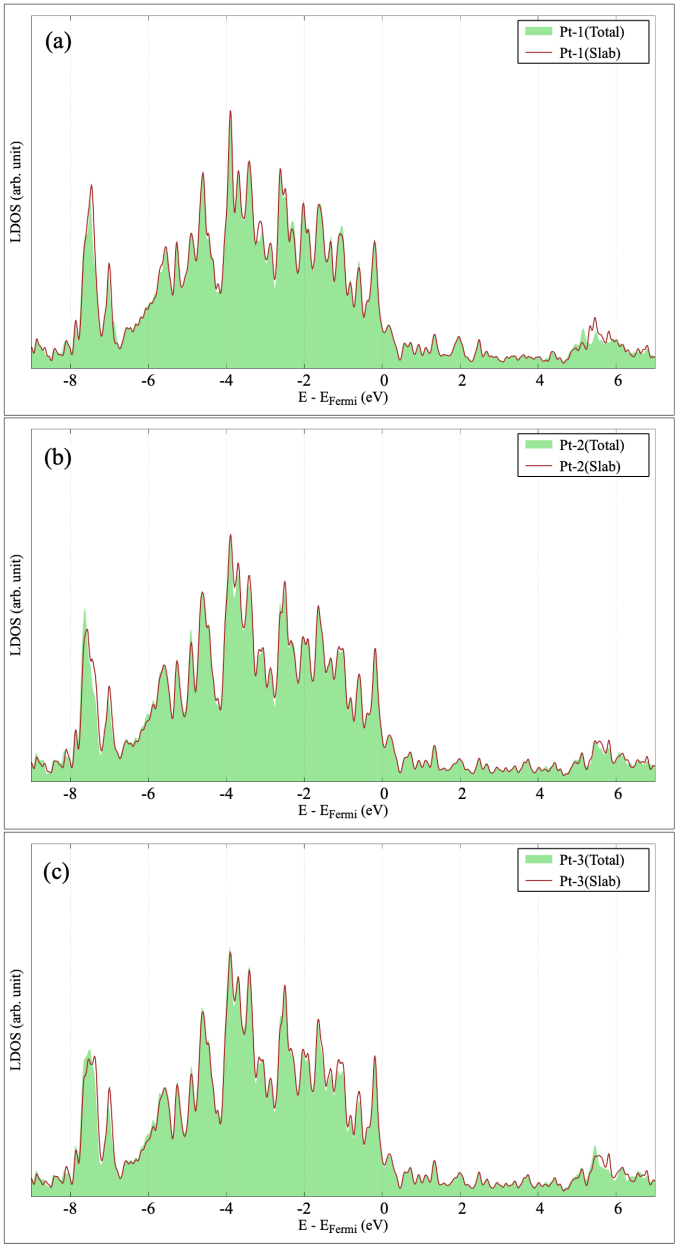

Fig. 4.7: Local density of states (LDOS) projected onto three selected surface Pt atoms (Pt-1, Pt-2, and Pt-3), shown for both the clean Pt slab (red line) and the full system (green filled area). Each panel corresponds to one Pt atom, with the Fermi level set to zero.

This strong overlap indicates that the local electronic environment of these surface Pt atoms is only minimally perturbed by the presence of Nafion and interfacial hydrogen. In other words, despite the charge redistribution observed in the CDD analysis, the electronic structure of Pt remains nearly identical to that of the clean slab. Therefore, we conclude that no significant modification of the LDOS occurs for the surface Pt atoms when moving from the

isolated slab to the full Pt+H+Nafion system, confirming that the interfacial interactions are too weak to alter the characteristic Pt electronic states.

❖ Config. 2

In Configuration 2, the Nafion monomer was initially positioned near the Pt surface through its $–CF_3$ terminal group, with an initial separation of approximately 2.53 Å, as shown in Fig. 4.8 (a). After full structural relaxation, Fig. 4.8 (b) reveals that the distance between the $–CF_3$ group and the Pt surface increases to about 3.72 Å. This increase in separation indicates a repulsive interaction on this side of the molecule, effectively pushing the $–CF_3$ group away from the surface. At the same time, the rest of the Nafion structure undergoes a reorientation, rotating and adjusting its position to adopt a more favorable adsorption configuration. This behavior highlights the competition between repulsion at the hydrophobic end ($–CF_3$) and attractive interactions from other functional groups, ultimately determining the final adsorption geometry of Nafion on the Pt surface.

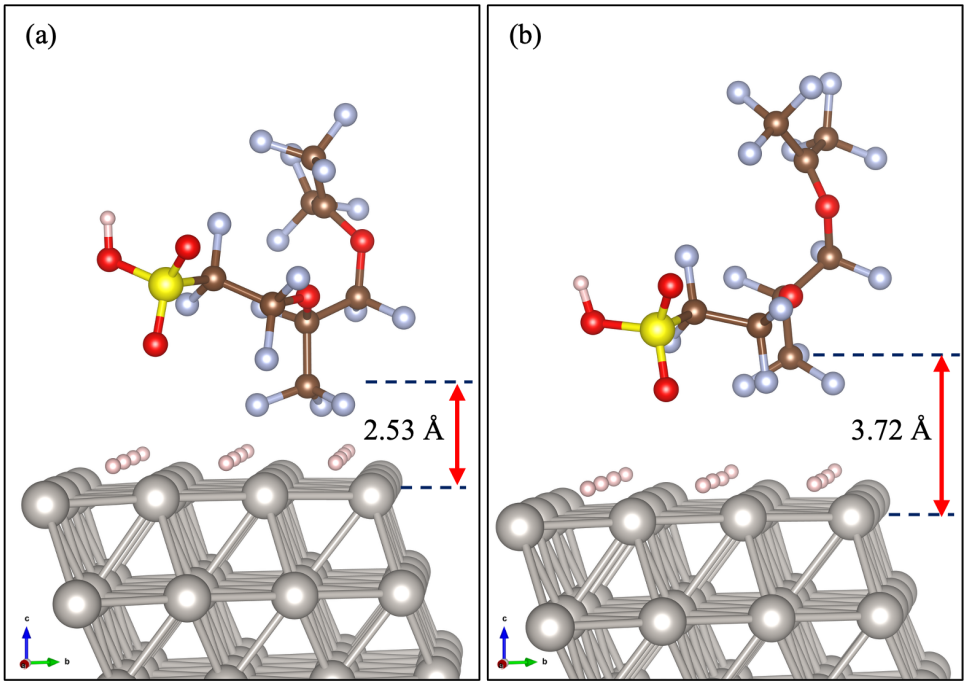

Fig. 4.8: Initial (a) and relaxed (b) structure of config. 2. The Nafion monomer is initially placed at a distance of 2.53 Å from the Pt(111) surface with hydrogen atoms occupying the fcc hollow sites. The $–CF_3$ group of Nafion is oriented toward the surface. Gray: platinum atom; Yellow: sulfur atom; Silver: fluorine atom; Red: oxygen atom; Brown: carbon atom; Light-pink: hydrogen atom.

In Fig. 4.9, the charge density difference (CDD) is illustrated for Configuration 2. The CDD map reveals a small but noticeable charge redistribution at the interface: a slight charge accumulation and depletion appear around the surface Pt atoms (Pt-1, Pt-2, and Pt-3) and the hydrogen atom on the Pt surface (H-2). Additionally, a more pronounced charge accumulation is observed around the O-1 atom of the sulfonic acid group, which is oriented toward the Pt surface. In contrast, the remaining atoms of the Nafion monomer exhibit only minimal charge rearrangement, indicating that the interfacial electronic interaction in this configuration is relatively weak and highly localized.

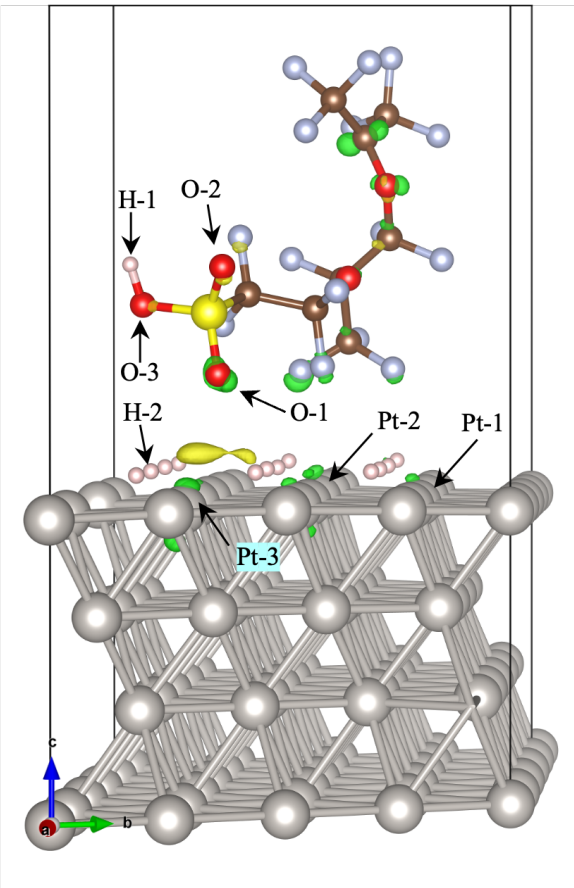

Fig. 4.9: Charge density difference (CDD) at the interface for configuration 2. Isosurfaces (isosurface level is set as 0.001 e/Å^3) depict charge redistribution, with green indicating electron accumulation and yellow indicating electron depletion. Gray: platinum atom; Yellow: sulfur atom; Silver: fluorine atom; Red: oxygen atom; Brown: carbon atom; Light-pink: hydrogen atom.

Fig. 4.10 presents the LDOS of the two selected hydrogen atoms: H-1, which belongs to the Nafion monomer, and H-2, which resides on the Pt surface (as identified previously in Fig. 4.9). These two hydrogens play different chemical roles and experience very different electronic environments, which is clearly reflected in their LDOS profiles.

For H-1, comparing the LDOS of the isolated Nafion monomer with that of the full Pt+H+Nafion system shows that its electronic states shift slightly toward lower energies when the monomer is placed near the Pt surface. This small downward shift indicates a weak perturbation caused by the presence of the metallic substrate and nearby species. Importantly, for both cases, Nafion alone and the total system, H-1, does not exhibit any states near the Fermi level. This absence of states around E_{Fermi} confirms that H-1 does not participate in any significant electronic interaction with the Pt surface and remains chemically inert in this interfacial configuration.

A different behavior is observed for H-2, the hydrogen atom adsorbed on the Pt surface. Its LDOS shows a clear set of states in the range of about -8 to -6 eV, characteristic of hydrogen–metal bonding interactions. Moreover, the LDOS of H-2 also shows non-zero states at the Fermi level, as highlighted in the inset. The presence of states at E_{Fermi} is typical for atoms directly bonded or electronically coupled to a metallic surface, indicating hybridization between the hydrogen 1*s* orbital and the Pt *d*-band. The total-system LDOS and slab-only LDOS for H-2 are nearly identical, suggesting that the Nafion monomer does not significantly modify the

local electronic environment of the surface hydrogen. Altogether, the LDOS results show that H-1 (in Nafion) experiences only weak, long-range perturbations from the Pt surface, whereas H-2 (on Pt) is strongly hybridized with the metallic states, maintaining its metallic character even in the presence of the monomer.

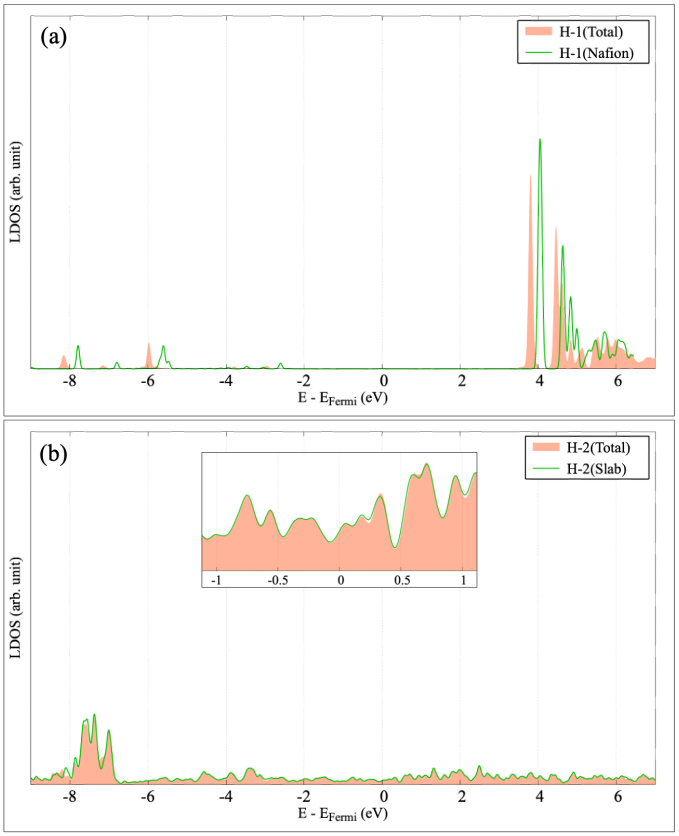

Fig. 4.10: Local density of states (LDOS) for the two selected hydrogen atoms: (a) H-1 belonging to the Nafion monomer, shown for the isolated Nafion structure and for the full Pt+H+Nafion system; and (b) H-2 located on the Pt surface, compared between the slab-only and total configurations. The inset in panel (b) highlights the LDOS near the Fermi level ($E - E_{Fermi} = 0$).

The LDOS of the three oxygen atoms in configuration 2 are shown in Fig. 4.11. As illustrated, the electronic structure of all O atoms displays very similar features, reflecting their equivalent chemical environment within the Nafion sulfonate group. Across the three panels, the LDOS profiles of the oxygen atoms in the Nafion structure exhibit nearly identical features, reflecting their equivalent chemical environment within the sulfonate group. In all cases, the comparison between the isolated Nafion configuration (blue curves) and the full Pt+H+Nafion system (red curves) shows a slight downward shift of the occupied states toward lower energies relative to the Fermi level. This shift indicates a modest stabilization of the O-atom electronic states upon interaction with the Pt surface and nearby hydrogen, consistent with weak O–Pt coupling that perturbs but does not fundamentally alter their electronic character. Notably, none of the oxygen atoms develop states at the Fermi level, confirming that they remain electronically insulating and do not contribute to interfacial conductivity.

Beyond this small energy shift, the LDOS lineshape remains remarkably consistent across O-1, O-2, and O-3, both in the occupied region (-8 to -2 eV) and in the unoccupied region around $4 - 6$ eV. This uniformity suggests that the interaction strength with the Pt surface is similar for each oxygen atom and that the underlying sulfonate group preserves its molecular

identity even in the presence of the metallic substrate. Overall, the LDOS behavior highlights a mild but systematic interaction between Nafion and Pt, characteristic of physical adsorption where electronic redistribution occurs without significant hybridization or chemical bonding.

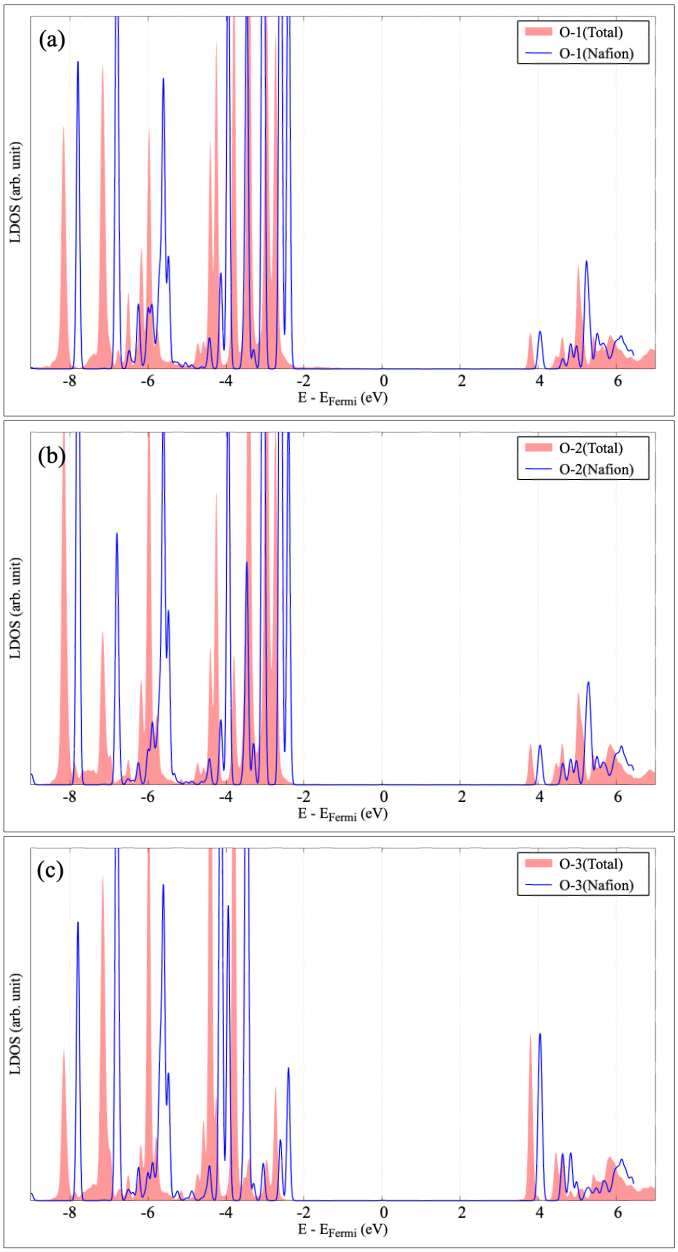

Fig. 4.11: Local density of states (LDOS) for the three selected oxygen atoms (O-1, O-2, and O-3) of the Nafion sulfonate group in configuration 2. Each panel compares the LDOS of the oxygen atom in the total system (Pt+H+Nafion) with that of the isolated Nafion monomer.

The LDOS of the three selected Pt surface atoms in configuration 2 are shown in Fig. 4.12. In all cases, the LDOS of each Pt atom in the full Pt+H+Nafion system closely overlaps with the LDOS of the corresponding atom in the clean Pt slab. This near-perfect overlap indicates that the presence of Nafion and the nearby hydrogen atom produces only a minimal perturbation of the electronic states of Pt at the interface. The characteristic d-band features between approximately -7 eV and 0 eV remain essentially unchanged, and the density of states at the

Fermi level is preserved, confirming that the metallic nature of the Pt surface is unaffected by the adsorption of the polymer in this configuration.

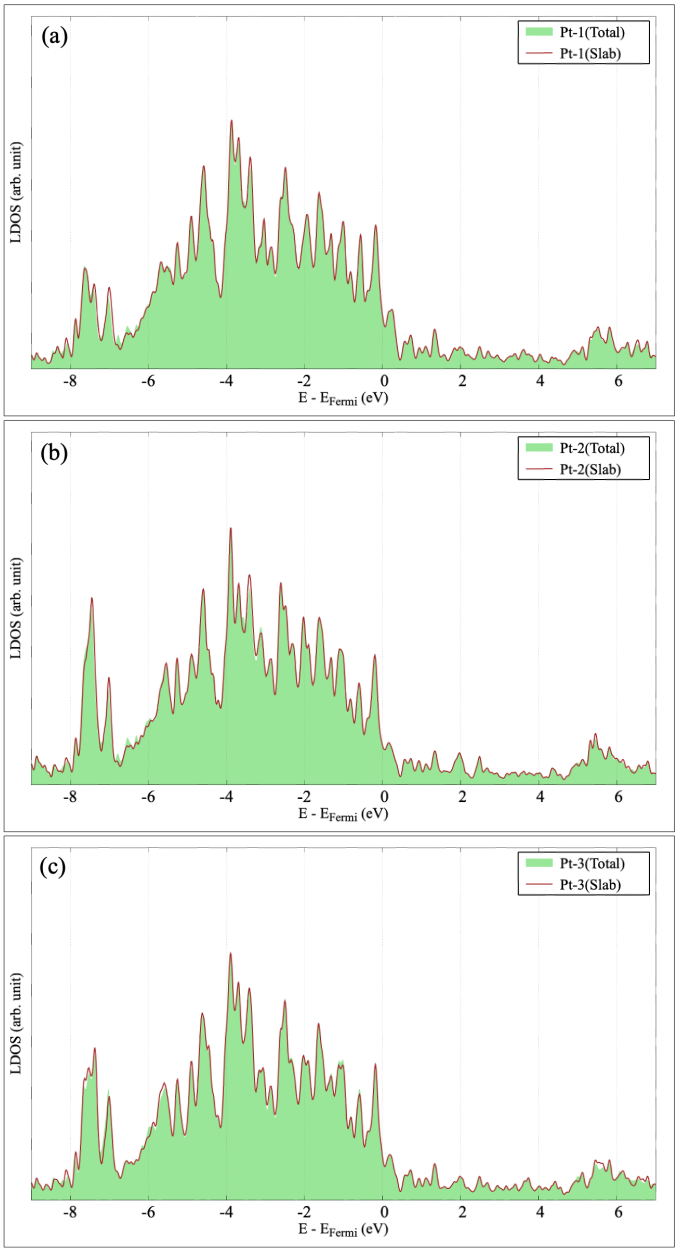

Fig. 4.12: Local density of states (LDOS) for three representative Pt atoms on the surface slab in configuration 2, comparing the clean Pt slab (red line) with the full Pt+H+Nafion system (green shaded area). Each panel corresponds to one Pt atom, with the Fermi level set to zero.

Beyond this overall similarity, the small differences between the total and slab LDOS curves fall within the range expected for weak physisorption, where the interaction is governed by minor charge rearrangements rather than the formation of chemical bonds or significant orbital hybridization. The preservation of the Pt *d*-band structure, together with the absence of O- or H-induced features in the LDOS of the Nafion atoms, indicates that the polymer interacts only weakly with the surface. Given that both subsystems remain essentially neutral, any interaction present is likely dominated by long-range van der Waals forces. Taken together, these

results show that the Pt surface retains its intrinsic electronic character and that the influence of Nafion on Pt is limited to subtle, non-disruptive perturbations. This behavior aligns with typical fuel-cell operating conditions, where Nafion interacts with Pt mainly through electrostatic and hydrogen-bonding effects rather than strong covalent bonding.

❖ Config. 3

In the last configuration (Config. 3), the Nafion monomer is placed on the Pt+H surface with its hydrophobic backbone, as shown in Fig. 3.7 (the main chain), in order to probe the interaction of this non-polar side with the Pt+H surface. The initial and optimized geometries of this configuration are reported in Fig. 4.13. Upon structural relaxation, the Nafion monomer moves away from the substrate, increasing the separation between the polymer and the Pt surface (from about 2.1 Å in the initial guess to roughly 3.6 Å in the final structure). This behavior indicates a weak interaction between the hydrophobic side of Nafion and the Pt+H surface, with the polymer tending to maximize its distance from the metal rather than forming specific adsorption bonds, in clear contrast to the behavior of the sulfonate group.

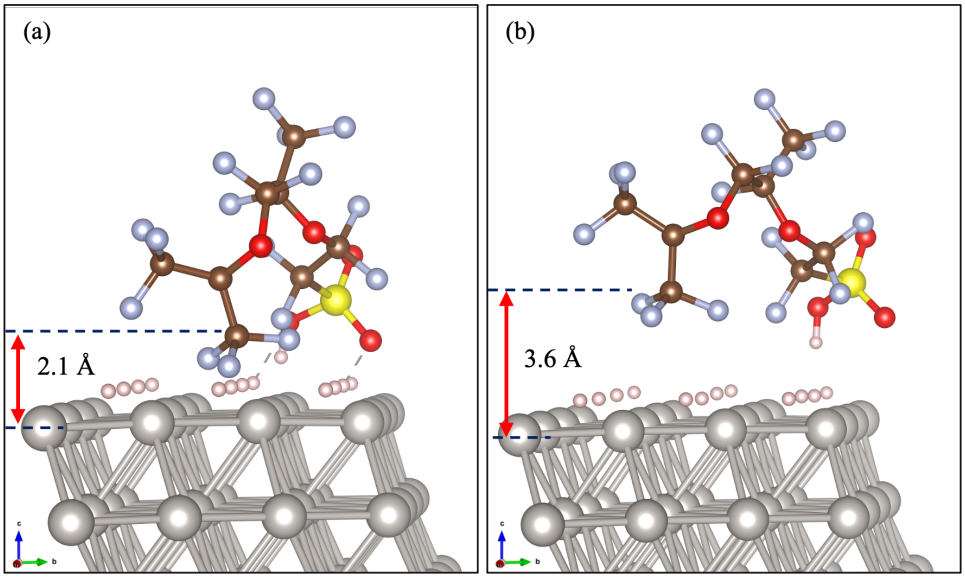

Fig. 4.13: Initial (a) and optimized (b) geometries of configuration 3, where the hydrophobic backbone of the Nafion monomer is oriented toward the Pt+H surface. Upon relaxation, the polymer retracts from the substrate, increasing the separation from approximately 2.1 Å to 3.6 Å. This outward displacement reflects the weak affinity of the hydrophobic side of Nafion for the Pt+H surface and the absence of specific adsorption interactions in this configuration. Gray: platinum atom; Yellow: sulfur atom; Silver: fluorine atom; Red: oxygen atom; Brown: carbon atom; Light-pink: hydrogen atom.

As in the previous configurations, the charge density difference (CDD) for configuration 3 is presented in Fig. 4.14. The CDD reveals a pronounced charge depletion around the hydrogen atoms adsorbed on the Pt surface, as well as around the acidic hydrogen of the $–SO_3H$ group in Nafion. In contrast, the remaining atoms of the Nafion backbone exhibit only minor charge redistribution, consistent with the weak interaction expected for the hydrophobic side of the polymer. The atoms highlighted by arrows in Fig. 4.14 are those selected for the LDOS analysis in the following section. The overall CDD pattern further supports the structural result of configuration 3, namely that the hydrophobic backbone does not participate in significant elec-

tronic exchange with the Pt+H surface, while the acidic hydrogen and nearby oxygen atoms remain the primary sites of interfacial charge rearrangement.

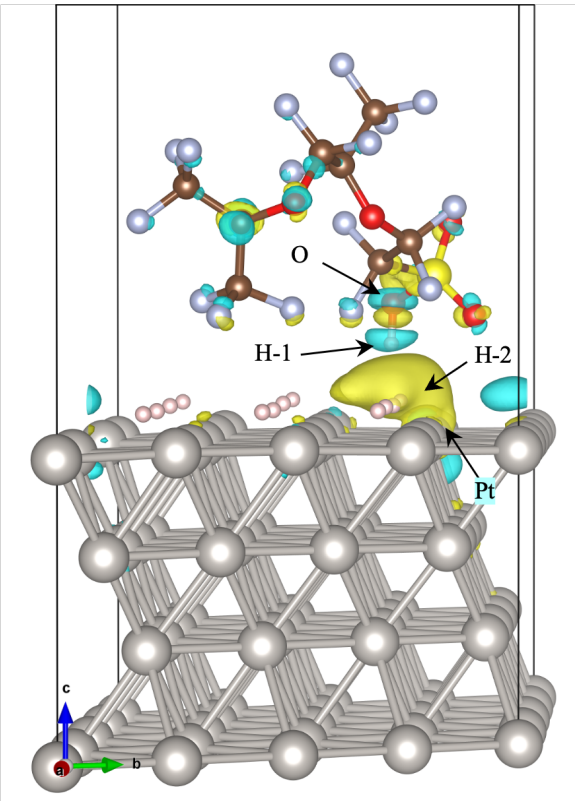

Fig. 4.14: Charge density difference (CDD) for configuration 3, showing the interaction between the hydrophobic side of the Nafion monomer and the Pt+H surface. A pronounced charge depletion appears around the surface H atoms on Pt and the acidic hydrogen of the $–SO_3H$ group. The atoms marked with arrows correspond to the sites selected for the LDOS analysis presented in the following figure. Gray: platinum atom; Yellow: sulfur atom; Silver: fluorine atom; Red: oxygen atom; Brown: carbon atom; Light-pink: hydrogen atom.

The LDOS of the selected atoms for configuration 3 is reported in Fig. 4.15. For H-1, located in the $-SO_3H$ group of Nafion [Fig. 4.15 (a)], the LDOS of the atom in the full Pt+H+Nafion system shifts slightly upward toward the Fermi level compared to the isolated Nafion case, and a small but noticeable contribution appears directly at the Fermi level (highlighted in the inset). This indicates that the acidic hydrogen participates in a weak electronic redistribution when the polymer approaches the Pt+H surface, consistent with the charge depletion observed in the CDD.

For H-2 adsorbed on the Pt surface [Fig. 4.15 (b)], the LDOS of the full Nafion/Pt+H system closely matches that of the hydrogen-covered Pt slab in the absence of Nafion. The persistence of states around the Fermi level in both cases indicates that this surface hydrogen remains electronically coupled to the metallic substrate and is only weakly affected by the presence of the distant polymer backbone in configuration 3.

The oxygen atom selected from the $–SO_3H$ group [Fig. 4.15 (c)] also exhibits a slight upward shift of its occupied states in the total system relative to the isolated Nafion monomer. A small density of states emerges around the Fermi level (zoomed region), which mirrors the behavior of H-1 and again points to modest charge rearrangement localized on the sulfonic acid moiety.

Finally, the Pt atom shown in Fig. 4.15 (d) retains its characteristic d-band shape, with only

minor deviations between the total system and the clean slab. The green-filled curve is slightly larger than the slab LDOS at specific energy windows, but the Fermi-level region and the overall electronic structure remain essentially unchanged. This confirms that the hydrophobic backbone of Nafion in configuration 3 does not significantly perturb the electronic states of the Pt surface.

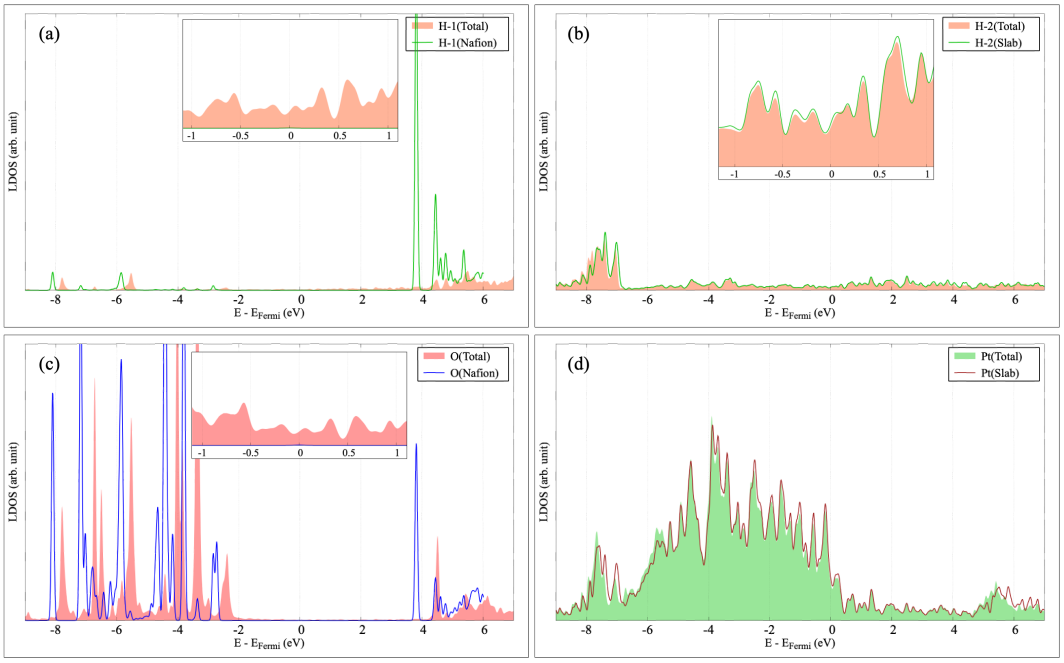

Fig. 4.15: Local density of states (LDOS) for selected atoms in configuration 3. (a) LDOS of H-1 in the $–SO_3H$ group of Nafion, showing an upward shift toward the Fermi level and the appearance of a small state at E_{Fermi} in the total system (inset). (b) LDOS of H-2 adsorbed on the Pt surface, which remains nearly identical to the clean slab and retains states at the Fermi level in both cases. (c) LDOS of the selected oxygen atom in the $–SO_3H$ group, exhibiting a slight upward shift and a small density of states near the Fermi level (zoomed inset). (d) LDOS of a representative Pt surface atom, showing only minor differences between the total system and the clean slab, with the Pt d-band structure essentially preserved.

Across the three configurations, a consistent picture emerges of how a Nafion monomer interacts with a Pt surface decorated with adsorbed hydrogen. When the sulfonic acid group is oriented toward the surface, the polymer adopts a shorter equilibrium separation (from approximately 2.8 Å to 3.5 Å) and exhibits localized charge rearrangements involving the acidic hydrogen and neighboring oxygen atoms, while the Pt surface remains largely metallic and only weakly perturbed. When the hydrophobic $–CF_2–$ backbone is facing the substrate, the monomer instead withdraws from the surface, producing minimal electronic overlap and essentially no modification of the Pt electronic structure. Taken together, these results indicate a weak interaction between the sulfonic acid group and the hydrogen-covered Pt surface, with the $–SO_3H$ moiety remaining at an equilibrium separation of approximately 3.5–3.7 Å. No significant interaction is observed between the surface and the remaining parts of the Nafion monomer, which primarily act as an inert, non-interacting backbone.

To more realistically model the environment of an operating fuel cell, the next step introduces H_2O molecules at the interface, since interfacial water layers exert a decisive influence on the structural, electronic, and proton-transport properties of polymer–electrode assemblies.

4.2 Nafion on the Hydrated Pt Surface (Pt+H_2O)

To extend the analysis toward more realistic fuel-cell conditions, this section incorporates explicit water molecules at the Pt/Nafion interface. In this study, two hydration levels are modeled by introducing either three or six H_2O molecules per sulfonic acid group. Although these hydration schemes do not reproduce the full complexity of bulk water, they allow the interfacial Pt/Nafion interactions to be isolated in a controlled manner. This strategy is consistent with earlier DFT investigations of hydrated Nafion interfaces and captures the essential features of proton-transfer mechanisms [256, 301].

The preferential adsorption geometry of water on Pt(111) is a key factor governing its electrochemical behavior. The orientation adopted by H_2O molecules affects their response to electric fields, their propensity for dissociation, and the stability and structure of interfacial water clusters. Previous DFT studies show that water favors top sites on the platinum surface, lying nearly parallel to the surface at a separation of about 2.21 Å [261–263]. Building on this understanding, simplified Pt(111)/Nafion model systems are constructed to explore how the interfacial organization between Nafion and the catalyst influences fuel-cell performance. The models include a degraded Nafion monomer, explicit water molecules, and a Pt(111) slab representing the electrode.

In these systems, the Nafion monomer is placed on the Pt surface with varying orientations of the sulfonate group and fluorocarbon backbone. Numerous studies indicate that the relative positioning of Nafion and water molecules is a determining factor for ion transport and interfacial proton mobility [302–305]. Water molecules located approximately 2.21 Å above the Pt surface can form interconnected channels that facilitate ion transfer between the electrode and the polymer matrix [263]. In contrast, the Nafion monomer itself is generally positioned farther from the metal, at a distance of around 2.8 Å [301]. Following this framework, the simulated systems in the present work consist of a four-layer Pt(111) slab, one Nafion monomer, and either three (low hydration) or six (high hydration) water molecules, depending on the targeted hydration level [306].

❖ Config. 1

In the first configuration, the Nafion monomer is positioned on the Pt surface with its sulfonate group oriented toward the metal, and the sulfur atom placed at an initial separation of 2.8 Å from the surface [301]. Three water molecules are arranged above the Pt surface at a distance of approximately 2.21 Å, consistent with the preferred adsorption geometry of H_2O on Pt(111) [263]. The initial and optimized geometries of this system are shown in Fig. 4.16 (a) and Fig. 4.16 (b), respectively.

During structural relaxation, an OH fragment dissociates from the sulfonate group of Nafion. This species behaves as a hydroxyl radical, which may subsequently acquire an electron to form a hydroxide anion (OH^-). Following dissociation, the OH group interacts strongly with the Pt surface. One possible pathway involves the OH abstracting a hydrogen atom from a nearby water molecule, forming H_2O and regenerating the hydroxyl radical, suggesting a potentially cyclic mechanism. Alternatively, the OH group may directly adsorb onto the Pt surface. Reported Pt–O bond lengths for adsorbed hydroxyl species range from 2.10 Å to 2.15 Å, shorter and stronger than the typical Pt–O separation reported for molecular water adsorption ($\approx$ 2.21 Å) [263, 307].

The formation of Pt–O bonds, together with the adsorption of water molecules at distances between 2.12 Å and 2.15 Å, induces an upward relaxation of the two uppermost Pt layers, as indicated by the arrow in Fig. 4.16 (b). This distortion reflects a local expansion of the Pt surface region, a structural response commonly associated with strong adsorbate–metal interactions.

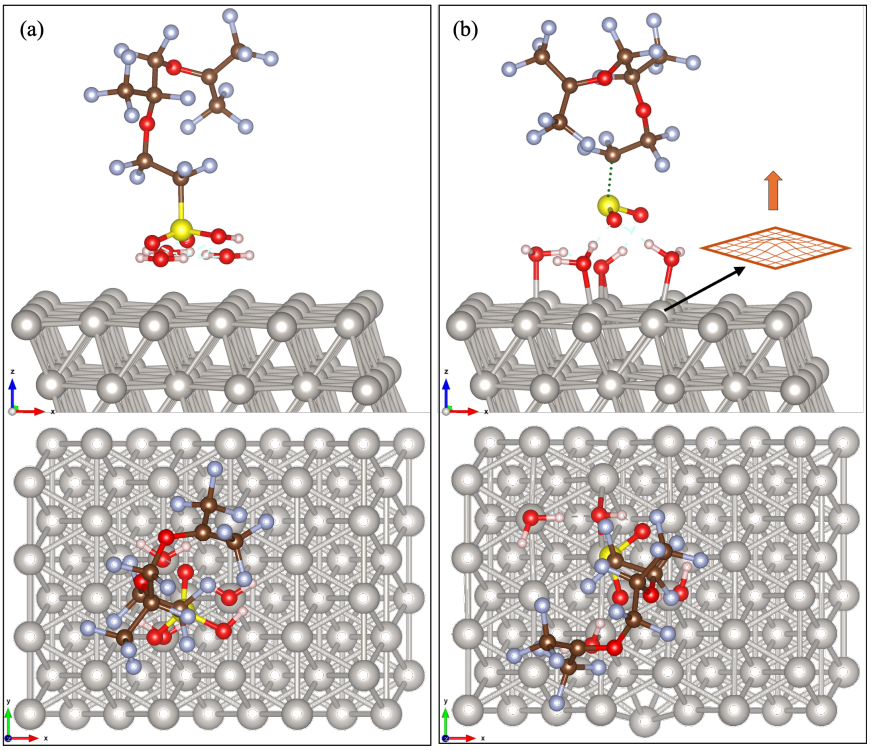

Fig. 4.16: (a) Initial structure of the Pt(111)–water–Nafion interface shown from the side view ($z - x$ plane) and top view ($y - x$ plane); (b) Corresponding optimized structure viewed from the same orientations. The Nafion monomer is initially placed at a distance of 2.8 Å from the Pt(111) surface. The dashed line shows the elongated C–S bond. Gray: platinum atom; Yellow: sulfur atom; Silver: fluorine atom; Red: oxygen atom; Brown: carbon atom; Light-pink: hydrogen atom.

To elucidate the interfacial behavior at the electronic level, a detailed examination of charge redistribution and orbital hybridization is essential. In this work, the electronic structure of the interface is analyzed through the three-dimensional charge density difference (CDD) and the local density of states (LDOS) projected onto selected atoms. The 3D-CDD reveals the spatial pattern of electron accumulation and depletion induced by adsorption, while the LDOS highlights the emergence or suppression of electronic states near the Fermi level.

To complement these qualitative insights, we further quantified interfacial charge redistribution using Bader charge analysis and interaction energies. The Bader method provides a direct measure of the net electron gain or loss for each atom at the interface [308–311]. Together, these complementary approaches offer a consistent and comprehensive interpretation of charge transfer among the Pt(111) surface, the interfacial water molecules, and the Nafion monomer.

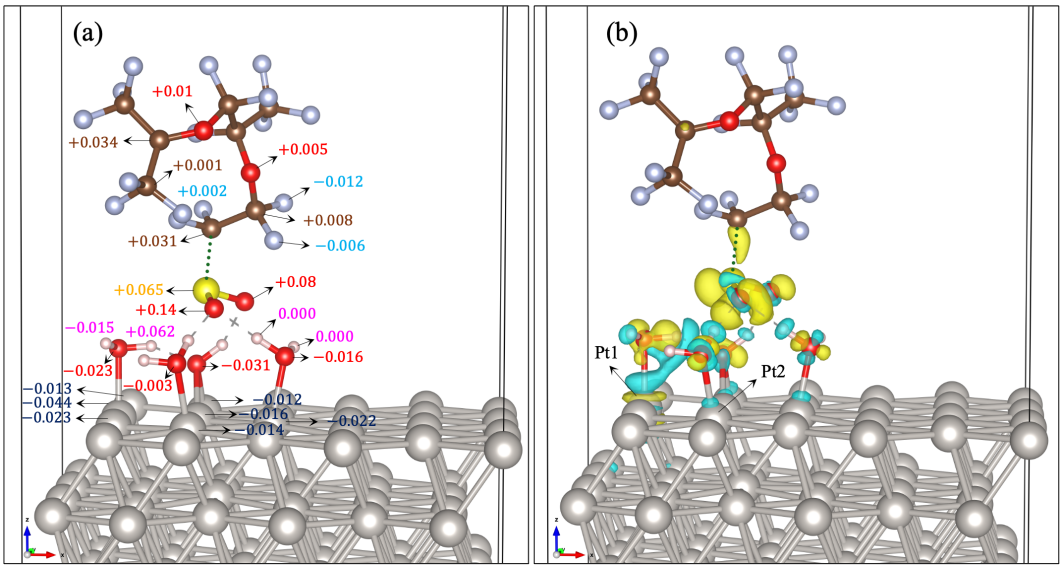

Fig. 4.17: (a) Bader charge distribution of the Pt(111)/Nafion interface, showing the net electron gain (positive values) and loss (negative values) for each atom obtained from Bader analysis of the charge density difference (CDD). The values highlight the charge transfer from surface Pt atoms toward the sulfonic group and the interfacial water molecules, with the S and selected O atoms exhibiting the largest charge accumulation. (b) Three-dimensional charge density difference (CDD) isosurface illustrating the spatial regions of electron accumulation (yellow) and depletion (cyan) upon adsorption of the degraded Nafion monomer (isosurface level is set as 0.008 e/Å^3). The CDD visualization confirms the trends revealed by the Bader charges and reveals the localized hybridization at the Pt surface atoms (Pt1 and Pt2). Together, the Bader and CDD analyses provide a consistent picture of charge redistribution and interfacial electronic coupling at the Pt(111)/Nafion interface.

Figure Fig. 4.17 presents a combined view of the Bader charge analysis and the three-dimensional charge density difference (CDD) isosurface for the Pt(111)/Nafion interface. Panel (a) reports the Bader charges obtained by integrating the charge-density difference within each atomic basin. Because the analysis is performed on $\Delta\rho$ rather than on the total electron density, the resulting Bader values correspond directly to the net electron gain or loss for each atom (Δq), instead of the absolute electron population. In this convention, negative values indicate electron depletion, whereas positive values represent electron accumulation relative to the isolated fragments. As shown in Fig. 4.17 (a), the surface Pt atoms undergo small but systematic electron depletion ($\Delta q \approx -0.01$ to $-0.02\ e$), while atoms within the sulfonic group, particularly sulfur and specific oxygen atoms, display the largest electron accumulation (up to $+0.14\ e$). These trends reveal a net charge flow from the Pt surface toward the acidic, hydrated region of the Nafion monomer.

Panel (b) displays the corresponding 3D-CDD isosurface, highlighting spatial regions of electron accumulation (yellow) and depletion (cyan) upon adsorption. The CDD map reinforces the Bader results: electron depletion is concentrated around the Pt1 and Pt2 surface atoms, while pronounced electron accumulation is found near the oxygen and sulfur atoms of the sulfonic head group. The strong consistency between the Δq values and the CDD visualization confirms that the electronic coupling at the Pt(111)/Nafion interface is mediated primarily through the sulfonic moiety and the adjacent interfacial water network. Collectively, the Bader and CDD analyses yield a coherent and physically transparent picture of charge redistribution across the interface.

Further insight into the interfacial interaction is obtained by examining the LDOS of selected Pt surface atoms and of the three oxygen atoms of the –SO_3H group [Fig. 4.18]. In panel (a), the LDOS of Pt1 and Pt2 in the clean Pt(111) slab (without Nafion and water) is compared with the LDOS of the same atoms in the fully hydrated Pt+H_2O+Nafion system. When Nafion and water are present, the Pt LDOS shows a slight redistribution of spectral weight: some states are shifted from below to above the Fermi level, and additional features appear around -8 eV. Overall, the Pt d-band remains largely intact, indicating that the electronic structure of the metal is only moderately perturbed by the adsorbates.

Panels (b)–(d) display the LDOS of the oxygen atoms in three distinct situations: (*i*) in the fully optimized Pt+H_2O+Nafion system (red), (*ii*) in the isolated Nafion monomer taken in its final optimized geometry (configuration 1, blue), and (*iii*) in the isolated Nafion monomer in its initial geometry (yellow). Comparing cases (*iii*) and (*ii*) isolates the effect of structural distortion of the monomer, while the change from (*ii*) to (*i*) captures the additional impact of charge transfer between Pt, water, and Nafion. In the isolated monomer, O1 and O2 are equivalent and therefore display very similar LDOS (yellow areas in panels (b) and (c)), whereas O3 already differs because it is the oxygen bonded to the acidic hydrogen. For O1 and O2, structural relaxation [case (*iii*) $\rightarrow$ (*ii*)] broadens and separates the peaks and shifts them slightly to higher energies. When the monomer is brought into contact with the hydrated Pt surface [case (*ii*) $\rightarrow$ (*i*)], these peaks move further upward, and two narrow features appear at the Fermi level. This behavior reflects hybridization between the O *p* states and the Pt surface states, mediated by the water molecules that bridge the sulfonate group and the metal; the Fermi-level peaks correspond to these hybridized interfacial states.

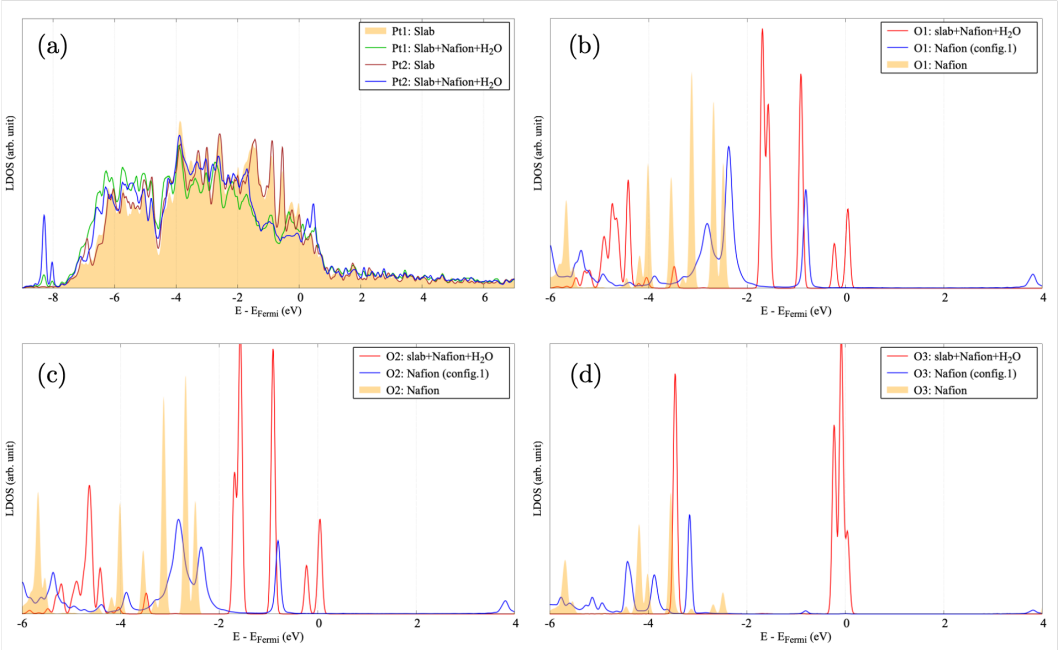

Fig. 4.18: Local density of states (LDOS) for (a) the selected Pt surface atoms and (b–d) the three oxygen atoms of the –SO_3H group in configuration 1 of the hydrated Pt+H_2O+Nafion interface. Each panel compares the LDOS of the fully optimized interface with the isolated Pt slab and with the isolated Nafion monomer in both its initial and optimized geometries.

For O3 (panel (d)), the evolution of the LDOS is much more dramatic. In the final optimized interface, the OH group has detached from the sulfonic group and binds directly to the Pt surface, and the LDOS develops a strong concentration of states near the Fermi level.

The final spectrum is characterized by two intense peaks: one around -3.5 eV and another centered at the Fermi level. These narrow features arise from Pt–O bonding and antibonding states associated with the chemisorbed OH species, confirming that this oxygen atom plays a central role in the formation of strong interfacial bonds and in the redistribution of charge at the Pt/H_2O/Nafion interface.

❖ Config. 2

In configuration 2, the Nafion monomer is initially positioned with its –SO_3H group placed approximately 4 Å above the Pt(111) surface. The initial and optimized geometries are shown in Fig. 4.19, sections (a) and (b), respectively. Upon structural relaxation, the polymer drifts toward the metal surface, reducing the separation to about 2.8 Å, consistent with previously reported adsorption distances for sulfonate, containing fragments on Pt(111) [301]. During this process, the –SO_3H group transfers its proton to a neighboring water molecule, forming a hydronium ion (H_3O^+), while the –SO_3^- moiety remains bonded to the polymer backbone.

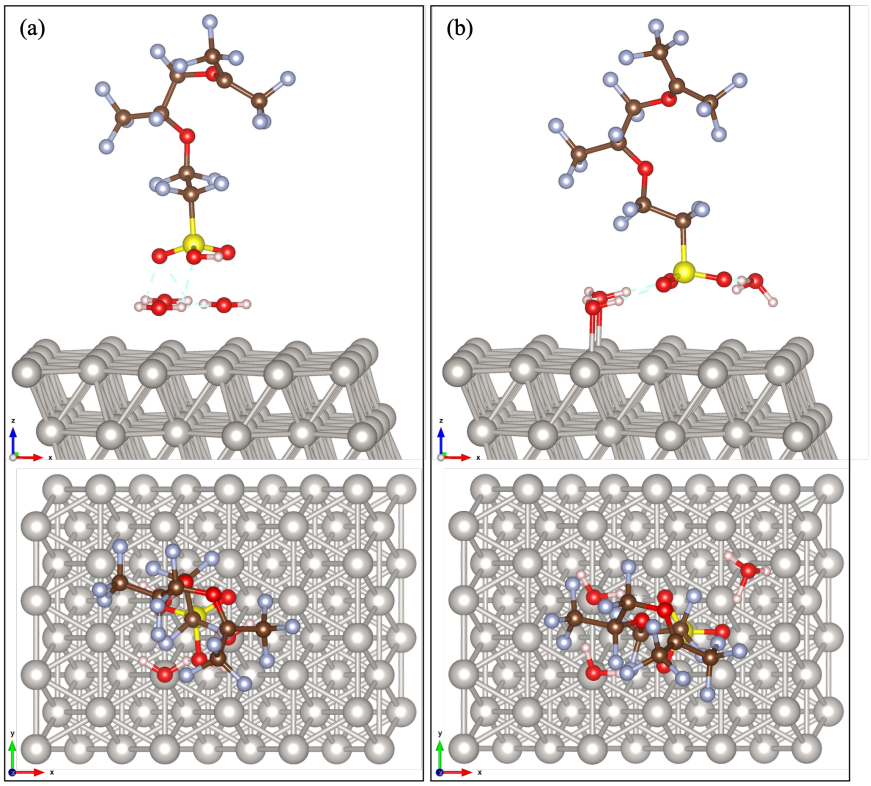

Fig. 4.19: (a) Initial structure of the Pt(111)–water–Nafion interface shown from the side view ($z-x$ plane) and top view ($y-x$ plane); (b) Corresponding optimized structure viewed from the same orientations. The Nafion monomer is initially placed at a distance of 4 Å from the Pt(111) surface. Gray: platinum atom; Yellow: sulfur atom; Silver: fluorine atom; Red: oxygen atom; Brown: carbon atom; Light-pink: hydrogen atom.

Unlike configuration 1 [see Fig. 4.16 (b)], the Pt surface in this configuration shows no major structural distortion, and the –SO_3 group preserves its original bonding geometry within the Nafion monomer. Two of the interfacial water molecules bind to Pt, forming Pt–O bonds of 2.14 Å and 2.27 Å. Fig. 4.20 presents the Bader charge analysis together with the corresponding three-dimensional CDD isosurface for configuration 2. In panel (a), the Bader charges,

computed from the charge density difference ($\Delta\rho$), quantify the net electron gain or loss for each atom. The results indicate that the surface Pt atoms undergo modest electron depletion, whereas atoms in the hydrated sulfonic region of Nafion, particularly those forming the H_3O^+ species and the oxygen atoms of the $-SO_3$ group, display noticeable electron accumulation. This pattern reflects a charge-transfer process mediated by the strong acidity of the sulfonic group and its hydrogen-bonding network under enhanced hydration.

Panel (b) shows the CDD isosurface, where yellow and cyan denote charge accumulation and depletion, respectively. The CDD reveals alternating regions of accumulation and depletion extending from the H_3O^+ molecule toward the sulfonate oxygens, indicating a continuous polarization pathway across the hydrated interface. The localized depletion around Pt1 and Pt2, combined with accumulation within the sulfonic domain, is fully consistent with the Bader trends and demonstrates how protonated water reshapes the electronic landscape at the Pt(111)/Nafion interface.

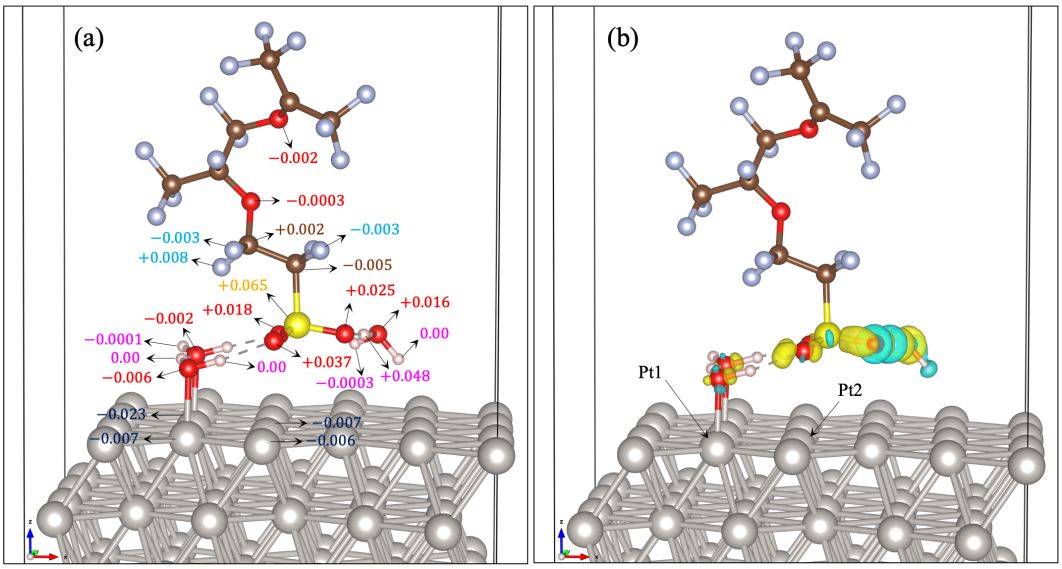

Fig. 4.20: (a) Bader charge distribution showing the net electron gain (positive values) and loss (negative values) for atoms within the Pt(111)/Nafion/H_2O interface. The values indicate moderate charge transfer from the surface Pt atoms toward the sulfonic group and interfacial water molecules. (b) Three-dimensional charge density difference (CDD) isosurface highlighting regions of electron accumulation (yellow) and depletion (cyan) (isosurface level is set as 0.008 e/Å^3). The CDD pattern reveals localized hybridization at the Pt1 and Pt2 sites and confirms the charge-redistribution trends observed in the Bader analysis.

In contrast to configuration 1, the LDOS of configuration 2 reflects the absence of a significant charge transfer from the Pt surface, consistent with the lack of structural distortion of the top Pt layers. Most of the electronic redistribution instead occurs within the hydrophilic region of Nafion, particularly around the sulfonate oxygens. The projected LDOS for the relevant atoms is shown in Fig. 4.21. Panel (a) reports the LDOS of Pt1 and Pt2 (the surface atoms indicated in Fig. 4.20). Both atoms exhibit nearly identical spectral features at and around the Fermi level, confirming that the presence of Nafion and interfacial water only weakly perturbs the metallic states. A slight reduction in the occupied states just below the Fermi level, accompanied by a small increase in the spectral weight around -4 eV, is visible for Pt1, but the overall d-band shape is essentially preserved.

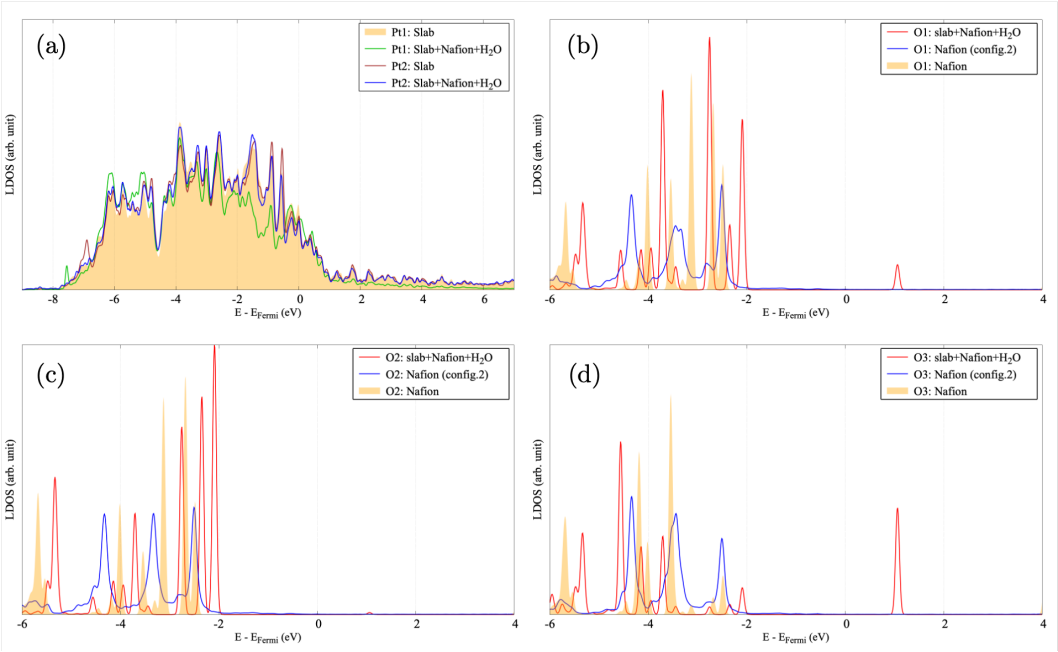

Fig. 4.21: Local density of states (LDOS) for (a) the selected Pt surface atoms and (b–d) the three oxygen atoms of the $–SO_3H$ group in configuration 2 of the hydrated $Pt+H_2O$+Nafion interface. Each panel compares the LDOS of the fully optimized interface with the isolated Pt slab and with the isolated Nafion monomer in both its initial and optimized geometries.

Panels (b)–(d) show the LDOS of the three oxygen atoms O1, O2, and O3 in the $–SO_3H$ group. Unlike configuration 1, none of the oxygen atoms display states at the Fermi level. Instead, all three exhibit a clear gap of approximately 3 eV between the highest occupied and lowest unoccupied states. In this configuration, the LDOS of O3 becomes more similar to those of O1 and O2 because its hydrogen atom has transferred to a water molecule, yielding a hydronium ion. Nevertheless, the peak intensities of O3 differ: the final occupied peak is smaller, while the onset of unoccupied states shows a more pronounced peak. This redistribution reflects an electron transfer from bonding to antibonding character across the Fermi level, consistent with O3 being the oxygen atom closest to, and most strongly influenced by, the hydronium ion formed during the optimization.

❖ Config. 3

In the third configuration, the Nafion monomer is initially placed with its $–CF_3$ side chain oriented toward the Pt(111) surface, with the closest carbon atom positioned approximately 2 Å above the metal. The initial and optimized geometries are shown in Fig. 4.22 (a) and Fig. 4.22 (b), respectively. After structural relaxation, the optimized structure shows that the presence of Nafion pushes the uppermost Pt layer slightly downward, with this displacement extending into the second Pt layer as well. This downward relaxation reduces the ability of the surface Pt atoms to interact uniformly with the H_2O molecules. As a result, only one water molecule remains strongly adsorbed, forming a Pt–O bond of 2.08 Å, while the remaining two water molecules shift farther from the surface, at distances of 2.4 Å and 3.5 Å, indicating much weaker interactions.

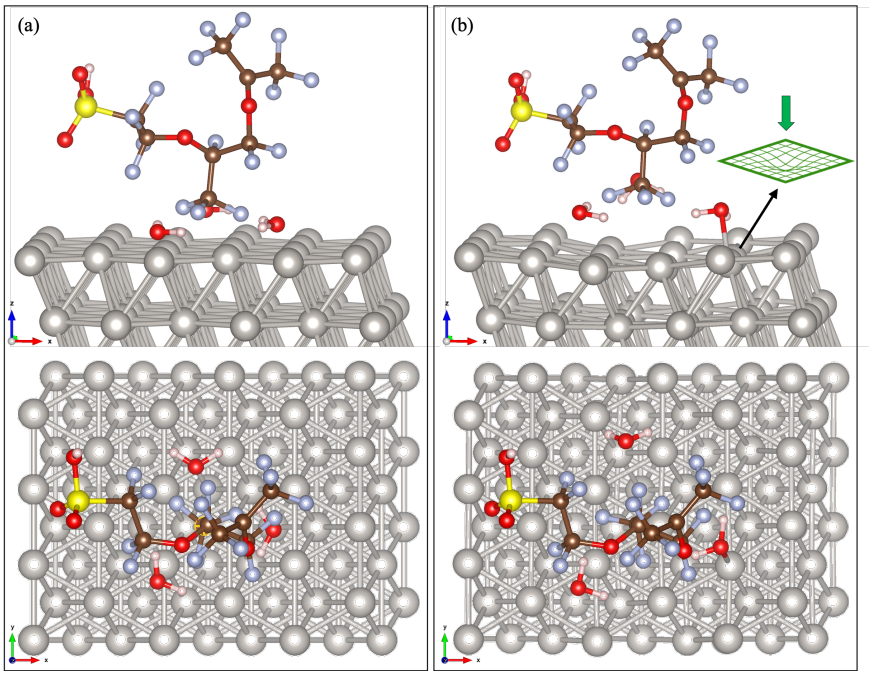

Fig. 4.22: (a) Initial structure of the Pt(111)-water-Nafion interface shown from the side view ($z - x$ plane) and top view ($y - x$ plane); (b) Corresponding optimized structure viewed from the same orientations. The Nafion monomer is initially placed toward the surface from its CF_3 side group. Gray: platinum atom; Yellow: sulfur atom; Silver: fluorine atom; Red: oxygen atom; Brown: carbon atom; Light-pink: hydrogen atom.

Using the same analysis applied to configurations 1 and 2, Fig. 4.23 shows the Bader charge distribution and the corresponding three-dimensional CDD isosurface for configuration 3, where the Nafion monomer approaches the Pt(111) surface through its CF_3 terminal group. As seen in panel (a), the Bader charges are extremely small for nearly all atoms, typically below $\pm 0.01\, e$, indicating that only negligible electron transfer occurs between the polymer, the interfacial water molecule, and the surface Pt atoms in this configuration. The CF_3 moiety, being highly electronegative and chemically inert, does not participate in strong interactions or charge-sharing pathways with the metal surface, and consequently, the electron redistribution around the sulfonic group is also minimal. Panel (b) displays the corresponding CDD isosurface, where the regions of electron accumulation (yellow) and depletion (cyan) are weak and spatially confined. The most noticeable features appear around the fluorine atoms (F1 and F2) and the adjacent Pt surface site (Pt1), but these perturbations remain localized and do not extend into the interfacial region, in contrast to configurations where the sulfonic group or H_3O^+ interacts directly with Pt. Taken together, the Bader and CDD analyses clearly demonstrate that the CF_3-oriented Nafion monomer exhibits the weakest electronic coupling to Pt(111), resulting in minimal charge redistribution at the interface in configuration 3.

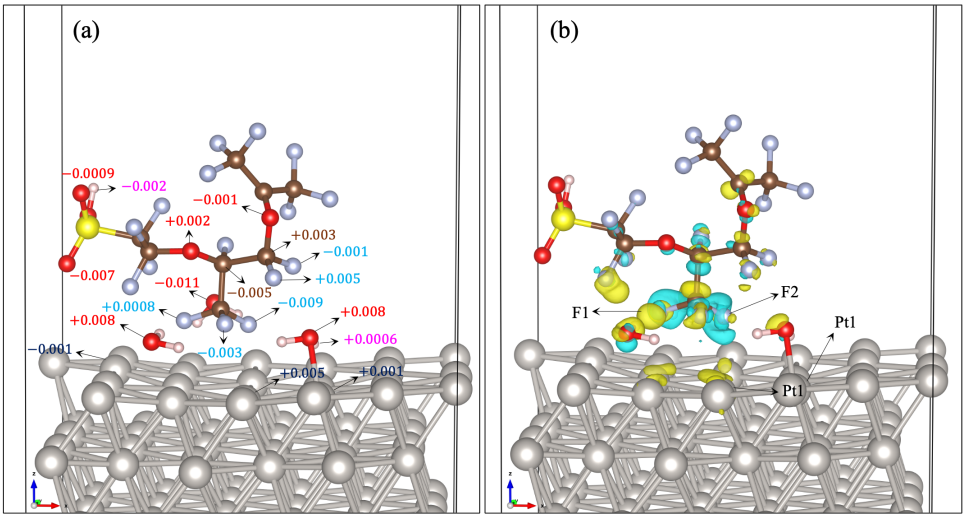

Fig. 4.23: (a) Bader charge distribution for the Pt(111)/Nafion/H_2O interface when the Nafion monomer is oriented toward the surface through its CF_3 group. The atomic Bader values show only very small electron gain and loss across Nafion, the interfacial water molecule, and the top Pt atoms, indicating weak charge transfer in this configuration. (b) Three-dimensional charge density difference (CDD) isosurface, highlighting regions of charge accumulation (yellow) and depletion (cyan) (isosurface level is set as 0.002 e/Å^3). The CDD is mainly localized around the fluorine atoms (F1, F2) and the nearby surface Pt atoms (Pt1), confirming the limited electronic coupling between the CF_3-terminated Nafion and the Pt(111) surface.

Fig. 4.24 (a–d) present the LDOS for selected atoms in configuration 3. Panel (a) displays the LDOS of the chosen Pt surface atoms. The Pt1 LDOS shows a noticeable depletion of states in the energy range between -2 and 0 eV and an enhancement of spectral weight around -6 eV, indicating a modest redistribution of d states upon interaction with Nafion and H_2O. In contrast, Pt2 exhibits only minor changes with respect to the clean slab, confirming that the perturbation of the metallic surface remains relatively localized.

To analyze the interaction of the –CF_3 group with the H_2O molecules and the Pt surface, two fluorine atoms of this group (F1 and F2) were selected for the LDOS analysis, as indicated by the arrows in Fig. 4.23 (b). Panels (b) and (c) show the LDOS of F1 and F2, respectively, while panel (d) reports the LDOS of the oxygen atom O3 of the sulfonic group. For both F1 and F2, the LDOS exhibits a characteristic trend: when only the structural distortion of Nafion is considered, the peaks shift to higher energies (green curves), whereas the inclusion of the full chemical environment (Nafion+H_2O+Pt) causes the LDOS to move back toward lower energies (red curves), relative to the isolated Nafion monomer (yellow curves). This behavior reflects the competition between intramolecular rearrangement and interfacial bonding. As expected, the LDOS of O3 shows only small shifts in all cases; in particular, the empty states at 1 eV (observed in configuration 2) and at the Fermi level (observed in configuration 1) are absent here, consistent with the weaker electronic coupling of the sulfonic group in this geometry.

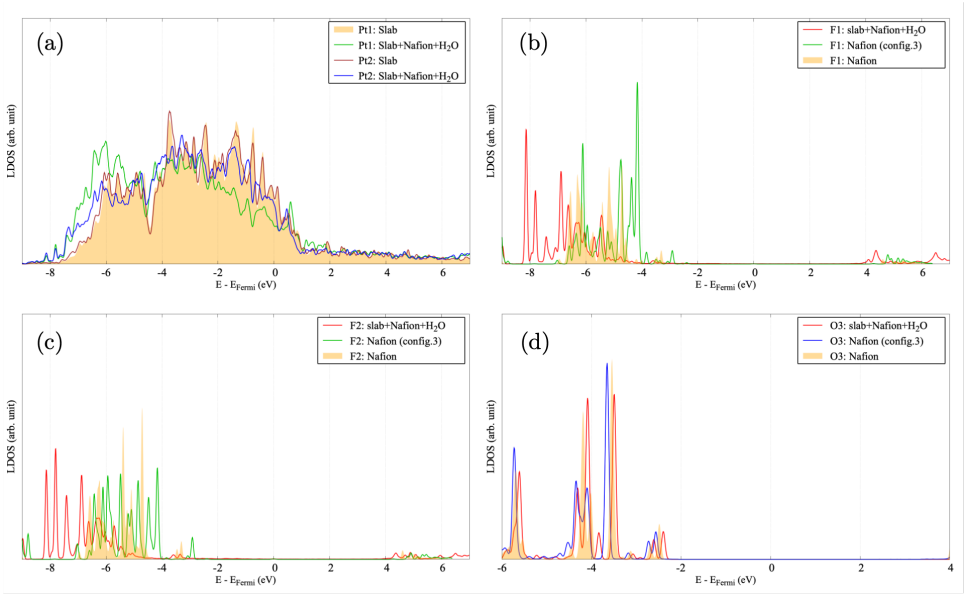

Fig. 4.24: Local density of states (LDOS) for configuration 3. Panel (a) LDOS of the selected Pt surface atoms. Panels (b) and (c) LDOS of the fluorine atoms F1 and F2 in the $–CF_3$ group. Panel (d) LDOS of the oxygen atom O3 of the sulfonic group. Each panel compares the fully optimized Pt+Nafion+H_2O interface with the isolated Pt slab and with the isolated Nafion monomer in both its initial and optimized geometries.

4.3 Interaction of Pristine Nafion with the Hydrated Pt Surface

To assess how chemical degradation affects the interfacial behavior of Nafion, the first configuration of the Pt+H_2O+Nafion system is now revisited using a pristine Nafion monomer containing all 17 fluorine atoms. The initial and optimized geometries of this configuration are shown in Fig. 4.25 (a) and (b), respectively. The optimized structure reveals several notable differences in the interfacial arrangement compared with the degraded Nafion system.

At the Pt surface, two water molecules remain adsorbed, each forming an O–Pt bond with lengths of 2.14 Å and 2.15 Å, consistent with typical molecular water adsorption on Pt(111). The third water molecule undergoes substantial chemical change: it loses both of its hydrogen atoms, one of which becomes bonded to the O1 atom of the Nafion $–SO_3H$ group, while the second hydrogen relocates beneath the sulfur atom at a distance of 1.38 Å, close to the characteristic S–H bond length of approximately 1.34 Å. The remaining oxygen atom of this dissociated water molecule adsorbs onto the Pt surface, forming an O–Pt bond in the range of 2.02–2.05 Å, indicative of a stronger interaction than that of intact water molecules. Overall, the optimized geometry shows that pristine Nafion promotes the dissociation of one interfacial water molecule and facilitates proton transfer toward the sulfonic acid group, while simultaneously maintaining strong O–Pt bonding at the surface. This behavior highlights the sensitivity of interfacial chemistry to the molecular integrity of Nafion and provides a direct structural basis for comparing degraded and pristine polymer environments.

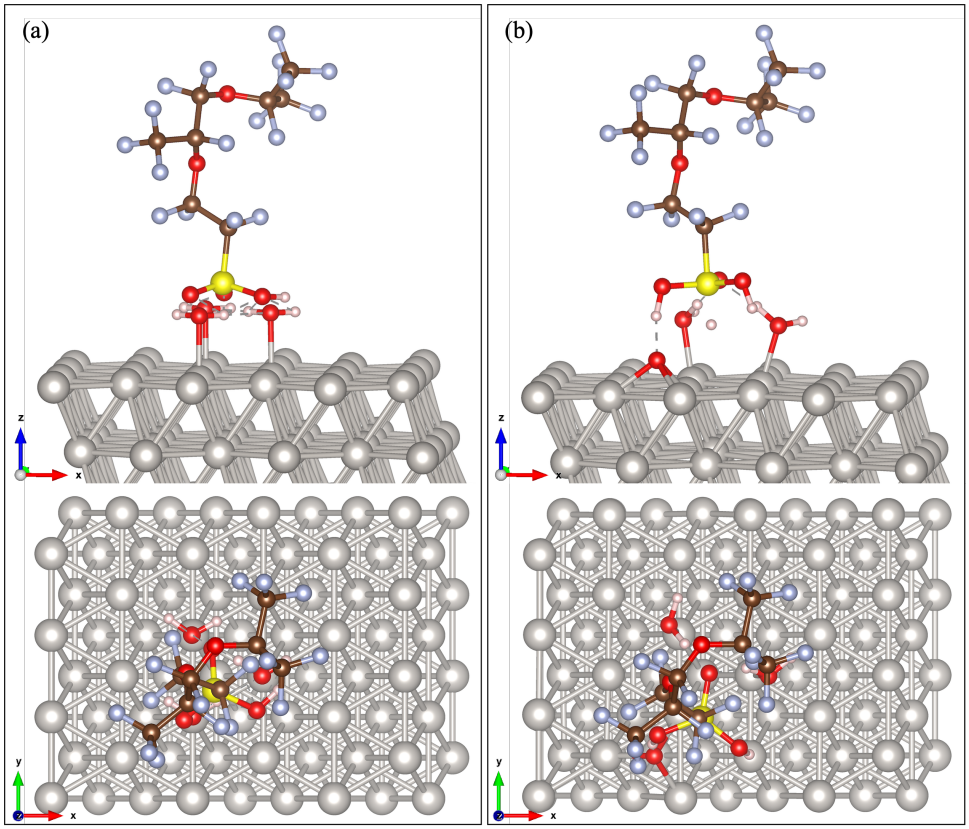

Fig. 4.25: (Initial (a) and optimized (b) geometries of configuration 1 for the Pt+H_2O+Nafion interface using pristine Nafion (17 fluorine atoms). Upon optimization, two water molecules remain molecularly adsorbed on the Pt surface, while the third water molecule dissociates: one hydrogen transfers to the O1 atom of the –SO_3H group and the second hydrogen binds beneath the sulfur atom. The oxygen of the dissociated water adsorbs onto the Pt surface with an O–Pt bond length of 2.02–2.05 Å. Gray: platinum atom; Yellow: sulfur atom; Silver: fluorine atom; Red: oxygen atom; Brown: carbon atom; Light-pink: hydrogen atom.

Fig. 4.26 illustrates the charge density difference (CDD) at the interface between Pt(111), H_2O molecules, and pristine Nafion. The green and yellow isosurfaces (isosurface level: 0.008) represent regions of charge accumulation and charge depletion, respectively. Pronounced charge rearrangement appears around the water molecules adsorbed on the Pt surface and around the oxygen atoms interacting with these molecules. The spatial distribution of these isosurfaces highlights the localized nature of the Pt–O interactions formed upon adsorption and the proton-transfer events occurring at the Nafion side chain. Two Pt atoms at the surface, labeled Pt1 and Pt2, are indicated in the figure; these atoms are selected for the LDOS analysis discussed in the following section.

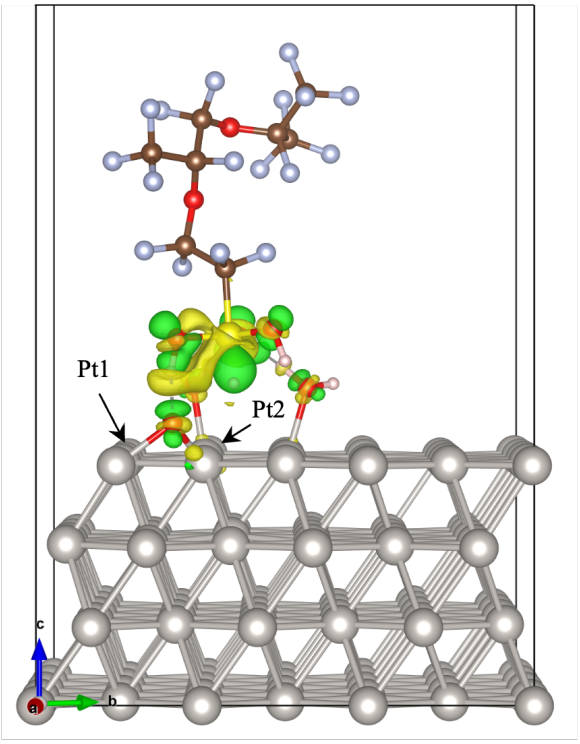

Fig. 4.26: Charge density difference (CDD) at the Pt(111)/H_2O/pristine-Nafion interface. Green and yellow isosurfaces (isosurface level: 0.008) indicate charge accumulation and depletion, respectively. The highlighted Pt surface atoms (Pt1 and Pt2) are selected for the LDOS analysis presented in the subsequent figure. Gray: platinum atom; Yellow: sulfur atom; Silver: fluorine atom; Red: oxygen atom; Brown: carbon atom; Light-pink: hydrogen atom.

Fig. 4.27 shows the LDOS of the two Pt surface atoms indicated by arrows in Fig. 4.26, comparing their electronic structure in the presence of pristine Nafion (17 fluorine atoms) and degraded Nafion (16 fluorine atoms). In both systems, the LDOS retains the characteristic Pt(111) *d*-band shape extending from approximately -8 eV to the Fermi level, indicating that the metallic character of the surface is preserved. However, subtle differences emerge in the way the electronic states are redistributed. In the pristine-Nafion interface, only minor deviations from the clean slab are observed, with slight enhancements around -6 eV and -3.5 eV and almost no perturbation near the Fermi level. By contrast, the degraded-Nafion system induces a more significant reshaping of the Pt LDOS: the spectral weight decreases in the region between -2 and 0 eV, while additional density accumulates in the lower-energy part of the *d*-band (around -6 to -4 eV). These differences indicate that degraded Nafion interacts more strongly with the Pt surface, leading to a more pronounced redistribution of Pt *d*-states compared with the pristine polymer.

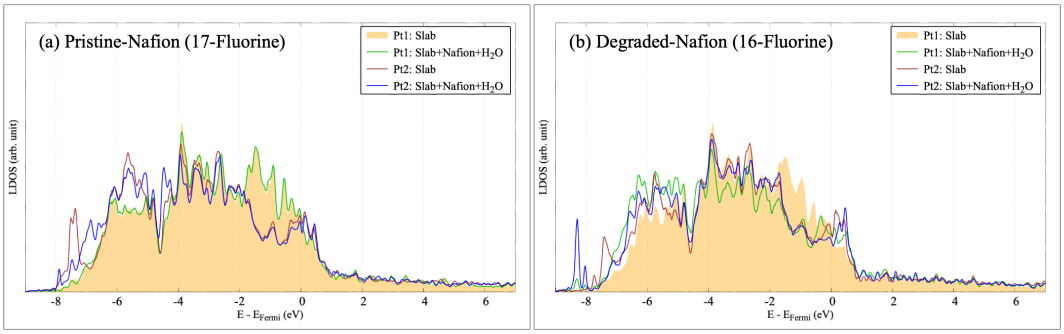

Fig. 4.27: Local density of states (LDOS) of the two selected Pt surface atoms for pristine Nafion (17 fluorine atoms) and degraded Nafion (16 fluorine atoms). The LDOS of the full Pt+Nafion+H_2O interfaces is compared with that of the isolated Pt slab to highlight the differences in electronic redistribution induced by pristine and degraded polymer environments.

Fig. 4.28 (a, c, and e) show the LDOS of the three oxygen atoms (O1, O2, and O3, respectively) in the –SO_3H group for the system with pristine Nafion (17 fluorine atoms), while panels (b, d, and f) report the corresponding LDOS for the degraded Nafion monomer (16 fluorine atoms). In the pristine case, all three oxygens exhibit a clear gap of about 2–3 eV around the Fermi level, with the highest occupied states located below $E - E_{Fermi} \approx -1$ eV and the lowest unoccupied states above $E - E_{Fermi} \approx 1$ eV. This behavior is consistent across O1, O2, and O3 and is preserved when going from the isolated Nafion monomer (yellow) to the optimized monomer geometry (blue) and to the full Pt+Nafion+H_2O interface (red), indicating that pristine Nafion maintains an electronically insulating character at the sulfonic group even in contact with the metal and water. In the degraded Nafion system (right column), the LDOS of the same oxygen changes more dramatically. For O1 and O2 [Fig. 4.28 (b) and (d)], the main occupied peaks shift closer to the Fermi level and additional spectral weight appears within the gap region, so that the red curves for the full interface now display states extending up to, and in some cases across, E_{Fermi}. The effect is even more pronounced for O3 [panel (f)], where sharp peaks arise around $E - E_{Fermi} \approx -1$ eV and near the Fermi level, reflecting stronger hybridization with the Pt and water states. Overall, the comparison between pristine and degraded Nafion shows that degradation narrows or closes the gap at the Fermi level for the sulfonate oxygens, promoting the formation of interfacial states that can participate in charge transfer processes at the Pt/Nafion interface.

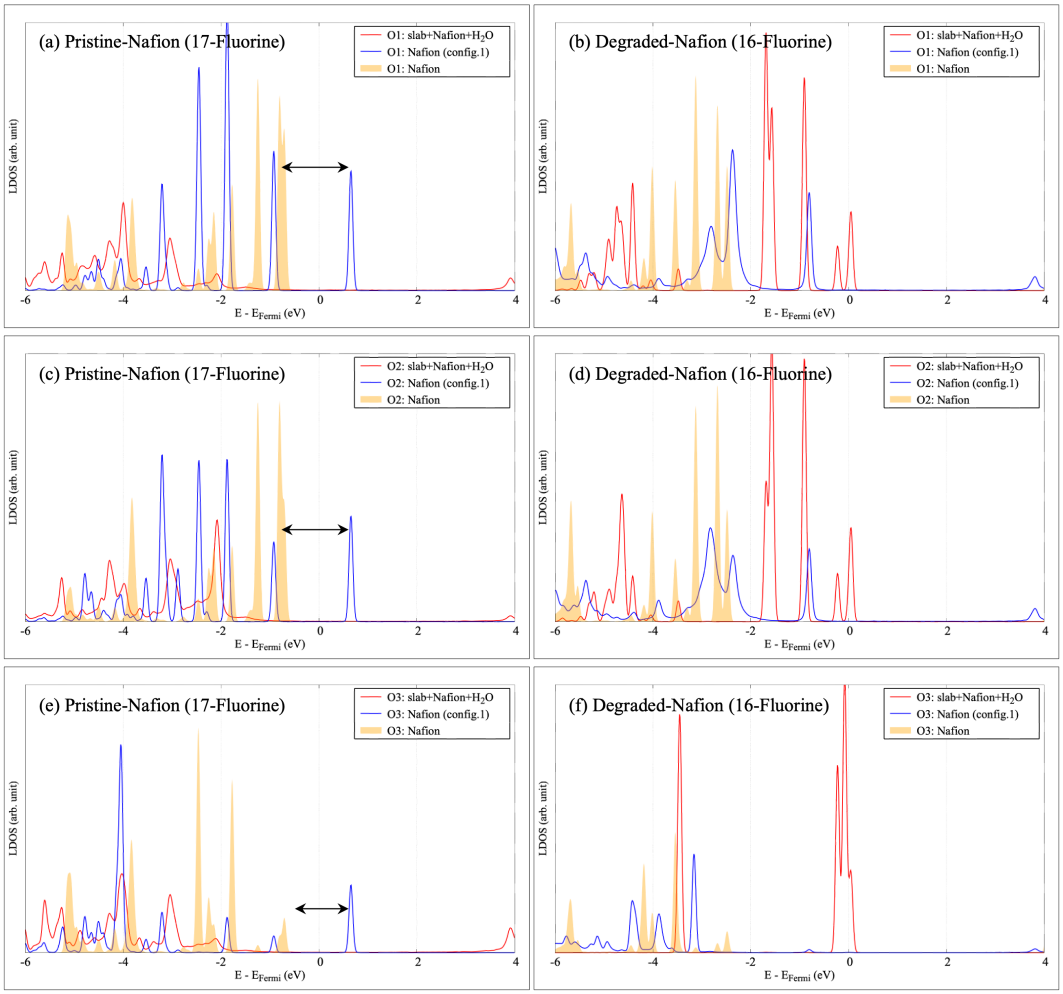

Fig. 4.28: Local density of states (LDOS) of the three oxygen atoms (O1, O2, O3) in the –SO_3H group for pristine Nafion (17 fluorine atoms, left panels) and degraded Nafion (16 fluorine atoms, right panels). Each plot compares the LDOS of the full Pt+Nafion+H_2O interface with those of the isolated Nafion monomer in its initial and optimized geometries, illustrating the changes in electronic structure induced by polymer degradation.

4.4 Discussion

Table 4.1 provides the interaction energy (eV) and total energies (Ry) of each system. The interaction energy between Nafion and hydrated Pt(111) was evaluated as:

$$E_{int}(eV) = E_{Pt+H_2O+Nafion} - (E_{Pt+H_2O} + E_{Nafion}) \qquad \text{(Eq. 4.2)}$$

The calculated interaction energies at low hydration ($\lambda = 3$) establish a clear hierarchy of interfacial binding strengths across the three configurations. Configuration 1 exhibits the most negative interaction energy (-8.83 eV), confirming a strong and direct coupling between the SO_3H group and the Pt(111) surface. This large binding strength is fully consistent with the pronounced charge transfer, formation of Pt–OH species, and significant surface distortion observed in the CDD, the Bader charge, and LDOS analyses. Configuration 2 shows an in-

termediate interaction energy (−4.42 eV), reflecting a water-mediated interface in which proton transfer to H_2O occurs without substantial electronic hybridization with the metal. This moderate binding supports the conclusion that hydrated Nafion–Pt contact is both structurally stable and energetically favorable. Configuration 3 exhibits the weakest binding (−1.46 eV), in line with the minimal charge transfer, absence of interfacial states near the Fermi level, and the predominantly hydrophobic character of the CF_3–Pt interaction. These quantitative results reinforce the electronic-structure trends: strong binding correlates with polymer and surface disruption (Config. 1), moderate water-mediated binding stabilizes the interface (Config. 2), and weak binding corresponds to electronically decoupled, hydrophobic contact (Config. 3).

Although configuration 2 possesses the lowest absolute total energy among the relaxed structures, configuration 1 yields the most negative interaction energy because the interaction term isolates only the adhesion between Nafion and hydrated Pt, removing the internal deformation energies of the individual subsystems. Thus, the stronger binding in configuration 1 arises from direct Pt–sulfonate coupling, whereas configuration 2 remains energetically favored overall due to minimal structural distortion of Nafion, Pt, and the interfacial water network.

Table 4.1: Interaction energy (eV) and final energy (in Ry) for all configurations at low hydration level ($\lambda = 3$).

Quantity	Config. 1	Config. 2	Config. 3
Interaction energy * (eV)	−8.8284 (pristine: −7.3091)	−4.4164	−1.4554
Final energy (Ry)	−26246.3725 (pristine: −26295.6421)	−26246.5271	−26246.1344

* *The interaction energies (eV) correspond to adsorption energies, following the standard DFT definition:* $E_{\text{ads}} = E_{\text{system}} - (E_{\text{surface}} + E_{\text{adsorbate}})$.

The interfacial behavior predicted by our DFT calculations is in close agreement with available experimental observations of Nafion–Pt contacts. For Configuration 1, the formation of Pt–OH species, electron depletion on surface Pt atoms, and partial detachment of the sulfonate group are consistent with operando and XPS measurements reporting Pt oxidation, Pt–O(H) formation, and strong ionomer-catalyst interactions under low-humidity conditions [312]. Although direct structural measurements of a single sulfonate group on Pt(111) are not available, EXAFS and XAS studies of ionomer-coated Pt nanoparticles reveal Pt–O coordination distances of 2.0–2.2 Å, matching the Pt–O separations obtained in our DFT optimizations. In Configuration 2, the preservation of the Pt electronic structure and the absence of Fermi-level hybridization with the sulfonate group agree with thin-film XPS measurements showing minimal S 2p and C 1s core-level shifts for hydrated Nafion on Pt, where the interaction is mediated by interfacial water rather than direct chemisorption. Furthermore, the proton-transfer pathway identified in Configuration 2, formation of H_3O^+ through water-mediated hydrogen-bond networks, is consistent with established proton-conduction models and spectroscopic evidence for Grotthuss-type proton hopping in hydrated Nafion [313]. Finally, the negligible charge transfer and insulating behavior of the $–CF_3$ termination in Configuration 3 reflect the known inertness of fluorinated polymer chains on noble metals, where adsorption is dominated by weak van der Waals forces and leads to minimal work-function modification. Together, these comparisons show that the three modeled configurations capture experimentally relevant regimes of the Nafion-Pt interface.

From a structural-stability perspective, Configuration 1 is particularly unfavorable. The Pt surface atoms undergo substantial lateral distortion and local volume expansion, while the

Nafion monomer shows clear degradation of its sulfonic acid group. This degradation likely results from the transfer of an OH fragment from the $–SO_3H$ group to the Pt surface, which increases the polymer–surface separation. Detachment of OH species may arise from the weakened sulfonate environment and/or proximity of water molecules, as suggested by the behavior observed when optimization begins from Configuration 2. Such interactions become increasingly probable at higher hydration levels, where water molecules compete for hydrogen bonding with the ionomer.

In Configuration 2, the H^+ transfer from Nafion to the electrode proceeds through interfacial water molecules. This mechanism is typically favored under high-hydration conditions, where aligned water molecules form a "water wire" capable of supporting proton transport via a hopping process between adjacent molecules [314]. Our results indicate that a similar mechanism can emerge even at low hydration, provided that a minimal hydrogen-bond network is present.

This mechanism likely involves stepwise proton hopping in which H^+ originating from the Nafion membrane transfers between neighboring water molecules before reaching the electrode surface. The self-reorganization ability of hydrated Nafion is often associated with its capacity to maintain continuous ionic channels, which support such proton migration. In the optimized structure, after proton transfer to a surface water molecule and subsequent formation of H_3O^+, the previously elongated C–S bond (2.10 Å) contracts to 1.89 Å, indicating that the sulfonate group returns to a stable and chemically intact configuration. However, while the relaxed geometry suggests retention of an undissociated $–SO_3H$ group, this should not be interpreted as evidence of a full self-healing process. DFT optimizations identify thermodynamically favorable minima but do not provide kinetic insight into sulfonate dissociation, radical formation, or reattachment pathways. Experimental studies show that hydrated Nafion exhibits partial reversibility of sulfonic acid dissociation and dynamic reorganization of ionic domains [233,313,315], consistent with our observation that hydration stabilizes an intact $–SO_3^-$ group. Thus, the structural recovery observed here is best understood as a favorable rearrangement under hydrated conditions rather than a long-timescale self-healing process.

The results also highlight the importance of the initial molecular configuration when modeling hydrated Nafion/Pt interfaces. When the Nafion monomer is placed close to the surface ($\approx$ 2.8 Å), the optimized structure exhibits repulsion, whereas placing it farther away ($\approx$ 4 Å) leads to attraction. Notably, the energetic pathways and structural mechanisms that drive relaxation differ between these cases. Among the three models, Configuration 3 exhibits the smallest charge transfer, likely due to the $–CF_3$-terminated interface. This outcome confirms that interfacial binding of Nafion to hydrated Pt occurs predominantly through the sulfonic acid group. In this configuration, the polymer is effectively repelled from the hydrated Pt surface, consistent with the weak, non-polar character of fluorinated terminal groups.

To visualize the detailed sequence of bond-breaking and bond-forming events occurring during structural relaxation, Fig. 4.29 illustrates the spontaneous transformation pathways for configurations 1 and 2 at two hydration levels ($\lambda = 3$ and $\lambda = 6$). For configuration 1, panels (a) and (b) show the atomic steps and corresponding energy drops under low and high hydration, respectively. At low hydration [Fig. 4.29 (a)], the water molecules rotate toward the surface, and the sulfonic group approaches the interfacial region. Limited water availability forces the $–SO_3H$ group to remain largely undissociated, enabling dehydration reactions that form sulfonic anhydrides ($–SO_2$) and hydroxyl radicals (OH). These OH species bind strongly to the Pt surface, consistent with the literature on sulfonic acid decomposition at metal interfaces [316, 317]. Subsequent steps involve hydrogen rearrangement, formation of new water molecules, and progressive degradation of the Nafion terminal group, as reflected by the elongated S–C bond lengths reported in Table 4.2.

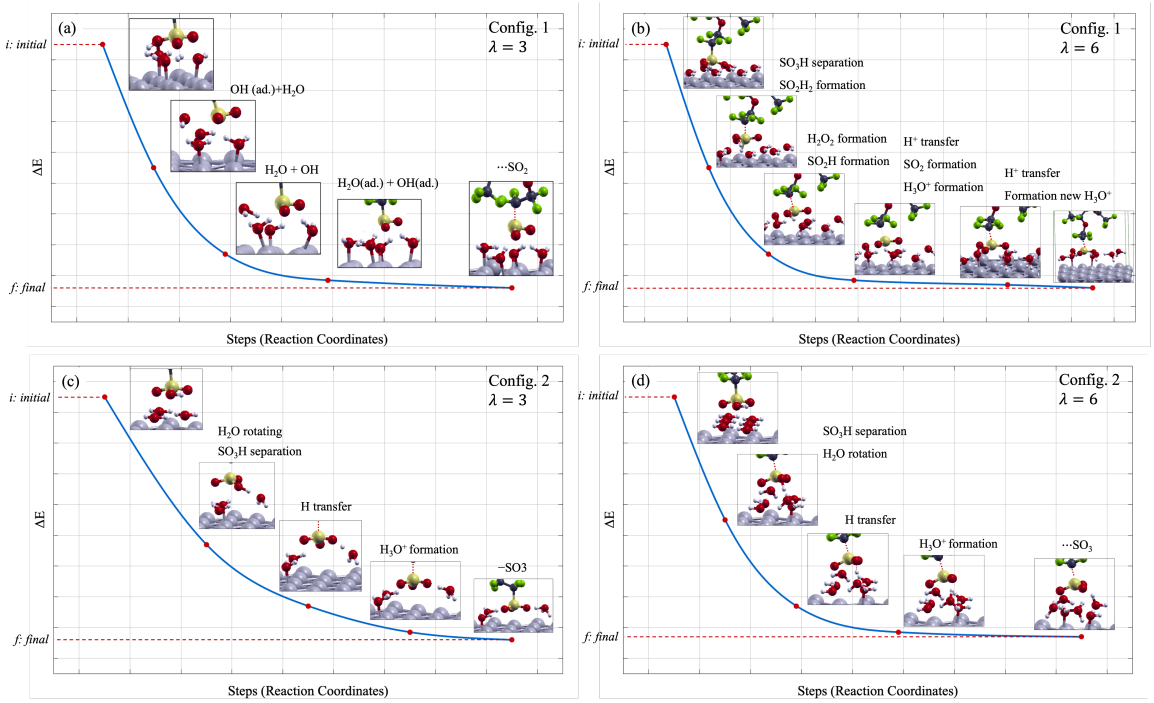

Fig. 4.29: Schematic of total energy differences (eV) between structures in the mechanism of (a) configuration 1 under low hydration level ($\lambda = 3$): OH formation and interaction with H_2O and SO_3H group separation, (b) configuration 1 under high hydration level ($\lambda = 6$): H_2O_2 formation and Grotthuss mechanism, (c) configuration 2 under low hydration level ($\lambda = 3$): approaching of Nafion to the surface, Nafion modification, and formation of H_3O^+, and (d) configuration 2 under high hydration level ($\lambda = 6$): SO_3H detachment and formation a H_3O^+. Gray: platinum atom; Yellow: sulfur atom; Green: fluorine atom; Red: oxygen atom; Dark-blue: carbon atom; Light-pink: hydrogen atom.

At high hydration [Fig. 4.29 (b)], an early detachment of the –SO_3H group occurs, forming SO_2H and eventually SO_2 species. Water molecules participate in forming H_2O_2 and hydronium ions, and proton transfer progresses along water chains through a Grotthuss-type mechanism. Water molecules that stabilize on the Pt surface adopt O–Pt distances of 2.15 Å to 2.40 Å, while others move away and realign to continue proton hopping.

Table 4.2: Bond lengths (Å) for Pt–O, S–O, and S–C in various configurations.

Bond Type	**C1 ($\lambda = 3$)**	**C1 ($\lambda = 6$)**	**C2 ($\lambda = 3$)**	**C2 ($\lambda = 6$)**	**C3 ($\lambda = 3$)**
Pt–O	2.10	2.40	2.27	2.09	2.08
S–O	1.53	1.51	1.46	1.45	1.42
S–C *	2.06	1.97	1.89	1.93	1.84

* *Reference S–C bond length in isolated Nafion is 1.89 Å.*

For configuration 2, the corresponding mechanistic steps are shown in Fig. 4.29 (c) and (d). At low hydration [panel (c)], the initial rearrangement of water molecules facilitates proton extraction from the –SO_3H group, forming a hydronium ion. The remaining SO_3^- group strengthens its bonding to the positively charged polymer backbone, preserving structural integrity. The resulting S–C bond length (1.89 Å) matches the expected value for an intact sulfonic

group. At high hydration [panel (d)], similar steps occur, but only one hydronium ion forms and no subsequent proton hopping chain is observed, unlike configuration 1. Here, the main hydration-dependent difference is a slight elongation of the S–C bond from 1.89 Å to 1.93 Å, suggesting partial, but not complete, weakening of this linkage. Overall, these results demonstrate that hydration level, interfacial geometry, and the nature of the Nafion functional group collectively govern the stability, charge-transfer behavior, and chemical pathways of the hydrated Pt/Nafion interface.

To disentangle the effects of polymer degradation from intrinsic polymer–surface interactions, a reference comparison with pristine Nafion is essential. In the pristine case, the monomer remains at a larger equilibrium distance from the hydrogen-covered Pt surface, and no significant deformation of the metal slab is observed. The reaction pathways are correspondingly smoother, characterized by limited charge rearrangement and the absence of spontaneous bond breaking or pronounced proton-transfer events. This behavior contrasts sharply with the degraded Nafion configurations, where enhanced interfacial polarization and structural rearrangements are evident.

Although the chemical modification involves the loss of a single fluorine atom from the Nafion backbone, its impact on the optimized interfacial structure is substantial. The removal of fluorine locally disrupts the highly electronegative and insulating character of the polymer, introducing a more polarizable site that reduces electronic screening and enhances coupling between the sulfonic group and the Pt surface. This localized change in electronic structure amplifies charge redistribution at the interface, facilitating stronger polarization effects and, in some configurations, inducing surface deformation and reactive pathways that are absent in pristine Nafion. These findings highlight how seemingly minor chemical defects can qualitatively alter polymer–metal interactions through electronic-structure-driven mechanisms.

❖ **Summary:**

Config. 1 – sulfonate directly on Pt:

This configuration exhibits the strongest electronic coupling among the three models. The sulfonic acid group of Nafion interacts directly with the Pt surface, driving substantial charge transfer from Pt atoms to interfacial oxygen species (sulfonate and water), as shown by CDD and Bader analyses. The LDOS reveals the emergence of new occupied states near the Fermi level at the sulfonate oxygen sites and at Pt–OH bonds, confirming significant orbital hybridization. This redistribution of charge destabilizes both the polymer end group and the metal surface: Pt atoms are drawn outward, and the sulfonate begins to dissociate. Although this configuration promotes reactive Pt–OH formation, it does so at the cost of polymer degradation and surface disruption, consistent with previous reports of sulfonate-induced Pt oxidation and membrane instability [316].

Config. 2 – hydrated interface:

In this configuration, interfacial water mediates the Nafion–Pt interaction, producing a more stable and electrostatically governed interface. Proton transfer from the $–SO_3H$ group to water forms H_3O^+, creating a local dipolar arrangement, but no significant charge is withdrawn from Pt, whose LDOS remains essentially unchanged. The sulfonate group retains its insulating character, with no hybridization and no states appearing near the Fermi level. This moderated interaction preserves the structural integrity of both polymer and catalyst. Such behavior is in strong agreement with XPS studies showing minimal core-level shifts for hydrated Nafion

on Pt and with theoretical models emphasizing the role of interfacial water in enabling proton transfer without perturbing the electronic structure of the metal [318–320].

Config. 3 – hydrophobic $–CF_3$ contact:

When the $–CF_3$ terminal group faces the Pt surface, interfacial charge transfer becomes negligible. CDD analysis reveals only weak local polarization, and LDOS confirms that neither Pt nor $–CF_3$ orbitals contribute states near the Fermi level. The Pt–water interaction is simultaneously weakened, with only a single water molecule maintaining surface contact. The $–CF_3$ group remains electronically isolated and prevents hydrogen bonding or proton-transfer pathways from forming. This configuration, therefore, represents a weakly interacting, nonfunctional interface. While structurally benign, it is likely detrimental to catalytic performance due to the absence of both ionic and electronic coupling, consistent with earlier findings on inert fluoropolymer, metal interfaces showing minimal work function modification and no evidence of chemisorption [233].

**"The task is not so much to see what no one has yet seen,
but to think what nobody has yet thought,
about that which everybody sees."**

— Erwin Schrödinger —
Nobel Prize Laureate in Physics – 1933

5. Interfacial Behavior of PVDF Binders on Oxidized Silicon for LIB Anodes

The interfacial behavior of poly(vinylidene fluoride) (PVDF) binders on oxidized Si(110) surfaces is investigated through formation-energy calculations, structural relaxations, charge density differences (CDD), and local density of states LDOS analysis. The study first evaluates how oxygen coverage stabilizes the silicon surface, then examines adsorption of α- and β-PVDF, emphasizing the influence of polymer phase, molecular orientation, and surface functionalization. By contrasting the non-polar α-phase with the polar β-phase, the work highlights how dipole alignment, OH formation, and charge redistribution govern adhesion strength and interfacial stability. The comparison of both phases identifies the atomic-scale mechanisms most relevant for optimizing binder performance in next-generation silicon anodes.

❖ Chapter Outline

- **Formation and Adsorption Energy (Sec. 5.1)**
  - This section introduces the oxidation of the Si(110) surface through formation-energy analysis and quantifies PVDF–surface interactions by comparing adsorption energies across phases, orientations, and oxygen coverages.
- **Interfacial Behavior of α-PVDF on Oxidized Si(110) (Sec. 5.2)**
  - This section investigates how the non-polar α-PVDF chain accommodates oxidized Si surfaces, focusing on structural rearrangements and the modest charge redistribution revealed through CDD and LDOS calculations.
- **Interfacial Behavior of β-PVDF on Oxidized Si(110) (Sec. 5.3)**
  - This section explores the interaction of polar β-PVDF with oxidized Si(110), showing how dipole alignment and surface termination control adhesion strength and lead to more substantial electronic coupling at the interface.
- **Comparative Interfacial Behavior of α- and β-PVDF (Sec. 5.4)**
  - This section contrasts the two PVDF phases, clarifying how differences in polarity, orientation, and response to oxygen functionalization dictate their interfacial behavior and suitability as binders for silicon anodes.

5.1 Formation and Adsorption Energy

To investigate how surface oxidation modifies the reactivity of Si(110), the formation energy (E_{form}) was calculated for two different oxygen coverages using:

$$E_{form} = E_{(slab+O)} - E_{slab} - n_O E_O \quad \text{(Eq. 5.1)}$$

where $E_{(slab+O)}$ is the total energy of the oxidized slab, E_{slab} is the energy of the pristine Si(110) surface, n_O is the number of adsorbed oxygen atoms, and E_O is the energy of atomic oxygen evaluated from the energy per atom of O_2 in the same simulation cell. The calculated values reveal a clear stabilization trend: the formation energy decreases from -0.197 eV for a coverage of four oxygen atoms to -0.724 eV for a coverage of fourteen oxygen atoms. This increasingly negative formation energy indicates that oxidation progressively stabilizes the surface, mainly through saturation of Si dangling bonds.

Fig. 5.1 shows the initial and optimized configurations of the oxidized surfaces. Panels (a) and (b) correspond to the four-oxygen case, while (c) and (d) show the fourteen-oxygen configuration. In both systems, oxygen atoms insert into the surface by forming bridging Si–O–Si linkages. After optimization, the Si–O bond lengths fall within the range 1.62–1.73 Å, and the Si–O–Si angles ($\measuredangle$ SiOSi) span from 99.25° to 144.88°, consistent with sub-stoichiometric silicon oxides reported in the literature. Higher oxygen coverage leads to a denser and more connected network of these linkages, further contributing to surface stabilization.

With the oxidized surface characterized, the interaction between PVDF and Si(110)/O was examined by computing the adsorption energy (E_{ads}) for a variety of configurations according to:

$$E_{ads} = E_{(slab+binder+O)} - E_{(slab+O)} - E_{(binder)} \quad \text{(Eq. 5.2)}$$

where $E_{(slab+binder+O)}$ is the total energy of the combined binder+surface system, $E_{(slab+O)}$ is the energy of the oxidized slab alone, and $E_{(binder)}$ is the energy of the isolated binder evaluated in the same supercell. Table 5.1 summarizes the adsorption energies for both the α- and β-phases of PVDF, for two oxygen coverages, and for two molecular orientations (H-facing vs. F-facing). For comparison, the final column lists the adsorption energies on an oxygen-free Si(110) surface. The results confirm that oxidation substantially modifies the surface reactivity: in several cases, most notably for the α-phase on the 14-oxygen surface, oxygen dramatically enhances PVDF binding relative to the pristine silicon surface. This enhancement reflects the increased polarity and stronger interaction potential of the oxidized surface, where Si–O terminations can couple more effectively with the dipolar PVDF chains.

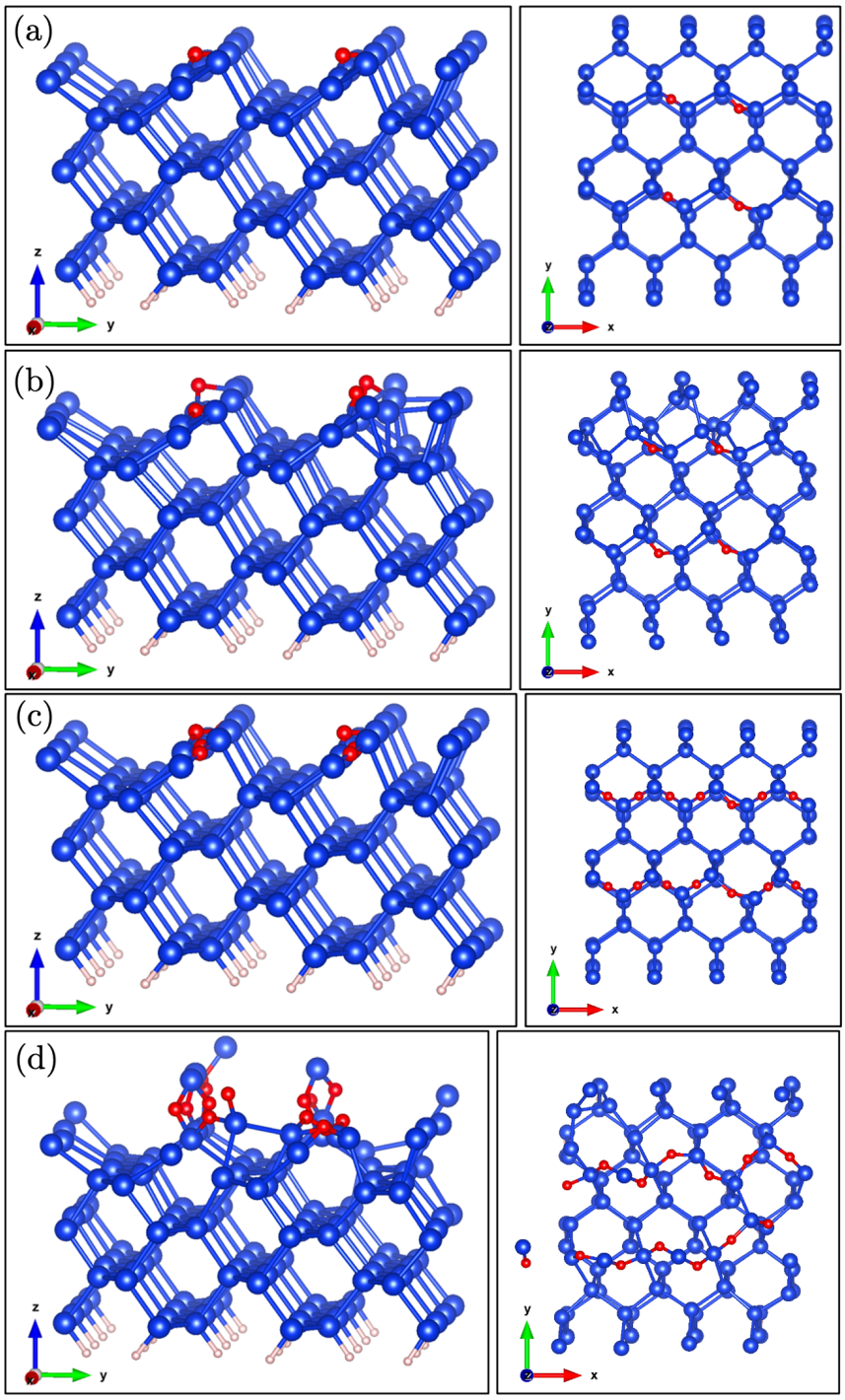

Fig. 5.1: $y-z$, and $x-y$ planar views of the Si(110) slab: (a) initial and (b) optimized structure of Si(110) with 4 atoms of oxygen at the surface. (c) initial and (d) optimized structure of Si(110) with 14 atoms of oxygen at the surface. Blue: silicon atom; Red: oxygen atom; Light-pink: hydrogen atom.

Table 5.1: Adsorption energy (eV) of selected minimum-energy configurations. The configurations include both the α and β phases of PVDF, two oxygen coverages, the surface-facing side (H/F), and the in-plane polymer orientation. The last column reports adsorption energies on O-free Si surfaces for comparison.

Si Surface	PVDF Phase	Oxygen Coverage	Side Facing	Direction	E_{ads} (eV)	E_{ads} (eV) (O-free)
Si(110)	α	4 oxygens	Fluorine	y	-0.690	-0.539
Si(110)	α	4 oxygens	Hydrogen	x	-0.540	-0.557
Si(110)	α	14 oxygens	Fluorine	xy	-2.463	-0.424
Si(110)	α	14 oxygens	Hydrogen	xy	-1.136	-0.538
Si(110)	β	4 oxygens	Fluorine	x	-0.303	-0.404
Si(110)	β	4 oxygens	Hydrogen	x	-0.781	-0.567
Si(110)	β	14 oxygens	Fluorine	y	-0.165	-0.331
Si(110)	β	14 oxygens	Hydrogen	x	-1.517	-0.568

Fig. 5.2 summarizes how the adsorption energy of PVDF on Si(110) varies with polymer phase (α vs. β), surface-facing group (H or F), and degree of oxidation, highlighting the strong dependence of interfacial binding on both the surface chemistry and the molecular structure of the binder. For the α-phase, the trend is remarkably systematic: independent of whether the hydrogen or fluorine side is oriented toward the surface, increasing oxygen coverage consistently strengthens adsorption. As seen in the figure, the adsorption energy of the fluorine-facing configuration becomes markedly more negative when the oxygen content increases from 4 to 14 atoms (from -0.690 to -2.463 eV), and a similar stabilization occurs for the hydrogen-facing configuration (from -0.540 to -1.136 eV). This monotonic behavior reflects the role of surface oxidation in saturating Si dangling bonds, thereby enhancing electronic coupling and producing stronger PVDF–Si interactions.

In contrast, the β-phase displays orientation-dependent adsorption behavior. When the hydrogen side of β-PVDF faces the surface, higher oxygen content again leads to stronger binding, with the adsorption energy decreasing from -0.781 eV at 4 oxygen atoms to -1.517 eV at 14 oxygen atoms. However, the fluorine-facing configurations show the opposite trend: adsorption weakens progressively with increasing oxygen coverage, evolving from -0.303 eV (4 oxygen atoms) to only -0.165 eV (14 oxygen atoms). As visible in Fig. 5.2, the fluorine-facing β-phase consistently occupies the region of weakest adsorption. This inversion arises because fluorine atoms preferentially bind to unsaturated Si dangling bonds; once oxygen passivates these reactive sites, the fluorine–Si interaction pathway is suppressed, leading to reduced adhesion. The behavior is further influenced by the intrinsic dipole of β-PVDF: when the hydrogen side faces the negatively polarized oxidized surface, the molecular and surface dipoles align attractively; when the fluorine side faces the surface, the dipoles oppose each other, generating a repulsive component that becomes stronger with increasing oxidation.

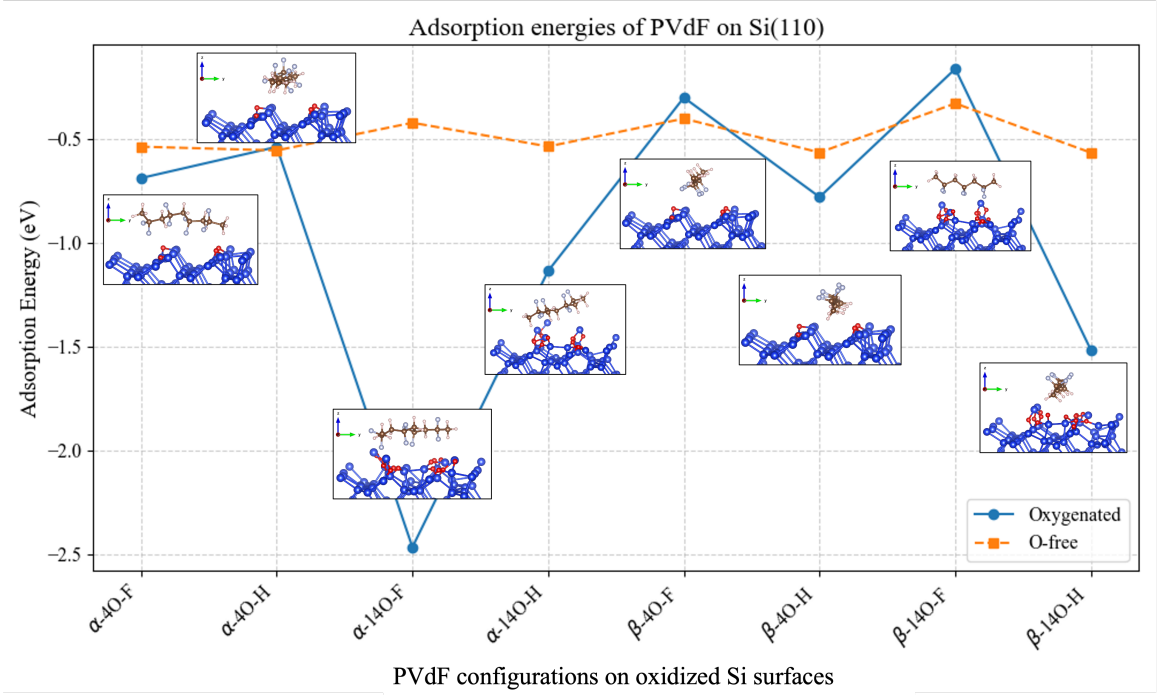

Fig. 5.2: Adsorption energies of α- and β-phase PVDF on Si(110) surfaces with different oxygen coverages, compared with O-free Si surfaces. The plot highlights the dependence of adsorption stability on binder phase, surface orientation (H/F side), and oxygen content. Blue: silicon atom; Red: oxygen atom; Light-pink: hydrogen atom; Gray: fluorine atom; Brown: carbon atom.

Taken together, the results in Fig. 5.2 show that oxidation does not simply strengthen or weaken adsorption. Instead, it introduces a highly selective response that depends on the polymer phase and on which molecular side approaches the surface. These findings underscore that optimizing PVDF–Si interfacial stability for LIB anodes requires not only controlling the oxygen content of the silicon surface but also accounting for binder orientation and phase-dependent dipole interactions.

5.2 Interfacial Response of Non-Polar α-PVDF on Oxidized Si(110)

The adsorption geometries of α-PVDF on oxidized Si(110) are presented in Fig. 5.3 (a–d). In panel (a): *i*, the polymer is initially placed on a surface containing four oxygen atoms, with its fluorine-rich side oriented toward the substrate. After structural relaxation, panel (a): *f* shows that the chain undergoes a noticeable rotation: the segment on the right tilts downward and adsorbs onto the surface, whereas the left portion is repelled, producing an asymmetric configuration.

In Fig. 5.3 (b), the optimized structure remains largely similar to the initial arrangement, indicating a comparatively weak interaction between the binder and the 4-oxygen surface. Only small distortions appear on the oxidized Si(110), where surface oxygen atoms form weak, non-covalent contacts with the hydrogen atoms of the polymer chain.

A very different behavior emerges when the number of oxygen atoms is increased to 14. Panels (c) and (d) show that the higher oxygen coverage induces substantial reconstruction of the Si surface, which begins to resemble a silica-like (SiO_2) morphology. The formation of multiple Si–O–Si bridges, with typical Si–O bond lengths around 1.6 Å, reflects the progressive

oxidation and partial transition toward an amorphous oxide network.

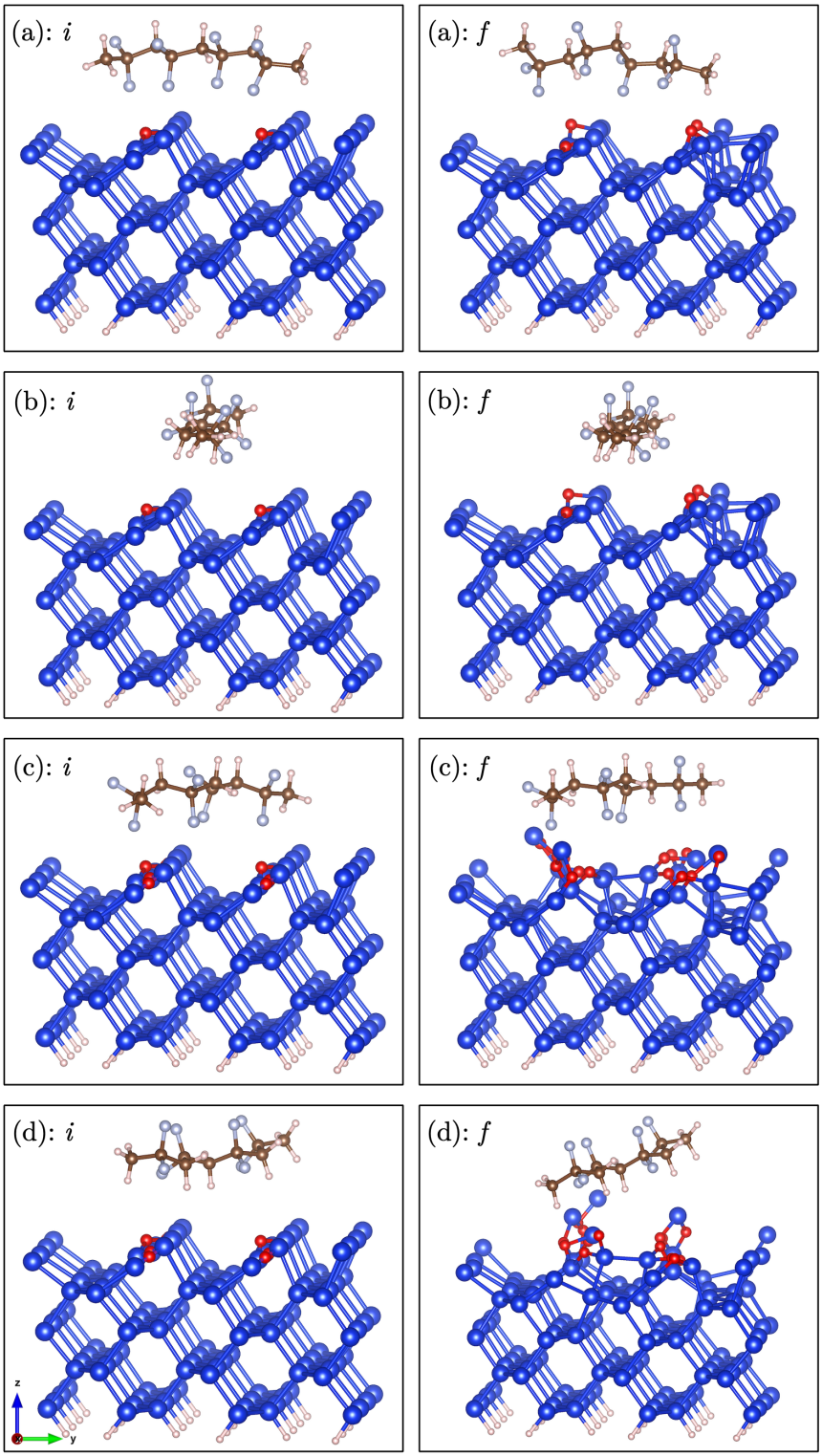

Fig. 5.3: Adsorption of α-PVDF with 4 oxygen atoms on the Si surface: (a) facing the fluorine side, (b) facing the hydrogen side. Adsorption with 14 oxygen atoms on the Si surface: (c) facing the fluorine side, and (d) facing the hydrogen side. i and f correspond to the $i$nitial and $f$inal structures. Blue: silicon atom; Red: oxygen atom; Light-pink: hydrogen atom; Gray: fluorine atom; Brown: carbon atom.

The interaction of the polymer with the surface also becomes more orientation-selective. When the fluorine side is directed toward the substrate, the binder tends to rotate during relaxation, indicating a preference for placing its hydrogen side closer to the oxidized surface. As shown in Fig. 5.3 (d), the optimized configuration reveals an asymmetric adsorption profile: the hydrogen atoms on the left side approach the silicon surface to approximately 3.53 Å, while those on the right side remain farther away at about 5.64 Å. This pattern reflects simultaneous attraction and repulsion across the polymer backbone, driven by the local distribution of surface oxygen and the polarity of the α-PVDF chain.

In the following section, the charge density difference (CDD) and local density of states (LDOS) are examined to provide deeper insight into the adsorption and binding mechanisms of PVDF on Si surfaces. These analyses allow us to assess charge transfer and interfacial electronic structure for both O-free and oxidized substrates, clarifying how surface chemistry influences the stability and interaction strength of the polymer-silicon interface.

Fig. 5.4 presents the LDOS obtained by summing the s- and p-orbital projections of a representative surface Si atom for all investigated configurations. The comparison proceeds from the clean Si surface (green shaded region), to the partially and fully oxidized surfaces (yellow curves), and finally to the surfaces interacting with α-PVDF, both in the absence (red curves) and presence (blue curves) of oxygen. Each panel corresponds to one of the four adsorption geometries shown earlier, and the insets highlight the region around the Fermi level, where the effects of oxidation and binding become most evident.

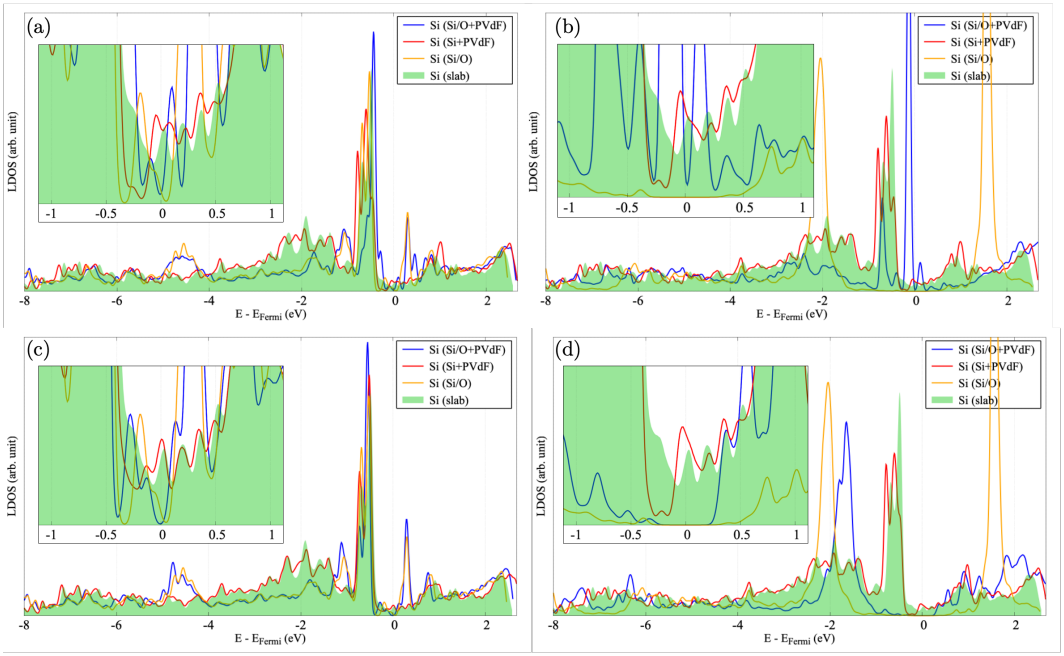

Fig. 5.4: Local density of states of a Si atom at the top of the surface in 4 different configurations as indicated in the legend. Filled green: on the pristine Si surface, yellow: on the oxidized Si surface, red: on the pristine Si surface with α-PVDF, blue: on the oxidized Si surface with α-PVDF. In panels (a) and (b), the oxidized surface includes 4 and 14-oxygen atoms, respectively, and the binder faces the surface with the fluorine side. In panels (c) and (d), the oxidized surface includes 4 and 14-oxygen atoms, respectively, and the binder faces the surface with its hydrogen side. In the insets, the focus is on the energy region of the Fermi level ($E - E_{Fermi} = 0$).

For the pristine Si surface, distinct peaks appear at the Fermi level (green shaded region), originating from under-coordinated Si atoms with unsaturated dangling bonds. These states

persist when α-PVDF is adsorbed on the O-free surface (red curves), indicating that the polymer alone does not passivate the reactive Si sites.

Upon oxidation, a clear suppression of the Fermi-level states is observed. In the partially oxidized structures [panels (a) and (c)], the intensity of these peaks is reduced but not fully eliminated, reflecting incomplete passivation of the surface. Full oxidation [panels (b) and (d)] completely removes the Fermi-level states (yellow curves), consistent with the formation of Si–O bonds that saturate the dangling bonds and stabilize the surface.

When α-PVDF is adsorbed onto the partially oxidized surfaces (blue curves in panels (a) and (c)), the LDOS remains essentially unchanged relative to the oxidized surface alone, revealing a weak interaction between PVDF and the Si(110)/O interface. The situation differs markedly for the fully oxidized surface. When the H-side of the binder faces the surface [panel (d)], a small but finite gap is preserved around the Fermi level, slightly narrower than in the binder's absence but still characteristic of a passivated, electronically stable interface. In contrast, when the F-side is oriented toward the fully oxidized surface [panel (b)], new states reappear at the Fermi level, indicating localized interfacial electronic states. These arise from Si–F interactions at the interface, as confirmed by the charge-density difference analysis in Fig. 5.5.

Overall, the LDOS analysis shows that while full oxidation stabilizes the Si(110) surface, it does not eliminate its chemical reactivity toward fluorinated PVDF segments. In contrast, interactions involving the hydrogen side of the polymer retain a more passivated electronic structure, suggesting a more benign and stable interface when the H-side is directed toward the oxidized silicon.

Fig. 5.5 (a, b, d, and e) displays the CDD for the four adsorption geometries of α-PVDF. The patterns reveal a complex distribution of charge accumulation and depletion, largely dictated by the intrinsic "TGTG" conformation of the polymer chain, which exposes alternating F and H atoms toward the Si(110) surface.

When the fluorine-rich side of the binder is oriented toward the surface [panel (a)], charge depletion appears on the underlying Si atoms, while charge accumulation is observed on the fluorine atoms, consistent with the strong electronegativity of F. Simultaneously, charge accumulation on surface oxygen atoms and depletion on neighboring H atoms suggest the presence of O–H dipolar interactions. Increasing the oxygen content on the surface [panel (b)] preserves this overall pattern but enhances the magnitude of charge accumulation near oxidized Si sites, indicating a more polarized interface.

When the hydrogen side faces the surface [panel (d)], the CDD pattern reverses: charge accumulates on the surface Si atoms while charge is depleted on the H atoms of the binder. This signature is consistent with weak Si–H interactions. At higher oxygen coverage [panel (e)], these effects become even more pronounced. The yellow charge-accumulation regions distributed on the surface oxygen atoms indicate stronger O–Si and O–binder interactions. Altogether, the CDD maps suggest that interfacial binding arises primarily through weak Si–H or Si–F charge transfer, modulated by the degree of surface oxidation.

These trends are further supported by the LDOS analysis in Fig. 5.5 (c) and Fig. 5.5 (f), which present the projected electronic densities of states for a representative fluorine atom (F-side adsorption) and hydrogen atom (H-side adsorption), respectively. For each case, three scenarios are compared: (*i*) adsorption on the O-free surface, (*ii*) adsorption on the partially oxidized surface (4 O atoms), and (*iii*) adsorption on the highly oxidized surface (14 O atoms). In all configurations, the PVDF-derived electronic states lie more than 3 eV below the Fermi level, well separated from the surface-derived states. This energetic separation confirms that PVDF binds through long-range electrostatic and van der Waals interactions, without significant hybridization with the Si or Si–O states at the Fermi level. The weak charge transfer inferred from the CDD is therefore consistent with the LDOS.

The evolution of peak positions with increasing oxidation shows opposite trends for F and H. For the F-facing configurations [panel (c)], the PVDF peaks shift to higher energies relative to the Fermi level as the oxidation level increases, reflecting reduced charge transfer as the surface becomes increasingly passivated. In contrast, for the H-facing configurations [panel (f)], the peaks shift to lower energies with higher oxygen content, indicating enhanced interaction of H with the more polarized oxidized surface. This is also reflected in the peak intensities between -4 eV and -3 eV: fluorine exhibits stronger interaction with the O-free surface (green curve), whereas hydrogen interacts more strongly with the highly oxidized surface (red curve).

Together, the CDD and LDOS analyses demonstrate that the nature and strength of the PVDF-Si(110) interaction depend critically on which side of the polymer faces the surface and on the degree of oxidation. Fluorine couples more strongly to unsaturated Si sites, whereas hydrogen interacts preferentially with oxidized regions, providing a microscopic explanation for the orientation-dependent adsorption energies discussed earlier.

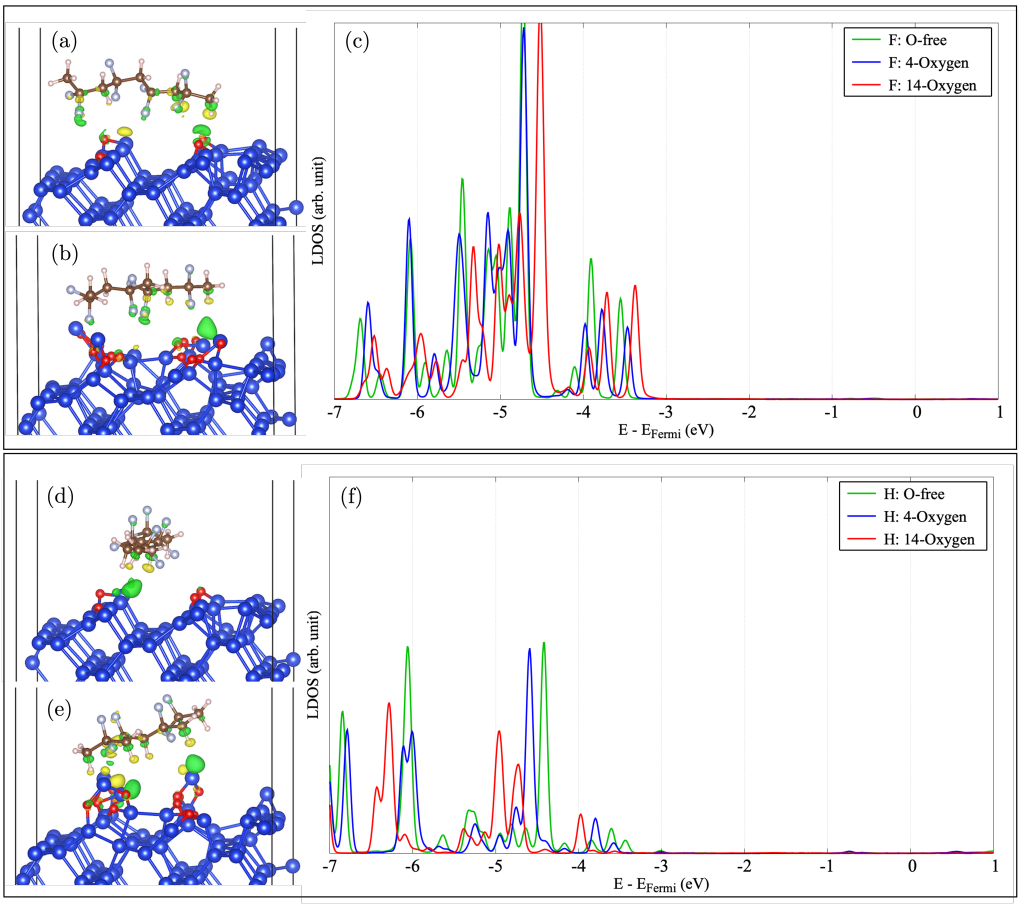

Fig. 5.5: Charge density difference ($\Delta\rho$) maps for the adsorption of α-PVDF on Si(110)/O surfaces with 4 and 14 oxygen atoms are shown in panels (a), (b), (d), and (e). In panels (a) and (b), the binder interacts with the surface through its fluorine side, while in panels (d) and (e) it faces the surface with its hydrogen side. Panels (c) and (f) report the LDOS of a representative fluorine atom (c) and hydrogen atom (f) of the binder for the O-free, 4-O, and 14-O surfaces. Green and yellow isosurfaces (isosurface level = 0.001 e/Å^3) indicate charge accumulation and depletion, respectively. Blue: silicon; red: oxygen; light-pink: hydrogen; gray: fluorine; brown: carbon.

5.3 Dipole-Mediated Adhesion of Polar β-PVDF on Oxidized Si(110)

A similar approach has been applied to investigate the adsorption behavior of the β-phase of PVDF. Unlike the α-phase, the β-phase adopts an all-trans ("TTTT") chain conformation, which presents a more uniform and extended molecular backbone. This regular geometry simplifies the interpretation of the interfacial interactions, since the polymer dipole and the orientation of its terminating groups remain well defined throughout the adsorption process.

The minimum-energy configurations of β-PVDF on Si(110)/O are shown in Fig. 5.6 (a–d). When the fluorine-rich side of the polymer is oriented toward the surface [panels (a) and (c)], the binder undergoes a noticeable rotational motion accompanied by a mild repulsion from the substrate. This behavior is reflected in the Si–F separation: the initial distance of approximately 3.023 Å increases to 3.388 Å after structural relaxation. At the same time, the oxidized Si(110) surface undergoes a partial reconstruction, forming O–Si–O bridge motifs reminiscent of the early stages of SiO_2 network formation. These structural adjustments are consistent with the reduced affinity of fluorine for an already oxygen-saturated surface, where Si dangling bonds are largely passivated.

In contrast, the configurations in Fig. 5.6 (b) and (d) reveal a distinctly different behavior when the hydrogen side of β-PVDF faces the surface. In these cases, the binder exhibits an attractive interaction with the substrate, drawing closer during relaxation. The Si–H separation decreases from an initial value of 3.129 Å to 2.77 Å in the optimized geometry, indicating a more favorable coupling between the hydrogen-terminated polymer surface and the oxidized Si sites. The absence of fluorine-facing repulsion and the presence of polarized O–Si bonds at the interface allow the H-terminated side of the polymer to align more effectively with the local electrostatic field of the surface.

Overall, the β-phase results reinforce the orientation-dependent nature of PVDF adsorption: fluorine-facing configurations tend toward repulsion and rotation, while hydrogen-facing configurations consistently stabilize the interface.

A similar analysis is performed for the β-phase of PVDF. Owing to its all-trans ("TTTT") backbone, the interpretation of the interfacial behavior becomes more direct than in the α-phase. The minimum-energy adsorption structures are shown in Fig. 5.6 (a–d). When the fluorine side faces the surface (panels (a) and (c)), β-PVDF undergoes a rotation during relaxation and experiences a net repulsion from the substrate. This repulsion manifests as an increase in the Si–F distance, which changes from an initial value of 3.023 Å to 3.388 Å after optimization. At the same time, the Si surface reconstructs, forming O–Si–O bridge units reminiscent of SiO_2. In contrast, when the hydrogen side interacts with the surface (panels (b) and (d)), the binder is attracted toward the substrate. The H–Si distance decreases from 3.129 Å initially to 2.77 Å, indicating a strengthening of the interfacial interaction.

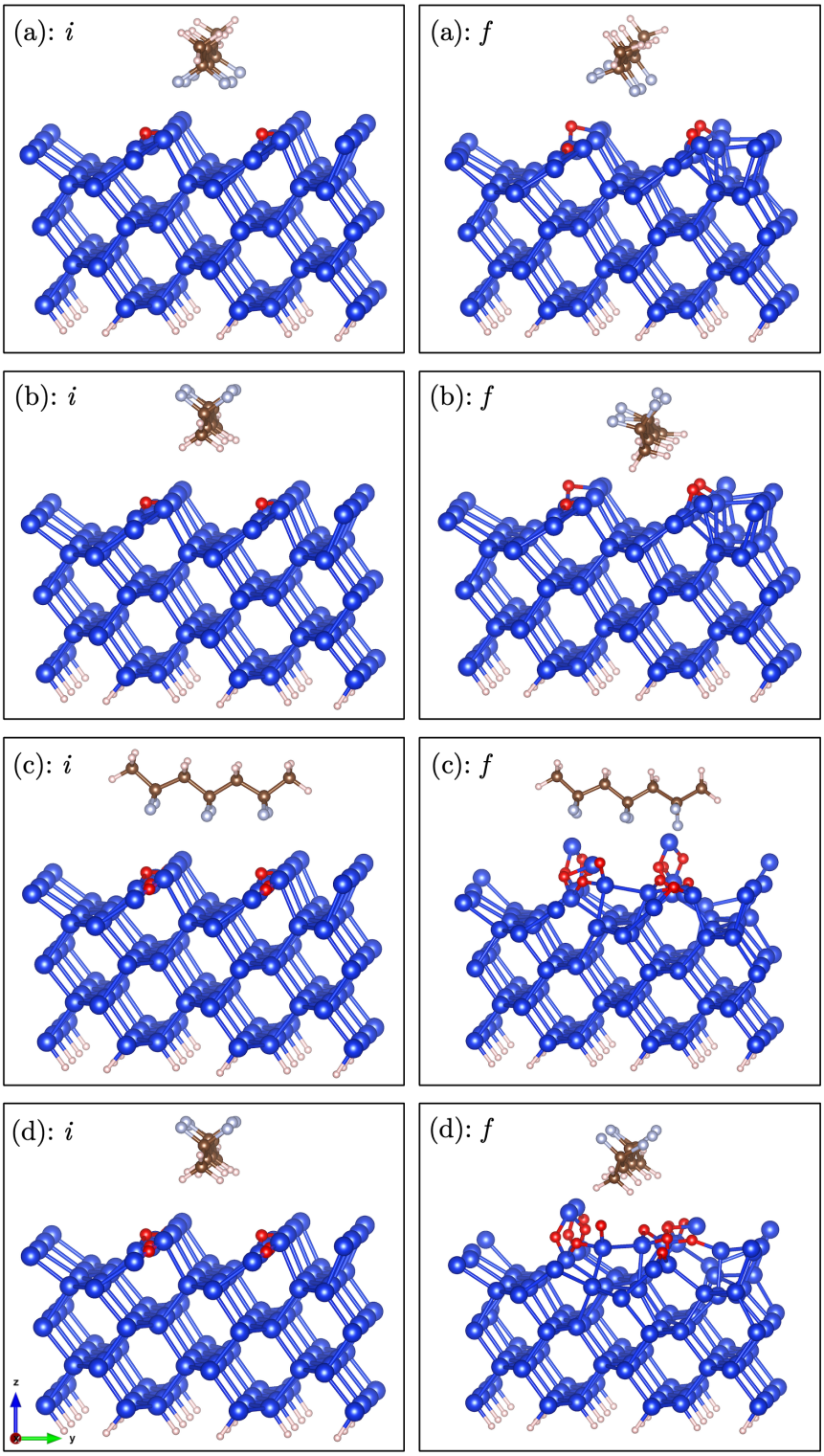

Fig. 5.6: Adsorption of β-PVDF with 4 oxygen atoms on the Si surface: (a) facing the fluorine side, (b) facing the hydrogen side. Adsorption with 14 oxygen atoms on the Si surface: (c) facing the fluorine side, and (d) facing the hydrogen side. i and f correspond to the $i$nitial and $f$inal structures. Blue: silicon atom; Red: oxygen atom; Light-pink: hydrogen atom; Gray: fluorine atom; Brown: carbon atom.

Fig. 5.7 presents the LDOS of a surface Si atom for these configurations. As in the α-phase,

the pristine Si surface (green area) exhibits characteristic peaks at the Fermi level due to the presence of under-coordinated surface Si atoms. These surface states progressively diminish as the oxidation level increases and completely disappear in the fully oxidized case (yellow line in Fig. 5.7 (b, and d)). When β-PVDF is adsorbed on the oxidized surfaces (blue lines), new states emerge near the Fermi level. These states are markedly more pronounced when the fluorine side faces the surface, reflecting Si–F bonding contributions [Fig. 5.7 (b)]. For the hydrogen-facing orientation, the interfacial states arise instead from Si–H and O–H interactions [Fig. 5.7 (d)], consistent with the attractive character of the relaxed structures.

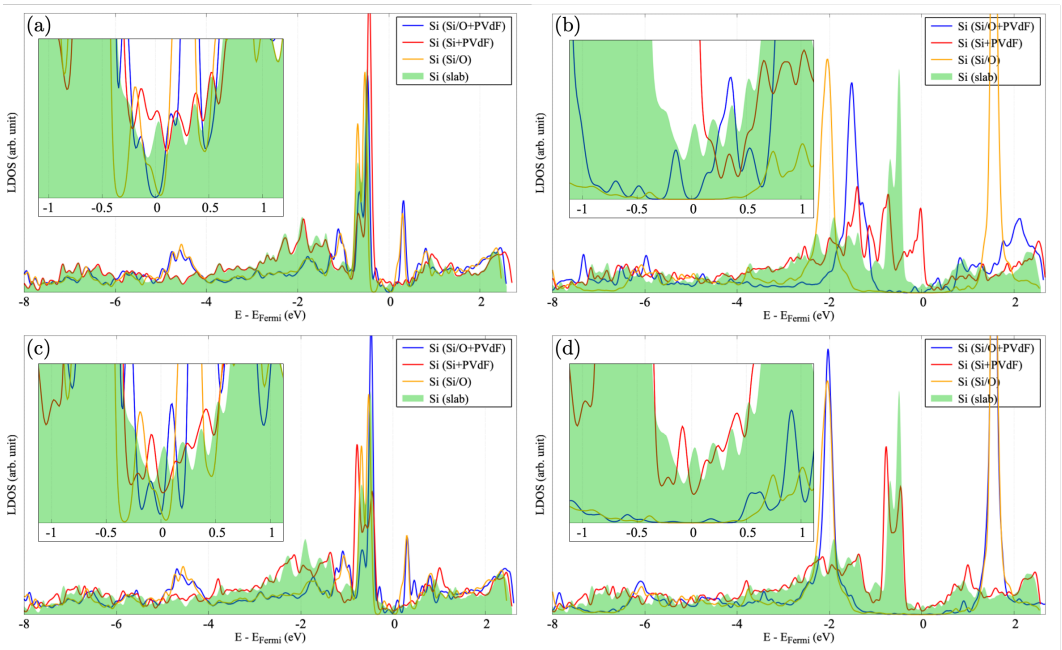

Fig. 5.7: Local density of states of a Si atom at the top of the surface in 4 different configurations as indicated in the legend. Filled green: on the pristine Si surface, yellow: on the oxidized Si surface, red: on the pristine Si surface with β-PVDF, blue: on the oxidized Si surface with β-PVDF. In panels (a) and (b), the oxidized surface includes 4 and 14-oxygen atoms, respectively, and the binder faces the surface with the fluorine side. In panels (c) and (d), the oxidized surface includes 4 and 14-oxygen atoms, respectively, and the binder faces the surface with its hydrogen side. In the insets, the focus is around the Fermi level ($E - E_{Fermi} = 0$).

The CDD maps in Fig. 5.8 (a, b, d, and e) further clarify the charge-transfer mechanisms. For the fluorine-facing cases [Fig. 5.8 (a, b)], both at 4 and 14 oxygen atoms, a modest charge depletion occurs on the interfacial Si atoms (yellow regions), accompanied by a small charge accumulation on a fluorine atom in the binder (green region). This pattern indicates weak but non-negligible Si–F interactions. Increasing oxygen coverage enhances the amount of charge localized on the oxygen-rich surface, consistent with reduced surface reactivity and the repulsive behavior seen in the relaxed structures.

When the hydrogen side faces the surface [Fig. 5.8 (d, and e)], the charge-transfer pattern changes significantly. Larger regions of charge depletion appear on the hydrogen atoms of the binder, while both Si and O atoms at the interface experience charge accumulation. This redistribution reflects a stronger and more direct Si–H interaction, which increases in magnitude with higher oxygen coverage.

These conclusions are reinforced by the projected LDOS of selected F and H atoms shown in Fig. 5.8 (c, and f). For the F-facing interface, the fluorine-projected states lie deep within

the valence band (below -4 eV), and their peaks shift to lower energies as the oxidation level increases. This shift results from an accumulation of electronic charge on fluorine, consistent with weakened binding and increasing adsorption energies on oxygen-rich surfaces.

Conversely, when hydrogen faces the surface [Fig. 5.8 (f)], the H-projected LDOS shifts upward in energy as oxygen coverage increases, with peaks gradually approaching the Fermi level. This trend signals a depletion of electronic charge on hydrogen, exactly what is observed in the corresponding CDD, and confirms the strengthening of the interfacial Si–H interaction. The progressively more negative adsorption energies in this orientation reflect this enhanced binding.

Overall, the β-phase exhibits a clear orientation-dependent interaction with the oxidized Si(110) surface: Si–F interactions weaken monotonically with increasing oxidation, whereas Si–H interactions strengthen, driven by charge transfer and the formation of partially ionic Si–H/O–H interfacial motifs. This strong contrast is visible across the structural relaxations, CDD patterns, and LDOS trends, and highlights the central role of polymer orientation in determining the stability and electronic character of PVDF–Si interfaces.

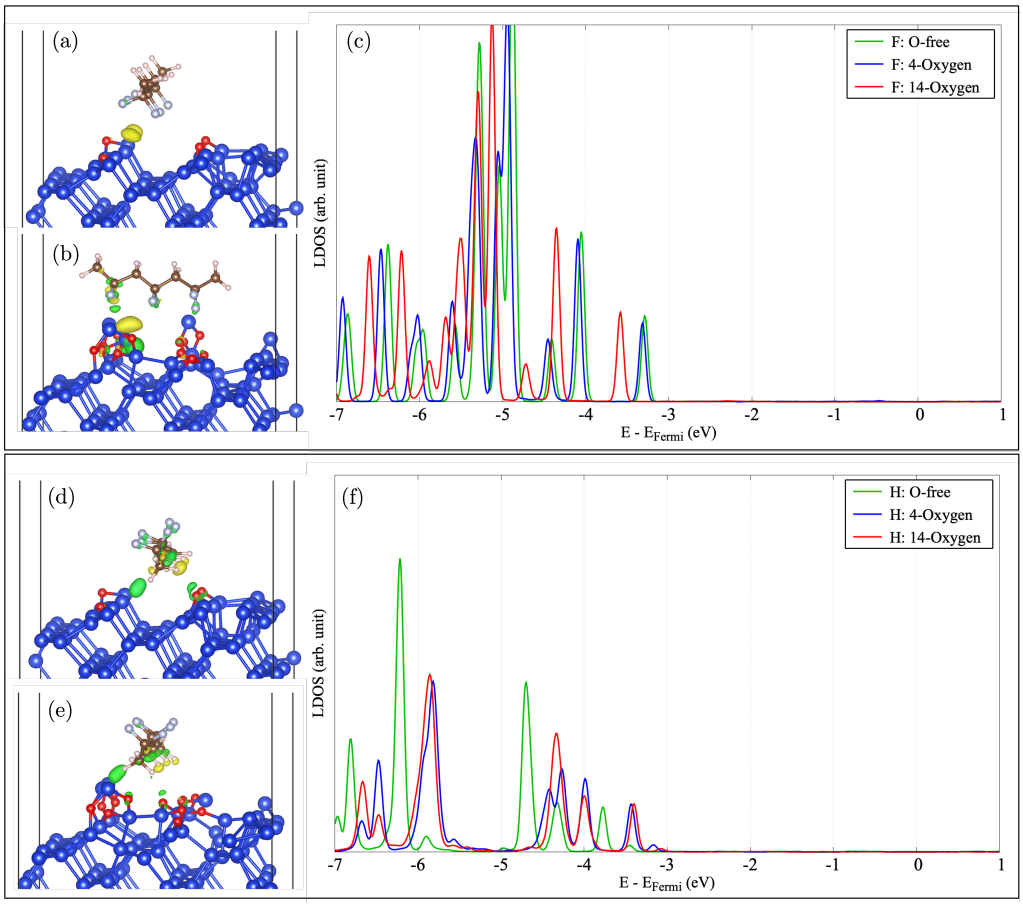

Fig. 5.8: Charge density difference ($\Delta\rho$) maps for the adsorption of β-PVDF on Si(110)/O surfaces with 4 and 14 oxygen atoms are shown in panels (a), (b), (d), and (e). In panels (a) and (b), the binder faces the surface with its fluorine side, while in panels (d) and (e) it faces the surface with its hydrogen side. Panels (c) and (f) report the LDOS of a representative fluorine atom (c) and hydrogen atom (f) of the binder for the O-free, 4-O, and 14-O surfaces. Green and yellow isosurfaces (isosurface level = 0.001 e/Å^3) indicate charge accumulation and charge depletion, respectively. Blue: silicon; red: oxygen; light-pink: hydrogen; gray: fluorine; brown: carbon.

5.4 Comparative Interfacial Behavior of α- and β-PVDF

The contrasting behaviors of the α- and β-phases of PVDF at the Si(110)/O interface, visible both in the LDOS and in the optimized geometries [Fig. 5.3 and Fig. 5.6], can be rationalized by considering the intrinsic polarity of the two crystalline forms. The α-phase is non-polar, whereas the β-phase carries a strong permanent dipole along the polymer backbone. This structural distinction dictates not only how each polymer approaches the oxidized silicon surface but also how it redistributes charge and adapts during adsorption.

For α-PVDF, the absence of a permanent dipole results in generally weaker adhesion to oxidized silicon. The polymer tends to re-orient itself so that hydrogen atoms face the surface, occasionally distorting its own chain to induce a local dipole aligned with the surface polarization. This orientation is favorable because it enables the formation of reversible hydrogen bonds with surface oxygen atoms, an effect that may enhance adaptability and contribute to self-healing behavior under lithiation and delithiation cycles.

In contrast, β-PVDF displays stronger adhesion only when its hydrogen-bearing side faces the oxidized Si surface. Its high polarity aligns naturally with the surface dipole, reinforcing interfacial stability and reducing the likelihood of mechanical detachment during cycling [321,322]. Existing literature has mainly examined PVDF as a cathode binder, where optimized α/β ratios improve cycling performance [323]. In Si-based anodes, however, tuning this phase balance may also be critical for optimizing adhesion, mechanical resilience, and compatibility with co-polymers used for enhanced conductivity or self-healing.

❖ Effect of Surface OH Groups on β-PVDF Binding

To deepen the understanding of interfacial interactions, we also investigate how hydroxyl (–OH) formation on the Si(110)/O surface influences β-PVDF adsorption. Since real oxidized silicon surfaces commonly include OH terminations, their electronic and structural impact is essential for realistic modeling. To simulate OH formation, a hydrogen atom was initially positioned 1.5 Å above a surface oxygen atom. After relaxation, the hydrogen binds to the surface, forming a stable –OH group. The β-PVDF monomer was then adsorbed with either its fluorine or hydrogen side facing the OH-terminated surface.

Fluorine side facing the OH-terminated surface:

When the fluorine side of β-PVDF faces the surface, the adsorption energy becomes -0.366 eV, slightly stronger than the corresponding O-only surface (-0.303 eV). In the relaxed geometry [Fig. 5.9 (a)], the binder subtly rotates toward the OH group. The CDD plot [Fig. 5.9 (b)] shows a clear charge accumulation on the fluorine atom directed toward the newly formed OH, demonstrating that Si–O–H polarization enhances long-range electrostatic attraction.
The LDOS analysis [Fig. 5.10] focuses on atoms experiencing the largest charge rearrangements:

- **Si LDOS** reveals that the empty surface state just above the Fermi level (blue line in Fig. 5.10 (a)) is almost completely suppressed after OH formation (red area), indicating surface passivation.
- **F LDOS** [Fig. 5.10 (b)] remains largely unchanged, but subtle shifts at -4 to -6 eV suggest modified hybridization due to the F–OH interaction.
- **O LDOS** [Fig. 5.10 (c)] broadens and shifts after OH formation, reflecting a changed chemical environment.

- **H LDOS** [Fig. 5.10 (d)] clearly distinguishes the OH-derived hydrogen, which exhibits a unique peak around -6 eV, confirming its active participation at the interface.

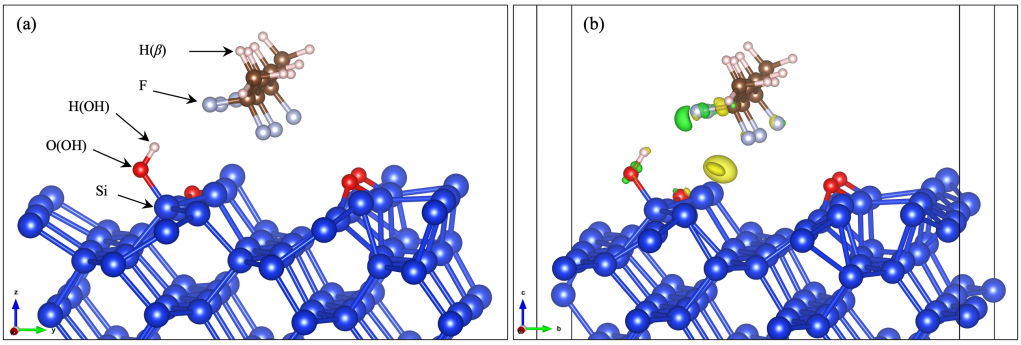

Fig. 5.9: (a) Optimized adsorption geometry of β-PVDF on the Si(110)/O surface in the presence of a surface hydrogen atom. During relaxation, the hydrogen binds to a surface oxygen, forming an –OH group that induces a rotation of the fluorine-facing β-PVDF monomer toward the hydroxyl site. (b) charge density difference (CDD) map for the same configuration, showing charge accumulation (green) on the fluorine atom of the binder and charge depletion (yellow) on the Si–O–H region of the surface. These features highlight the attractive interaction between the F atoms of PVDF and the newly formed OH group. The isosurface level is 0.001 e/Å^3. Blue: Si; red: O; light-pink: H; gray: F; brown: C.

Overall, OH termination stabilizes the silicon surface, enhances electrostatic attraction with fluorine, and modifies local hybridization without introducing states at the Fermi level.

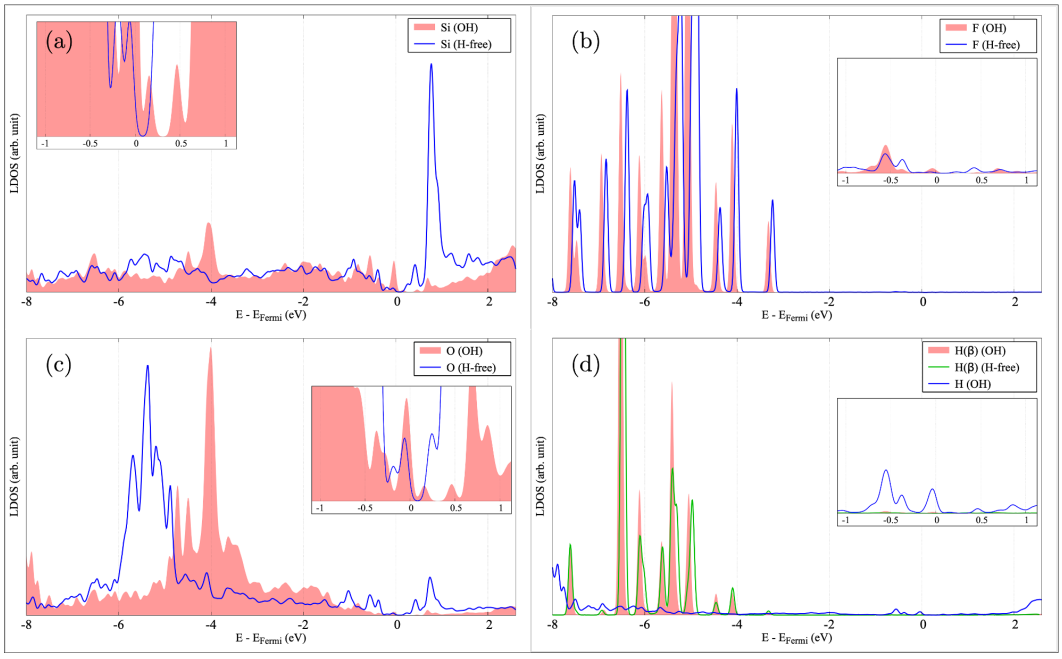

Fig. 5.10: Local density of states (LDOS) of the β-phase of PVDF fluorine-side interface on a Si surface with hydrogen (OH-terminated) and without hydrogen (H-free). The LDOS is shown for selected atoms: silicon in (a), fluorine in (b), oxygen in (c), and hydrogen in (d).

Hydrogen side facing the OH-terminated surface:

The adsorption energy for the hydrogen-exposed β-PVDF becomes -0.723 eV, slightly weaker than on the O-only surface (-0.781 eV). Upon relaxation, the polymer rotates toward the OH group and approaches the surface more closely [Fig. 5.11 (a)]. The CDD plot [Fig. 5.11 (b)] reveals strong charge accumulation around surface O and Si atoms and depletion on the binder's hydrogens, indicating intensified Si–H and O–H interactions, and a stronger dipole–dipole alignment.

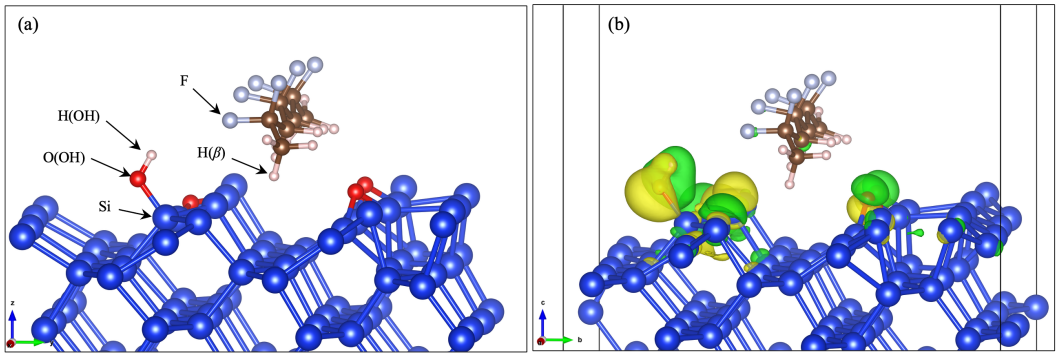

Fig. 5.11: (a) Optimized adsorption geometry of β-PVDF on the Si(110)/O surface when the hydrogen side of the polymer faces the substrate. Upon relaxation, the surface hydrogen binds to an oxygen atom, forming an –OH group that pulls the β-PVDF chain closer and induces a slight axial rotation toward the hydroxyl site. (b) charge density difference (CDD) map for the same configuration, showing pronounced charge accumulation (green) on surface Si and O atoms and charge depletion (yellow) on the hydrogen atoms of the binder. These features indicate enhanced Si–H and O–H interactions and a stronger interfacial coupling in the presence of surface OH groups. The isosurface level is 0.001 e/Å^3. Blue: Si; red: O; light-pink: H; gray: F; brown: C.

LDOS features [Fig. 5.12] further clarify these effects:

- **Si LDOS** [Fig. 5.12 (a)] shows increased intensity near the Fermi level, pointing to enhanced interfacial reactivity.
- **F LDOS** [Fig. 5.12 (b)] develops new features close to the Fermi level in the OH case, revealing modified bonding pathways.
- **O LDOS** [Fig. 5.12 (c)] shifts significantly toward the Fermi level ($\approx$1 eV), consistent with deeper involvement in interfacial bonding.
- **H LDOS** [Fig. 5.12 (d)] distinguishes clearly between polymer hydrogens and the OH-derived H, which exhibits unique states that reflect its structural and electronic role in stabilizing the interface.

These results show that OH formation amplifies the polarity-driven interaction betweenβ-PVDF and the surface, particularly when the hydrogen side faces the interface.

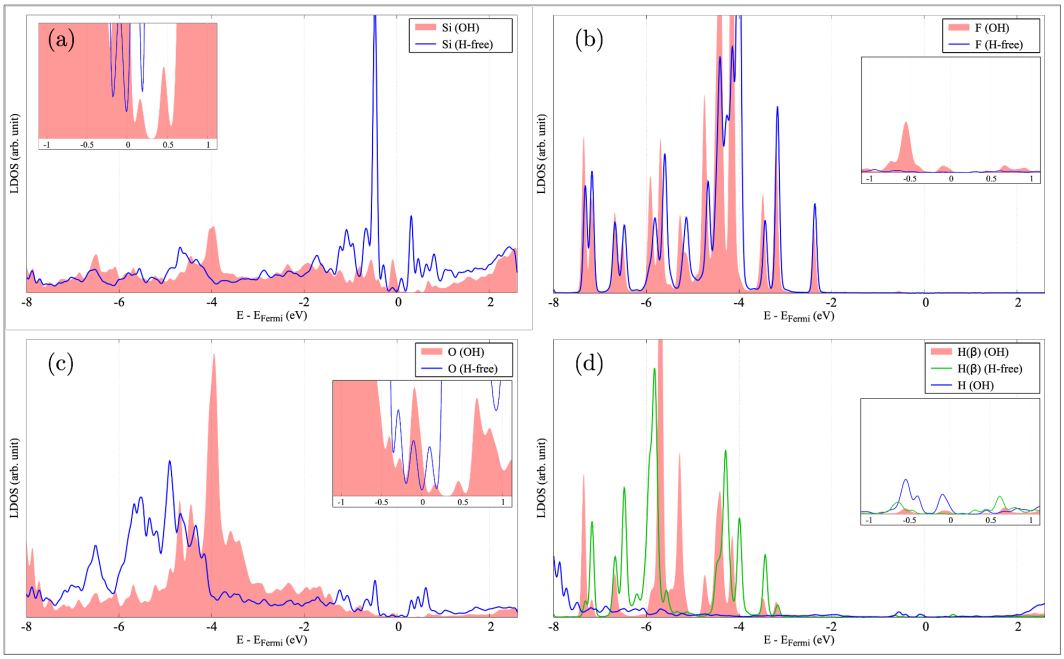

Fig. 5.12: Local density of states (LDOS) of the β-PVDF hydrogen-side interface on a Si surface with hydrogen (OH-terminated) and without hydrogen (H-free). The LDOS is shown for selected atoms: silicon in (a), fluorine in (b), oxygen in (c), and hydrogen in (d).

❖ **Summary of $\alpha - \beta$ Interfacial Behavior:**

In summary:

- **α-PVDF (non-polar)**
  - Adsorbs weakly on oxidized Si(110).
  - Interaction occurs mainly via hydrogen atoms and reversible hydrogen bonding.
  - Less sensitive to additional surface terminations such as OH.
  - More adaptable but less strongly bound.
- **β-PVDF (polar)**
  - Exhibits orientation-dependent binding.
  - Strong adsorption occurs when its hydrogen side aligns with the oxidized Si surface dipole.
  - OH groups significantly enhance binding through added charge transfer and polarization.
  - More rigid but provides stronger, more stable interfacial adhesion.

These differences highlight the crucial role of PVDF phase selection for silicon-based anodes. Tailoring the α/β ratio could enable binders that simultaneously offer strong adhesion, mechanical resilience, and adaptive behavior under cycling conditions.

"I think nature's imagination
is so much greater than man's,
she's never going to let us relax."
— Richard P. Feynman —
Nobel Prize Laureate in Physics – 1965

Conclusions

This dissertation has examined, from first principles, the fundamental mechanisms governing polymer–electrode interactions in two technologically critical electrochemical systems: proton exchange membrane fuel cells (PEMFCs) and lithium-ion batteries (LIBs). Across both studies, a common theme emerges: the performance, stability, and durability of electrochemical devices are intimately linked to the atomic-scale structure and chemistry of their interfaces. By combining systematic configuration sampling with charge-density difference (CDD) analysis and local density of states (LDOS) calculations, this work provides a clear microscopic picture of how polymer orientation, functional groups, hydration, and surface chemistry dictate interfacial charge transfer and structural stability.

For PEMFCs, the results reveal that the orientation and placement of a Nafion monomer at the Pt(111) surface control not only the magnitude but also the nature of charge transfer. In the case of degraded Nafion (16-F), placing the hydrophilic $–SO_3H$ group too close to the hydrogen-covered Pt surface leads to spontaneous OH radical formation, accompanied by monomer degradation and noticeable deformation of the Pt lattice. By contrast, for pristine Nafion (17-F), structural optimization follows a different, non-reactive pathway, characterized by weaker interfacial polarization and the absence of radical formation or significant surface distortion. Conversely, increasing the initial separation allows for an optimized atomic arrangement with hydronium formation without polymer degradation, preserving the surface structure and yielding the most energetically favorable configuration. When Nafion interacts through its $–CF_3$ group, charge redistribution is minimal, no proton transfer occurs, and the Pt surface undergoes a small contraction. These findings clarify how unwanted degradation pathways originate at the Pt/Nafion interface and demonstrate that controlling monomer orientation and interface spacing is essential for stabilizing proton-transfer pathways in PEMFCs. The study also advances the field by providing a fully electronic, DFT-based description of the Pt/Nafion interface, an area previously dominated by classical molecular modeling and dynamics approaches.

For LIBs, the comparative analysis of α- and β-phase PVDF adsorbed on oxidized Si(110) surfaces reveals clear polarity-dependent interfacial behavior. The nonpolar α-phase exhibits weaker adhesion mediated primarily through reversible H-bond interactions, and its response to oxygen coverage is modest. In contrast, the polar β-phase displays strong orientation-dependent interactions: its hydrogen-terminated side adheres robustly to oxidized Si due to favorable dipole alignment, while the fluorine-terminated side interacts weakly and is further destabilized by surface oxygen saturation. The introduction of surface OH groups amplifies these effects by modifying local charge transfer and inducing additional polarization, with β-PVDF showing a markedly stronger response than the α-phase. This systematic comparison establishes that polymer polarity, orientation, and surface functionalization are decisive factors governing binder–silicon adhesion, key for mitigating delamination, stabilizing the SEI, and improving long-term cycling.

Taken together, these results underscore the broader significance of interface engineering

in electrochemical devices. They demonstrate that the nanoscale arrangement of functional groups, hydration, and surface terminations can either promote desirable ion-transfer pathways or trigger degradation mechanisms. The insights obtained here provide actionable design principles for next-generation materials: tailoring Nafion orientation and hydration structure to stabilize PEMFC catalyst layers, and selecting or modifying PVDF phases to enhance adhesion and interfacial stability in silicon anodes. More broadly, the atomistic mechanisms identified in this work highlight the importance of polarity matching, controlled surface functionalization, and the deliberate manipulation of local electrostatics in the design of high-performance, durable electrochemical interfaces.

Bibliography

[1] Larminie, J., Dicks, A. & McDonald, M. Fuel cell systems explained. (J. Wiley Chichester, UK,2003)

[2] Ormerod, R. Solid oxide fuel cells. *Chemical Society Reviews*. **32**, 17-28 (2003)

[3] O'hayre, R., Cha, S., Colella, W. & Prinz, F. Fuel cell fundamentals. (John Wiley & Sons,2016)

[4] Cook, B. Introduction to fuel cells and hydrogen technology. *Engineering Science And Education Journal*. **11**, 205-216 (2002)

[5] Hissel, D., Turpin, C., Astier, S., Boulon, L., Bouscayrol, A., Bultel, Y., Candusso, D., Caux, S., Chupin, S., Colinart, T. & Others A review on existing modeling methodologies for PEM fuel cell systems. *Fundamentals And Developments Of Fuel Cells Cenference*. (2008)

[6] Wang, Y., Yang, X., Sun, Z. & Chen, Z. A systematic review of system modeling and control strategy of proton exchange membrane fuel cell. *Energy Reviews*. **3**, 100054 (2024)

[7] Costamagna, P. FUEL CELLS – OVERVIEW | Modeling. *Encyclopedia Of Electrochemical Power Sources*. pp. 309-320 (2009)

[8] Bossel, U. Fuel Cells: From Birth to Maturity. (Springer Nature,2024)

[9] Grimes, P. Historical pathways for fuel cells. The new electric century. *Fifteenth Annual Battery Conference On Applications And Advances (Cat. No. 00TH8490)*. pp. 41-45 (2000)

[10] Stambouli, A. & Traversa, E. Solid oxide fuel cells (SOFCs): a review of an environmentally clean and efficient source of energy. *Renewable And Sustainable Energy Reviews*. **6**, 433-455 (2002)

[11] Appleby, A. From Sir William Grove to today: fuel cells and the future. *Journal Of Power Sources*. **29**, 3-11 (1990)

[12] Stone, C. & Morrison, A. From curiosity to "power to change the world®". *Solid State Ionics*. **152** pp. 1-13 (2002)

[13] National Museum of American History Phosphoric Acid Fuel Cell. (Smithsonian Institution,2004), http://americanhistory.si.edu/fuelcells/phos/pafcmain.htm, [Online; accessed 25.04.1990]

[14] Wee, J. Applications of proton exchange membrane fuel cell systems. *Renewable And Sustainable Energy Reviews*. **11**, 1720-1738 (2007)

[15] Lee, J., Baek, S., Jung, H., Kang, H., Chung, J. & Suh, I. Development of a 250kW power conditioning system for molten carbonate fuel cell power generation system. *2007 International Conference On Electrical Machines And Systems (ICEMS)*. pp. 354-358 (2007)

[16] Khaligh, A., Rahimi, A., Lee, Y., Cao, J., Emadi, A., Andrews, S., Robinson, C. & Finnerty, C. Digital control of an isolated active hybrid fuel cell/Li-ion battery power supply. *IEEE Transactions On Vehicular Technology*. **56**, 3709-3721 (2007)

[17] Segura, F., Durán, E. & Andújar, J. Design, building and testing of a stand alone fuel cell hybrid system. *Journal Of Power Sources*. **193**, 276-284 (2009)

[18] Stambouli, A. & Traversa, E. Fuel cells, an alternative to standard sources of energy. *Renewable And Sustainable Energy Reviews*. **6**, 295-304 (2002)

[19] Vasallo, M., Andújar, J., Garcıá, C. & Brey, J. A methodology for sizing backup fuel-cell/battery hybrid power systems. *IEEE Transactions On Industrial Electronics*. **57**, 1964-1975 (2009)

[20] Williamson, S., Emadi, A. & Shahidehpour, M. Distributed fuel cell generation in restructured power systems. *IEEE Power Engineering Society General Meeting, 2004.*. pp. 2079-2084 (2004)

[21] Chen, F., Fernandes, T., Roche, M. & Graça Carvalho, M. Investigation of challenges to the utilization of fuel cell buses in the EU vs transition economies. *Renewable And Sustainable Energy Reviews*. **11**, 357-364 (2007)

[22] Andújar, J., Segura, F. & Vasallo, M. A suitable model plant for control of the set fuel cell-DC/DC converter. *Renewable Energy*. **33**, 813-826 (2008)

[23] Kim, T. & Kwon, S. MEMS fuel cell system for portable power source: Integration of methanol reformer, PROX, and fuel cell. *2008 IEEE 21st International Conference On Micro Electro Mechanical Systems*. pp. 980-983 (2008)

[24] Abdullah, M. & Gan, Y. Feasibility study of a mini fuel cell to detect interference from a cellular phone. *Journal Of Power Sources*. **155**, 311-318 (2006)

[25] Ross, D. Power struggle [power supplies for portable equipment]. *Iee Review*. **49**, 34-38 (2003)

[26] Kirubakaran, A., Jain, S. & Nema, R. A review on fuel cell technologies and power electronic interface. *Renewable And Sustainable Energy Reviews*. **13**, 2430-2440 (2009)

[27] Alhassan, M., Garba, M. & Others Design of an alkaline fuel cell. *Leonardo Electron. J. Pract. Technol*. **5** pp. 99-106 (2006)

[28] National Fuel Cell Research Center Phosphoric Acid Fuel Cell. (University of California,2009), http://www.nfcrc.uci.edu/EnergyTutorial/pafc.html, [Online; accessed 25.04.2025]

[29] U.S. Department of Defense Fuel Cell Test and Evaluation Center (FCTec) Phosphoric Acid Fuel Cell (PAFC). (U.S. Department of Defense,2010), http://www.fctec.com/fctec_about.asp, [Online; accessed 25.04.2025]

[30] Wikipedia contributors Phosphoric acid fuel cell. (Wikipedia, The Free Encyclopedia,2023), https://en.wikipedia.org/wiki/Phosphoric_acid_fuel_cell, [Online; accessed 25.04.2025]

[31] Will, J., Mitterdorfer, A., Kleinlogel, C., Perednis, D. & Gauckler, L. Fabrication of thin electrolytes for second-generation solid oxide fuel cells. *Solid State Ionics*. **131**, 79-96 (2000)

[32] Singhal, S. Advances in solid oxide fuel cell technology. *Solid State Ionics*. **135**, 305-313 (2000)

[33] Tanaka, K., Wen, C. & Yamada, K. Design and evaluation of combined cycle system with solid oxide fuel cell and gas turbine. *Fuel*. **79**, 1493-1507 (2000)

[34] Sahibzada, M., Steele, B., Barth, D., Rudkin, R. & Metcalfe, I. Operation of solid oxide fuel cells at reduced temperatures. *Fuel*. **78**, 639-643 (1999)

[35] Chudej, K., Bauer, M., Pesch, H. & Schittkowski, K. Numerical simulation of a molten carbonate fuel cell by partial differential algebraic equations. *From Nano To Space: Applied Mathematics Inspired By Roland Bulirsch*. pp. 57-70 (2008)

[36] Sopian, K. & Daud, W. Challenges and future developments in proton exchange membrane fuel cells. *Renewable Energy*. **31**, 719-727 (2006)

[37] Therdthianwong, A., Saenwiset, P. & Therdthianwong, S. Cathode catalyst layer design for proton exchange membrane fuel cells. *Fuel*. **91**, 192-199 (2012)

[38] U.S. Department of Energy, Energy Efficiency and Renewable Energy Information Center Comparison of Fuel Cell Technologies. (U.S. Department of Energy,2008), https://www.hydrogen.energy.gov, [Online; accessed 25.04.2025]

[39] McNicol, B., Rand, D. & Williams, K. Fuel cells for road transportation purposes-yes or no?. *Journal Of Power Sources*. **100**, 47-59 (2001)

[40] Mekhilef, S., Saidur, R. & Safari, A. Comparative study of different fuel cell technologies. *Renewable And Sustainable Energy Reviews*. **16**, 981-989 (2012)

[41] Wang, C. Fundamental models for fuel cell engineering. *Chemical Reviews*. **104**, 4727-4766 (2004)

[42] Hirschenhofer, J., Stauffer, D., Engleman, R. & Klett, M. Fuel Cell Handbook, Parsons Corporation. *Reading, PA*. **19607** (1998)

[43] Osmieri, L. & Meyer, Q. Recent advances in integrating platinum group metal-free catalysts in proton exchange membrane fuel cells. *Current Opinion In Electrochemistry*. **31** pp. 100847 (2022)

[44] Khotseng, L. Oxygen reduction reaction. *Electrocatalysts For Fuel Cells And Hydrogen Evolution-Theory To Design*. **10** (2018)

[45] Li, C., Tan, H., Lin, J., Luo, X., Wang, S., You, J., Kang, Y., Bando, Y., Yamauchi, Y. & Kim, J. Emerging Pt-based electrocatalysts with highly open nanoarchitectures for boosting oxygen reduction reaction. *Nano Today*. **21** pp. 91-105 (2018)

[46] Eikerling, M. & Kornyshev, A. Modelling the performance of the cathode catalyst layer of polymer electrolyte fuel cells. *Journal Of Electroanalytical Chemistry*. **453**, 89-106 (1998)

[47] Zhang, J. PEM fuel cell electrocatalysts and catalyst layers: fundamentals and applications. (Springer Science & Business Media,2008)

[48] Ross, P. [Title of the Paper or Presentation]. *Proceedings Of The National Fuel Cell Seminar*. (1980,7,14)

[49] Landsman, D. & Luczak, F. Noble metal-chromium alloy catalysts and electrochemical cell. (1982)

[50] Beard, B. & Ross, P. The structure and activity of Pt-Co alloys as oxygen reduction electrocatalysts. *Journal Of The Electrochemical Society*. **137**, 3368 (1990)

[51] Watanabe, M., Tsurumi, K., Mizukami, T., Nakamura, T. & Stonehart, P. Activity and stability of ordered and disordered Co-Pt alloys for phosphoric acid fuel cells. *Journal Of The Electrochemical Society*. **141**, 2659 (1994)

[52] Stonehart, P. Development of alloy electrocatalysts for phosphoric acid fuel cells (PAFC). *Journal Of Applied Electrochemistry*. **22**, 995-1001 (1992)

[53] Mukerjee, S. Particle size and structural effects in platinum electrocatalysis. *Journal Of Applied Electrochemistry*. **20**, 537-548 (1990)

[54] Freund, A., Lang, J., Lehmann, T. & Starz, K. Improved Pt alloy catalysts for fuel cells. *Catalysis Today*. **27**, 279-283 (1996)

[55] Mukerjee, S. & Srinivasan, S. Enhanced electrocatalysis of oxygen reduction on platinum alloys in proton exchange membrane fuel cells. *Journal Of Electroanalytical Chemistry*. **357**, 201-224 (1993)

[56] Shim, J., Yoo, D. & Lee, J. Characteristics for electrocatalytic properties and hydrogen–oxygen adsorption of platinum ternary alloy catalysts in polymer electrolyte fuel cell. *Electrochimica Acta*. **45**, 1943-1951 (2000)

[57] Antolini, E., Passos, R. & Ticianelli, E. Electrocatalysis of oxygen reduction on a carbon supported platinum–vanadium alloy in polymer electrolyte fuel cells. *Electrochimica Acta*. **48**, 263-270 (2002)

[58] Neergat, M., Shukla, A. & Gandhi, K. Platinum-based alloys as oxygen–reduction catalysts for solid–polymer–electrolyte direct methanol fuel cells. *Journal Of Applied Electrochemistry*. **31** pp. 373-378 (2001)

[59] Shukla, A., Raman, R., Choudhury, N., Priolkar, K., Sarode, P., Emura, S. & Kumashiro, R. Carbon-supported Pt–Fe alloy as a methanol-resistant oxygen-reduction catalyst for direct methanol fuel cells. *Journal Of Electroanalytical Chemistry*. **563**, 181-190 (2004)

[60] Abdullah, N. & Kamarudin, S. Titanium dioxide in fuel cell technology: An overview. *Journal Of Power Sources*. **278** pp. 109-118 (2015)

[61] Lewera, A., Timperman, L., Roguska, A. & Alonso-Vante, N. Metal–support interactions between nanosized Pt and metal oxides (WO3 and TiO2) studied using X-ray photoelectron spectroscopy. *The Journal Of Physical Chemistry C*. **115**, 20153-20159 (2011)

[62] Wang, Y., Wilkinson, D. & Zhang, J. Synthesis of conductive rutile-phased Nb 0.06 Ti 0.94 O 2 and its supported Pt electrocatalysts (Pt/Nb 0.06 Ti 0.94 O 2) for the oxygen reduction reaction. *Dalton Transactions*. **41**, 1187-1194 (2012)

[63] Park, K. & Seol, K. Nb-TiO2 supported Pt cathode catalyst for polymer electrolyte membrane fuel cells. *Electrochemistry Communications*. **9**, 2256-2260 (2007)

[64] Kumar, A. & Ramani, V. Ta0. 3Ti0. 7O2 electrocatalyst supports exhibit exceptional electrochemical stability. *Journal Of The Electrochemical Society*. **160**, F1207 (2013)

[65] Kim, J., Kwon, G., Chun, H. & Kim, Y. Enhancement of activity and durability through Cr doping of TiO2 supports in Pt electrocatalysts for oxygen reduction reactions. *ChemCatChem*. **6**, 3239-3245 (2014)

[66] Huang, S., Ganesan, P. & Popov, B. Electrocatalytic activity and stability of niobium-doped titanium oxide supported platinum catalyst for polymer electrolyte membrane fuel cells. *Applied Catalysis B: Environmental*. **96**, 224-231 (2010)

[67] Grot, W. Perfluorinated cation-exchange polymers. *Chemie Ingenieur Technik*. **47** pp. 617-617 (1975)

[68] Steele, B. & Heinzel, A. Materials for fuel-cell technologies. *Nature*. **414**, 345-352 (2001)

[69] Dell, R., Dell, R. & Rand, D. Understanding batteries. (Royal society of chemistry,2001)

[70] Kim, T., Song, W., Son, D., Ono, L. & Qi, Y. Lithium-ion batteries: outlook on present, future, and hybridized technologies. *Journal Of Materials Chemistry A*. **7**, 2942-2964 (2019)

[71] Yoshio, M., Brodd, R. & Kozawa, A. Lithium-ion batteries. (Springer,2009)

[72] Scrosati, B., Hassoun, J. & Sun, Y. Lithium-ion batteries. A look into the future. *Energy & Environmental Science*. **4**, 3287-3295 (2011)

[73] Jolivet, L., Leprince, M., Moncayo, S., Sorbier, L., Lienemann, C. & Motto-Ros, V. Review of the recent advances and applications of LIBS-based imaging. *Spectrochimica Acta Part B: Atomic Spectroscopy*. **151** pp. 41-53 (2019)

[74] Manthiram, A. Materials challenges and opportunities of lithium ion batteries. *The Journal Of Physical Chemistry Letters*. **2**, 176-184 (2011)

[75] Zhan, R., Wang, X., Chen, Z., Seh, Z., Wang, L. & Sun, Y. Promises and challenges of the practical implementation of prelithiation in lithium-ion batteries. *Advanced Energy Materials*. **11**, 2101565 (2021)

[76] Walter, M., Kovalenko, M. & Kravchyk, K. Challenges and benefits of post-lithium-ion batteries. *New Journal Of Chemistry*. **44**, 1677-1683 (2020)

[77] Asimov, I. Asimov's biographical encyclopedia of science and technology: the lives and achievements of 1195 great scientists from ancient times to the present, chronologically arranged. *(No Title)*. (1972)

[78] Buchmann, I. Batteries in a portable world: a handbook on rechargeable batteries for non-engineers. (2001)

[79] Tarascon, J. & Armand, M. Issues and challenges facing rechargeable lithium batteries. *Nature*. **414**, 359-367 (2001)

[80] Obama, B. The irreversible momentum of clean energy. *Science*. **355**, 126-129 (2017)

[81] York, R. Do alternative energy sources displace fossil fuels?. *Nature Climate Change*. **2**, 441-443 (2012)

[82] Wuest, M. Lithium-ion Batteries: Basics and Applications. (Springer,2018)

[83] Nitta, N., Wu, F., Lee, J. & Yushin, G. Li-ion battery materials: present and future. *Materials Today*. **18**, 252-264 (2015)

[84] Manthiram, A. An outlook on lithium ion battery technology. *ACS Central Science*. **3**, 1063-1069 (2017)

[85] Nzereogu, P., Omah, A., Ezema, F., Iwuoha, E. & Nwanya, A. Anode materials for lithium-ion batteries: A review. *Applied Surface Science Advances*. **9** pp. 100233 (2022)

[86] Korthauer, R. Lithium-ion batteries: basics and applications. (Springer,2018)

[87] Roy, P. & Srivastava, S. Nanostructured anode materials for lithium ion batteries. *Journal Of Materials Chemistry A*. **3**, 2454-2484 (2015)

[88] Hossain, M., Chowdhury, M., Hossain, N., Islam, M. & Mobarak, M. Advances of lithium-ion batteries anode materials—A review. *Chemical Engineering Journal Advances*. **16** pp. 100569 (2023)

[89] Ma, H., Cheng, F., Chen, J., Zhao, J., Li, C., Tao, Z. & Liang, J. Nest-like silicon nanospheres for high-capacity lithium storage. *Advanced Materials (Weinheim)*. **19** (2007)

[90] Bourderau, S., Brousse, T. & Schleich, D. Amorphous silicon as a possible anode material for Li-ion batteries. *Journal Of Power Sources*. **81** pp. 233-236 (1999)

[91] Dimov, N., Kugino, S. & Yoshio, M. Carbon-coated silicon as anode material for lithium ion batteries: advantages and limitations. *Electrochimica Acta*. **48**, 1579-1587 (2003)

[92] Su, X., Wu, Q., Li, J., Xiao, X., Lott, A., Lu, W., Sheldon, B. & Wu, J. Silicon-based nanomaterials for lithium-ion batteries: a review. *Advanced Energy Materials*. **4**, 1300882 (2014)

[93] Zhang, W. A review of the electrochemical performance of alloy anodes for lithium-ion batteries. *Journal Of Power Sources*. **196**, 13-24 (2011)

[94] Fuchsbichler, B., Stangl, C., Kren, H., Uhlig, F. & Koller, S. High capacity graphite–silicon composite anode material for lithium-ion batteries. *Journal Of Power Sources*. **196**, 2889-2892 (2011)

[95] Beattie, S., Loveridge, M., Lain, M., Ferrari, S., Polzin, B., Bhagat, R. & Dashwood, R. Understanding capacity fade in silicon based electrodes for lithium-ion batteries using three electrode cells and upper cut-off voltage studies. *Journal Of Power Sources*. **302** pp. 426-430 (2016)

[96] Hwang, S., Lee, J. & Yoon, W. Electrochemical behavior of carbon-coated silicon monoxide electrode with chromium coating in rechargeable lithium cell. *Journal Of Power Sources*. **244** pp. 620-624 (2013)

[97] Arora, P. & Zhang, Z. Battery separators. *Chemical Reviews*. **104**, 4419-4462 (2004)

[98] Scrosati, B. History of lithium batteries. *Journal Of Solid State Electrochemistry*. **15**, 1623-1630 (2011)

[99] Liu, C., Neale, Z. & Cao, G. Understanding electrochemical potentials of cathode materials in rechargeable batteries. *Materials Today*. **19**, 109-123 (2016)

[100] Daniel, C., Mohanty, D., Li, J. & Wood, D. Cathode materials review. *AIP Conference Proceedings*. **1597**, 26-43 (2014)

[101] Whittingham, M. Lithium batteries and cathode materials. *Chemical Reviews*. **104**, 4271-4302 (2004)

[102] Xu, B., Qian, D., Wang, Z. & Meng, Y. Recent progress in cathode materials research for advanced lithium ion batteries. *Materials Science And Engineering: R: Reports*. **73**, 51-65 (2012)

[103] Taminato, S., Hirayama, M., Suzuki, K., Tamura, K., Minato, T., Arai, H., Uchimoto, Y., Ogumi, Z. & Kanno, R. Lithium intercalation and structural changes at the LiCoO2 surface under high voltage battery operation. *Journal Of Power Sources*. **307** pp. 599-603 (2016)

[104] Amatucci, G., Tarascon, J. & Klein, L. Cobalt dissolution in LiCoO2-based non-aqueous rechargeable batteries. *Solid State Ionics*. **83**, 167-173 (1996)

[105] Jo, M., Noh, M., Oh, P., Kim, Y. & Cho, J. A new high power LiNi0. 81Co0. 1Al0. 09O2 cathode material for lithium-ion batteries. *Advanced Energy Materials*. **4**, 1301583 (2014)

[106] Hwang, S., Chang, W., Kim, S., Su, D., Kim, D., Lee, J., Chung, K. & Stach, E. Investigation of changes in the surface structure of Li x Ni0. 8Co0. 15Al0. 05O2 cathode materials induced by the initial charge. *Chemistry Of Materials*. **26**, 1084-1092 (2014)

[107] Sathiya, M., Hemalatha, K., Ramesha, K., Tarascon, J. & Prakash, A. Synthesis, structure, and electrochemical properties of the layered sodium insertion cathode material: NaNi1/3Mn1/3Co1/3O2. *Chemistry Of Materials*. **24**, 1846-1853 (2012)

[108] Zhang, X., Jiang, W., Mauger, A., Gendron, F., Julien, C. & Others Minimization of the cation mixing in Li1+ x (NMC) 1- xO2 as cathode material. *Journal Of Power Sources*. **195**, 1292-1301 (2010)

[109] Li, Q., Li, G., Fu, C., Luo, D., Fan, J. & Li, L. K+-doped Li1. 2Mn0. 54Co0. 13Ni0. 13O2: a novel cathode material with an enhanced cycling stability for lithium-ion batteries. *ACS Applied Materials & Interfaces*. **6**, 10330-10341 (2014)

[110] Shao-Horn, Y., Croguennec, L., Delmas, C., Nelson, E. & O'Keefe, M. Atomic resolution of lithium ions in LiCoO2. *Nature Materials*. **2**, 464-467 (2003)

[111] Xia, H., Luo, Z. & Xie, J. Nanostructured LiMn2O4 and their composites as high-performance cathodes for lithium-ion batteries. *Progress In Natural Science: Materials International*. **22**, 572-584 (2012)

[112] Lee, M., Lee, S., Oh, P., Kim, Y. & Cho, J. High performance LiMn2O4 cathode materials grown with epitaxial layered nanostructure for Li-ion batteries. *Nano Letters*. **14**, 993-999 (2014)

[113] Zhang, Y., Huo, Q., Du, P., Wang, L., Zhang, A., Song, Y., Lv, Y. & Li, G. Advances in new cathode material LiFePO4 for lithium-ion batteries. *Synthetic Metals*. **162**, 1315-1326 (2012)

[114] Zhang, W. Structure and performance of LiFePO4 cathode materials: A review. *Journal Of Power Sources*. **196**, 2962-2970 (2011)

[115] Wang, Y. & Zhong, W. Development of electrolytes towards achieving safe and high-performance energy-storage devices: a review. *ChemElectroChem*. **2**, 22-36 (2015)

[116] Janz, G. Nonaqueous electrolytes handbook. (Elsevier,2012)

[117] Bruce, P. & Vincent, C. Polymer electrolytes. *Journal Of The Chemical Society, Faraday Transactions*. **89**, 3187-3203 (1993)

[118] Zhang, S. A review on the separators of liquid electrolyte Li-ion batteries. *Journal Of Power Sources*. **164**, 351-364 (2007)

[119] An, S., Li, J., Daniel, C., Mohanty, D., Nagpure, S. & Wood III, D. The state of understanding of the lithium-ion-battery graphite solid electrolyte interphase (SEI) and its relationship to formation cycling. *Carbon*. **105** pp. 52-76 (2016)

[120] Cheng, X., Zhang, R., Zhao, C., Wei, F., Zhang, J. & Zhang, Q. A review of solid electrolyte interphases on lithium metal anode. *Advanced Science*. **3**, 1500213 (2016)

[121] Bülter, H., Peters, F., Schwenzel, J. & Wittstock, G. Spatiotemporal Changes of the Solid Electrolyte Interphase in Lithium-Ion Batteries Detected by Scanning Electrochemical Microscopy. *Angewandte Chemie International Edition*. **53**, 10531-10535 (2014)

[122] Peled, E. & Menkin, S. SEI: past, present and future. *Journal Of The Electrochemical Society*. **164**, A1703 (2017)

[123] Ramos-Sanchez, G., Soto, F., Martinez De La Hoz, J., Liu, Z., Mukherjee, P., El-Mellouhi, F., Seminario, J. & Balbuena, P. Computational studies of interfacial reactions at anode materials: initial stages of the solid-electrolyte-interphase layer formation. *Journal Of Electrochemical Energy Conversion And Storage*. **13**, 031002 (2016)

[124] Verma, P., Maire, P. & Novák, P. A review of the features and analyses of the solid electrolyte interphase in Li-ion batteries. *Electrochimica Acta*. **55**, 6332-6341 (2010)

[125] Heiskanen, S., Kim, J. & Lucht, B. Generation and evolution of the solid electrolyte interphase of lithium-ion batteries. *Joule*. **3**, 2322-2333 (2019)

[126] Obrovac, M. & Chevrier, V. Alloy negative electrodes for Li-ion batteries. *Chemical Reviews*. **114**, 11444-11502 (2014)

[127] Wen, C. & Huggins, R. Chemical diffusion in intermediate phases in the lithium-silicon system. *Journal Of Solid State Chemistry*. **37**, 271-278 (1981)

[128] Boukamp, B., Lesh, G. & Huggins, R. All-solid lithium electrodes with mixed-conductor matrix. *Journal Of The Electrochemical Society*. **128**, 725 (1981)

[129] Wu, H., Chan, G., Choi, J., Ryu, I., Yao, Y., McDowell, M., Lee, S., Jackson, A., Yang, Y., Hu, L. & Others Stable cycling of double-walled silicon nanotube battery anodes through solid–electrolyte interphase control. *Nature Nanotechnology*. **7**, 310-315 (2012)

[130] Liu, N., Lu, Z., Zhao, J., McDowell, M., Lee, H., Zhao, W. & Cui, Y. A pomegranate-inspired nanoscale design for large-volume-change lithium battery anodes. *Nature Nanotechnology*. **9**, 187-192 (2014)

[131] Choi, S., Kwon, T., Coskun, A. & Choi, J. Highly elastic binders integrating polyrotaxanes for silicon microparticle anodes in lithium ion batteries. *Science*. **357**, 279-283 (2017)

[132] Liu, T., Chu, Q., Yan, C., Zhang, S., Lin, Z. & Lu, J. Interweaving 3D network binder for high-areal-capacity Si anode through combined hard and soft polymers. *Advanced Energy Materials*. **9**, 1802645 (2019)

[133] Kim, J., Choi, W., Cho, K., Byun, D., Lim, J. & Lee, J. Effect of polyimide binder on electrochemical characteristics of surface-modified silicon anode for lithium ion batteries. *Journal Of Power Sources*. **244** pp. 521-526 (2013)

[134] Higgins, T., Park, S., King, P., Zhang, C., McEvoy, N., Berner, N., Daly, D., Shmeliov, A., Khan, U., Duesberg, G. & Others A commercial conducting polymer as both binder and conductive additive for silicon nanoparticle-based lithium-ion battery negative electrodes. *Acs Nano*. **10**, 3702-3713 (2016)

[135] Lopez, J., Mackanic, D., Cui, Y. & Bao, Z. Designing polymers for advanced battery chemistries. *Nature Reviews Materials*. **4**, 312-330 (2019)

[136] Wang, H., Wu, B., Wu, X., Zhuang, Q., Liu, T., Pan, Y., Shi, G., Yi, H., Xu, P., Xiong, Z. & Others Key factors for binders to enhance the electrochemical performance of silicon anodes through molecular design. *Small*. **18**, 2101680 (2022)

[137] Chen, Z., Christensen, L. & Dahn, J. Comparison of PVDF and PVDF-TFE-P as binders for electrode materials showing large volume changes in lithium-ion batteries. *Journal Of The Electrochemical Society*. **150**, A1073 (2003)

[138] Chen, Z., Christensen, L. & Dahn, J. Large-volume-change electrodes for Li-ion batteries of amorphous alloy particles held by elastomeric tethers. *Electrochemistry Communications*. **5**, 919-923 (2003)

[139] Liu, W., Yang, M., Wu, H., Chiao, S. & Wu, N. Enhanced cycle life of Si anode for Li-ion batteries by using modified elastomeric binder. *Electrochemical And Solid-State Letters*. **8**, A100 (2004)

[140] Chen, Z., Chevrier, V., Christensen, L. & Dahn, J. Design of amorphous alloy electrodes for Li-ion batteries: a big challenge. *Electrochemical And Solid-state Letters*. **7**, A310 (2004)

[141] Han, L., Liu, T., Sheng, O., Liu, Y., Wang, Y., Nai, J., Zhang, L. & Tao, X. Undervalued roles of binder in modulating solid electrolyte interphase formation of silicon-based anode materials. *ACS Applied Materials & Interfaces*. **13**, 45139-45148 (2021)

[142] Zhao, Y., Liang, Z., Kang, Y., Zhou, Y., Li, Y., He, X., Wang, L., Mai, W., Wang, X., Zhou, G. & Others Rational design of functional binder systems for high-energy lithium-based rechargeable batteries. *Energy Storage Materials*. **35** pp. 353-377 (2021)

[143] Gendensuren, B. & Oh, E. Dual-crosslinked network binder of alginate with polyacrylamide for silicon/graphite anodes of lithium ion battery. *Journal Of Power Sources*. **384** pp. 379-386 (2018)

[144] Lee, S., Koo, H., Kang, H., Oh, K. & Nam, K. Advances in polymer binder materials for lithium-ion battery electrodes and separators. *Polymers*. **15**, 4477 (2023)

[145] Hu, L., Zhang, X., Zhao, P., Fan, H., Zhang, Z., Deng, J., Ungar, G. & Song, J. Gradient H-Bonding Binder Enables Stable High-Areal-Capacity Si-Based Anodes in Pouch Cells. *Advanced Materials*. **33**, 2104416 (2021)

[146] Chen, H., Wu, Z., Su, Z., Chen, S., Yan, C., Al-Mamun, M., Tang, Y. & Zhang, S. A mechanically robust self-healing binder for silicon anode in lithium ion batteries. *Nano Energy*. **81** pp. 105654 (2021)

[147] Burdette-Trofimov, M., Armstrong, B., Korkosz, R., Tyler, J., McAuliffe, R., Heroux, L., Doucet, M., Hoelzer, D., Kanbargi, N., Naskar, A. & Others Understanding the solution dynamics and binding of a PVDF binder with silicon, graphite, and NMC materials and the influence on cycling performance. *ACS Applied Materials & Interfaces*. **14**, 23322-23331 (2022)

[148] Arabnejad, S., Yamashita, K. & Manzhos, S. Defects in crystalline PVDF: a density functional theory-density functional tight binding study. *Physical Chemistry Chemical Physics*. **19**, 7560-7567 (2017)

[149] Huang, W., Wang, W., Wang, Y., Qu, Q., Jin, C. & Zheng, H. Overcoming the fundamental challenge of PVDF binder use with silicon anodes with a super-molecular nano-layer. *Journal Of Materials Chemistry A*. **9**, 1541-1551 (2021)

[150] Zhang, Z., Fouchard, D. & Rea, J. Differential scanning calorimetry material studies: implications for the safety of lithium-ion cells. *Journal Of Power Sources*. **70**, 16-20 (1998)

[151] Lingappan, N., Kong, L. & Pecht, M. The significance of aqueous binders in lithium-ion batteries. *Renewable And Sustainable Energy Reviews*. **147** pp. 111227 (2021)

[152] Zhang, S. & Jow, T. Study of poly (acrylonitrile-methyl methacrylate) as binder for graphite anode and LiMn2O4 cathode of Li-ion batteries. *Journal Of Power Sources*. **109**, 422-426 (2002)

[153] Kuwabata, S., Tsumura, N., Goda, S., Martin, C. & Yoneyama, H. Charge-Discharge Properties of Composite of Synthetic Graphite and Poly (3-n-hexylthiophene) as an Anode Active Material in Rechargeable Lithium-Ion Batteries. *Journal Of The Electrochemical Society*. **145**, 1415 (1998)

[154] Parikh, P., Sina, M., Banerjee, A., Wang, X., D'Souza, M., Doux, J., Wu, E., Trieu, O., Gong, Y., Zhou, Q. & Others Role of polyacrylic acid (PAA) binder on the solid electrolyte interphase in silicon anodes. *Chemistry Of Materials*. **31**, 2535-2544 (2019)

[155] Shen, L., Shen, L., Wang, Z. & Chen, L. In situ thermally cross-linked polyacrylonitrile as binder for high-performance silicon as lithium ion battery anode. *ChemSusChem*. **7**, 1951-1956 (2014)

[156] Magasinski, A., Zdyrko, B., Kovalenko, I., Hertzberg, B., Burtovyy, R., Huebner, C., Fuller, T., Luzinov, I. & Yushin, G. Toward efficient binders for Li-ion battery Si-based anodes: polyacrylic acid. *ACS Applied Materials & Interfaces*. **2**, 3004-3010 (2010)

[157] Gao, S., Sun, F., Brady, A., Pan, Y., Erwin, A., Yang, D., Tsukruk, V., Stack, A., Saito, T., Yang, H. & Others Ultra-efficient polymer binder for silicon anode in high-capacity lithium-ion batteries. *Nano Energy*. **73** pp. 104804 (2020)

[158] Garsuch, R., Le, D., Garsuch, A., Li, J., Wang, S., Farooq, A. & Dahn, J. Studies of lithium-exchanged nafion as an electrode binder for alloy negatives in lithium-ion batteries. *Journal Of The Electrochemical Society*. **155**, A721 (2008)

[159] Komaba, S., Shimomura, K., Yabuuchi, N., Ozeki, T., Yui, H. & Konno, K. Study on polymer binders for high-capacity SiO negative electrode of Li-ion batteries. *The Journal Of Physical Chemistry C*. **115**, 13487-13495 (2011)

[160] Bridel, J., Azais, T., Morcrette, M., Tarascon, J. & Larcher, D. Key parameters governing the reversibility of Si/carbon/CMC electrodes for Li-ion batteries. *Chemistry Of Materials*. **22**, 1229-1241 (2010)

[161] Chen, H., Ling, M., Hencz, L., Ling, H., Li, G., Lin, Z., Liu, G. & Zhang, S. Exploring chemical, mechanical, and electrical functionalities of binders for advanced energy-storage devices. *Chemical Reviews*. **118**, 8936-8982 (2018)

[162] Oh, J., Geiculescu, O., DesMarteau, D. & Creager, S. Ionomer binders can improve discharge rate capability in lithium-ion battery cathodes. *Journal Of The Electrochemical Society*. **158**, A207 (2010)

[163] Singhal, A., Skandan, G., Amatucci, G., Badway, F., Ye, N., Manthiram, A., Ye, H. & Xu, J. Nanostructured electrodes for next generation rechargeable electrochemical devices. *Journal Of Power Sources*. **129**, 38-44 (2004)

[164] Wei, G., Lu, X., Ke, F., Huang, L., Li, J., Wang, Z., Zhou, Z. & Sun, S. Crystal habit-tuned nanoplate material of Li [Li1/3–2x/3NixMn2/3–x/3] O2 for high-rate performance lithium-ion batteries. *Advanced Materials*. **22**, 4364-4367 (2010)

[165] Spreafico, M., Cojocaru, P., Magagnin, L., Triulzi, F. & Apostolo, M. PVDF latex as a binder for positive electrodes in lithium-ion batteries. *Industrial & Engineering Chemistry Research*. **53**, 9094-9100 (2014)

[166] Zheng, H., Yang, R., Liu, G., Song, X. & Battaglia, V. Cooperation between active material, polymeric binder and conductive carbon additive in lithium ion battery cathode. *The Journal Of Physical Chemistry C*. **116**, 4875-4882 (2012)

[167] Szabo, A. & Ostlund, N. Modern quantum chemistry: introduction to advanced electronic structure theory. pp 207–420 (Courier Corporation,1996)

[168] Szabo, A. & Ostlund, N. Modern quantum chemistry: introduction to advanced electronic structure theory. pp 421–490 (Courier Corporation,1996)

[169] Schrödinger, E. Quantisierung als eigenwertproblem. *Annalen Der Physik*. **386**, 109-139 (1926)

[170] Born, M. & Oppenheimer, J. Zur Quantentheorie der Molekeln. *Annalen Der Physik*. **389**, 457-484 (1927)

[171] Hartree, D. The wave mechanics of an atom with a non-coulomb central field. Part II. Some results and discussion. *Mathematical Proceedings Of The Cambridge Philosophical Society*. **24**, 111-132 (1928)

[172] Jensen, F. Introduction to computational chemistry. (John wiley & sons,2017)

[173] Hohenberg, P. & Kohn, W. Density functional theory (DFT). *Phys. Rev*. **136**, B864 (1964)

[174] Kohn, W. & Sham, L. Self-consistent equations including exchange and correlation effects. *Physical Review*. **140**, A1133 (1965)

[175] Jones, R. Density functional theory: Its origins, rise to prominence, and future. *Reviews Of Modern Physics*. **87**, 897-923 (2015)

[176] Fermi, E. Statistical method to determine some properties of atoms. *Rend. Accad. Naz. Lincei*. **6**, 5 (1927)

[177] Hohenberg, P. & Kohn, W. Inhomogeneous electron gas. *Physical Review*. **136**, B864 (1964)

[178] Lieb, E. Density functionals for Coulomb systems. *Inequalities: Selecta Of Elliott H. Lieb*. pp. 269-303 (2002)

[179] Koch, W. & Holthausen, M. A chemist's guide to density functional theory. (John Wiley & Sons,2015)

[180] Perdew, J., Chevary, J., Vosko, S., Jackson, K., Pederson, M., Singh, D. & Fiolhais, C. Atoms, molecules, solids, and surfaces: Applications of the generalized gradient approximation for exchange and correlation. *Physical Review B*. **46**, 6671 (1992)

[181] Perdew, J., Ernzerhof, M. & Burke, K. Rationale for mixing exact exchange with density functional approximations. *The Journal Of Chemical Physics*. **105**, 9982-9985 (1996)

[182] Becke, A. Density-functional exchange-energy approximation with correct asymptotic behavior. *Physical Review A*. **38**, 3098 (1988)

[183] Ernzerhof, M. & Scuseria, G. Assessment of the Perdew-Burke-Ernzerhof exchange-correlation functional. *The Journal Of Chemical Physics*. **110**, 5029-5036 (1999)

[184] Waals, J. Over de Continuiteit van den Gas-en Vloeistoftoestand. (Sijthoff,1873)

[185] Berland, K., Cooper, V., Lee, K., Schröder, E., Thonhauser, T., Hyldgaard, P. & Lundqvist, B. van der Waals forces in density functional theory: a review of the vdW-DF method. *Reports On Progress In Physics*. **78**, 066501 (2015)

[186] Grimme, S. Semiempirical GGA-type density functional constructed with a long-range dispersion correction. *Journal Of Computational Chemistry*. **27**, 1787-1799 (2006)

[187] Barone, V., Casarin, M., Forrer, D., Pavone, M., Sambi, M. & Vittadini, A. Role and effective treatment of dispersive forces in materials: Polyethylene and graphite crystals as test cases. *Journal Of Computational Chemistry*. **30**, 934-939 (2009)

[188] Anisimov, V., Zaanen, J. & Andersen, O. Band theory and Mott insulators: Hubbard U instead of Stoner I. *Physical Review B*. **44**, 943 (1991)

[189] Solovyev, I., Dederichs, P. & Anisimov, V. Corrected atomic limit in the local-density approximation and the electronic structure of d impurities in Rb. *Physical Review B*. **50**, 16861 (1994)

[190] Anisimov, V., Aryasetiawan, F. & Lichtenstein, A. First-principles calculations of the electronic structure and spectra of strongly correlated systems: the LDA+ U method. *Journal Of Physics: Condensed Matter*. **9**, 767 (1997)

[191] Himmetoglu, B., Floris, A., De Gironcoli, S. & Cococcioni, M. Hubbard-corrected DFT energy functionals: The LDA+ U description of correlated systems. *International Journal Of Quantum Chemistry*. **114**, 14-49 (2014)

[192] Hubbard, J. Electron correlations in narrow energy bands. *Proceedings Of The Royal Society Of London. Series A. Mathematical And Physical Sciences*. **276**, 238-257 (1963)

[193] Anisimov, V., Solovyev, I., Korotin, M., Czyżyk, M. & Sawatzky, G. Density-functional theory and NiO photoemission spectra. *Physical Review B*. **48**, 16929 (1993)

[194] Liechtenstein, A., Anisimov, V. & Zaanen, J. Density-functional theory and strong interactions: Orbital ordering in Mott-Hubbard insulators. *Physical Review B*. **52**, R5467 (1995)

[195] Dudarev, S., Botton, G., Savrasov, S., Humphreys, C. & Sutton, A. Electron-energy-loss spectra and the structural stability of nickel oxide: An LSDA+ U study. *Physical Review B*. **57**, 1505 (1998)

[196] Aykol, M. & Wolverton, C. Local environment dependent GGA+ U method for accurate thermochemistry of transition metal compounds. *Physical Review B*. **90**, 115105 (2014)

[197] Franchini, C., Podloucky, R., Paier, J., Marsman, M. & Kresse, G. Ground-state properties of multivalent manganese oxides: Density functional and hybrid density functional calculations. *Physical Review B—Condensed Matter And Materials Physics*. **75**, 195128 (2007)

[198] Jain, A., Hautier, G., Ong, S., Moore, C., Fischer, C., Persson, K. & Ceder, G. Formation enthalpies by mixing GGA and GGA+ U calculations. *Physical Review B—Condensed Matter And Materials Physics*. **84**, 045115 (2011)

[199] Getsoian, A. & Bell, A. The influence of functionals on density functional theory calculations of the properties of reducible transition metal oxide catalysts. *The Journal Of Physical Chemistry C*. **117**, 25562-25578 (2013)

[200] Lutfalla, S., Shapovalov, V. & Bell, A. Calibration of the DFT/GGA+ U method for determination of reduction energies for transition and rare earth metal oxides of Ti, V, Mo, and Ce. *Journal Of Chemical Theory And Computation*. **7**, 2218-2223 (2011)

[201] Cococcioni, M. & De Gironcoli, S. Linear response approach to the calculation of the effective interaction parameters in the LDA+ U method. *Physical Review B—Condensed Matter And Materials Physics*. **71**, 035105 (2005)

[202] Hellmann, H. A new approximation method in the problem of many electrons. *The Journal Of Chemical Physics*. **3**, 61-61 (1935)

[203] Fermi, E. Sopra lo spostamento per pressione delle righe elevate delle serie spettrali. *Il Nuovo Cimento (1924-1942)*. **11** pp. 157-166 (1934)

[204] Gombás, P. Über die metallische Bindung. *Zeitschrift Für Physik*. **94** pp. 473-488 (1935)

[205] Weeks, J. & Rice, S. Use of pseudopotentials in atomic-structure calculations. *The Journal Of Chemical Physics*. **49**, 2741-2755 (1968)

[206] Wikipedia contributors Pseudopotential. (https://en.wikipedia.org/wiki/Pseudopotential,2023), [Online; accessed 30.04.2025]

[207] Pulay, P. Convergence acceleration of iterative sequences. The case of SCF iteration. *Chemical Physics Letters*. **73**, 393-398 (1980)

[208] Marzari, N. & Vanderbilt, D. Maximally localized generalized Wannier functions for composite energy bands. *Physical Review B*. **56**, 12847 (1997)

[209] Giannozzi, P., Baroni, S., Bonini, N., Calandra, M., Car, R., Cavazzoni, C., Ceresoli, D., Chiarotti, G., Cococcioni, M., Dabo, I. & Others QUANTUM ESPRESSO: a modular and open-source software project for quantumsimulations of materials. *Journal Of Physics: Condensed Matter*. **21**, 395502 (2009)

[210] Giannozzi, P., Andreussi, O., Brumme, T., Bunau, O., Nardelli, M., Calandra, M., Car, R., Cavazzoni, C., Ceresoli, D., Cococcioni, M. & Others Advanced capabilities for materials modelling with Quantum ESPRESSO. *Journal Of Physics: Condensed Matter*. **29**, 465901 (2017)

[211] Giannozzi, P., Baseggio, O., Bonfà, P., Brunato, D., Car, R., Carnimeo, I., Cavazzoni, C., De Gironcoli, S., Delugas, P., Ferrari Ruffino, F. & Others Quantum ESPRESSO toward the exascale. *The Journal Of Chemical Physics*. **152** (2020)

[212] Dal Corso, A. Pseudopotentials periodic table: From H to Pu. *Computational Materials Science*. **95** pp. 337-350 (2014)

[213] Perdew, J., Ruzsinszky, A., Csonka, G., Vydrov, O., Scuseria, G., Constantin, L., Zhou, X. & Burke, K. Restoring the density-gradient expansion for exchange in solids and surfaces. *Physical Review Letters*. **100**, 136406 (2008)

[214] Perdew, J. & Zunger, A. Self-interaction correction to density-functional approximations for many-electron systems. *Physical Review B*. **23**, 5048 (1981)

[215] Jain, A., Ong, S., Hautier, G., Chen, W., Richards, W., Dacek, S., Cholia, S., Gunter, D., Skinner, D., Ceder, G. & Others Commentary: The Materials Project: A materials genome approach to accelerating materials innovation. *APL Materials*. **1** (2013)

[216] Hanwell, M., Curtis, D., Lonie, D., Vandermeersch, T., Zurek, E. & Hutchison, G. Avogadro: an advanced semantic chemical editor, visualization, and analysis platform. *Journal Of Cheminformatics*. **4** pp. 1-17 (2012)

[217] Hinuma, Y., Pizzi, G., Kumagai, Y., Oba, F. & Tanaka, I. Band structure diagram paths based on crystallography. *Computational Materials Science*. **128** pp. 140-184 (2017)

[218] Momma, K. & Izumi, F. VESTA: a three-dimensional visualization system for electronic and structural analysis. *Applied Crystallography*. **41**, 653-658 (2008)

[219] Kokalj, A. XCrySDen—a new program for displaying crystalline structures and electron densities. *Journal Of Molecular Graphics And Modelling*. **17**, 176-179 (1999)

[220] Chin, Y., Buda, C., Neurock, M. & Iglesia, E. Selectivity of chemisorbed oxygen in C–H bond activation and CO oxidation and kinetic consequences for CH4–O2 catalysis on Pt and Rh clusters. *Journal Of Catalysis*. **283**, 10-24 (2011)

[221] Kurzman, J., Misch, L. & Seshadri, R. Chemistry of precious metal oxides relevant to heterogeneous catalysis. *Dalton Transactions*. **42**, 14653-14667 (2013)

[222] Galván, A., Calleja, J., Fañanás, F. & Rodrıǵuez, F. Catalytic generation and selective heterocoupling of two electron-rich alkenes.. *Angewandte Chemie International Edition*. **52** (2013)

[223] Korchak, V., Grishin, M., Bykhovskii, M., Gatin, A., Slutskii, V., Kharitonov, V., Tsyganov, S. & Shub, B. Ethylene Hydrogenation on a Platinum Nanocoating at Various Electric Potentials. *Russian Journal Of Physical Chemistry B*. **11** pp. 932-936 (2017)

[224] The Materials Project Materials Data on Pt by Materials Project. (United States,2020,7), https://doi.org/10.17188/1189002

[225] Waseda, Y., Hirata, K. & Ohtani, M. High-temperature thermal expansion of platinum, tantalum, molybdenum, and tungsten measured by X-ray diffraction. *High Temperatures-High Pressures*. **7**, 221-226 (1975)

[226] Stamenkovic, V., Mun, B., Arenz, M., Mayrhofer, K., Lucas, C., Wang, G., Ross, P. & Markovic, N. Trends in electrocatalysis on extended and nanoscale Pt-bimetallic alloy surfaces. *Nature Materials*. **6**, 241-247 (2007)

[227] Perdew, J., Burke, K. & Ernzerhof, M. Generalized gradient approximation made simple. *Physical Review Letters*. **77**, 3865 (1996)

[228] Needs, R., Godfrey, M. & Mansfield, M. Theory of surface stress and surface reconstruction. *Surface Science*. **242**, 215-221 (1991)

[229] Mauritz, K. & Moore, R. State of understanding of Nafion. *Chemical Reviews*. **104**, 4535-4586 (2004)

[230] Weber, A. & Newman, J. Modeling transport in polymer-electrolyte fuel cells. *Chemical Reviews*. **104**, 4679-4726 (2004)

[231] Shin, S., Nur, P., Kodir, A., Kwak, D., Lee, H., Shin, D. & Bae, B. Improving the mechanical durability of short-side-chain perfluorinated polymer electrolyte membranes by annealing and physical reinforcement. *ACS Omega*. **4**, 19153-19163 (2019)

[232] Hickner, M., Ghassemi, H., Kim, Y., Einsla, B. & McGrath, J. Alternative polymer systems for proton exchange membranes (PEMs). *Chemical Reviews*. **104**, 4587-4612 (2004)

[233] Kusoglu, A. & Weber, A. New insights into perfluorinated sulfonic-acid ionomers. *Chemical Reviews*. **117**, 987-1104 (2017)

[234] Cha, J. Morphological effect of side chain on H3O+ transfer inside polymer electrolyte membranes across polymeric chain via molecular dynamics simulation. *Scientific Reports*. **10**, 22014 (2020)

[235] Asghar, M., Zhang, W., Su, H., Zhang, J., Rhimi, B., Liu, H., Xing, L., Yan, X. & Xu, Q. A review of additional modifications of additives through hydrophilic functional groups for the application of proton exchange membranes in fuel cells. *Journal Of Power Sources*. **622** pp. 235353 (2024)

[236] Chen, C., Levitin, G., Hess, D. & Fuller, T. XPS investigation of Nafion® membrane degradation. *Journal Of Power Sources*. **169**, 288-295 (2007)

[237] Kundu, S., Simon, L. & Fowler, M. Comparison of two accelerated Nafion™ degradation experiments. *Polymer Degradation And Stability*. **93**, 214-224 (2008).

[238] Dafalla, A., Wei, L., Habte, B., Guo, J. & Jiang, F. Membrane electrode assembly degradation modeling of proton exchange membrane fuel cells: A review. *Energies*. **15**, 9247 (2022).

[239] Okonkwo, P., Belgacem, I., Emori, W. & Uzoma, P. Nafion degradation mechanisms in proton exchange membrane fuel cell (PEMFC) system: A review. *International Journal Of Hydrogen Energy*. **46**, 27956-27973 (2021).

[240] Xie, J., Ban, S., Liu, B. & Zhou, H. A molecular simulation study of chemical degradation and mechanical deformation of hydrated Nafion membranes. *Applied Surface Science*. **362** pp. 441-447 (2016).

[241] Bajaj, A., Liu, F. & Kulik, H. Uncovering Alternate Pathways to Nafion Membrane Degradation in Fuel Cells with First-Principles Modeling. *The Journal Of Physical Chemistry C*. **124**, 15094-15106 (2020).

[242] Zatoń, M., Rozière, J. & Jones, D. Current understanding of chemical degradation mechanisms of perfluorosulfonic acid membranes and their mitigation strategies: a review. *Sustainable Energy & Fuels*. **1**, 409-438 (2017).

[243] Ghassemzadeh, L., Peckham, T., Weissbach, T., Luo, X. & Holdcroft, S. Selective formation of hydrogen and hydroxyl radicals by electron beam irradiation and their reactivity with perfluorosulfonated acid ionomer. *Journal Of The American Chemical Society*. **135**, 15923-15932 (2013).

[244] Schiraldi, D. Perfluorinated polymer electrolyte membrane durability. *Journal Of Macromolecular Science, Part C: Polymer Reviews*. **46**, 315-327 (2006).

[245] Healy, J., Hayden, C., Xie, T., Olson, K., Waldo, R., Brundage, M., Gasteiger, H. & Abbott, J. Aspects of the chemical degradation of PFSA ionomers used in PEM fuel cells. *Fuel Cells*. **5**, 302-308 (2005).

[246] Zhou, C., Guerra, M., Qiu, Z., Zawodzinski, T. & Schiraldi, D. Chemical durability studies of perfluorinated sulfonic acid polymers and model compounds under mimic fuel cell conditions. *Macromolecules*. **40**, 8695-8707 (2007).

[247] Yu, T., Sha, Y., Liu, W., Merinov, B., Shirvanian, P. & Goddard III, W. Mechanism for degradation of Nafion in PEM fuel cells from quantum mechanics calculations. *Journal Of The American Chemical Society*. **133**, 19857-19863 (2011).

[248] Zhao, Y., Yamaguchi, M., Tsuchida, E., Choe, Y. & Ikeshoji, T. DFT studies of perfluorosulfonic acid ionomer degradation in fuel cells. *The Journal Of Physical Chemistry C*. **122**, 20135-20143 (2018).

[249] Hu, Y., Li, J. & Wang, S. Examination of the performance of degraded Nafion membrane with graphene oxide. *International Journal Of Hydrogen Energy*. **48**, 31734-31744 (2023)

[250] Li, H., Tang, Y., Wang, Z., Shi, Z., Wu, S., Song, D., Zhang, J., Fatih, K., Zhang, J., Wang, H. & Others A review of water flooding issues in the proton exchange membrane fuel cell. *Journal Of Power Sources*. **178**, 103-117 (2008)

[251] De Grotthuss, C. Memoir on the decomposition of water and of the bodies that it holds in solution by means of galvanic electricity. *Biochimica Et Biophysica Acta (BBA)-Bioenergetics*. **1757**, 871-875 (2006)

[252] Peckham, T. & Holdcroft, S. Structure-morphology-property relationships of non-perfluorinated proton-conducting membranes. *Advanced Materials*. **22**, 4667-4690 (2010)

[253] Cappadonia, M., Erning, J., Niaki, S. & Stimming, U. Conductance of Nafion 117 membranes as a function of temperature and water content. *Solid State Ionics*. **77** pp. 65-69 (1995)

[254] Kreuer, K. On the development of proton conducting materials for technological applications. *Solid State Ionics*. **97**, 1-15 (1997)

[255] Kreuer, K. On the development of proton conducting polymer membranes for hydrogen and methanol fuel cells. *Journal Of Membrane Science*. **185**, 29-39 (2001)

[256] Dokmaisrijan, S. & Spohr, E. MD simulations of proton transport along a model Nafion surface decorated with sulfonate groups. *Journal Of Molecular Liquids*. **129**, 92-100 (2006)

[257] Affoune, A., Yamada, A. & Umeda, M. Conductivity and surface morphology of Nafion membrane in water and alcohol environments. *Journal Of Power Sources*. **148** pp. 9-17 (2005)

[258] Jianbo, Z., Deok-im, J., Chunxin, J. & Shouzhong, Z. In Situ Surface-Enhanced Raman Spectroscopic Studies of Nafion Adsorption on Au and Pt Electrodes. (2012)

[259] Yagi, I., Inokuma, K., Kimijima, K. & Notsu, H. Molecular structure of buried perfluorosulfonated ionomer/Pt interface probed by vibrational sum frequency generation spectroscopy. *The Journal Of Physical Chemistry C*. **118**, 26182-26190 (2014)

[260] Ono, Y. & Nagao, Y. Interfacial structure and proton conductivity of Nafion at the Pt-deposited surface. *Langmuir*. **32**, 352-358 (2016)

[261] Ogasawara, H., Brena, B., Nordlund, D., Nyberg, M., Pelmenschikov, A., Pettersson, L. & Nilsson, A. Structure and bonding of water on Pt (111). *Physical Review Letters*. **89**, 276102 (2002)

[262] Michaelides, A., Ranea, V., De Andres, P. & King, D. General Model for Water Monomer Adsorption on Close-Packed Transition and Noble Metal Surfaces. *Physical Review Letters*. **90**, 216102 (2003)

[263] Nie, S., Feibelman, P., Bartelt, N. & Thürmer, K. Pentagons and heptagons in the first water layer on Pt (111). *Physical Review Letters*. **105**, 026102 (2010)

[264] Goodenough, J. & Park, K. The Li-ion rechargeable battery: a perspective. *Journal Of The American Chemical Society*. **135**, 1167-1176 (2013)

[265] Goodenough, J. & Kim, Y. Challenges for rechargeable Li batteries. *Chemistry Of Materials*. **22**, 587-603 (2010)

[266] Shi, S., Gao, J., Liu, Y., Zhao, Y., Wu, Q., Ju, W., Ouyang, C. & Xiao, R. Multi-scale computation methods: Their applications in lithium-ion battery research and development. *Chinese Physics B*. **25**, 018212 (2015)

[267] Urban, A., Seo, D. & Ceder, G. Computational understanding of Li-ion batteries. *Npj Computational Materials*. **2**, 1-13 (2016)

[268] Maji, R., Salvador, M., Ruini, A., Magri, R., Taskin, O., Yuca, N. & Degoli, E. Insights into the stability and reactivity of lithiated Si-binder interfaces for next generation lithium-ion batteries. *Journal Of Power Sources*. **610** pp. 234705 (2024)

[269] Zhang, M., Liang, N., Hao, D., Chen, Z., Zhang, F., Yin, J., Yang, Y. & Yang, L. Recent advances of SiOx-based anodes for sustainable lithium-ion batteries. *Nano Res. Energy*. **2** pp. e9120077 (2023)

[270] Maji, R., Salvador, M., Ruini, A., Magri, R. & Degoli, E. A first-principles study of self-healing binders for next-generation Si-based lithium-ion batteries. *Materials Today Chemistry*. **29** pp. 101474 (2023)

[271] Chen, T., Wu, J., Zhang, Q. & Su, X. Recent advancement of SiOx based anodes for lithium-ion batteries. *Journal Of Power Sources*. **363** pp. 126-144 (2017)

[272] Jiang, Y., Liu, S., Ding, Y., Jiang, J., Li, W., Huang, S., Chen, Z., Zhao, B. & Zhang, J. Modification based on primary particle level to improve the electrochemical performance of SiOx-based anode materials. *Journal Of Power Sources*. **467** pp. 228301 (2020)

[273] Jing, J., Zhang, C., Li, Q., Li, C., Yao, S., Li, T. & Bai, X. Study of commercial binders on the lithium storage performance of SiOx/G@ C anode. *Materials Chemistry And Physics*. **292** pp. 126797 (2022)

[274] You, Z., Lin, C., Zheng, P., Li, J., Feng, Q., Tao, J., Zheng, Y., Lin, Y., Huang, Z. & Li, J. Fluorine-Doping Carbon-Modified Si/SiOx to Effectively Achieve High-Performance Anode. *Small*. pp. 2407215 (2024)

[275] Wu, R., Du, X., Liu, T., Zhuang, X., Guan, P., Zhang, B., Zhang, S., Gao, C., Xu, G., Zhou, X. & Others Robust and Fast-Ion Conducting Interphase Empowering SiOx Anode Toward High Energy Lithium–Ion Batteries. *Advanced Energy Materials*. **14**, 2302899 (2024)

[276] Wu, H., Yu, G., Pan, L., Liu, N., McDowell, M., Bao, Z. & Cui, Y. Stable Li-ion battery anodes by in-situ polymerization of conducting hydrogel to conformally coat silicon nanoparticles. *Nature Communications*. **4**, 1943 (2013)

[277] Liu, N., Wu, H., McDowell, M., Yao, Y., Wang, C. & Cui, Y. A yolk-shell design for stabilized and scalable Li-ion battery alloy anodes. *Nano Letters*. **12**, 3315-3321 (2012)

[278] Gerbig, Y., Stranick, S., Morris, D., Vaudin, M. & Cook, R. Effect of crystallographic orientation on phase transformations during indentation of silicon. *Journal Of Materials Research*. **24**, 1172-1183 (2009)

[279] Yu, B. & Qian, L. Effect of crystal plane orientation on the friction-induced nanofabrication on monocrystalline silicon. *Nanoscale Research Letters*. **8** pp. 1-8 (2013)

[280] Xiao, C., Guo, J., Zhang, P., Chen, C., Chen, L. & Qian, L. Effect of crystal plane orientation on tribochemical removal of monocrystalline silicon. *Scientific Reports*. **7**, 40750 (2017)

[281] Nolan, M., Legesse, M. & Fagas, G. Surface orientation effects in crystalline–amorphous silicon interfaces. *Physical Chemistry Chemical Physics*. **14**, 15173-15179 (2012)

[282] Gupta, A., Bruce, J., McEleney, K., Freund, M. & Oliver, D. Monohydride signature as a key predictor of successful Si (110) surface functionalization. *RSC Advances*. **6**, 88239-88243 (2016)

[283] Fu, R., Zhang, K., Zaccaria, R., Huang, H., Xia, Y. & Liu, Z. Two-dimensional silicon suboxides nanostructures with Si nanodomains confined in amorphous SiO2 derived from siloxene as high performance anode for Li-ion batteries. *Nano Energy*. **39** pp. 546-553 (2017)

[284] Liu, Z., Yu, Q., Zhao, Y., He, R., Xu, M., Feng, S., Li, S., Zhou, L. & Mai, L. Silicon oxides: a promising family of anode materials for lithium-ion batteries. *Chemical Society Reviews*. **48**, 285-309 (2019)

[285] Majeed, M., Ma, G., Cao, Y., Mao, H., Ma, X. & Ma, W. Metal–Organic Frameworks-Derived Mesoporous Si/SiOx@ NC Nanospheres as a Long-Lifespan Anode Material for Lithium-Ion Batteries. *Chemistry–A European Journal*. **25**, 11991-11997 (2019)

[286] Fan, S., Zhou, X., Tang, J., Ma, Y. & Yang, J. Insights to the variation of oxygen content and reasons for improved electrochemical performance of annealing SiOx anodes for Li-ion battery. *Applied Surface Science*. **579** pp. 152179 (2022)

[287] Pan, Y. & Tzeng, Y. Silicon Nanoparticles in Graphene Sponge for Long-Cycling-Life and High-Capacity Anode of Lithium Ion Battery. *IEEE Transactions On Nanotechnology*. **18** pp. 1097-1102 (2019)

[288] Li, Z., Stetson, C., Frisco, S., Harvey, S., Huey, Z., Teeter, G., Engtrakul, C., Burrell, A., Li, X. & Zakutayev, A. The role of oxygen in lithiation and solid electrolyte interphase formation processes in silicon-based anodes. *Journal Of The Electrochemical Society*. **169**, 120512 (2022)

[289] Salah, M., Hall, C., Murphy, P., Francis, C., Kerr, R., Stoehr, B., Rudd, S. & Fabretto, M. Doped and reactive silicon thin film anodes for lithium ion batteries: A review. *Journal Of Power Sources*. **506** pp. 230194 (2021)

[290] Kalidas, N., Shen, X., Yuan, M., Zhao, X. & Lehto, V. Controlled surface oxidation of mesoporous silicon microparticles to achieve a stable Si/SiOx anode for lithium-ion batteries. *Microporous And Mesoporous Materials*. **344** pp. 112243 (2022)

[291] Widjaja, Y. & Musgrave, C. Atomistic mechanism of the initial oxidation of the clean Si (100)-(2×1) surface by O 2 and SiO 2 decomposition. *The Journal Of Chemical Physics*. **116**, 5774-5780 (2002)

[292] Incze, A., Del Sole, R. & Onida, G. Ab initio study of reflectance anisotropy spectra of a submonolayer oxidized Si (100) surface. *Physical Review B*. **71**, 035350 (2005)

[293] Witkowski, N., Gaál-Nagy, K., Fuchs, F., Pluchery, O., Incze, A., Bechstedt, F., Borensztein, Y., Onida, G. & Del Sole, R. All-optical determination of initial oxidation of Si (100) and its kinetics. *The European Physical Journal B*. **66** pp. 427-431 (2008)

[294] Zhang, Z., Minca, M., Deisl, C., Loerting, T., Menzel, A., Bertel, E., Zucca, R. & Redinger, J. H on Pt (110): An atypical chemisorption site at low coverages. *Physical Review B—Condensed Matter And Materials Physics*. **70**, 121401 (2004)

[295] Poelsema, B., Mechtersheimer, G. & Comsa, G. The interaction of hydrogen with platinum (s)- 9 (111)x(111) studied with helium beam diffraction. *Surface Science*. **111**, 519-544 (1981)

[296] Richter, L. & Ho, W. Vibrational spectroscopy of H on Pt (111): Evidence for universally soft parallel modes. *Physical Review B*. **36**, 9797 (1987)

[297] Olsen, R., Kroes, G. & Baerends, E. Atomic and molecular hydrogen interacting with Pt (111). *The Journal Of Chemical Physics*. **111**, 11155-11163 (1999)

[298] Shi, Q. & Sun, R. Adsorption manners of hydrogen on Pt (1 0 0),(1 1 0) and (1 1 1) surfaces at high coverage. *Computational And Theoretical Chemistry*. **1106** pp. 43-49 (2017)

[299] Vasić, D., Ristanović, Z., Pašti, I. & Mentus, S. Systematic DFT-GGA study of hydrogen adsorption on transition metals. *Russian Journal Of Physical Chemistry A*. **85**, 2373-2379 (2011)

[300] Mansour, H. & Iglesia, E. Theoretical and Experimental Assessments of Elementary Steps and Bound Intermediates in Catalytic H2–O2 Reactions on Dispersed Pt Nanoparticles. *The Journal Of Physical Chemistry C*. **127**, 4553-4569 (2023)

[301] Kang, H., Kwon, S., Lawler, R., Lee, J., Doo, G., Kim, H., Yim, S., Jang, S. & Lee, S. Nanostructures of nafion film at platinum/carbon surface in catalyst layer of PEMFC: Molecular dynamics simulation approach. *The Journal Of Physical Chemistry C*. **124**, 21386-21395 (2020)

[302] Sengupta, S. & Lyulin, A. Molecular modeling of structure and dynamics of Nafion protonation states. *The Journal Of Physical Chemistry B*. **123**, 6882-6891 (2019)

[303] Modestino, M., Kusoglu, A., Hexemer, A., Weber, A. & Segalman, R. Controlling nafion structure and properties via wetting interactions. *Macromolecules*. **45**, 4681-4688 (2012)

[304] Sengupta, S. & Lyulin, A. Molecular dynamics simulations of substrate hydrophilicity and confinement effects in capped Nafion films. *The Journal Of Physical Chemistry B*. **122**, 6107-6119 (2018)

[305] Jiang, S., Xiang, Q., Xie, Z., Yang, N., Liu, J., Li, L. & Wei, Z. Influence of the Pt/ionomer/water interface on the oxygen reduction reaction: insights into the micro-three-phase interface. *Chemical Science*. **15**, 19290-19298 (2024)

[306] Han, Z., Pei, S., Yu, C. & Zhou, Y. Understanding the mechanism of hydrogen transport in imidazolyl polymers doped Nafion membranes via molecular dynamics simulations: Case of PVMZ/Nafion. *International Journal Of Hydrogen Energy*. **72** pp. 437-448 (2024)

[307] Li, Y., Kottwitz, M., Vincent, J., Enright, M., Liu, Z., Zhang, L., Huang, J., Senanayake, S., Yang, W., Crozier, P., Nuzzo, R. & Frenkel, A. Dynamic structure of active sites in ceria-supported Pt catalysts for the water gas shift reaction. *Nature Communications* . **12**, 914 (2021)

[308] Henkelman, G., Arnaldsson, A. & Jónsson, H. A fast and robust algorithm for Bader decomposition of charge density. *Computational Materials Science*. **36**, 354-360 (2006)

[309] Sanville, E., Kenny, S., Smith, R. & Henkelman, G. Improved grid-based algorithm for Bader charge allocation. *Journal Of Computational Chemistry*. **28**, 899-908 (2007)

[310] Tang, W., Sanville, E. & Henkelman, G. A grid-based Bader analysis algorithm without lattice bias. *Journal Of Physics: Condensed Matter*. **21**, 084204 (2009)

[311] Yu, M. & Trinkle, D. Accurate and efficient algorithm for Bader charge integration. *The Journal Of Chemical Physics*. **134** (2011)

[312] Li, Y., Van Cleve, T., Sun, R., Gawas, R., Wang, G., Tang, M., Elabd, Y., Snyder, J. & Neyerlin, K. Modifying the electrocatalyst–ionomer interface via sulfonated poly (ionic liquid) block copolymers to enable high-performance polymer electrolyte fuel cells. *ACS Energy Letters*. **5**, 1726-1731 (2020)

[313] Paddison, S. & Paul, R. The nature of proton transport in fully hydrated Nafion®. *Physical Chemistry Chemical Physics*. **4**, 1158-1163 (2002)

[314] Lwoya, B. & Albert, J. Nanostructured block copolymers for proton exchange membrane fuel cells. *Energy And Environment Focus*. **4**, 278-290 (2015).

[315] Paddison, S. Proton conduction mechanisms at low degrees of hydration in sulfonic acid–based polymer electrolyte membranes. *Annual Review Of Materials Research*. **33**, 289-319 (2003)

[316] Tsuda, M., Diño, W. & Kasai, H. Behavior of hydrogen atom at Nafion–Pt interface. *Solid State Communications*. **134**, 601-605 (2005)

[317] Gubler, L., Dockheer, S. & Koppenol, W. Radical (HO•, H• and HOO•) formation and ionomer degradation in polymer electrolyte fuel cells. *Journal Of The Electrochemical Society*. **158**, B755 (2011)

[318] Shrivastava, U., Fritzsche, H. & Karan, K. Interfacial and bulk water in ultrathin films of nafion, 3M PFSA, and 3M PFIA ionomers on a polycrystalline platinum surface. *Macromolecules*. **51**, 9839-9849 (2018)

[319] Harada, M., Kudo, K. & Yamada, N. Compositional segregation in a cross section of wet nafion thin film on a platinum surface. *Chemistry Letters*. **48**, 51-54 (2019)

[320] Kawamoto, T., Aoki, M., Kimura, T., Chinapang, P., Mizusawa, T., Yamada, N., Nemoto, F., Watanabe, T., Tanida, H., Matsumoto, M. & Others Sublayered structures of hydrated nafion® thin film formed by casting on Pt substrate analyzed by X-ray absorption spectroscopy under ambient conditions and neutron reflectometry at temperature of 80 C and relative humidity of 30–80 %. *Electrochemistry*. **87**, 270-275 (2019)

[321] Wang, N., NuLi, Y., Su, S., Yang, J. & Wang, J. Effects of binders on the electrochemical performance of rechargeable magnesium batteries. *Journal Of Power Sources*. **341** pp. 219-229 (2017)

[322] Bera, B. & Sarkar, M. Piezoelectricity in PVDF and PVDF based piezoelectric nanogenerator: a concept. *IOSR J. Appl. Phys*. **9**, 95-99 (2017)

[323] Ren, Y., Wang, Y., Zhang, W., Yan, X. & Huang, B. Improved battery performance contributed by the optimized phase ratio of β and α of PVDF. *RSC Advances*. **9**, 29760-29764 (2019)

One day
We will once again
Find our doves

Then
Kindness and beauty
Will hold hands

The day
When the littlest song is a kiss
And when
Every human being
Is brethren to every other human being.

When no one locks their door,
Locks are fairy tales,
And the heart is all one needs to live.

The day
When the meaning of every word is to love,
So you wouldn't need to look for your last words.

The day
When the rhythm of every word is life,
And I will wait for that day,
Even if I'm no more.

ADAPTED FROM A POEM BY AHMAD SHAMLOU

IN MEMORY OF THOSE
WHO LOST THEIR LIVES DURING THE 2025–2026 PROTESTS IN IRAN,
IN THE PURSUIT OF DIGNITY, FREEDOM, AND HUMAN RIGHTS,
WHOSE COURAGE AND SACRIFICE WILL NOT BE FORGOTTEN ...